B.M. Caruta
Editor

NANOMATERIALS New Research

Contributors

Levent Aktas
M. Cengiz Altan
G. Carotenuto
Sudha Dharmavaram
Klaus Friedrich
Youssef K. Hamidi
Q. Jiang
Jae-Chun Lee
Ju-Hyeon Lee
J. C. Li
B. Martorana
L. Nicolais
Sung Park
P. Perlo
J.C. Pivin
Min Zhi Rong
Weon-Pil Tai
Bernd Wetzel
Ming Qiu Zhang

NOVA

NANOMATERIALS: NEW RESEARCH

NANOMATERIALS: NEW RESEARCH

B.M. CARUTA
EDITOR

Nova Science Publishers, Inc.
New York

NOTICE TO THE READER

Library of Congress Cataloging-in-Publication Data
Available upon request

ISBN: 978-1-60692-340-5

Published by Nova Science Publishers, Inc. ✣ New York

CONTENTS

PREFACE

Materials science includes those parts of chemistry and physics that deal with the properties of materials.

It encompasses four classes of materials, the study of each of which may be considered a separate field: metals; ceramics; polymers and composites. Materials science is often referred to as materials science and engineering because it has many applications. Industrial applications of materials science include processing techniques (casting, rolling, welding, ion implantation, crystal growth, thin-film deposition, sintering, glassblowing, etc.), analytical techniques (electron microscopy, x-ray diffraction, calorimetry, nuclear microscopy (HEFIB) etc.), materials design, and cost/benefit tradeoffs in industrial production of materials. This book presents new research directions in the very new field of nanomaterials.

In: Nanomaterials: New Research
Editor: B.M. Caruta, pp. 1-79
ISBN: 1-59454-369-0

Chapter 1

WEAR RESISTANT THERMOSETTING POLYMER BASED NANOCOMPOSITES

Ming Qiu Zhang[1*], Min Zhi Rong[1], Bernd Wetzel[2] and Klaus Friedrich[2]

[1]Materials Science Institute, Key Laboratory for Polymeric Composite and Functional Materials of Ministry of Education, Zhongshan University, Guangzhou 510275, P. R. China

[2]Institute for Composite Materials (IVW), University of Kaiserslautern, D-67663 Kaiserslautern, Germany

ABSTRACT

Thermosetting resins are finding increasing use in a wide range of engineering applications because of their on-the-spot processing characteristics, good affinity to heterogeneous materials, considerable creep and solvent resistance, and higher operating temperature. For example, they have been frequently incorporated with various inorganic particles as the binder to formulate wear resistant composite materials. The tribological properties of these composites, however, are factually far from the specifications demanded by consumers for various working conditions, especially in the case of protective coatings that should shield the substrates against mechanical wear. This is due to both the poor interfacial adhesion around the particle boundaries and the heterogeneous dispersion of the particles.

Since the predominant feature of nanoparticles lies in their ultra-fine dimension, a large fraction of the filler atoms can reside at the interface and can lead to a strong interfacial interaction when the nanoparticles are well dispersed on a nanometer level in the surrounding polymer matrix. As the interfacial structure plays a critical role in determining the composites' properties, nanocomposites coupled with a great number of interfaces are expected to provide unusual properties, and the shortcomings induced by

* Prof. Ming Qiu ZHANG; Materials Science Institute; Zhongshan University; Guangzhou 510275; P. R. China; Tel./Fax: +86-20-84036576; E-mail: ceszmq@zsu.edu.cn

the heterogeneity of conventional particles filled composites would also be avoided. On the other hand, the wear mechanisms involved in the nanocomposites are different from those of conventional composites because the fillers have the same size as the segments of the surrounding polymer chains. Severe wear caused by abrasion and particle pull-out associated with the accumulation of detached harder bulk particulate fillers adherent to the frictional surface is replaced by rather mild wear resulting from the fine individual debris which acts as a lubricant and contributes to material removal by polishing.
This chapter gives a brief but thorough review of the state of the art in the area of wear resistant nanocomposites and then carefully describes the progress made by the authors, which is focused on the surface pre-treatment of the nanoparticles and its effect on the trobological performance improvement of thermosetting nanocomposites.

1. INTRODUCTION

1.1. Particulate Filled Polymeric Composites Used for Tribological Applications

Composite materials have been employed in a vast range of applications because they offer combinations of properties unattainable with metals, ceramics or polymers alone. Especially particulate filled polymers form an interesting class of composites associated with specific microstructures, a viscoelastic nature, more preferable damage tolerance, chemical inertness, a better wear resistance, and, as a result, lower costs of routine maintenance. In this way, they can substitute traditional metallic components as self-lubricating materials employed in unlubricated, corrosive, low velocity and high loading circumstances.

Over the years, many species of inorganic particles have been used as fillers for polymers, such as solid lubricants, metal powders and oxides, and inorganic compounds. They not only act as a reinforcing agent for the bulk properties of the composites, but also impart specific properties. Regarding the effectiveness of these fillers in the modification of the wear and friction performance, hypotheses and mechanisms have been proposed by a number of researchers [1, 2], but until now, the tribological behavior of particulate filled polymers is still clouded with mysteries. In the case of thermoplastic composites, effects of fillers were mainly attributed to the following objectives:

I. modifying counterpart surface and supporting the applied load during wearing [3, 4];
II. increasing the shear strength of matrix, preventing the occurrence of large-scale destruction of polymer [5];
III. improving the adhesion of the transfer film into the counterface [6-12].

For thermosetting composites, relatively little works have been presented; recent studies were focused on fabric reinforced poly (vinyl butyral)-modified phenolic resin composites [13], unidirectionally oriented E-glass fiber reinforced epoxy composites [14], and silica filled epoxy-based coatings [15]. Nevertheless, some valuable findings are still available. For example, the adhesion between thermosetting binder and fillers should be strong enough because not only disintegration of the fillers but also detached particles were frequently

observed to be torn out of both the phenolic and epoxy resin composites when an indentor moved over the systems, resulting in sharp fluctuations in the measured coefficient of friction [16]. Yamaguchi et al [17] found that the wear rates of unsaturated polyesters and epoxy resins filled with different proportions of SiO_2 decreased significantly only at a high loading of 40 wt%, which is factually detrimental to the coating applications. Sekiguchi et al [18] studied the effects of species of conventional solid lubricants (PTFE, MoS_2, and graphite) on the tribological properties of newly synthesized thermosetting resins, i.e. condensed polycyclic aromatic (COPNA) resin. The results indicated that the most effective filler for wear reduction is graphite, while the friction coefficient is 0.35-0.8 times that of the unfilled version. Symonds and Mellor [15] stated that the silica particles in an epoxy matrix, exposed to wear loading, support a large fraction of the load. Since the particles fracture before they plastically deform, the true contact area and hence the frictional coefficient remain constant. Besides, the silica particles also reduced the wear of the coating by blocking the penetration of the steel asperity tips.

As known from short fiber reinforced composites, the fiber/polymer interfacial adhesion is greatly responsible for the wear resistance of polymer composite materials [19]. Since the weakest link of a fiber reinforced system lies at the interface, disintegration of filled materials generally takes place along interfacial boundaries. To solve this problem, chemical modifications of the fiber surfaces are used to essentially improve the wettability of the filler particles with the binder. Other approaches have overcome this problem by the creation of a self-reinforcement in the original polymers, and this was especially introduced by Song and Ehrenstein for wear resistant systems [20, 21]. Regarding the particulate filled systems, however, self-reinforcement mechanisms for improving the filler/matrix adhesion are not possible. Other results showed that the conventional filler treatments usually did not perform as outstandingly as expected because the composites were distinctly characterized by a heterogeneity on a micron scale of their structure, so that crack initiation and coalescence became much easier in the particulate-rich phase. Therefore, not only filler/matrix bonding but also the dispersion and geometry of fillers should be carefully considered. On the basis of this analysis, it can be concluded that the inhomogeneous distribution of micron size particles inevitably resulting from the conventional compounding process provides the composites with a fatal weak side, which accounts for the common three-body abrasive wear caused by the entrapped hard grits removed from the rubbing composites.

Nevertheless, incorporation of particulates was proved to be an effective way to modify polymers for tribological applications, because the latter mostly could not be used alone due to their higher coefficient of linear expansion, low thermal conductivity and unsatisfactory mechanical properties. Considering the above-stated inherent defects imparted by micron size particles, utilization of nanoparticles as fillers could be an optimum alternative to make the most of the technique based on the addition of particles.

1.2. Polymer Based Nanocomposites

Since the predominant feature of nanoparticles lies in their ultra-fine dimension, a large fraction of the filler atoms can reside at the interface and can lead to a strong interfacial interaction, but only if the nanoparticles are well dispersed on a nanometer level in the surrounding polymer matrix. As the interfacial structure plays a critical role in determining

the composites' properties, nanocomposites coupled with a great number of interfaces could be expected to provide unusual properties, and the shortcomings induced by the heterogeneity of conventional particles filled composites would also be avoided. On the other hand, the wear mechanisms involved in the nanocomposites would be different from those of conventional composites because the fillers have the same size as the segments of the surrounding polymer chains. Severe wear caused by abrasion and particle pull-out associated with the accumulation of detached harder bulk particulate fillers adherent to the frictional surface might be replaced by rather mild wear resulting from the fine individual debris which acts as a lubricant and contributes to material removal by polishing.

Recent progress indicated that polymer based nanocomposites acquired mechanical properties much higher than the usual systems at a rather low filler loading [22]. Although there are very few reports concerning the effect of nanoparticles on the tribological behavior of polymer composites, some scientists have made pilot investigations on nanoparticle/thermoplastics and nanoparticle/thermosetting composites. Wang et al [23, 24] investigated PEEK filled with nanometer-sized Si_3N_4 and SiO_2 particles by sliding the PEEK composite block against a carbon steel ring. It was found that the nanocomposites exhibited much lower wear rates and frictional coefficients than the neat PEEK matrix. Moreover, a thin, uniform and tenacious transfer film was formed on the ring surface, improving the tribological behavior of the composites. In addition, Wang et al [25] reported that the incorporation of nano-ZrO_2 (7wt %) into PEEK caused a considerable improvement in the tribological characteristics. It was found that the dominant wear mechanism changed from melting adhesive transfer wear to slight transfer wear, and finally to abrasive wear with increasing nano-ZrO_2 content. He et al [26] prepared nanoscale ceramic (TiC, Si_3N_4, B_4C)/PTFE multilayers by ion beam sputtering deposition at room temperature. Ball-on-disk tribological tests showed that the multilayers with optimized layer thickness arrangement had good performance in wear resistance. There was no obvious periodic variation in the friction coefficient. Schadler et al [27] produced silica/PA nanocomposite coatings using high-speed oxyfuel thermal spray processing; they found that the surface chemistry of the nano-silica affected the final coating properties. Silica particles with a hydrophobic surface resulted in higher scratch resistance than those with a hydrophilic surface.

It should be noticed that the smaller the size of filler particles is, the larger becomes their specific surface area, and the more likely the aggregation of the particles. Consequently, the so-called nanoparticle filled polymers sometimes contain a number of loosened clusters of particles (Fig.1), where the polymer binder is impoverished. This may exhibit properties even worse than conventional particle/polymer systems. Extensive material loss would thus occur as a result of disintegration and crumbling of the particle agglomerates under tribological conditions. It is therefore necessary to break down these nanoparticle agglomerates and to produce nanostructured composites. Some approaches have been developed in this direction as follows [22, 28-34]:

I. in-situ polymerization of metal alkoxides in organic matrices via sol-gel technique;
II. intercalation polymerization by inserting polymer chains into the sheets of smectite clay and other layered inorganic materials;
III. addition of organically modified nanoparticles to a polymer solution;
IV. in-situ polymerization of monomers at the presence of nanoparticles.

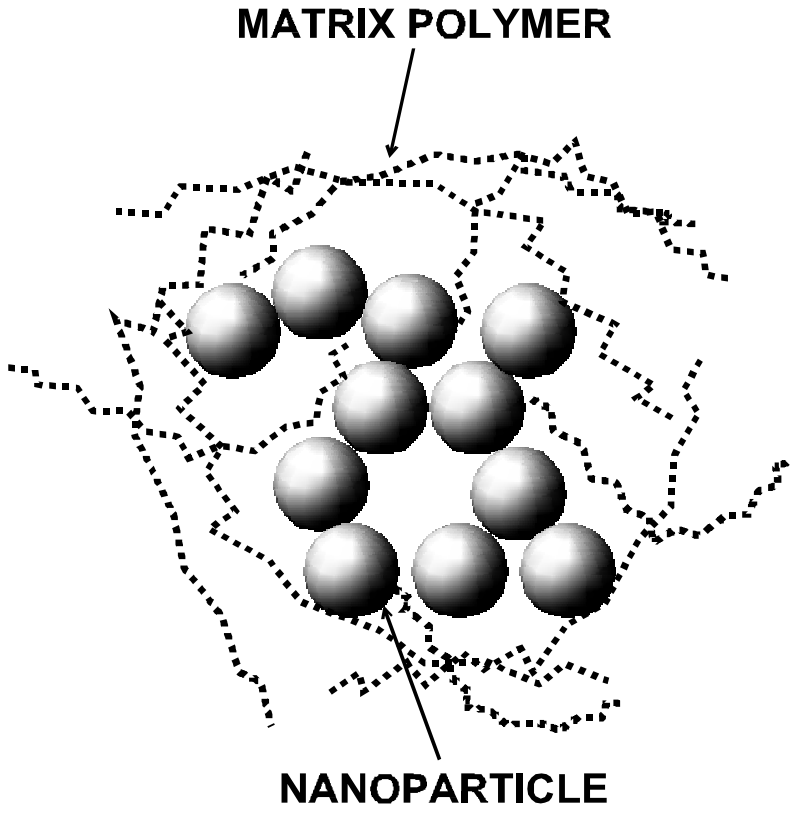

Figure1. Aggregated nanopaticles dispersed in a polymer matrix.

Since the above techniques are characterized by complex polymerization procedures and special conditions, and since they require polymerization equipment and solvent recovery, evidently a mass production of nanocomposites with cost effectiveness and applicability should better follow another route.

By examining the current technical level and the feasibility of the available processing methods, it can be concluded that the widely used compounding techniques (characterized by a direct mixing of the components) for the preparation of conventionally filled polymers is still the most convenient way. The problem is that nanoparticle agglomerates are also hard to be disconnected by the limited shear force during mixing. This is true even when a coupling agent is used [35]. Since the latter can only react with the exterior nanoparticles, the agglomerates will maintain their friable structure in the composite and can hardly provide properties improvement at all [36].

1.3. New Solutions

As convinced by the previous scientific achievements, the development of a new technique is always the most important methodology to overcome the difficulties. With respect to the above-mentioned strong tendency for nanoparticles to agglomerate, the particles should be effectively modified before being incorporated with polymer so as to obtain a

uniform dispersion state. According to our idea, nanoparticles are pretreated by irradiation to introduce grafting polymers onto the surface of the tiny particles not only outside but also inside the particle agglomerates. Owing to the low molecular weight nature, the monomers can penetrate into the agglomerated nanoparticles easily and react with the activated sites of the nanoparticles. In the course of grafting polymerization, the gap between the nanoparticles will be filled with grafting macromolecular chains, and the agglomerated nanoparticles will be separated further as a result (Fig.2). Besides, the surface of the nanoparticles will also become "hydrocarbon" due to an increased hydrophobicity resulting from the grafting polymer. This is beneficial for the filler/matrix miscibility and hence for the ultimate properties, as revealed in ref.[27]. When the pre-grafted nanoparticles are mechanically mixed with a thermosetting polymer, the former will keep their more stationary suspension state due to the interaction between the grafting polymer and the matrix. After curing of the mixture, filler/matrix adhesion would be substantially enhanced by the entanglement between the grafting polymer and the matrix polymer. This is different from composites filled with conventionally treated nanoparticle agglomerates, because direct contacts between the fillers would no longer appear due to the uniform coverage of grafting polymers on the surface of each nanoparticles even through the particles could not be dispersed completely in the form of primary nanoparticles.

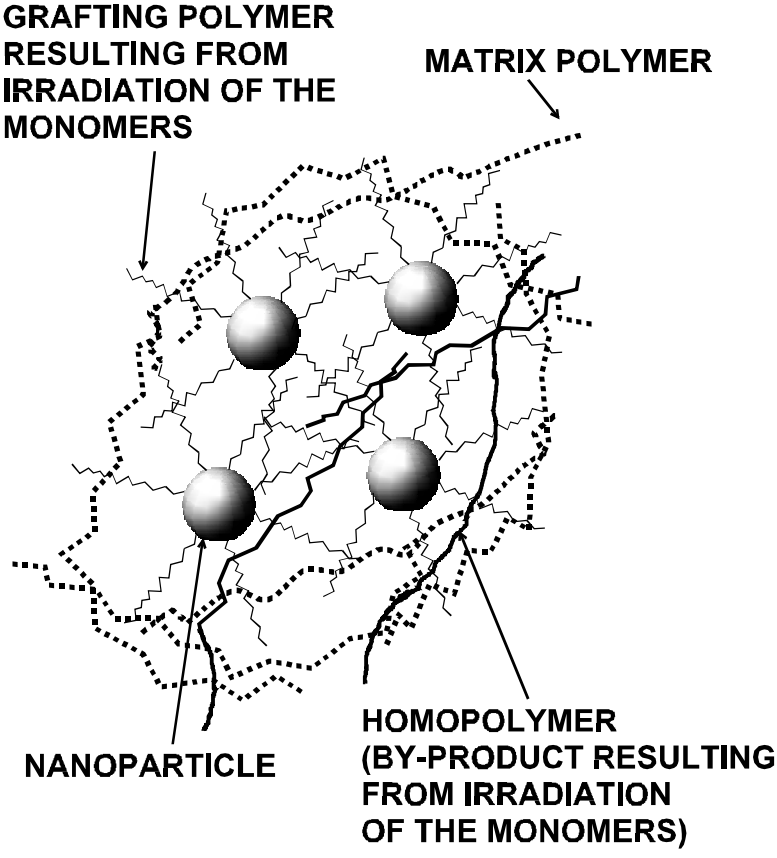

Figure 2. Schematic drawing of the possible structure of grafted nanoparticles dispersed in a polymer matrix.

In our preliminary work, polymerization by irradiation was applied to induce the grafting polystyrene, polymethyl methacrylate, polyethyl acrylate and polybutyl acrylate onto the surface of nanometer SiO_2 and $CaCO_3$ [37]. The experimental results showed that these grafting polymers were chemically bonded on the surface of the nanoparticles rather than physically coating them. When the grafted nanoparticles were incorporated with polypropylene by extrusion mixing, the dispersion homogeneity of the particles were improved remarkably, leading to a significant increase in the mechanical properties of the composites, and toughness in particular, at a filler concentration lower than 2% by volume [38].

The current chapter is concentrated on the development of inorganic nanoparticles/thermosetting polymer composites with remarkable tribological performance, which can be used e.g. as a candidate for coatings on hard composite rollers. A viable surface treatment of nanoparticles through grafting polymerization will be explored to break up the commercially available nanoparticle agglomerates and to improve the interfacial adhesion between the particles and the matrix resin. The proposed graft technique should make it possible to control the molecular structure of the grafting polymers so that the performance of the target composite materials can be tailored. Knowledge for an optimum formulation and preparation will be provided from a careful investigation of the effects of the nanoparticles on the wear reduction of the thermosetting polymer. Further conclusions can be drawn from the relationship between particle dispersion status and mixing process, as well as from an understanding of the friction and wear mechanisms involved in the nanocomposites. It can therefore be expected that the results of this project will be of certain universal significance and thus applicable for many inorganic nanoparticles/thermosetting composites in consideration of their potential use in various industrial applications.

2. PRETREATMENT OF INORGANIC NANOPARTICLES AND THE CORRELATED CHARACTERIZATION

In the following work, Al_2O_3 and SiC nanoparticles were chosen as the fillers due to the fact that the bulk materials of these inorganic substances are known to be of high wear resistance. Considering the agglomeration of these nanoparticles, grafting pretreatment has to be carried out as stated above.

Grafting polymer onto the surface of inorganic nanoparticles is a field of growing interests. Several works have been done with respect to improving the dispersibility of these particles in solvents and to their compatibility in polymer matrices [39-44]. Mostly, the grafting polymerization was conducted via two routes: (i) monomers were polymerized from the active compounds (initiators or comonomers) and then covalently attached to the inorganic particle surfaces; and (ii) ready-made polymers with reactive end-groups reacted with the functional groups on the particle surfaces. Various kinds of polymerization processes have been tried in the grafting investigations, including radical, anionic and cationic polymerizations. In our previous studies [38,45,46], the necessity of surface modification of nanoparticles in making polymer nanocomposites was elucidated. To develop an effective and versatile approach, an irradiation grafting technique was proposed to introduce polymers onto nano-silica. However, it was found that the molecular weight and the density of the

grafted macromolecules are quite difficult to be controlled, in addition to the complexity of the reaction details. A fine adjustment of the interfacial interaction in the subsequent composites is therefore restricted.

To solve this problem, the authors tried to graft polymers onto the surface of nanoparticles by a simple chemical reaction, which would make it possible to control the grafting polymer chains more easily. Considering that some kinds of coupling agents contain polymerizable groups, a surface treatment using these coupling agents followed by radical grafting polymerization should be feasible. In this work, polyacrylamide (PAAM) and polystyrene (PS) were introduced onto the surface of silane coupling agent pre-treated Al_2O_3 and SiC nanoparticles by aqueous and non-aqueous radical polymerization processes, respectively. The amide groups of PAAM would take part in the curing of epoxy resin and the encapsulation with PS is believed to be able to greatly increase the hydrophobicity of the particles and hence the compatibility with the polymer matrix. That is, these treatment approaches are selected for purposes of facilitating nanoparticles/matrix interfacial adhesion.

2.1. Materials and Nanoparticles Pretreatment

The nanosized alumina (γ-phase) was provided by Hua-Tai Co. Ltd., China, and possesses a specific surface area of 146.3m^2/g and an averaged diameter of 10.4nm. The SiC nanoparticles (α-phase) were also produced by Hua-Tai Co. Ltd., China, and provide a specific surface area of 15.3m^2/g, whereas the averaged diameter counts to 61nm. Prior to use, the particles were dried in an oven at 110^{o}C under vacuum for 24h in order to get rid of the physically absorbed and weakly chemically bonded species.

A KH570 silane coupling agent (γ-methacryloxypropyl trimethoxy silane), provided by Liao Ning Gazhou Chemical Industry Co. Ltd., China, was employed to introduce the reactive functional groups on the surface of the nanoparticles. Styrene was obtained from Shanghai Guanghua Chemical Agent Factory, China, and acrylamide was supplied by Guangzhou Chemical Agent Factory, China. The two types of monomers were identified as being a reagent grade. In non-aqueous systems, the azobis(isobutyronitrile, AIBN) was used as an initiator, and toluene, tetrahydrofunan (THF) and cyclohexane were chosen as solvents. For aqueous systems, a mixture of ammonium persulfate and sodium hydrogen sulfite (1:1 in mole) was used as the initiator, and deionized water was taken as a solvent. All the components of the recipes were used as received from the suppliers without further purification.

The introduction of reactive groups onto the surface of nanoparticles was achieved by the reaction of silane with the hydroxyl groups of the particles (Fig.3). A typical example can be given as follows: 2.0g alumina nanoparticles and 2.0g KH570 in 100 ml of 95% alcohol solution were charged into a 300ml flask equipped with a reflux condenser. The mixture was refluxed at the boiling temperature of the solution over different stirring times. After that, the alumina was centrifuged, and the precipitate was extracted with alcohol for 16h to remove the excess silane absorbed on the alumina. Then the treated alumina was air-dried and allowed to react at 80^{o}C under vacuum for 24h. The content of the double bonds introduced onto the alumina surfaces by the above treatment was detected according to the method stated in ref.[47].

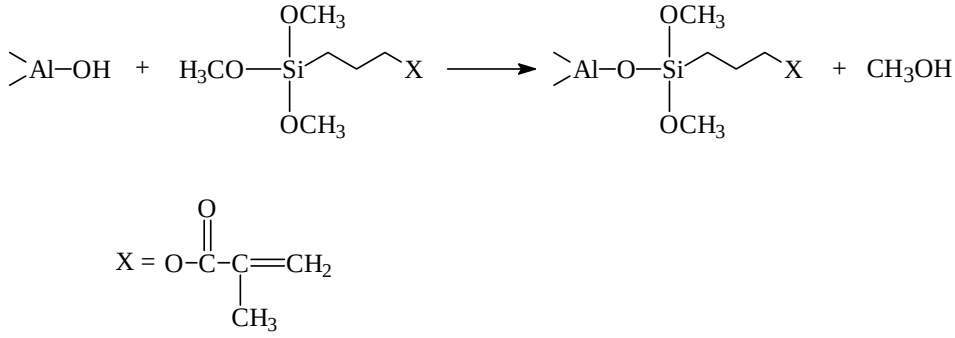

Figure 3. Schematic illustration of the reaction of KH570 silane coupling agent with the hydroxyl groups of alumina.

2.2. Graft Polymerization of Vinyl Monomers onto Nano-Al_2O_3

The graft polymerization reactions for both styrene and acrylamide monomers were performed in air environment in a flask equipped with a condenser at 70°C and 50°C, respectively. Firstly, the modified alumina and the solvent were put in the temperature-controlled reactor with stirring. When the reactant reached the desired temperature, the initiator and the monomer were added in four ways of feeding: (i) both the initiator and the monomer were added simultaneously in one batch; (ii) the initiator was charged alone, and then the monomer was added in one batch after 30min of reaction; (iii) similar to (ii), but the monomer was added by drip feeding; (iv) one third of the total dosage of the initiator was added, and then the monomer and the rest initiator were added in two equal batches after the alumina reacted with the first batch of initiator for a while. In all the cases, the concentration of the monomers and the initiators, as well as the reaction time, were changed in order to study their influence on the reaction processes and the degrees of reaction.

Compared with the untreated version, the infrared spectrum of the modified alumina exhibits absorptions at 1731, 1457 and 1409cm^{-1}, which are characteristic for the silane coupling agent (Fig.4). Correspondingly, a quantitative analysis indicates that the amount of double bonds introduced onto the particles increases with treating time (Fig.5). Having been treated for 4h, the double bonds reach a level of 0.77mmol/g, implying that about 66% hydroxyl groups on the surfaces of nano-alumina particles have been consumed for the introduction of these reactive groups. It can thus be deduced that the treatment employed in the present study resulted in a monolayer coverage of silane. Therefore, the nanoparticles with 0.77mmol/g of double bonds were used in the subsequent grafting reactions.

Graft polymerization of styrene and acrylamide was carried out at the presence of modified alumina in different solvents (Table 1). The data of percent grafting indicate that the monomers were successfully grafted onto the surface of alumina through covalent bonding. The formation of grafted polymers can be confirmed by the typical FTIR peaks in Fig.4. For PS-grafted alumina (Al_2O_3-g-PS), a series of absorptions at 1634, 1601, 1492 and 1452cm^{-1} evidence the existence of PS. For PAAM-grafted alumina (Al_2O_3-g-PAAM) a strong absorption of carboxyl groups in PAAM at 1666cm^{-1} occurs.

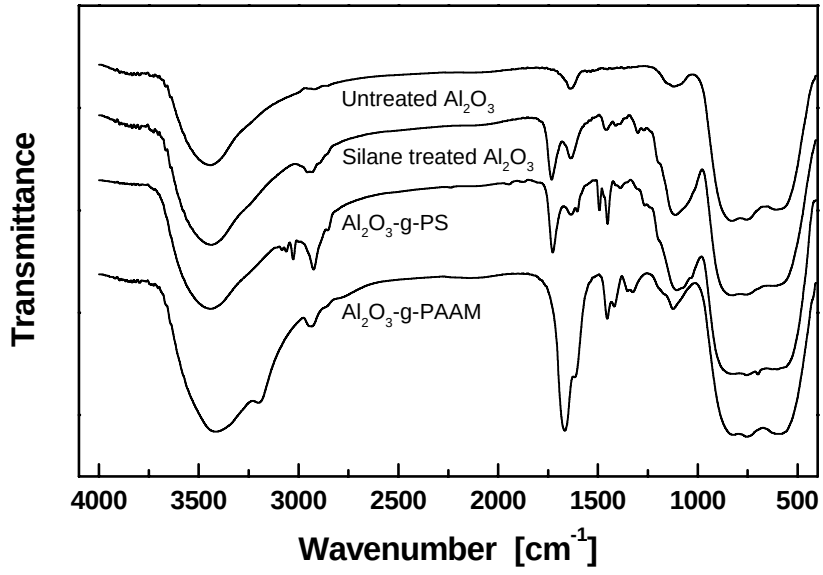

Figure 4. FTIR spectra of nanosized alumina before and after surface modification. Prior to the test, the non-grafted polymers were extracted from both Al_2O_3-g-PS and Al_2O_3-g-PAAM.

Table 1 Graft polymerization of styrene and acrylamide on the surface of silane modified alumina [a]

Grafted polymer on Al_2O_3	Monomer concentration (mol/L)	Initiator concentration (mol/L)	Solvent	Reaction temperature (^oC)	Reaction time (h)	γ_c [b] (%)	γ_g [c] (%)	γ_e [d] (%)
PS	0.5	0.001	Toluene	70	2	9.2	10.6	17.7
PS	0.5	0.001	THF	70	2	9.7	9.9	17.8
PS	0.5	0.001	Cyclohexane	70	2	9.6	10.9	18.5
PAAM	1.0	0.02	Deionized water	50	3	85.7	29.1	6.0

[a] The initiator and the monomer were added into the reaction system simultaneously.
[b] γ_c = monomer conversion.
[c] γ_g = percentage of grafting.
[d] γ_e = grafting efficiency.

On the other hand, Table 1 reveals that the reaction systems of Al_2O_3-g-PS with different solvents have nearly the same monomer conversion, percentage of grafting and grafting efficiency. This phenomenon may be related to the fact that all of these solvents are good solvents for PS. Under this circumstance, the grafted polymer exists in an extended conformation and hence has no blocking effect on the diffusion of the monomers towards the alumina surface. Based on this finding, the following reactions use toluene as the solvent because of its higher boiling point and convenience of temperature control.

Table 2 shows the number average molecular weight (M_n) and mass average molecular weight (M_w) of PS grafted onto alumina. It is interesting to note that the molecular weights of grafted PS change with the percentage of grafting. The higher values of γ_g (i.e. 33.9 and 39.7) correspond to higher molecular weights, as compared to the case of lower γ_g (i.e. 12.1). In

fact, the polymerization conditions for these samples were different. The molecular weights of the grafted PS should be a function of the concentrations of the monomer and the initiator. In general, the degree of polymerization (kinetic chain length) during a radical polymerization increases with increasing polymerization rate and monomer concentration, while it decreases with increasing initiator concentration [48]. However, this relationship seems not to be completely adapted in the present graft polymerization on alumina.

Table 2. Molecular weights of PS grafted onto alumina [a]

γ_g (%)	Monomer concentration (mol/L)	Initiator concentration (mol/L)	M_n (x10^4)	M_w (x10^4)	M_w/M_n	Grafted number μmol/g μmol/m^2	f_g [b] (%)
39.7	2.0	0.04	2.51	3.86	1.54	15.82 0.108	2.06
33.9	6.0	0.04	3.10	3.95	1.28	10.96 0.075	1.42
12.1	2.0	0.01	1.42	2.43	1.71	8.54 0.058	1.11

[a] The initiator and the monomer were added into the reaction system simultaneously. Toluene served as solvent.

b fg = (amount of double bonds consumed during polymerization)/(initial amount of double bonds)

The number of PS chains grafted onto alumina surfaces was calculated from the number average molecular weight (Table 2). Accordingly, the percentage of double bonds used for the grafting of PS onto the alumina surfaces, i.e. the reaction efficiency of the double bonds attached to the surfaces (f_g), can be obtained. The results reveal that only a few double bonds on the particle surfaces were utilized during the polymerization. For PAAM grafted nanoparticles, the molecular weight of the grafted polymer is not available due to the difficulty in separating the grafted PAAM from the particles as stated in the experimental part. Further efforts are needed in this aspect.

To check the effect of surface treatment, the dispersibility of polymer grafted alumina in a solvent (Al_2O_3-g-PS in THF and Al_2O_3-g-PAAM in acetone) was compared with the untreated alumina (Fig.6). The results show a remarkable improvement of dispersibility resulting from the surface grafting. Untreated alumina completely precipitates after a few hours. On the contrary, PS-grafted and PAAM-grafted alumina give a stable colloidal dispersion in the solvent. In addition, the alumina with a higher percentage of grafting tends to be more stable than that with a lower amount of grafting, indicating that the grafting polymer chains interfere with the agglomeration of alumina nanoparticles.

As different ways of feeding monomer and initiator were used in the course of graft polymerization, it is worth examining the effect of different ways of monomer feeding on the grafting reaction. It was found that these reaction procedures strongly influence especially the acrylamide grafting reaction (Table 3). In comparison with the results corresponding to the first way of feeding, the second feeding route hereby leads to a higher grafting percentage and grafting efficiency, but also to a lower monomer conversion. In the case of the third way of feeding, γ_c, γ_g and γ_e showed the lowest values.

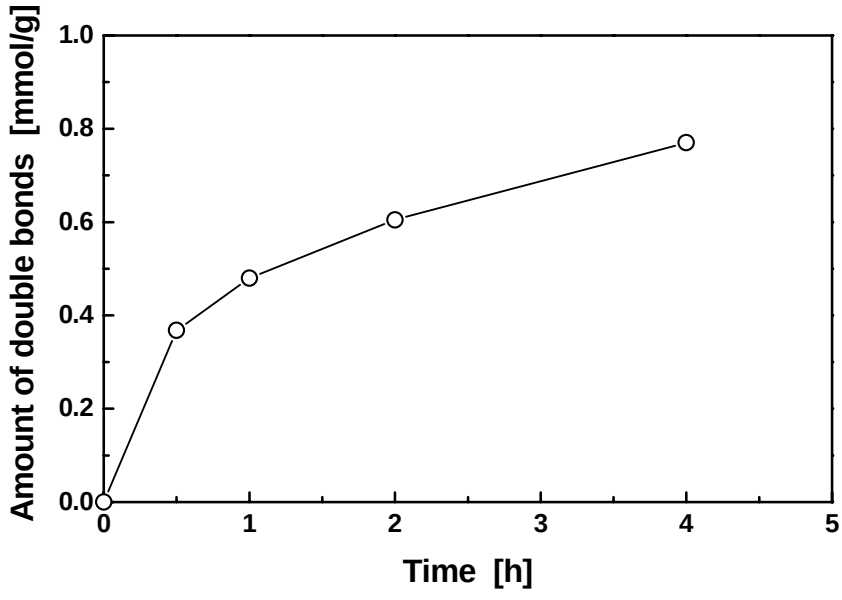

Figure 5. Amount of double bonds introduced onto the alumina surface as a function of reaction time.

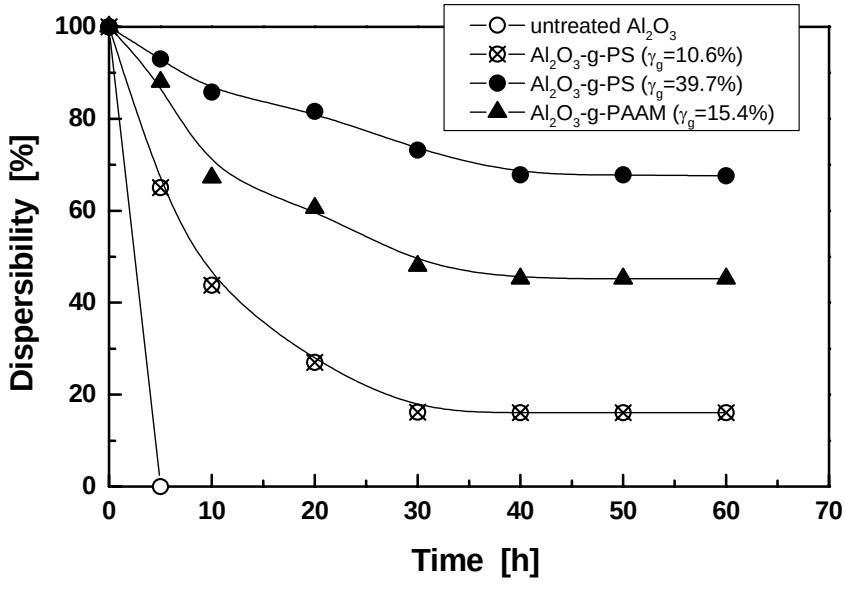

Figure 6. Dispersibility of Al_2O_3-g-PS in THF and Al_2O_3-g-PAAM in acetone at room temperature.

Table 3. Effect of feeding ways of monomer and initiator on the grafting reaction of PAAM [a]

Feeding way [b]	Monomer concentration (mol/L)	Initiator concentration (mol/L)	Reaction temperature (^oC)	Reaction time (h)	γ_c (%)	γ_g (%)	γ_e (%)
1	1.0	0.01	50	3	78.6	25.0	20.5
2	1.0	0.01	50	3	49.2	52.0	30.0
3	1.0	0.01	50	3	22.8	16.6	9.3

[a] Deionized water served as solvent.

[b] Details of the ways of feeding monomer and initiator are given in the experimental part.

In a radical polymerization, decomposition of the initiator is usually considered to proceed gradually (non-instantaneously). When both the monomer and the initiator were mixed together, radicals can be formed freely on the surface of the alumina at the beginning of the polymerization. Unfortunately, the surface double bonds can not be initiated at a latter stage of the polymerization because growing polymer radicals and/or grafted polymer chains block the diffusion of radicals towards the particle surface (Fig.7). When the modified alumina was allowed to react with the initiator firstly (i.e. the second way of feeding), more double bonds could be initiated, leading to both a higher percentage of grafting and grafting efficiency. For the third feeding way, the monomer was in a starved condition. The initiated double bonds on the alumina surfaces had to be terminated more seriously. In addition, the initiator was remarkably consumed even before all the monomer dripped into the reactor. This caused the reaction time for the monomers to be relatively insufficient, as indicated by the lowest γ_c, γ_g and γ_e values observed.

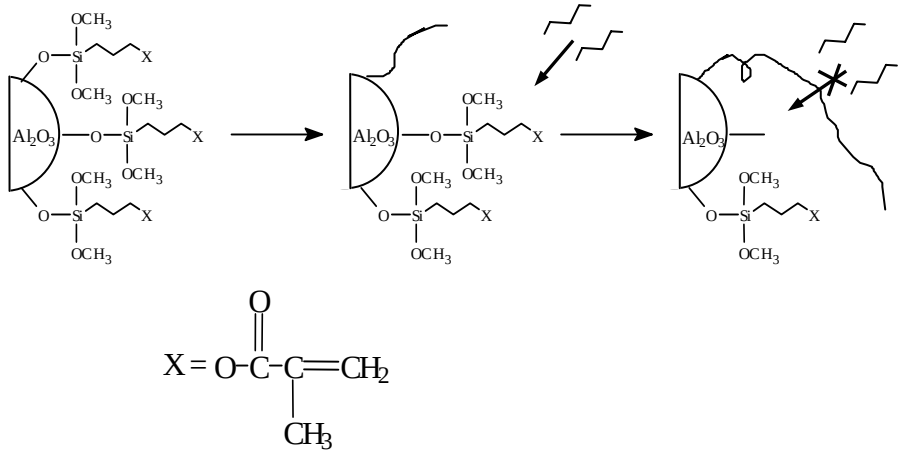

Figure 7. Schematic drawing of the blocking effect of the growing polymeric radicals and/or grafted polymer chains on the diffusion of radicals towards the alumina surface.

In contrast to the case of PAAM, the monomer feeding procedure scarcely influenced the styrene grafting reaction (Table 4). This may be due to the different solvent effect. Toluene is such a good solvent for PS that the blocking effect of grafted PS becomes no longer significant. Comparatively, water is not a very good solvent for PAAM, so that the monomer

feeding manner became a controlling factor for the grafting reaction. On the other hand, the initiator might have a longer life in the PS system. That is, the system had enough initiator even if the third feeding way was used. These resulted in an independence of the grafting polymerization of PS onto the alumina particles.

Table 4. Effect of feeding ways of monomer and initiator on the grafting reaction of PS [a]

Feeding way [b]	Monomer concentration (mol/L)	Initiator concentration (mol/L)	Reaction temperature (^oC)	Reaction time (h)	γ_c (%)	γ_g (%)	γ_e (%)
1	1.0	0.005	70	3	8.8	12.3	26.8
2	1.0	0.005	70	3	11.1	12.1	21.3
3	1.0	0.005	70	3	10.9	12.1	21.4

[a] Toluene served as solvent.

b Details of the ways of feeding monomer and initiator are given in the experimental part.

2.3. Graft Polymerization of Vinyl Monomers onto Nano-SiC

The grafting polymerization of styrene and acrylamide monomers onto SiC nanoparticles was conducted in slightly different ways. For producing PAAM grafted SiC (SiC-g-PAAM), the silane treated particles were put into a flask filled with water. After a sonication of 30min, the initiator (mixture of $NH_4S_2O_8$ and $NaHSO_3$ at a mole ratio of 1:1) was incorporated into the system at 30^{o}C in N_2 atmosphere. Having been stirred for 30min, acrylamide was added to the mixture with stirring to carry out the grafting polymerization. Then the resultant suspension was centrifuged and washed. The sludge represented the grafted nanoparticles.

To obtain PS grafted SiC (PS-g-SiC), the pretreated particles were mixed with toluene under sonication. When the reactor was kept at 80^{o}C and filled with N_2, AIBN was added with stirring. After one hour, styrene monomer was incorporated into the system. Similarly, the PS-g-SiC can be received from the precipitation of the resultant suspension.

Fig.8 illustrates the infrared spectra of untreated and treated particles. Due to the strong absorption of SiC as-received over a broad wavenumber range, many characteristic peaks of the treated nanoparticles are no longer perceivable. Nevertheless, the stretching mode of SiC at 890cm^{-1} can be seen in the spectrum of silane treated SiC, suggesting that KH570 silane coupling agent has been reacted with the hydroxyl groups on the SiC nanoparticles. In the case of SiC-g-PAAM, although the absorption due to amide at 1659cm^{-1} is unclear, the peaks at 801 and 1258cm^{-1} represent N-H and C-N vibrations, respectively. For SiC-g-PS, the peaks of phenyl rings at 1500~1480cm^{-1}and 1600cm^{-1} are hidden by the wide band of SiC, but the two peaks at 700~900cm^{-1}characterize C-H absorption of benzene rings. The above results prove that PAAM and PS have been chemically connected to the surface of SiC particles, respectively.

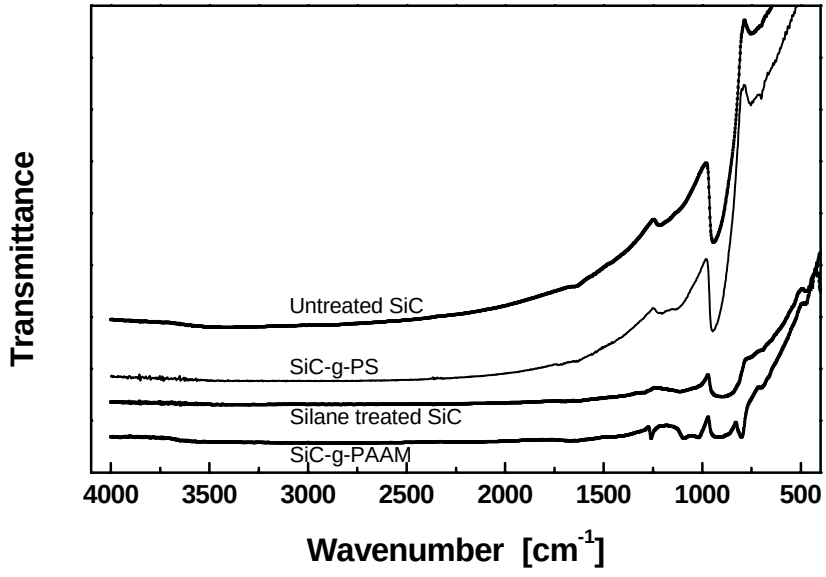

Figure 8. FTIR spectra of nanosized SiC before and after surface modification. Prior to the measurement, the non-grafted polymers were extracted from both SiC-g-PS and SiC-g-PAAM.

The experimental data of grafting polymerization of acrylamide monomer onto SiC nanoparticles are plotted in Fig.9. It is seen that the monomer conversion reaches the maximum of about 75% when the concentration of initiator approaches 3mmol/g. A comparatively lower or higher initiator concentration would result in a decreased monomer conversion. In the case of low initiator concentration, the fraction of free radicals generated in the solution is relatively low. As a result, the conversion rate of the monomers had to be low at a given monomer concentration. When the concentration of the initiator is rather high, the redox effect accompanied with the chain initiation would intensify the decomposition of PAAM chains and lead to a lower conversion of the monomers. With respect to the percentage of grafting, an increase in the concentration of the initiator always facilitates the initiation of the double bonds on the particles surface. This accounts for the continuous increase in the percentage of grafting. However, it should be noted that an unduly high initiator concentration would also increase the probability of radical termination between the growing chains. In this context, a proper selection of concentration of the initiator is necessary.

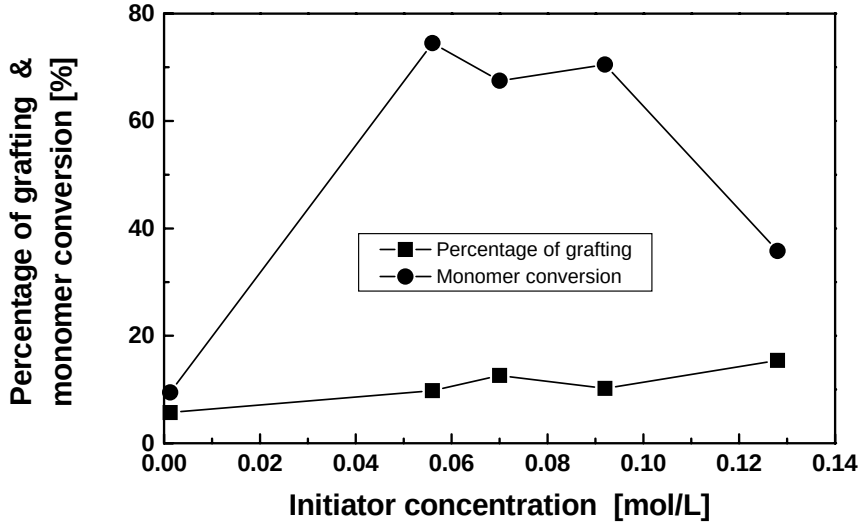

Figure 9. Grafting of acrylamide onto nano-SiC: effect of the initiator concentration on the monomer conversion and percentage of grafting (monomer concentration: 0.67mol/L, reaction time: 4h).

Fig.10 shows the effect of monomer concentration on the percentage of grafting. An approximately linear dependence can be found, implying that the percentage of grafting is closely related to the rate of chain growth. In the case of radical polymerization, the kinetic chain length is generally proportional to the monomer concentration. If the monomer concentration increases, the polymerization rate rises too, and in the same way, the molecular weight of the grafting polymer expands. This directly coincides with the findings of Lin et al. [49]: the molecular weight of PAAM increases with increasing monomer content if the polymerization of acrylamide is carried out in aqueous solution. Because the polymerization of acrylamide completes within a relatively short period of time, the percentage of grafting has to be significantly influenced by the content of the monomer.

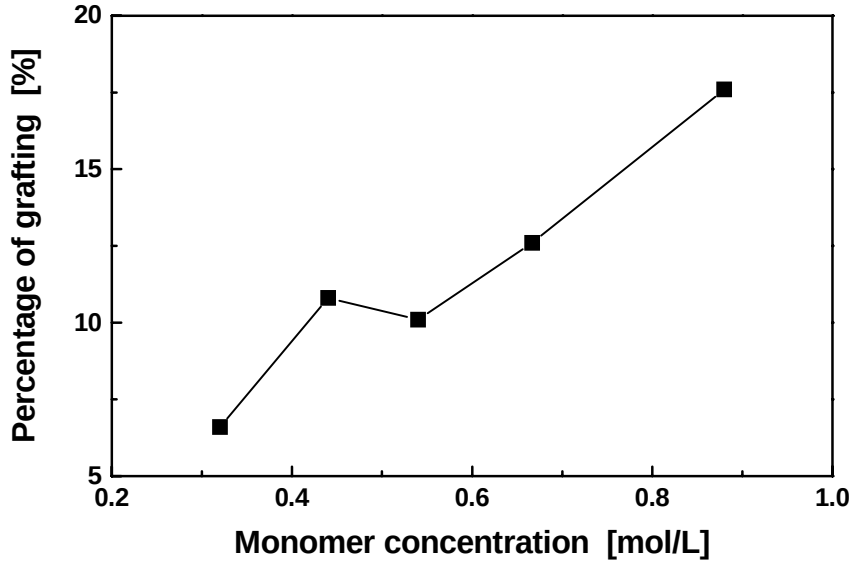

Figure 10. Effect of monomer concentration on the percentage of grafting of acrylamide onto nano-SiC (initiator concentration: 0.076mol/L, reaction time: 4h).

The effect of reaction time is an important factor of grafting polymerization (Fig.11). It is found that a reaction time longer than 2h is somewhat detrimental to the increase of monomer conversion and percentage of grafting. This is due to the degradation of PAAM molecules in the redox system. At the beginning of the polymerization, chain growth plays the leading role. Then, when the polymerization proceeds to a certain extent, the effect of molecular decomposition emerges. With the lapse of time molecular decomposition counteracts the chain growth remarkably. A further increase in the reaction time results therefore in the increased amount of low molecular weight PAAM, and these molecules can easily be lost during the isolation of the homopolymerized PAAM. The measured monomer conversion is thus reduced apparently, when the reaction time is extended. On the other hand, if the short PAAM segments carrying radicals slip through to the surface of the SiC nanoparticles, an increase in the percentage of grafting can be observed as the case of a reaction time of 7h (Fig.11). In summary, the time dependence of monomer conversion and percentage of grafting is a joint result of both competitive effects: chain growth and chain degradation.

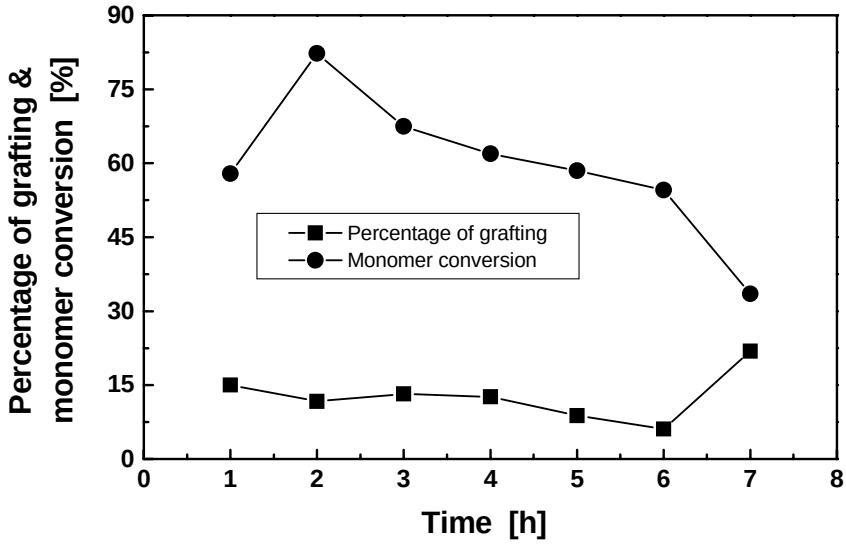

Figure 11. Grafting of acrylamide onto nano-SiC: effect of reaction time on the monomer conversion and percentage of grafting (monomer concentration: 0.67mol/L, initiator concentration: 0.076mol/L).

Grafting polymerization of styrene onto SiC nanoparticles is characterized in Fig.12. When the reaction time is shorter than 6h, the percentage of grafting is rather low. Afterwards, a linear increase in the percentage of grafting with rising time can be seen. In comparison to the data of PAAM grafting, the current percentage of grafting is quite low. This should be attributed to the morphology of the surface reactive groups on the SiC particles and the steric hindrance of the monomers. Since SiC contains C elements, the interaction between SiC particles and organics (i.e. the silane coupling agent and the growing chains) should be stronger than that between other inorganic particles and organics. In case the SiC particle-solvent interactions are weaker, the molecular chains containing reactive double bonds or radicals cannot take the extended form in the solution; they tightly wrap the particles. The attack on the particles launched by the monomers becomes rather difficult. Probably this effect is much severe in toluene. In addition, the steric hindrance of styrene is greater than acrylamide. At the early stage of polymerization it is more difficult for styrene monomers to get access to the reactive chain ends and start the chain growth. With increasing reaction time, some chain radicals are produced at the terminals of the coupling agent and the amount of the chain radicals in the solution keeps on increasing. The termination between the above two types of chain radicals results in the rise in percentage of grafting as shown in Fig.12.

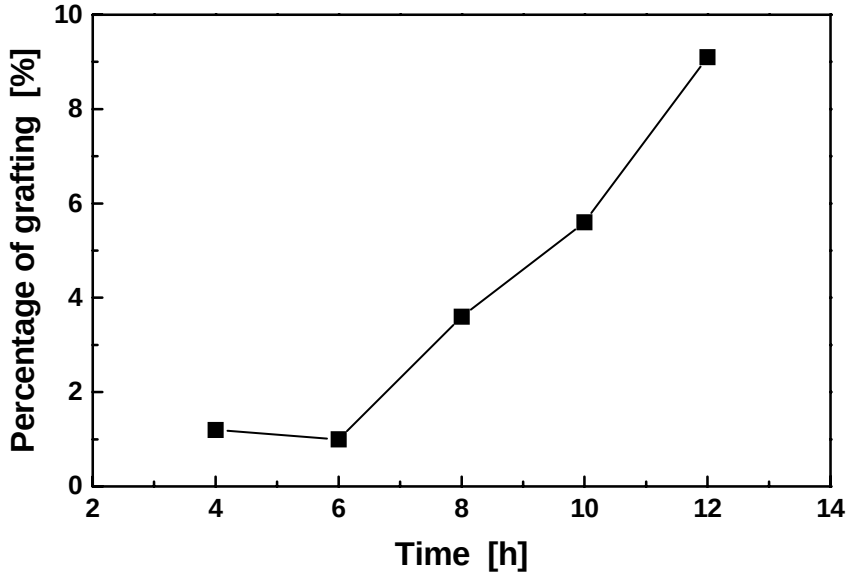

Figure 12. Effect of reaction time on the percentage of grafting of styrene onto nano-SiC (monomer concentration: 1.0mol/L, initiator concentration: 0.01mol/L).

The effect of initiator concentration on the percentage of grafting of styrene onto SiC nanoparticles is illustrated in Fig.13. Although there is an increasing trend in the percentage of grafting with the fraction of the initiator, the variation is not obvious enough. Within the entire range of initiator concentration, the percentage of grafting changes between 4.5~6.5%. As analyzed above, due to the steric hindrance effect between the monomers and the growing chains, an increase in the initiator concentration increases the quantity of the radicals in the solution but cannot effectively improve the ability of chain growth. Only when the probability of termination between the chain radicals on the nanoparticles and those in the solution is increased as a result of a rise in initiator concentration, the percentage of grafting can be increased accordingly.

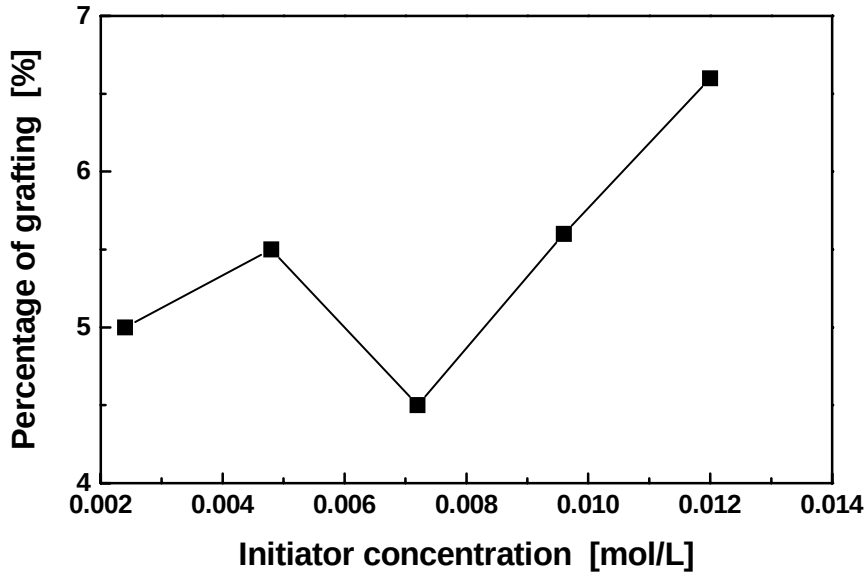

Figure 13. Effect of initiator concentration on the percentage of grafting of styrene onto nano-SiC (monomer concentration: 1.0mol/L, reaction time: 4h).

To check the quality of grafting polymerization on the nanoparticles, the dispersibility of the particles are compared in Fig.14. The untreated particles cannot give a stable dispersion in the solvent. Although the suspension was stirred by sonication, the particles completely precipitated within 15h. In contrast, the grafted particles exhibit good dispersibility in the solvent. About 40% of the particles remained in the suspension after 40h. Fig.14 shows furthermore that the dispersibility of SiC-g-PS is better than that of SiC-g-PAAM owing to the fact that the solvent THF possesses a better miscibility with PS than with PAAM. Based on these results it can be deduced that the grafted nanoparticles would also have a much better miscibility with other polymers when preparing polymer composites. The properties of the composites would thus be effectively enhanced.

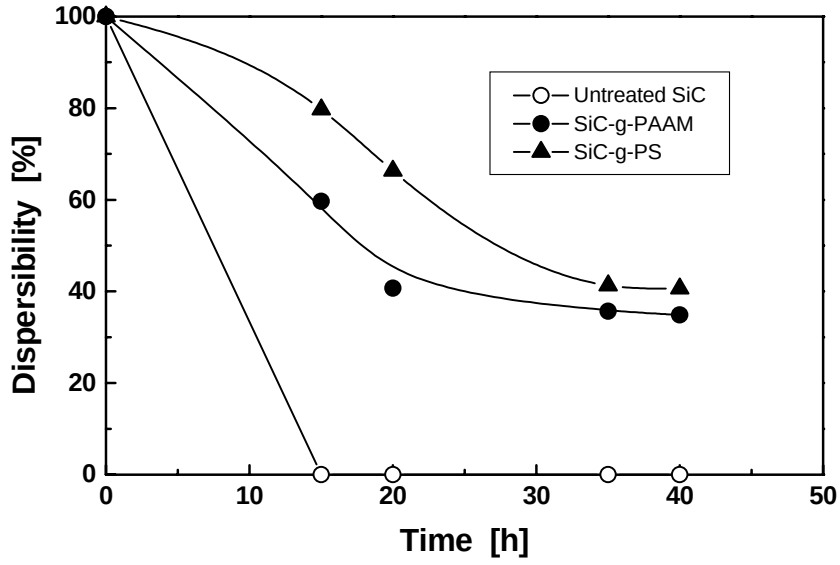

Figure 14. Dispersibility of SiC nanoparticles in THF at room temperature.

2.4. Treatment of SiO_2 and Si_3N_4 Nanoparticles

To make comparative investigations, nano-SiO_2 and nano-Si_3N_4 particles were also involved in our work. The nano-SiO_2 with an average primary particle size of 9nm was purchased from Zhoushan Nanomaterials Co., China. The nano-Si_3N_4 with a specific surface area of $52m^2/g$ and an average primary particle size of 16.8nm were provided by Hua-Tai Co. Ltd., China

The typical grafting of SiO_2 proceeded as follows. The nanoparticles were preheated at 120^oC in vacuum for 24h to eliminate possible absorbed water on the surface of the particles. Then the particles were mixed with acetone solution of acrylamide by sonication. The mixture was irradiated by ^{60}Co γ-ray at a dose rate of 1Mrad/h at room temperature. After exposure to a dose of 4Mrad, the solvent was recovered and the dried residual powder could be compounded with epoxy directly. To obtain homopolomerized PAAM individually, certain amounts of the irradiation products were extracted with water in a Soxhlet's apparatus at room temperature. The residual material (i.e. SiO_2 with the unextractable grafting PAAM) was immersed in 10~20% HF solution to remove the inorganic particles so that the grafting PAAM could be recovered. By using thermogravimetric analysis (TGA), it was known that percent grafting and grafting efficiency of the irradiation products are 10.3% and 53.7%, respectively.

To confirm that PAAM has been grafted onto nano-silica, FTIR study of the particles and the products of graft treatment was conducted. As shown by the infrared spectrum of PAAM grafted SiO_2 (SiO_2-g-PAAM) in Fig.15, the stretching modes of carbonyl in amide and CN in amide appear at 1665 and $1454cm^{-1}$, respectively. The two peaks can also be observed in the spectra of homopolymerized PAAM and grafting PAAM, but the CN peak appears at a lower

wave number of 1427cm^{-1} in the spectra of grafting PAAM, suggesting the chemical environment of grafting PAAM is slightly different from that of homopolymerized PAAM. For the grafting PAAM isolated from SiO_2-g-PAAM, the absorption due to inter-molecular hydrogen bonds at 2900~3700cm^{-1} is much broader than that of homopolymerized PAAM. In addition, there is a twin-peak at 3341 and 3413cm^{-1} that is absent in the spectrum of PAAM homopolymer. This can be attributed to the hydroxyl on PAAM generated when silica in SiO_2-g-PAAM was removed by HF solution. That is, during the grafting polymerization, PAAM had been covalently connected with SiO_2 besides physical absorption.

Treatment of Si_3N_4 with coupling agent proceeded as follows. 2.0g Si_3N_4 nanoparticles was charged into the mixture of 8.0g KH550 (γ-aminopropyl trimethoxy silane) in 200ml of 95% alcohol solution, and the reaction was kept for 8h under refluxing condition. Then, the particles were centrifuged, extracted with alcohol for 24hr, and dried in vacuum (60^{o}C, 24h). The content of the attached silane is 6.5wt% as detected by element analysis.

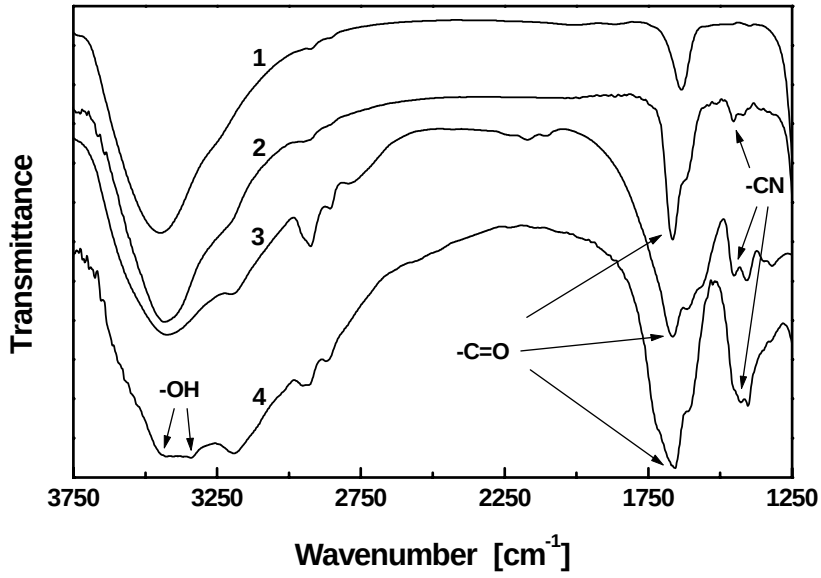

Figure 15. FTIR spectra of (1) SiO_2, (2) SiO_2-g-PAAM, (3) homopolymerized PAAM, and (4) grafting PAAM.

2.5. Manufacturing of Nanoparticles/Epoxy Composites

Bisphenol-A epoxy resin (type E-51) and 4, 4'-diaminodiphenylsulfone (DDS) were provided by Guangzhou Dongfeng Chemical Co., China. The composite materials were prepared by compounding the fillers (unmodified or modified) with preweighted quantities of epoxy at 80^{o}C with stirring for 3h and sonication for 1h, respectively, to distribute the particles homogeneously within the matrix. Then the blends were heated to 130^{o}C and the curing agent DDS was added with stirring for 10min. Finally, the mixture was filled into a mould and placed in vacuum for 50min to get rid of air bubbles. For curing the composites,

the procedures listed below were followed step by step: 3h at 100°C, 2h at 140°C, 2h at 180°C and 2h at 200°C.

2.6. Curing Kinetics

Study of the curing kinetics is essential for understanding and designing the curing process of thermosetting composites. As shown in Fig.16, the peak exothermic temperature of nano-Al_2O_3/epoxy composites increases with a rise in the heating rate of the differential scanning calorimetric (DSC) measurement. In addition, species and content of nanoparticles also have important influence on the composites curing reaction. At given heating rate, the peak exothermic temperatures of nano-Al_2O_3/epoxyand nano-Si_3N_4/epoxy composites shift towards low temperature regime as filler loading is increased (Fig.17(a) and (b)). Similar phenomena have been reported in other epoxy based composites [50]. In contrast, the peak exothermic temperature of nano-SiC/epoxy composites increased slightly with increasing the particles fraction (Fig.17(c)). Clearly, nano-Al_2O_3 and nano-Si_3N_4 accelerate the curing of epoxy, while nano-SiC decelerates the reaction.

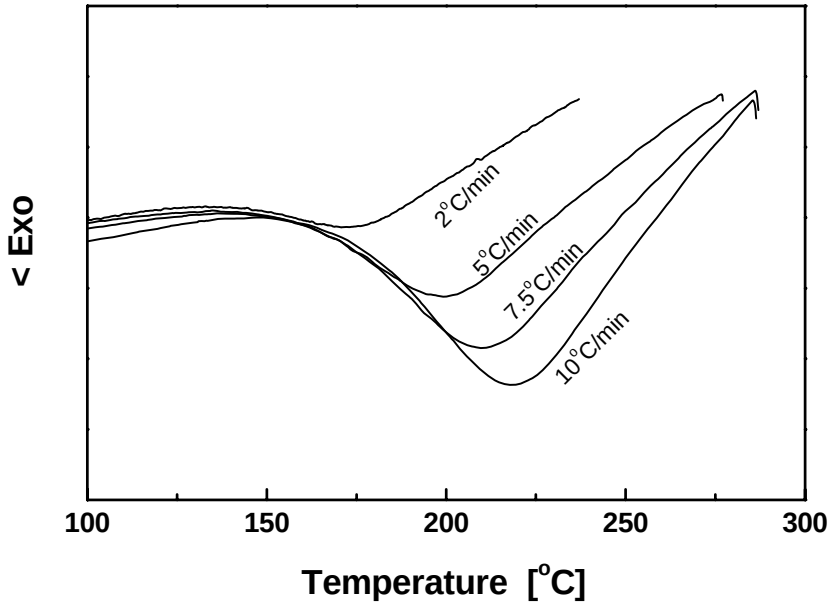

Figure 16. DSC scans of nonisothermal curing processes of nano-Al_2O_3/epoxy composites at different heating rates (Content of nano-Al_2O_3: 1.92vol%).

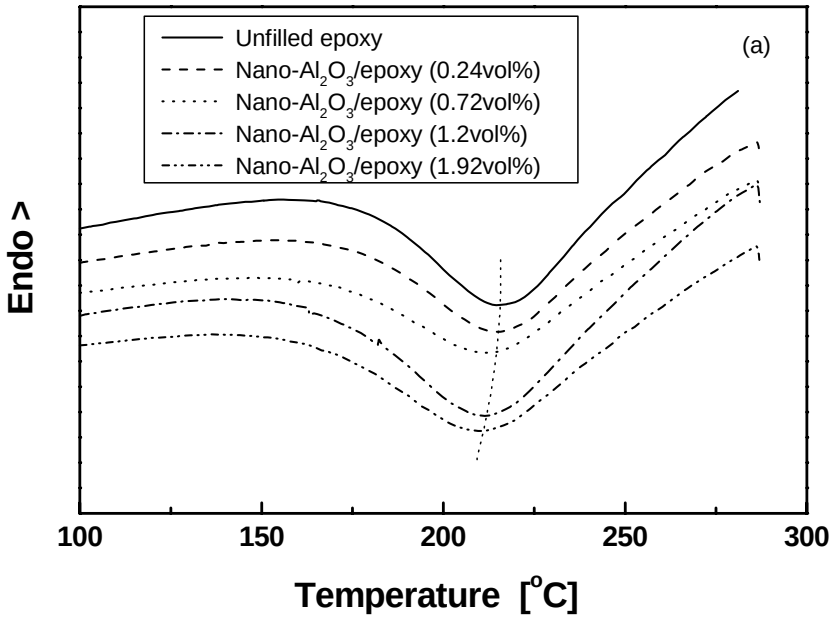
Unfilled epoxy
Nano-Al2O3/epoxy (0.24vol%)
Nano-Al2O3/epoxy (0.72vol%)
Nano-Al2O3/epoxy (1.2vol%)
Nano-Al2O3/epoxy (1.92vol%)
(a)
Endo >
100
150
200
250
300
Temperature [°C]

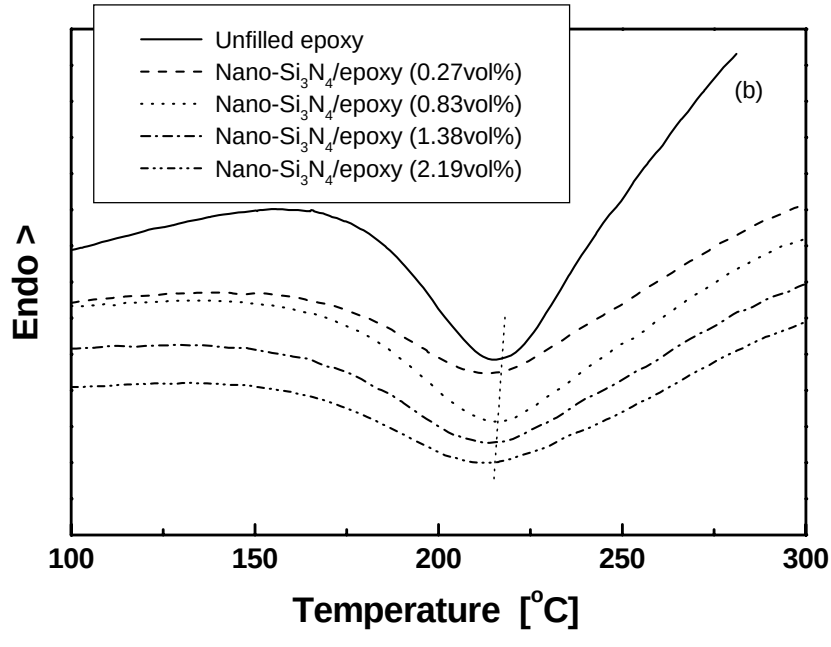
Unfilled epoxy
Nano-Si3N4/epoxy (0.27vol%)
Nano-Si3N4/epoxy (0.83vol%)
Nano-Si3N4/epoxy (1.38vol%)
Nano-Si3N4/epoxy (2.19vol%)
(b)
Endo >
100
150
200
250
300
Temperature [°C]

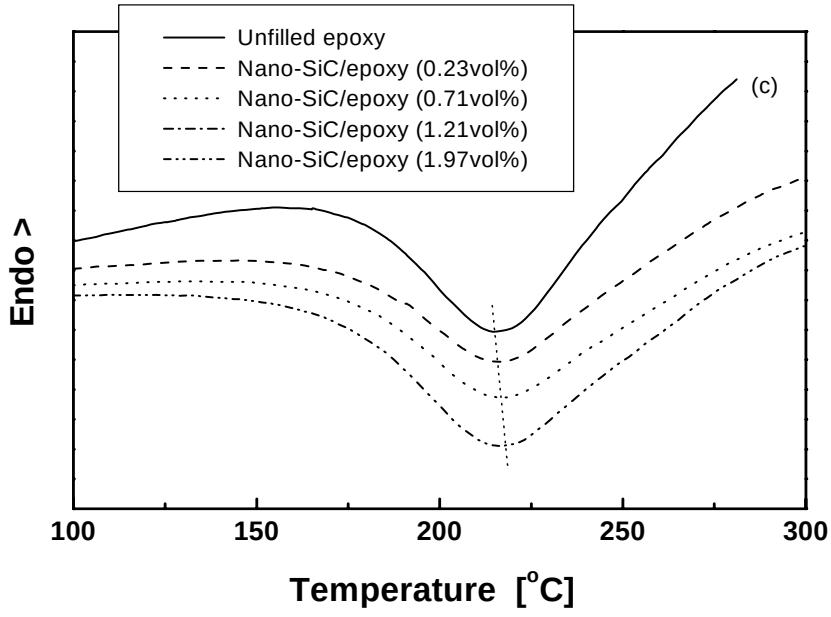

Figure 17. DSC scans of nonisothermal curing processes of (a) nano-Al_2O_3/epoxy, (b) nano-Si_3N_4/epoxy, and (c) nano-SiC/epoxy composites at a heating rate of 7.5°C/min.

To quantify the above effects, Kissinger equation [51], Crane equation [52] and Arrhenius equation are used and the corresponding results are listed in Table 5.

Table 5. Activation energy, E, pre-exponential factor, A, reaction order, n, and rate constant, K, of curing reaction of different nanoparticles/epoxy composites

Composites	Nanoparticles (vol%)	E (kJ/mol)	n	K (s^{-1})
Epoxy	0	62.1	0.89	7.0×10^{-4}
Nano-Al_2O_3/epoxy	0.24	62.4	0.93	8.5×10^{-4}
	0.72	67.9	0.93	5.0×10^{-2}
	1.20	58.8	0.91	6.3×10^{-2}
	1.92	53.8	0.90	5.1×10^{-2}
Nano-Si_3N_4/epoxy	0.27	67.1	0.91	4.4×10^{-3}
	0.83	65.0	0.90	2.0×10^{-3}
	1.38	57.7	0.88	2.1×10^{-3}
	2.19	50.7	0.93	2.1×10^{-3}
Nano-SiC/epoxy	0.23	55.6	0.89	8.0×10^{-4}
	0.71	65.0	0.90	7.1×10^{-4}
	1.21	57.8	0.89	7.4×10^{-4}
	1.97	68.0	0.91	6.6×10^{-4}

* K represents the rate constant of curing at 180°C.

As shown in Table 5, the activation energy of curing reaction of nano-Al_2O_3/epoxy decreases with increasing the filler content and the rate constant is greatly increased. Nano-Si_3N_4 composites also exhibit similar dependence, but less as significant as the former system. These coincide with the results illustrated in Fig.17. For nano-SiC/epoxy composites, however, the changes in both E and K are marginal and the value of E becomes higher at higher filler loading.

Basically, due to the strong interaction between the nanoparticles and the epoxy resin resulting from the specific surface feature of nanoparticles, the curing reaction kinetics of the nanocomposites might be different from neat epoxy resin. The above-observed accelerating effect results from the hydroxyl groups on the nanoparticles' surfaces (donors of hydrogen bonding). The more the surface hydroxyl groups, the higher the activity of the particles. Since nano-Al_2O_3 particles possess much higher amount of hydroxyl groups than nano-SiC [53, 54], it is reasonable to understand the evident acceleration perceived in nano-Al_2O_3/epoxy system. On the other hand, the incorporation of the nanoparticles must raise the viscosity of the composite system (before curing) and/or the strong interaction between the nanoparticles and the matrix polymer would hinder the molecular motion of epoxy, which disfavor the curing of epoxy. Therefore, the effect exerted by the nanoparticles is a competition of the two opposite factors. In the case of nano-Al_2O_3 and nano-Si_3N_4 particles, the effect of acceleration is measured because of the higher amount of their surface hydroxyl groups. For nano-SiC, the hindrance effect plays the leading role as a result of the fewer surface hydroxyl groups. From Table 5, it is known that the curing reaction orders of the three composites are almost the same, suggesting that the nanoparticles don't change the curing mechanism of epoxy.

To look into the influence of graft treatment of nanoparticles, grafted nano-SiO_2 particles are used. Similarly, when the particles are incorporated into epoxy, the curing kinetics of the resin is changed significantly (Fig.18). Evidently, the unmodified silica nanoparticles hinder the curing reaction to a certain extent and lead to a shift of the temperature dependence of conversion towards higher temperature. In contrast, the addition of grafted silica nanoparticles accelerates curing of epoxy, probably due to the catalytic effect of the active hydrogen atoms in amide of PAAM. This behavior is indicative of an improved processability of the system in practice.

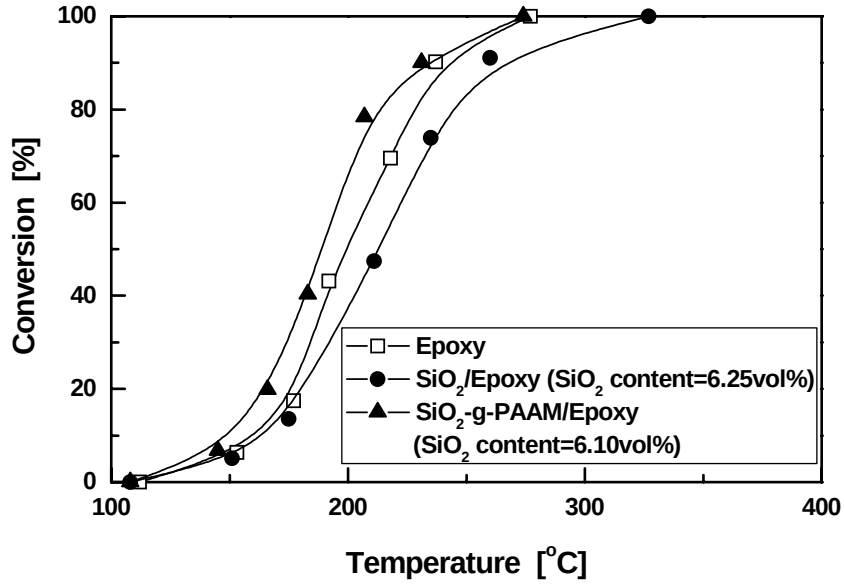

Figure 18. Nonisothermal curing behavior of epoxy and its composites at a heating rate of 2°C/min.

To further understand the curing reaction kinetics of the composites, the results of non-isothermal DSC measurements are used to determine the activation energy, the pre-exponential factor, and the reaction order of curing kinetics of the materials once more (Table 6).

Table 6. Curing characteristics of epoxy and its composites at 2.17vol% nanosilica content

Materials	Epoxy	SiO_2/Epoxy	SiO_2-g-PAAM/Epoxy
E (kJ/mol)	68.9	69.4	57.8
LnA	8.4	8.6	5.6
n	1.25	1.35	1.23

By comparing the kinetic data, it can be seen that the presence of the nanoparticles in epoxy does not change the overall reaction mechanism. In comparison with the neat epoxy resin, the increase in the activation energy of the SiO_2/epoxy system suggests that the unmodified nanoparticles slightly decelerate the curing reaction. In contrast, the grafted nanoparticles tends to have a promotive effect on the curing of epoxy, as revealed by the decreased activation energy. Considering the fact that the pre-exponential factor of SiO_2-g-PAAM/epoxy composites is significantly reduced, probably due to the steric hindrance generated by the grafting polymers adhering to the nanoparticles, a comprehensive evaluation of the influence of the nanoparticles on the curing behavior of epoxy has to be made by examining the reaction rate constants.

Fig.19 illustrates Arrhenius plots of rate constant lnK of the materials as a function of the reciprocal temperature. The results demonstrate that SiO_2/epoxy has almost the same rate constant as epoxy. For SiO_2-g-PAAM/epoxy, the rate constant is higher than that of the

former two systems at a temperature below 205°C, but it becomes lower when the temperature exceeds 205°C. It is generally agreed that the reaction mechanism for the addition of amine to epoxy takes into account the phenomenon of catalysis by hydrogen bond donors. Such a catalytic effect is via hydrogen bonding of the hydroxyl group to the oxygen of the glycidyl ether in the transition state [55]. Therefore, the appearance of the active hydrogen atoms in amide of PAAM grafted nanosilica favors the curing reaction. Since hydrogen bond formation and dissociation in a polymer are thermally reversible, a large portion of hydrogen bonds has to be dissociated at elevated temperature. As a result, diffusion control plays the leading role in SiO_2-g-PAAM/epoxy composites at a temperature higher than 205°C (Fig.19).

In fact, the composites used in this work were cured below 205°C (refer to the experimental part). It means that the grafted nanosilica accelerates the curing reaction of epoxy over the entire curing temperature range and thus improves the processability of the system in practice.

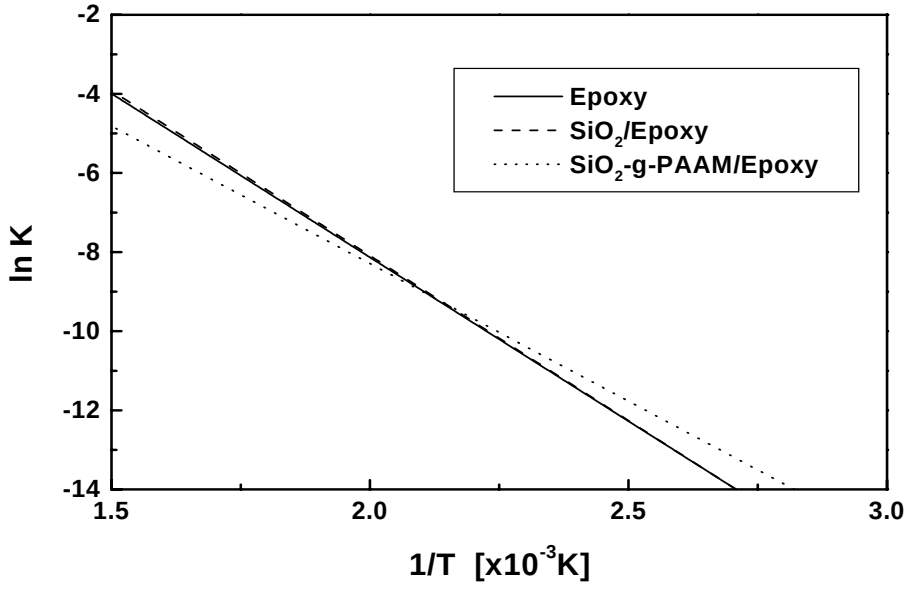

Figure 19. Temperature dependence of rate constant characterizing curing processes of epoxy and its composites at 2.17vol% nanosilica content.

2.7. Interfacial Interaction

To examine the possible interaction between the nanoparticles and epoxy, a series of tests were carried out. For nano-Al_2O_3 and nano-Si_3N_4, the particles were mixed with epoxy, and then the blends were cured in the absence of any curing agent following the aforesaid composites curing procedures. Afterwards, the blends were extracted by acetone to remove the uncured epoxy, and Fourier transform infrared spectroscopy (FTIR) was adopted to check the changes in the chemical structures of the related materials. Due to the strong absorbability

of SiC particles, their FTIR spectrum were not collected. As shown in Fig.20, on the spectrum of epoxy one can find the peak corresponding to the stretching mode of C-H of arylene at 3060cm^{-1}, the vibration modes of phenyl rings at 1510 and 1606.7cm^{-1}, the stretching mode of C-O-C of Ar-O-R at 1247.8cm^{-1}. All these characteristic absorptions are not perceivable on the spectrum of either nano-Al_2O_3 or nano-Si_3N_4, but appear on the spectra of the blends with the nanoparticles. It means epoxy has been covalently adhered to the both the untreated and grafted nanoparticles.

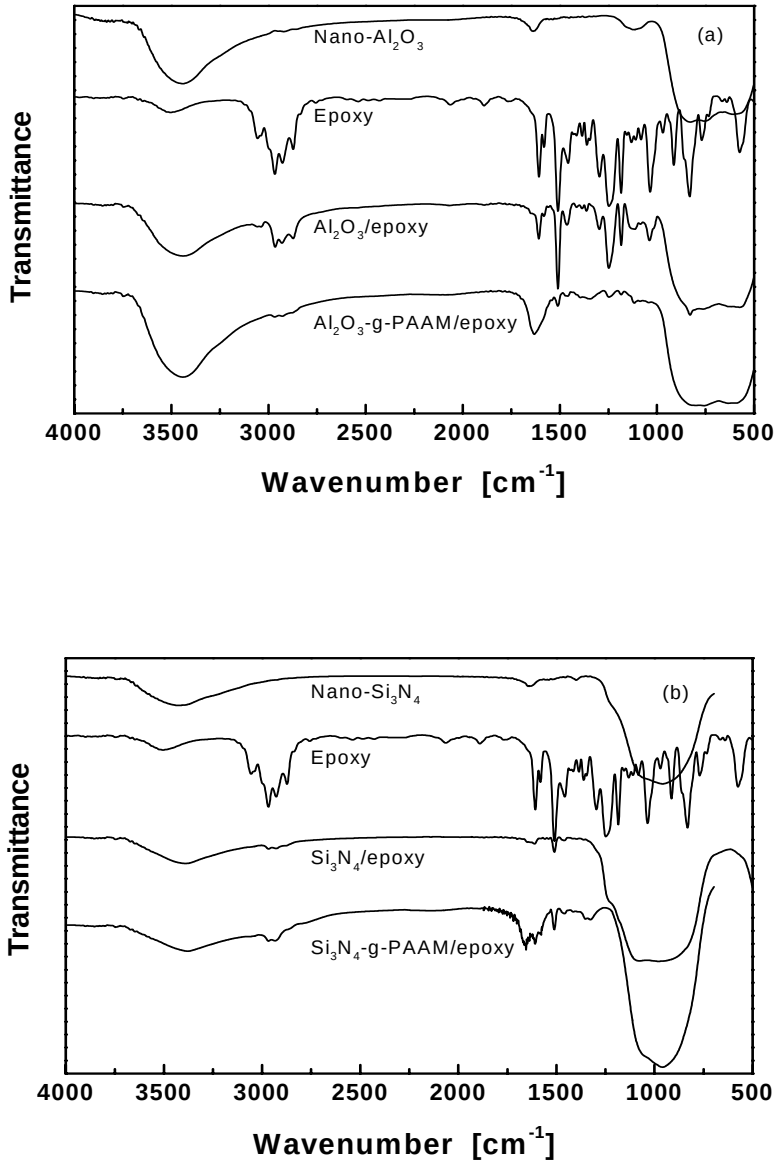

Figure 20. FTIR spectra of epoxy and its composites filled with (a) nano-Al_2O_3 and (b) nano-Si_3N_4. In all the materials there is no curing agent.

For purposes of revealing the reaction details between the grafting PAAM onto the nanoparticles and epoxy, a model system consists of PAAM homopolymer and epoxy (1/2 by weight) excluding other curing agents was thermally treated following the same curing sequence as that applied for producing the composites. Visual inspection indicated that the blends of PAAM and epoxy became consolidated after curing and the resultant product can only be swollen by acetone instead of dissolve in the solvent. In addition, comparison of the infrared spectra of the materials can also yield interesting information. As illustrated by the spectrum of PAAM in Fig.21, the C=O peak at 1665cm^{-1}, the NH_2 peak at 1616cm^{-1} and the CN peak at 1454cm^{-1} correspond to the primary amide. In the case of PAAM/epoxy blends, however, the spectrum profile has been changed as a result of transformation of partial primary amide groups and band overlap due to the incorporation of epoxy. Since the CNH peak at 1530~1550cm^{-1}, a characteristic peak of secondary amide, is not perceived, and the carbonyl peak appears at 1656cm^{-1} instead, it can be deduced that this carbonyl peak in association with the low wavenumber shift (compared with the carbonyl peak position of primary amide) represents the existence of tertiary amide connected with donor group. This evidences the reaction between PAAM and epoxy during curing. It can thus be concluded from the above visual observation and spectral analyses that PAAM is able to take part in the curing reaction of epoxy. Such a chemical bonding between the PAAM chains grafted onto the nanoparticles and surrounding epoxy networks would certainly enhance the filler/matrix adhesion in the composites.

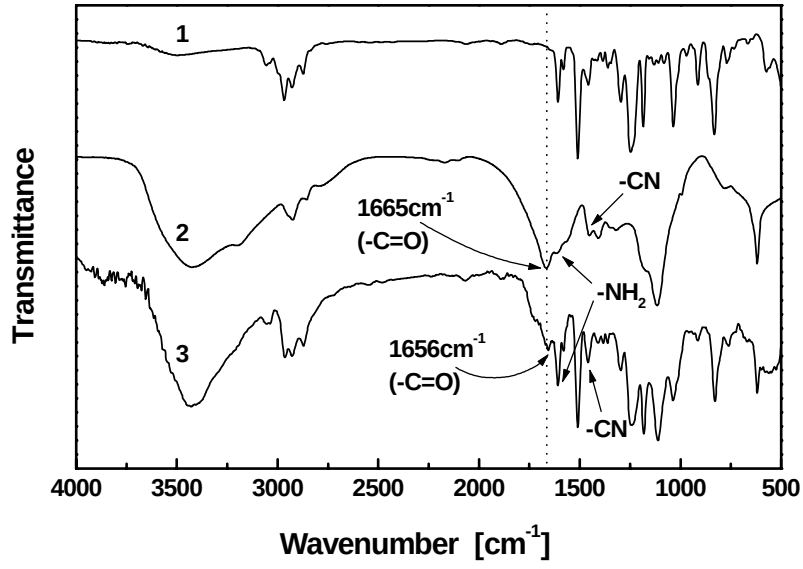

Figure 21. FTIR spectra of (1) epoxy without any curing agent, (2) PAAM, and (3) cured blends of PAAM and epoxy (1/2 w/w).

Dynamic mechanical analysis is a useful tool to monitor interfacial interaction in composite materials Fig.22 illustrates the mechanical loss spectra of mamo-Si_3N_4/epoxy

composites. In contrast to the conventional composites [56], whose damping factor at glass transition, Tan δ_{T_g}, is lower than that of the matrix, the internal friction peak intensity of epoxy shown in Fig.22 is weaker than the filled versions. Besides, the glass transition temperature characterized by the α-peak temperature of epoxy is also higher than those of the composites. This phenomenon might result from (i) a weak interfacial interaction in the case of stiff interphase [57] or (ii) a strong interfacial interaction in the case of ductile interphase [58]. Considering that impact tests reveal the ability of the particles to induce plastic deformation, it can be deduced that the latter factor plays the leading role. In fact, this estimation is supported by the calculation of Kubat parameter B [59]:

$$B = \frac{Tan\delta_c}{(1-V_f)Tan\delta_m} - 1 \qquad (1)$$

where Tan δ_c and Tan δ_m denote the damping factors of the composites and the matrix, respectively, and V_f is the filler volume fraction. By using the Tan δ_{T_g} data of the materials shown in Fig.22, the values of B for the composites are yielded: 0.04 (V_f=0.27vol%), 0.51 (V_f=0.83vol%), 0.40 (V_f=1.38vol%), and 0.36 (V_f=2.19vol%). As B approaching 0 corresponds to strong interfacial bonding in the composites, it is known that the nanocomposites at the lowest filler fraction (V_f=0.27vol%) has the highest filler/matrix adhesion.

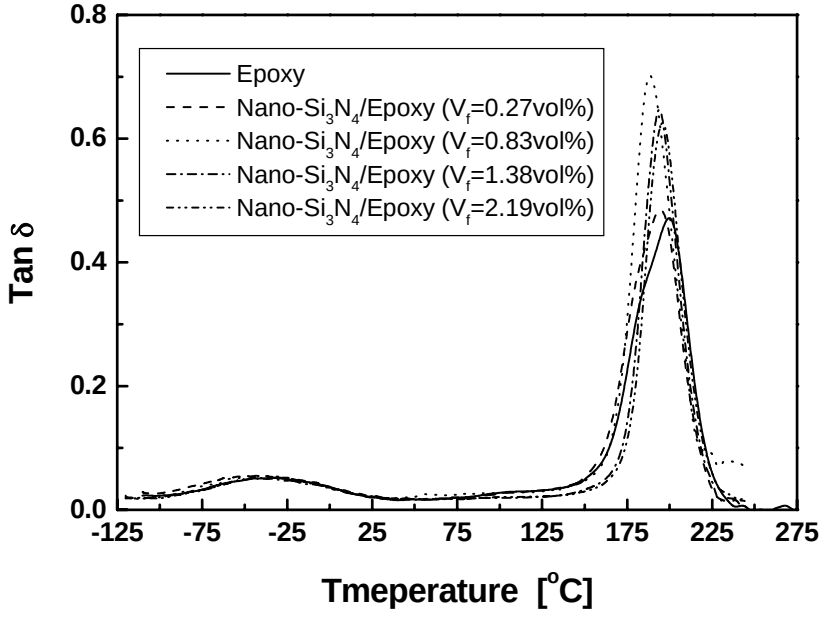

Figure 22. Temperature dependence of internal friction, Tanδ, of nano-Si_3N_4/epoxy composites measured at 1Hz.

Table 7 further lists the peak temperatures and activation enthalpies of the β relaxation, ΔH_β, of the composites. The values of the latter parameters were obtained from Arrhenius regression. β relaxation has been assigned to motions of the $O\text{-}CH_2\text{-}CHOH\text{-}CH_2$ hydroxypropylether units and cooperative motions involving hydroxypropylether units and amine crosslinking points that are present in all these systems [60, 61]. The greater ΔH_β values of the composites than that of unfilled epoxy induced by the addition of nano-Si_3N_4 means that the particles/matrix interaction is so strong that the motion of alcohol ether in epoxy is greatly obstructed and the crosslinking density is changed to a certain extent as well.

The results of dynamic mechanical analysis of nano-SiO2/epoxy composites are given in Table 8. Activation enthalpies of the β relaxation are ranked in the order: epoxy < SiO_2/epoxy < SiO_2-g-PAAM/epoxy. According to the above discussion, it is known that the strong interactions between the particles and the matrix have been established. This is particular true when grafted nanosilica appears. With respect to the glass transition temperature, the composites filled with treated and untreated nanoparticles have almost the same values. The increase in T_g can be attributed to the decreased mobility of chain segments of epoxy resin as a result of the filler/matrix interaction. Considering molecular mechanisms, it is evident that the additional chemical bonding between grafting PAAM and epoxy exerts a more significant influence on the secondary relaxation of epoxy than on the primary transition.

Table 7. Characterization of β relaxation of nano-Si_3N_4/epoxy composites

V_f (vol%)	Peak temperature of β relaxation (^oC)				ΔH_β (kJ/mol)
	30Hz	10Hz	3Hz	1Hz	
0	-13.8	-22.8	-31.4	-35.9	56.6
0.27	-16.8	-25.2	-33.6	-41.3	75.8
0.83	-19.5	-26.2	-33.2	-41.0	103.6
1.38	-16.4	-22.34	-29.8	-37.6	80.7
2.19	-16.2	-23.8	-30.4	-36.6	78.7

Table 8. Characteristic parameters of dynamic mechanical performance of epoxy and its composites at 2.17vol% nanosilica content

Materials	Epoxy	SiO_2/Epoxy	SiO_2-g-PAAM/Epoxy
ΔH_β (kJ/mol)	48.3	54.0	73.9
T_g* (^oC)	217.5	225.1	225.8

* T_g: glass transition temperature determined from the peak temperature of the α transition at 10Hz

3. FRICTION AND WEAR PROPERTIES

3.1. Friction and Wear Properties of Nano-Al_2O_3/Epoxy Composites

The sliding wear rate of nano-Al_2O_3/epoxy composites is illustrated in Fig.23 as a function of nano-alumina particle content. The degrees of the particles pretreatments are listed in Table 9. From Fig.23, it is seen that the high wear rate of unfilled epoxy due to the

three-dimensional crosslinking network is greatly decreased by adding nano-Al_2O_3 particles. As compared to the composites with untreated nanoparticles, the low wear rates of the composites filled with treated nano-Al_2O_3 particles keep almost unchanged with filler content up to ~2vol%. The phenomenon is similar to what is reported in ref.[62] in spite of the fact that the testing configurations and conditions are different. Figs.24 and 25 give the results of other composites and clearly show that the wear resistance of unfilled epoxy is decreased by one order of magnitude when treated nano-Al_2O_3 is incorporated.

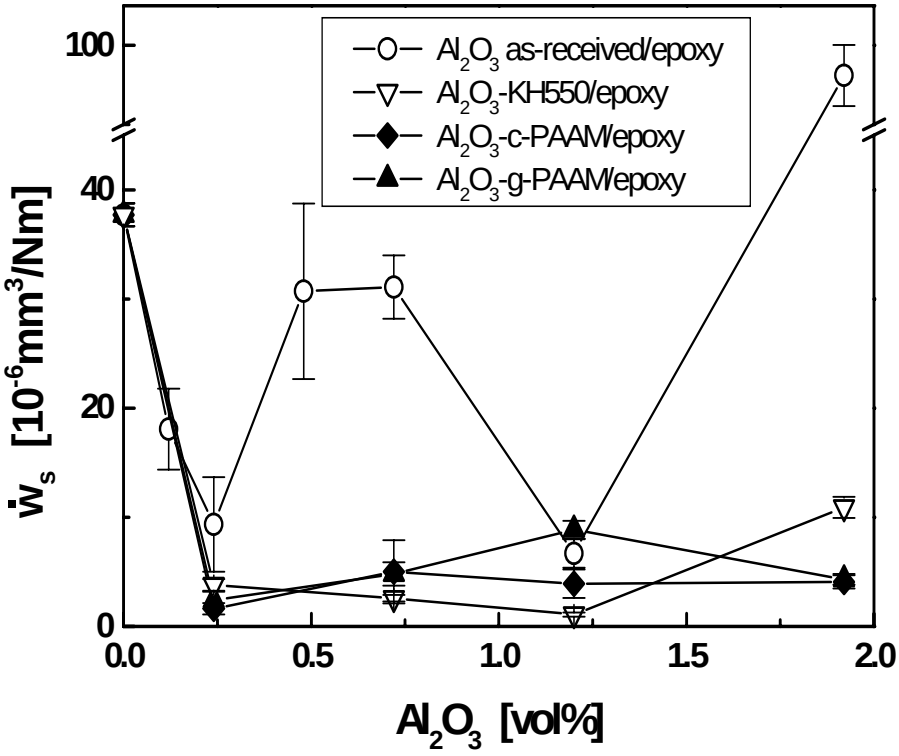

Figure 23. Specific wear rate, $\dot{w}_s$, of nano-Al_2O_3/epoxy composites as a function of volume fraction of nano-Al_2O_3. Test conditions: p=3MPa, v=0.4m/s.

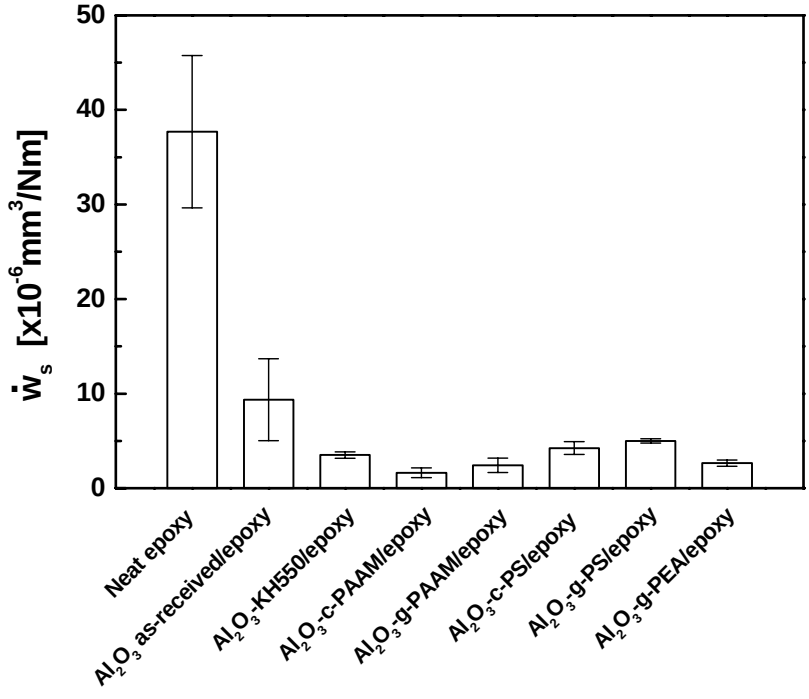

Figure 24. Specific wear rate, $\dot{w}_s$, of nano-Al_2O_3/epoxy composites at a volume fraction of nano-Al_2O_3 of 0.24vol%. Test conditions: p=3MPa, v=0.4m/s.

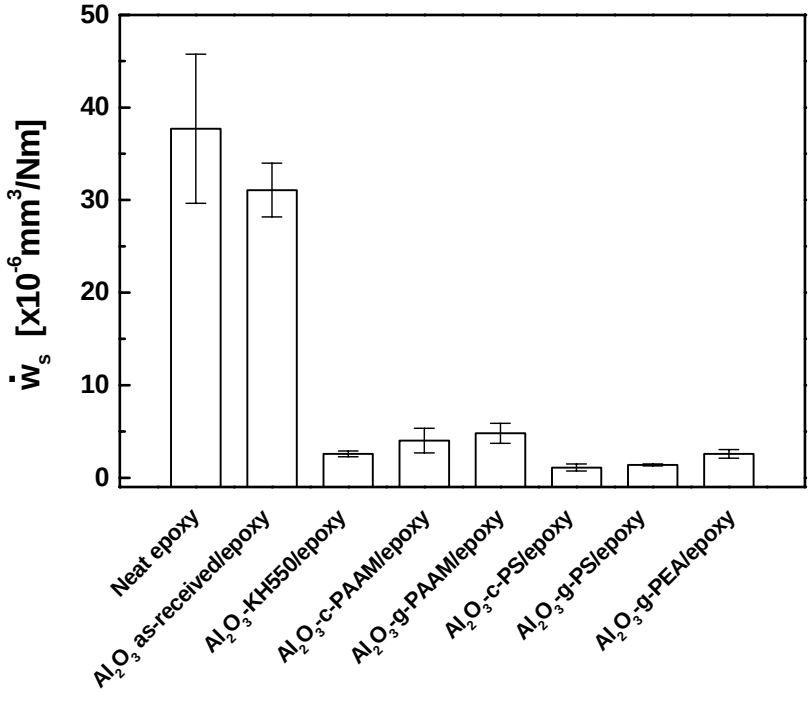

Figure 25. Specific wear rate, $\dot{w}_s$, of nano-Al_2O_3/epoxy composites at a volume fraction of nano-Al_2O_3 of 0.72vol%. Test conditions: p=3MPa, v=0.4m/s.

Table 9. Amounts of the chemicals adhered to Al_2O_3 nanoparticles

Treated particles	Al_2O_3-KH550	Al_2O_3-c-PAAM	Al_2O_3-c-PS	Al_2O_3-c-PEA	Al_2O_3-g-PAAM	Al_2O_3-g-PS	Al_2O_3-g-PEA
$W_{chem/alumina}$* (%)	2.2	15	15.5	20.5	10	9.1	14.6

*$W_{chem/alumina}$: relative amount of the chemical adhered to the particles = weight of the chemical adhered to the particles / weight of Al_2O_3. Al_2O_3-KH550 means the nanosized alumina particles have been treated by KH550 silane. Al_2O_3-c-PAAM, Al_2O_3-c-PS and Al_2O_3-c-PEA denote that the particles are grafted by polyacrylamide, polystyrene and polyethyl acrylate without removing the homopolymers generated during the graft polymerization. Having experienced extraction with proper solvents, the grafted nanoparticles are symbolized by Al_2O_3-g-PAAM, Al_2O_3-g-PS and Al_2O_3-g-PEA, respectively, meaning the particles are accompanied only with the unextractable grafting polymers.

For untreated nano-Al_2O_3 filled epoxy composites, the decrement of wear rate is marginal especially when filler content is greater than 0.24vol%. It resembles the case of untreated nano-Al_2O_3/ultra-high-molecular-weight-polyethylene [63], meaning that the composites cannot effectively entrap the particles and prevent substantial material removal.

Besides improving the wear resistance, the nanoparticles also reduce frictional coefficient of epoxy as shown in Figs.26, 27 and 28. Evidently, the composites with treated nanoparticles have lower frictional coefficients than those with untreated ones. At a content of nano-Al_2O_3 of 0.24vol%, for example, the frictional coefficient of Al_2O_3-c-PAAM/epoxy is 0.35 that amounts to 61% of the value of unfilled epoxy and 69% of the value of untreated nano-Al_2O_3/epoxy. Meanwhile, the specific wear rate of Al_2O_3-c-PAAM/epoxy with the same filler concentration is decreased by 97% and 88% respectively, as compared with the values of unfilled epoxy and untreated nano-Al_2O_3/epoxy.

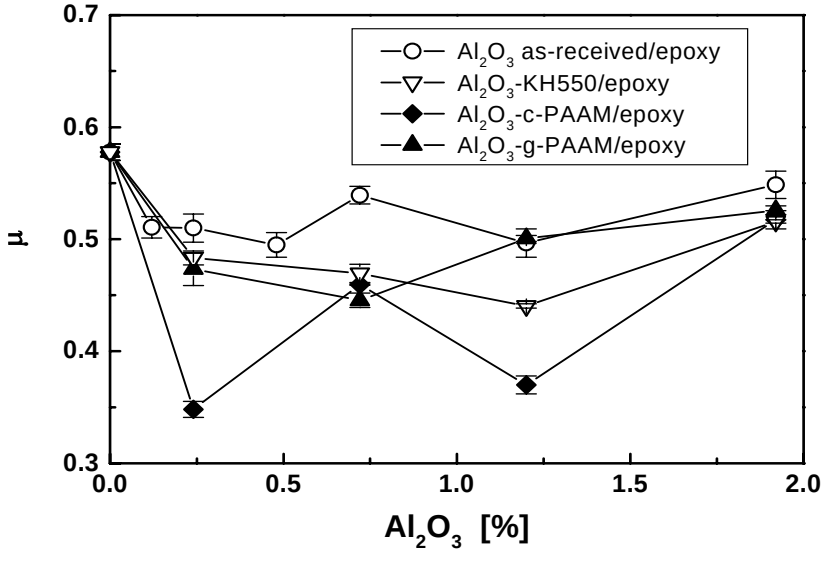

Figure 26. Frictional coefficient, μ, of nano-Al_2O_3/epoxy composites as a function of volume fraction of nano-Al_2O_3. Test conditions: p=3MPa, v=0.4m/s.

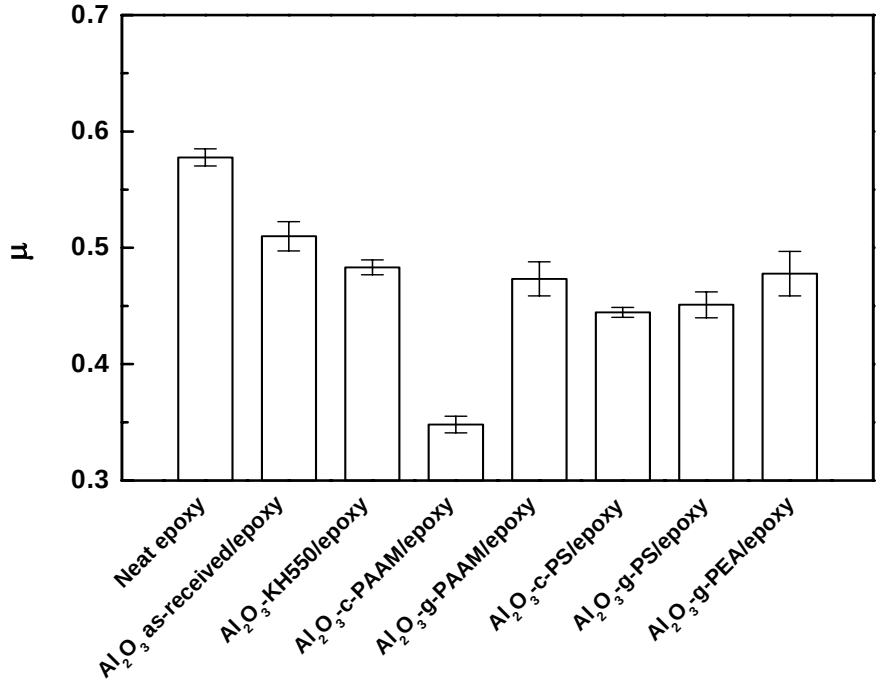

Figure 27. Frictional coefficient, μ, of nano-Al_2O_3/epoxy composites at a volume fraction of nano-Al_2O_3 of 0.24vol%. Test conditions: p=3MPa, v=0.4m/s.

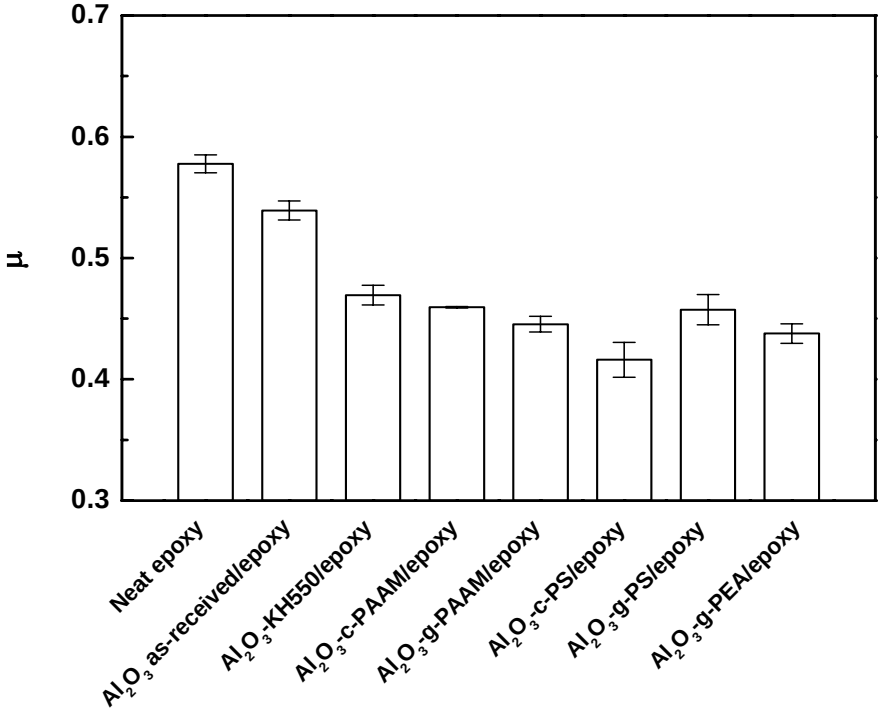

Figure 28. Frictional coefficient, μ, of nano-Al_2O_3/epoxy composites at a volume fraction of nano-Al_2O_3 of 0.72vol%. Test conditions: p=3MPa, v=0.4m/s.

The difference in improving the friction reducing and wear resisting ability of epoxy between the composites with untreated and treated nano-alumina should result mainly from the filler/filler adhesion strength. The treatments employed in the present work can either build up chemical bonding between the nanoparticles and epoxy (for the composites with KH550 treated nano-Al_2O_3 and PAAM grafted nano-Al_2O_3), or improving the interfacial miscibility (for epoxy reinforced by PS grafted nano-Al_2O_3 and PEA grafted nano-Al_2O_3). With respect to the untreated nanoparticles, they have to present themselves in the composites in the form of agglomerates because of the hydrophilic nature of the particles and the limited dispersion force during blending with epoxy. Inside the nanoparticle agglomerates, the particles are bound only by hydrogen bonds and van der Waals bonds. When the composites with the untreated nanoparticles are subjected to wearing, damage induced by localized shear stress concentration at the loosened nanoparticle agglomerates would occur on a relatively large scale and produce bigger blocks of wear debris. These are disadvantageous to the improvement of tribological performance of the matrix. In the case of the composites with enhanced interaction inside and outside the nanoparticle agglomerates, the resistance to periodic frictional stress is greatly increased. Detachment of nanoparticles and small amount of the surrounding matrix plays the leading role in material removal due to wear. The detached nanoparticles might also act as solid lubricants. These account for the low wear rates and frictional coefficients of the composites.

On the other hand, the effect of homopolymers (generated during graft polymerization) on the grafted nanoparticles/epoxy composites is also revealed in Figs.24, 25, 27 and 28. In most cases, the presence of the homopolymers helps to further improve the wear and friction performance of the composites. For example, the wear rate of Al_2O_3-c-PAAM/epoxy is lower than that of Al_2O_3-g-PAAM/epoxy (Figs.24 and 25), and frictional coefficient of Al_2O_3-c-PS/epoxy is lower than Al_2O_3-g-PS/epoxy (Figs.27 and 28). It is believed that the filler/matrix interaction is partially shielded by the homopolymers in the case of Al_2O_3-c-PAAM/epoxy and Al_2O_3-c-PS/epoxy composites. When the composites rub against the steel counterface, the nano-Al_2O_3 particles in Al_2O_3-c-PAAM/epoxy and Al_2O_3-c-PS/epoxy might break away from the binding of the matrix more easily than those in Al_2O_3-g-PAAM/epoxy and Al_2O_3-g-PS/epoxy composites, providing solid lubricating effect. In addition, for the nano-Al_2O_3 particles right on the rubbing surface of Al_2O_3-c-PAAM/epoxy and Al_2O_3-c-PS/epoxy, the surrounding grafting polymers and homopolymers can also lubricate the wear processes.

The lubricating effect of the nanoparticles can be partly evidenced by the microhardness of the materials' surfaces before and after the sliding wear tests (Fig.29). For unfilled epoxy, the microhardness of the worn pin surface is remarkably lowered as compared to the value of the unworn one. It reflects the deteriorated microstructure of epoxy led by the repeated frictional force and high frictional temperature. When nano-Al_2O_3 is added, the microhardness of the worn pin surface of the composites is either the same as or slightly lower than that of the unworn pin surface. Clearly, the severe wear in the case of unfilled epoxy has been changed to mild one due the nanoparticles.

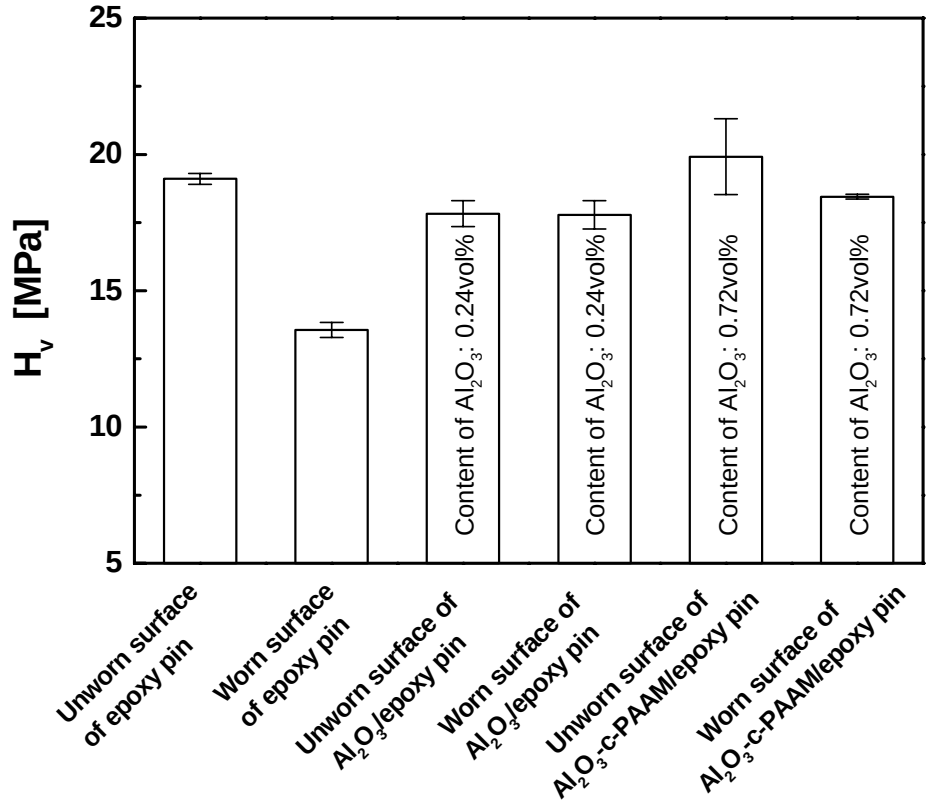

Figure 29. Vickers microhardness, H_v, of the materials' surfaces before and after sliding wear tests.

To have more information about the variation in wear behavior due to the addition of the nanoparticles, morphologies of the worn pins' surfaces are examined by SEM at an identical magnification (Fig.30). Severe damages characterized by the disintegration of top layer are observed in unfilled epoxy (Fig.30(a)). The material removal takes the form of larger blocks, which might be captured between the steel counterface and the test pin, and abrade the specimen surface leading to even more substantial material loss. In the case of filled composites, the appearances are completely different and become rather smooth. Although the ploughing grooves are still visible on the composites with untreated nano-Al_2O_3 (Fig.30(b)), the groove depths are quite shallow on the composites with treated nano-Al_2O_3 (Figs.30(c~f)) or simply invisible (Fig.30(g)). It suggests that polishing predominates the wear processes of the latter composites.

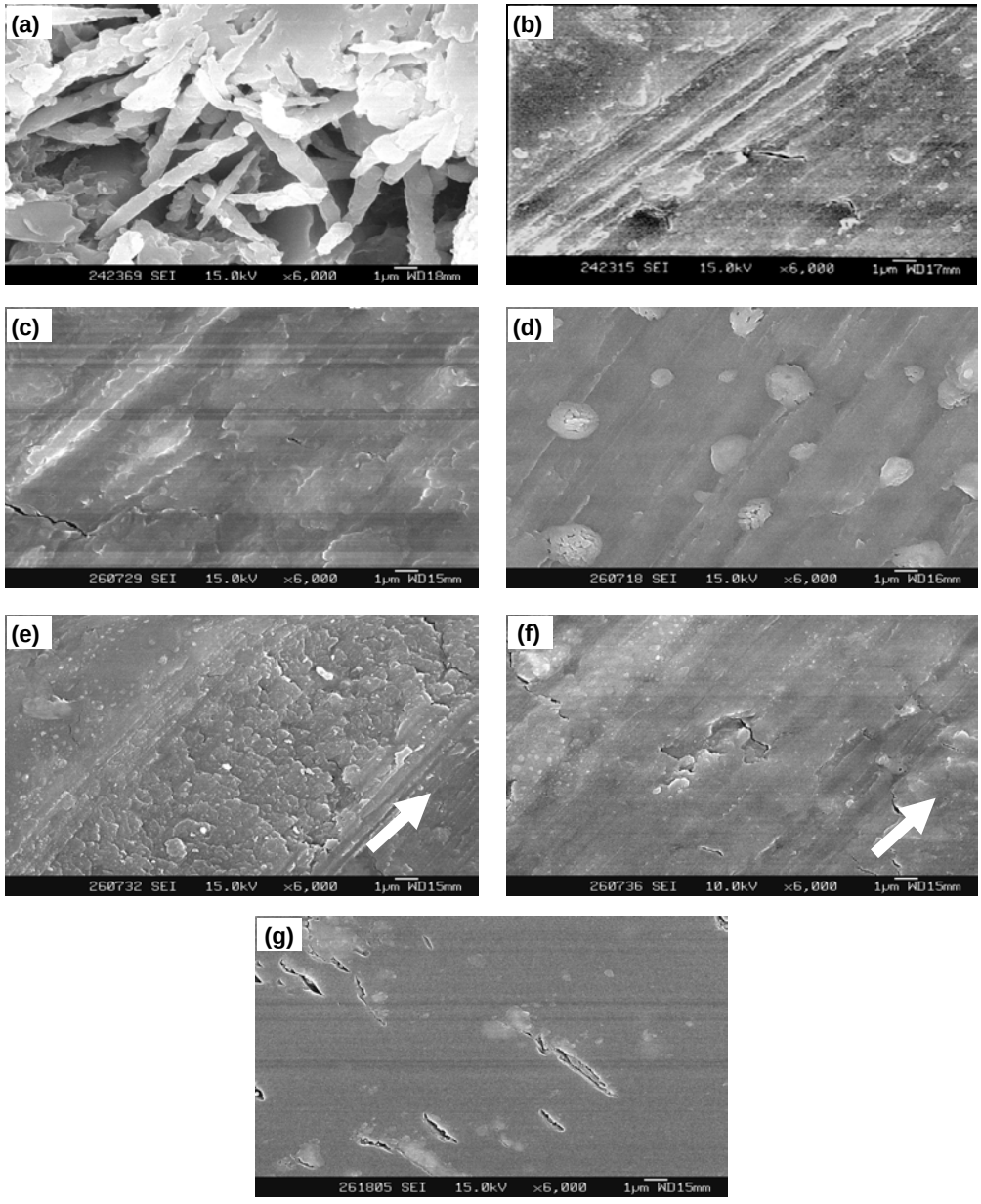

Figure 30. SEM photos of the worn surfaces of (a) unfilled epoxy and its composites filled with (b) untreated nano-Al_2O_3, (c) Al_2O_3-KH550, (d) Al_2O_3-c-PAAM, (e) Al_2O_3-g-PAAM, (f) Al_2O_3-g-PS, and (g) Al_2O_3-g-PEA at a volume fraction of nano-Al_2O_3 of 0.24vol%. The arrows indicate the sliding direction. Test conditions for the sliding wear: p=3MPa, v=0.4m/s.

It is noted that some cracks across the wear tracks are perceivable on the composites' worn surfaces (Figs.30(b), (c), (f) and (g)). They might be nucleated at sub-surface layer as a result of shear deformation induced by the traction of the harder asperities. The scale-like damage patterns (Figs.30(e) and (f)) resulting from the coalescence of the cracks imply that the effect of fatigue-delamination [64] is the main wear mechanism. It can thus be concluded

that the abrasive wear of unfilled epoxy is replaced by fatigue wear when the treated nano-Al_2O_3 particles are compounded, while the wear mode of untreated nano-Al_2O_3/epoxy is a mixture of abrasive wear and fatigue wear.

Table 10 lists the elements on the steel counterpart surface before and after the wear tests, which are determined by X-ray energy distribution spectra (EDS). Having rubbed with epoxy, sulfur appears on the surface of the steel ring, implying the transfer from epoxy to the counterface. When the specimen is changed into untreated nano-Al_2O_3/epoxy composite, both sulfur and aluminum can be detected. It further proves substances transfer across the frictional surfaces. It is worth noting that the contents of sulfur and aluminum on the steel ring surface are increased as the ring has rubbed against Al_2O_3-g-PAAM/epoxy composite. This suggests that tribochemically induced transfer film [65] can be more effectively built up on the steel counterface thereby decreasing wear, as compared to the case of untreated nano-Al_2O_3/epoxy composite. According to the X-ray photoelectron spectra (XPS) analysis of the worn surfaces of the composites (Fig.31), it is known that under the joint action of high frictional temperature and pressure the aluminum no longer presents itself only in the form of Al_2O_3 but additionally reacts with Fe and S, respectively. Therefore, the above-stated formation of the transfer film is thermodynamically favorable.

Table 10. Surface elemental analysis of the steel counterpart

	Elements and content (%)			
	Fe	S	Al	Si
Steel ring before wear test	98.65	0	0	0.22
Steel ring rubbed against epoxy pin	98.55	0.42	0	0.21
Steel ring rubbed against untreated nano-Al_2O_3/epoxy composite pin at a volume fraction of nano-Al_2O_3 of 0.24vol%	98.41	0.31	0.2	0.1
Steel ring rubbed against Al_2O_3-g-PAAM/epoxy composite pin at a volume fraction of nano-Al_2O_3 of 0.24vol%	97.5	0.58	0.4	0.19

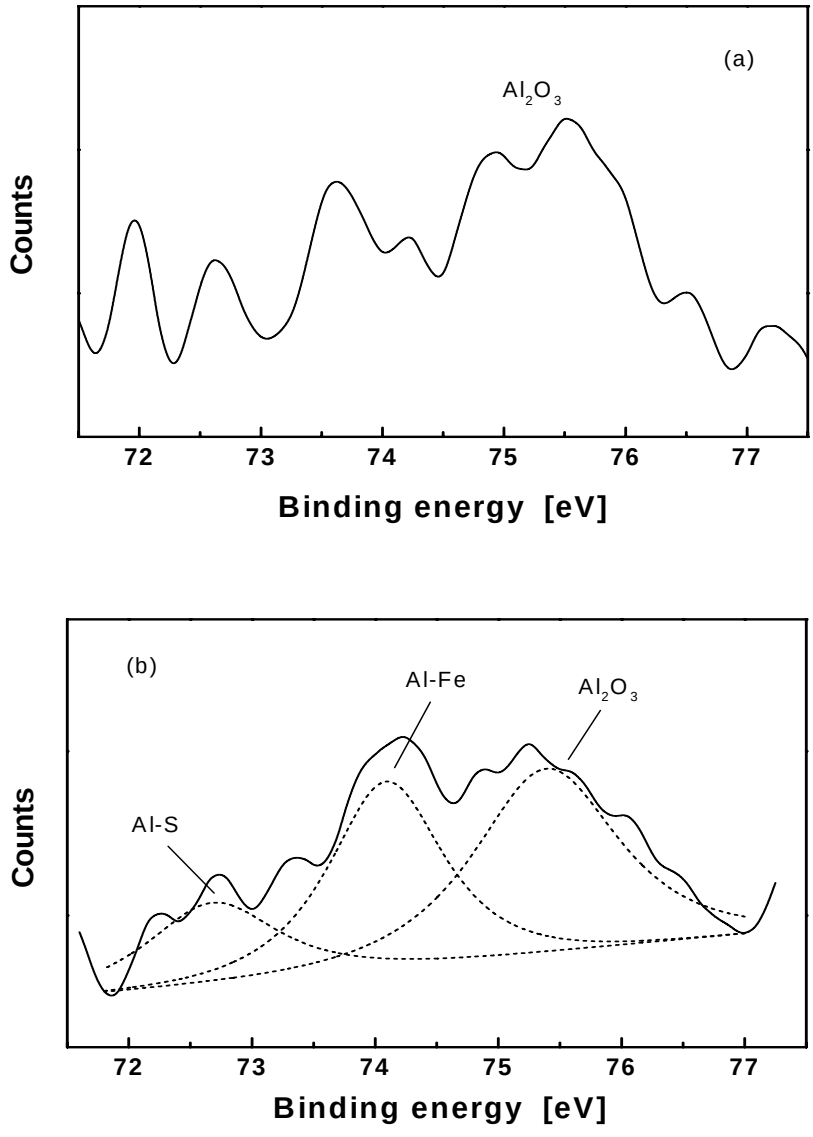

Figure 31. Al 2p spectra of the pin surface of (a) unworn nano-Al_2O_3/epoxy composites and (b) worn nano-Al_2O_3/epoxy composites at a volume fraction of nano-Al_2O_3 of 0.24vol%.

3.2. Friction and Wear Properties of Nano-SiC/Epoxy Composites

The tribological performance of epoxy and its composites filled with SiC nanoparticles are given in Fig.32. Both treated and untreated SiC nanoparticles are able to reduce the frictional coefficient of epoxy (Fig.32(a)). Especially when the content of the particles is 0.2vol%, the composites' frictional coefficients exhibit the lowest values among the results. Comparatively, the grafted SiC nanoparticles provide more significant solid lubricating

effect. With a rise in the filler loading, however, the frictional coefficients of the materials increase, suggesting that the particles cannot be dispersed homogeneously in the case of increased amount of the particles and agglomeration of the fillers is disadvantageous to the lubrication between the composites and the steel counterpart. The profiles of the worn pins' surfaces (Fig.33) indicate that the resistance of the composites to surface shear failure is improved as a result of the incorporation of the nanoparticles. The roughness of the frictional surfaces decreases remarkably, and the wear process is actually characterized by polishing.

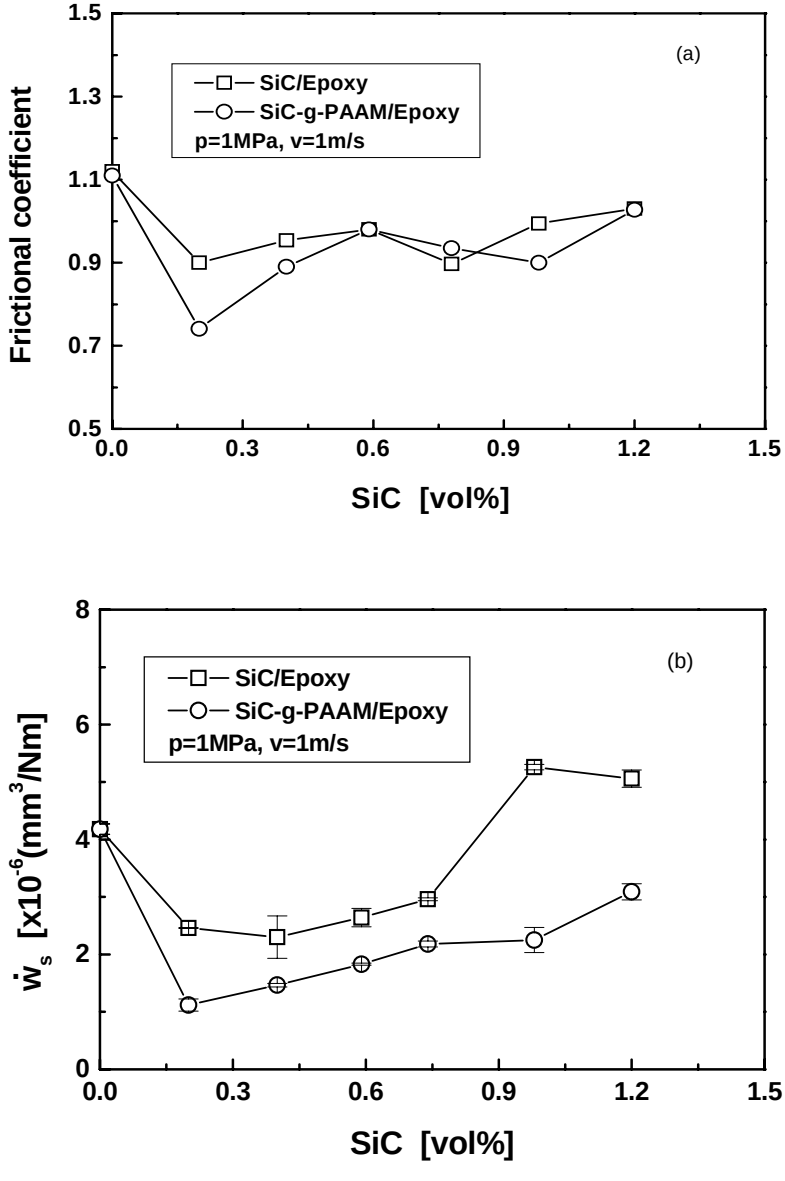

Figure 32. Friction coefficient (a) and specific wear rate (b) of nano-SiC filled epoxy composites as a function of filler content.

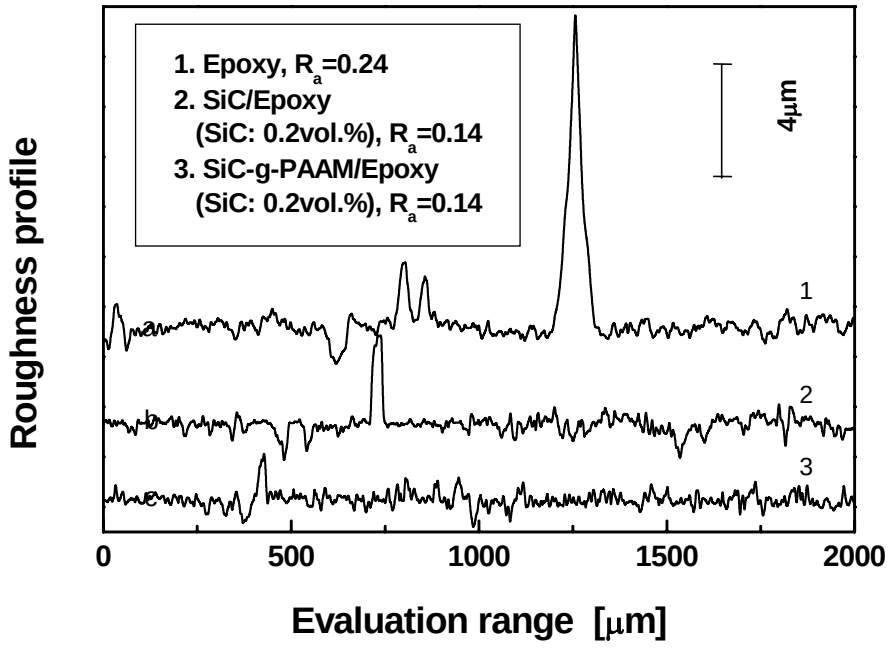

Figure 33. Profile scans of the worn surfaces of (a) epoxy, (b) SiC/epoxy and (c) SiC-g-PAAM/epoxy composites (Content of SiC: 0.2vol.%, Wear test conditions: block-on-ring, p=1MPa, v=1m/s).

Similar to the results of frictional coefficient measurements, the addition of SiC nanoparticles can also lead to decreased wear rate (Fig.32(b)). It is worth noting that the wear rates of the composites with grafted SiC nanoparticles are lower than those of the composites with untreated SiC within the entire range of filler content of interests. Although the wear rates of the composites increase with a rise in the particles content, the variation is more significant in the system of SiC/epoxy. For the content of SiC of 1~1.2vol%, for example, SiC/epoxy exhibits wear rate even higher than that of unfilled epoxy. These manifest that smaller amount of well-distributed nanoparticles can reinforce the matrix effectively [45], and prevent the composites from wear failure. Owing to the introduction of the grafting polymer chains, the interfacial adhesion between the nanoparticles and the matrix is further enhanced and thus the wear resistance can also be raised accordingly. When the concentration of the nanoparticles increases, the particles are hard to be dispersed and many weak interfaces form inside the agglomerated nanoparticles. As a result, the particles would be removed from the matrix easily under the action of frictional force and the composites' wear rate has to be increased. Surface grafting treatment overcomes the aforesaid defects to a certain extent, so that SiC-g-PAAM/epoxy composites still have higher wear resistance than SiC/epoxy in the case of higher filler fraction.

As in-situ polymerization was employed during surface grafting onto the nanoparticles, homopolymers of the monomers were inevitably produced. For simplifying the influencing factors, however, the grafted nanoparticles used in the composites cited in Figs.32 and 33 were extracted prior to the composites preparation to remove the homopolymerized PAAM.

In consideration of the fact that large quantity of solvent and longer time are required for separating homopolymers from the grafted products in practical applications, it is necessary to study the influence of the homopolymers accompanying the grafted nanoparticles on the tribological performance of the composites. As shown in Fig.34, in the case of relatively low filler content (0.2vol%), the appearance of the homopolymers in the grafted nanoparticles leads to higher wear rate of the composites (SiC-c-PAAM/epoxy) than that of the composites with grafted SiC particles excluding the homopolymerized PAAM (SiC-g-PAAM/epoxy). At the particle content of 0.98vol%, on the contrary, the wear rate of SiC-c-PAAM/epoxy becomes slightly lower than that of SiC-g-PAAM/epoxy. It is interesting that SiC-c-PAAM/epoxy (0.98vol%) and SiC-c-PAAM/epoxy (0.2vol%) have similar wear rates regardless of their particles content, implying the shielding effect of the homopolymers.

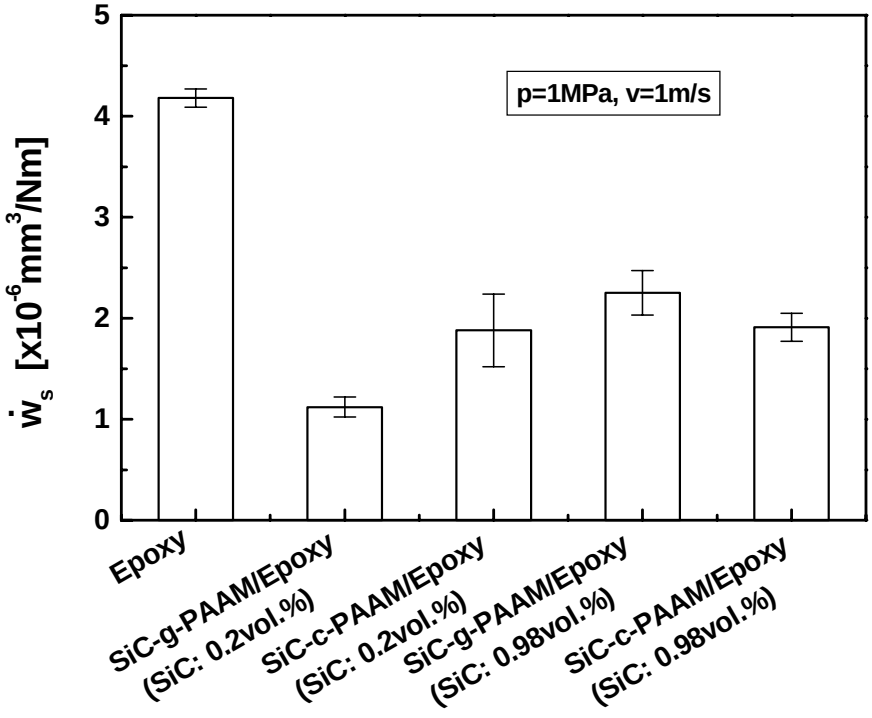

Figure 34. Effect of homopolymers generated during grafting onto nano-SiC particles on the wear rate of epoxy based composites.

For obtaining more information about the roles of the nanoparticles and their grafted versions, the pressure dependence of the wear rate of the composites is illustrated in Fig.35. Clearly, the wear rate of unfilled epoxy is increased by two orders of magnitude when the contact pressure increases from 1 to 3MPa. As the pressure is 5MPa, rupture of the epoxy specimen occurs and the value of wear rate can no longer be determined. In contrast, although the wear rates of SiC/epoxy and SiC-g-PAAM/epoxy composites increase with a rise in pressure, under the pressure of 3MPa they are only 1/5 and 1/40 of that of unfilled epoxy,

respectively. Even in the case of 5MPa, steady wear is perceived in the two composites, and SiC-g-PAAM/epoxy composites exhibit much higher wear resistance than SiC/epoxy. According to the effect of reinforcement on the friction and wear of polymers [66], it is known that well dispersed nanoparticles are able to effectively bear the load transferred from the matrix and reduce the probability of fatigue wear of the composites. Since the grafting polymers (i.e. PAAM) of SiC-g-PAAM has taken part in the curing reaction of epoxy [67], the strong interfacial bonding would inhibit the fatigue induced crack propagation. Therefore, the wear rate of SiC-g-PAAM/epoxy composites is still lower than that of SiC/epoxy composites under higher pressure (i.e. 5MPa).

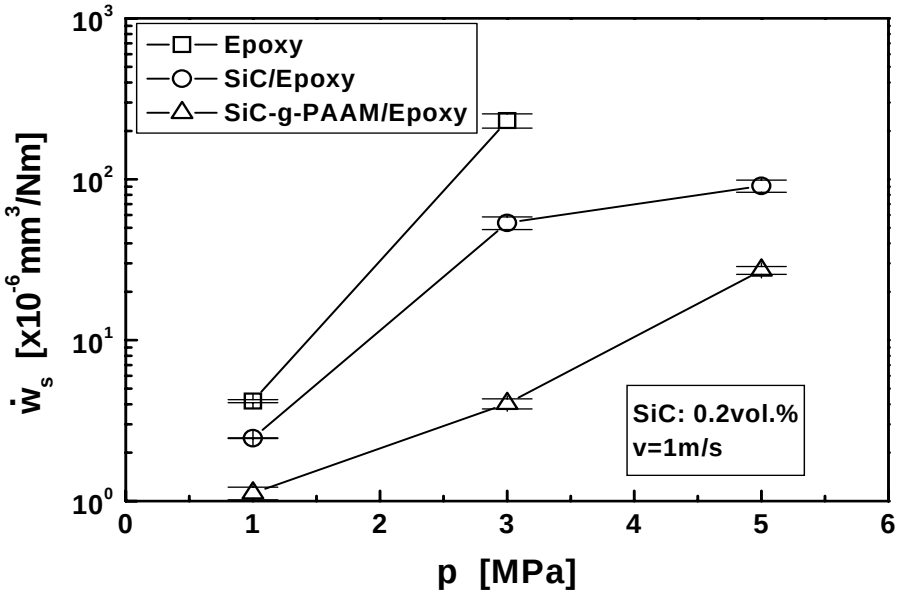

Figure 35. Effect of contact pressure on the wear rate of nano-SiC filled epoxy composites.

Surface morphological observation is a useful tool to estimate wear mechanism of materials. From the worn surfaces in Fig.36 it is seen that the cracks originate beneath the surface layer of unfilled epoxy block (Fig.36(a) and (b)). Due to the repeated friction, severe fatigue wear is presented on the neat epoxy and large fragments are detached from the surface as characterized by rather high wear rate (Fig.32(b)). Comparatively, the worn surfaces of SiC/epoxy composites are much less rough and the cracks are initiated right on the surfaces of the specimens (Fig.36(c) and (d)). When the grafted SiC nanoparticles are added, the worn surfaces become very smooth and remain high integrity (Fig.36(e) and (f)). Only trifling deformation that produces tiny wear debris appears (Fig.36(f)).

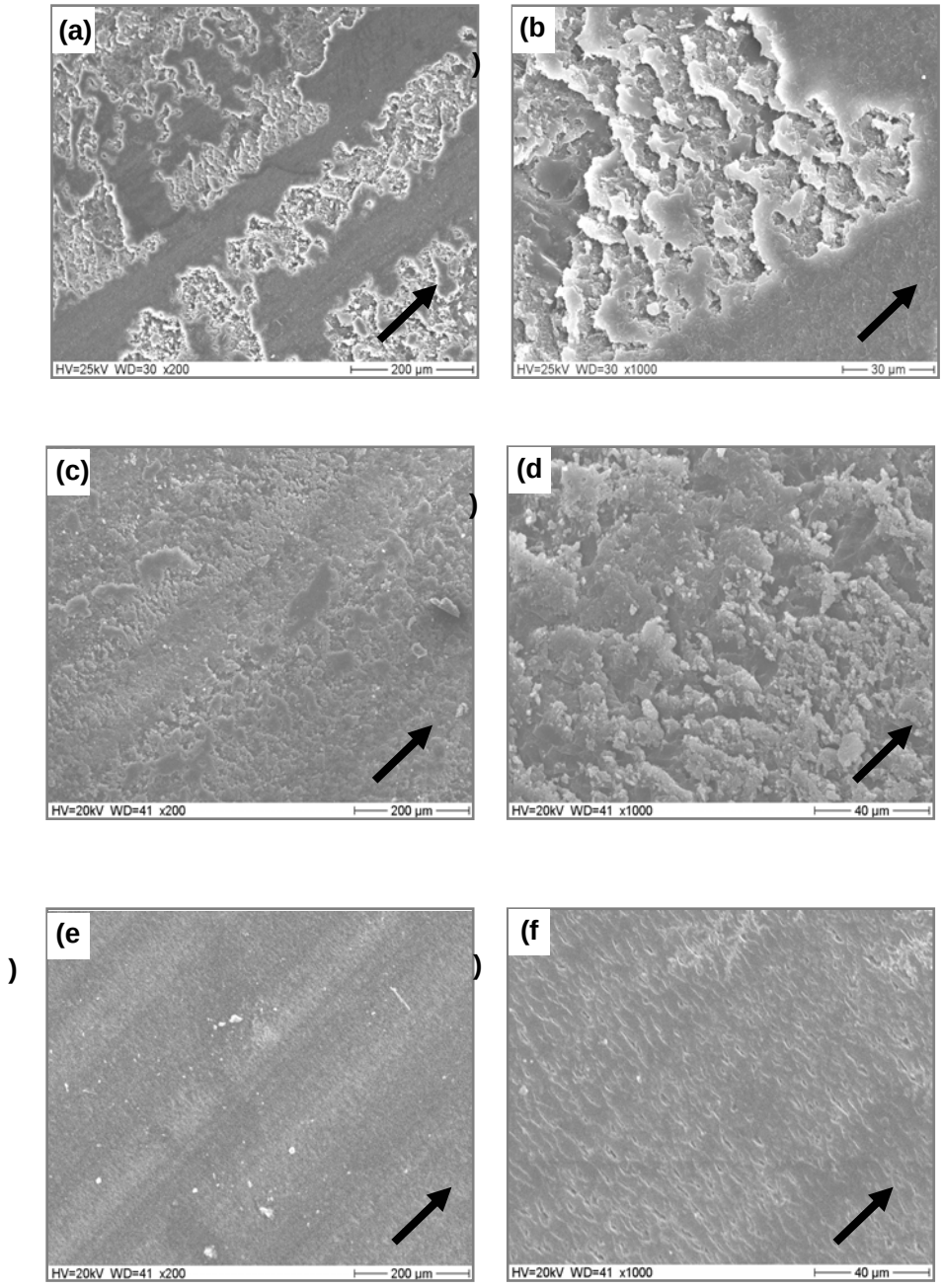

Figure 36. SEM photos of worn surfaces of (a, b) epoxy, (c, d) SiC/epoxy and (e, f) SiC-g-PAAM/epoxy composites (The arrows show the sliding directions. Content of SiC: 0.2vol.%, Wear test conditions: p=3MPa, v=1m/s).

Surface microhardness of the composites is plotted in Fig.37. The SiC nanoparticles either before or after the grafting treatment can raise the hardness of epoxy resin. Even though the content of the particles is quite low, composites' microhardness is higher than that of the unfilled epoxy. It means the load bearing ability of the nanoparticles has been brought into

play at low filler loading. This coincides with the above results of frictional coefficient and wear rate of the composites. With a rise in the particulates content, agglomeration of the fillers becomes severe so that the composites' surface microhardness tends to decrease.

Unlubricated sliding wear is closely related to the frictional heat. It is thus important to examine the thermal deformation behavior of the composites, which would help to understand the tribological properties of the composites. As shown in Fig.38, the addition of grafted SiC nanoparticles improves the resistance to thermal deformation of epoxy. Both the deformation at the same temperature and the maximum deformation of SiC-g-PAAM/epoxy composites are evidently lower than those of unfilled epoxy and SiC/epoxy composites. Therefore, it is expected that material removal of SiC-g-PAAM/epoxy composites due to wearing is more difficult as compared to the case of unfilled epoxy and SiC/epoxy composites.

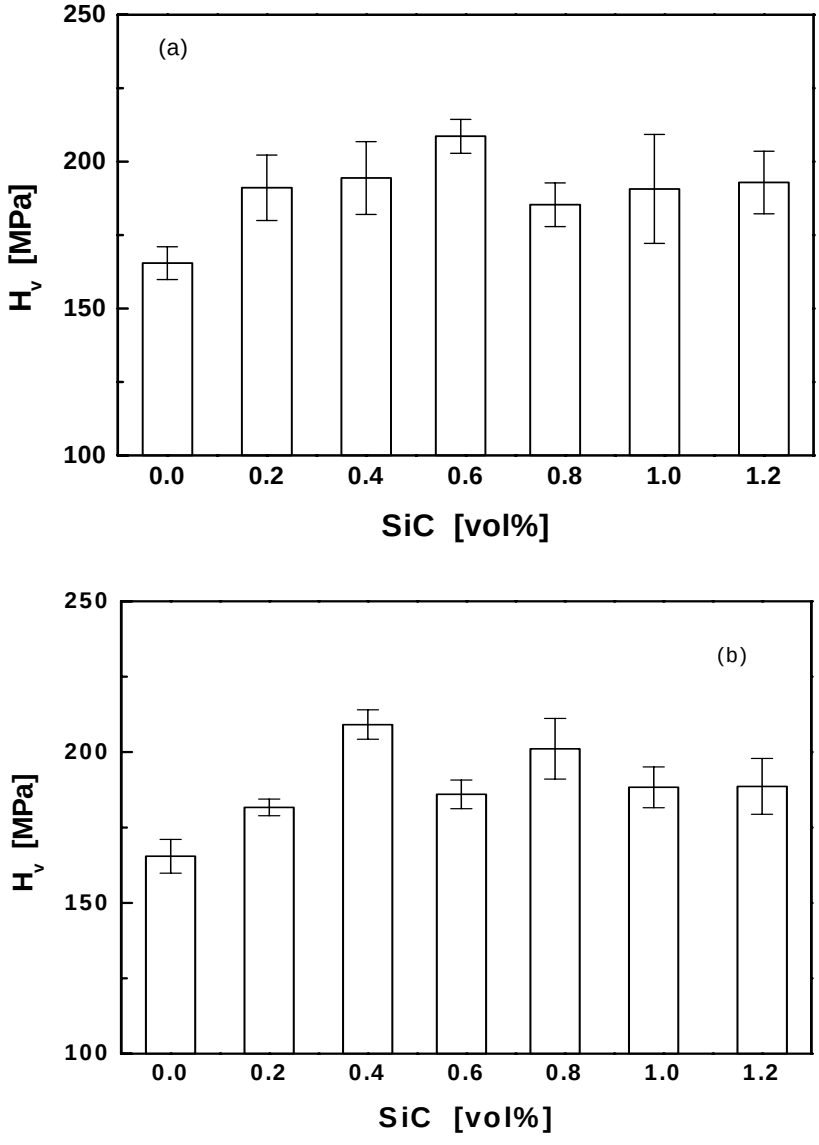

Figure 37. Microhardness of (a) SiC/epoxy and (b) SiC-g-PAAM/epoxy composites.

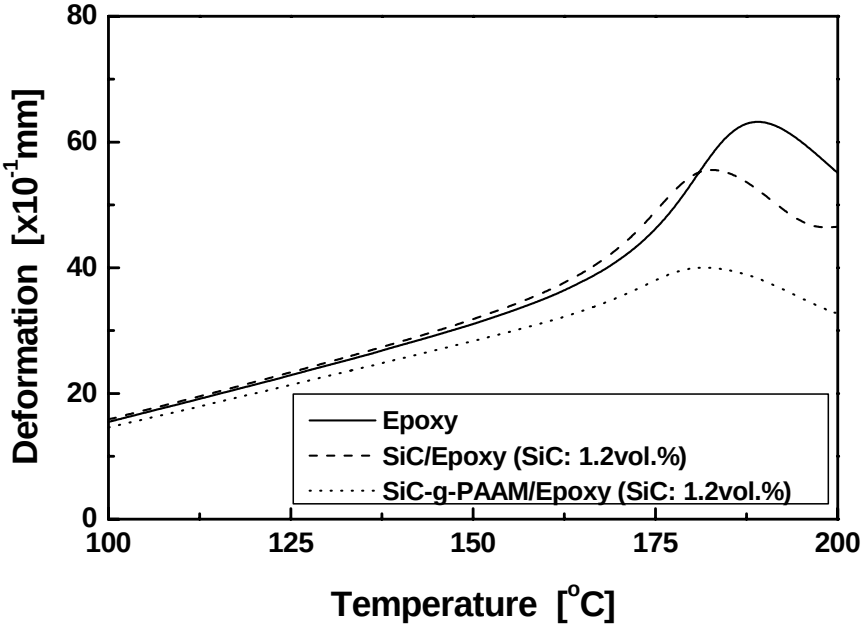

Figure 38. Heat distortion behavior of epoxy and its composites.

3.3. Friction and Wear Properties of Nano-SiO_2/Epoxy Composites

Fig.39 and Fig.40 show the sliding wear properties of the composites as a function of silica content. Frictional coefficient, μ, of the composites with unmodified silica nanoparticles keeps almost the same as that of neat matrix up to a filler fraction of about 4vol% (Fig.39). In contrast, the grafted particles can obviously reduce the value of μ even at low filler loadings. Similarly, a substantial decrease in specific wear rate, $\dot{w}_s$, can be observed in SiO_2-g-PAAM filled composites with a rise in filler content and all of the $\dot{w}_s$ values are lower than those of untreated nano-SiO_2 filled versions, although the untreated nanoparticles can also result in decreased $\dot{w}_s$ with respect to the unfilled epoxy. In the filler content varying from 2 to 6vol%, the wear resistance of epoxy is increased by a factor of about 20 by the addition of SiO_2-g-PAAM. Compared with the fact that 40wt% micron-sized SiO_2 (180μm) particles were needed to acquire a significant decrease in wear rate of epoxy [17], the present systems are clearly characterized by broader applicability.

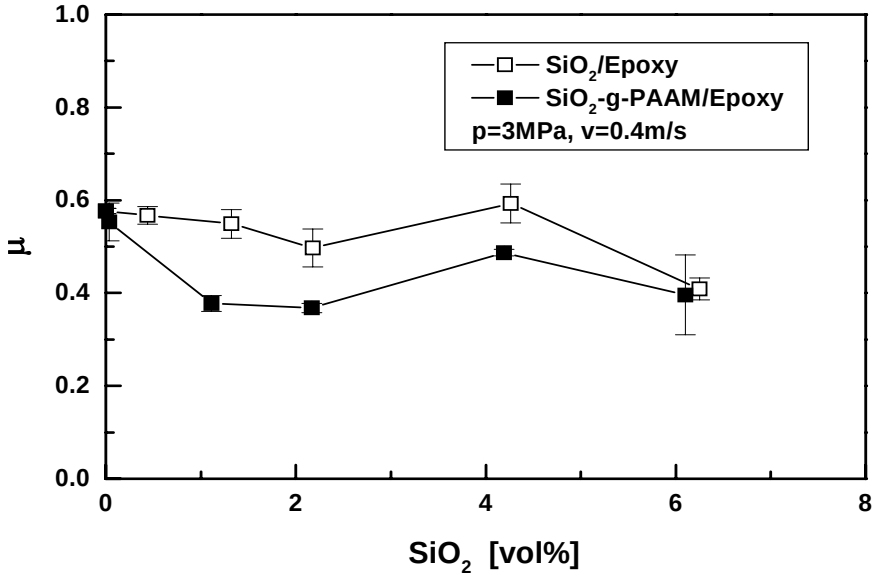

Figure 39. Filler content dependence of frictional coefficient, μ, of epoxy and its composites.

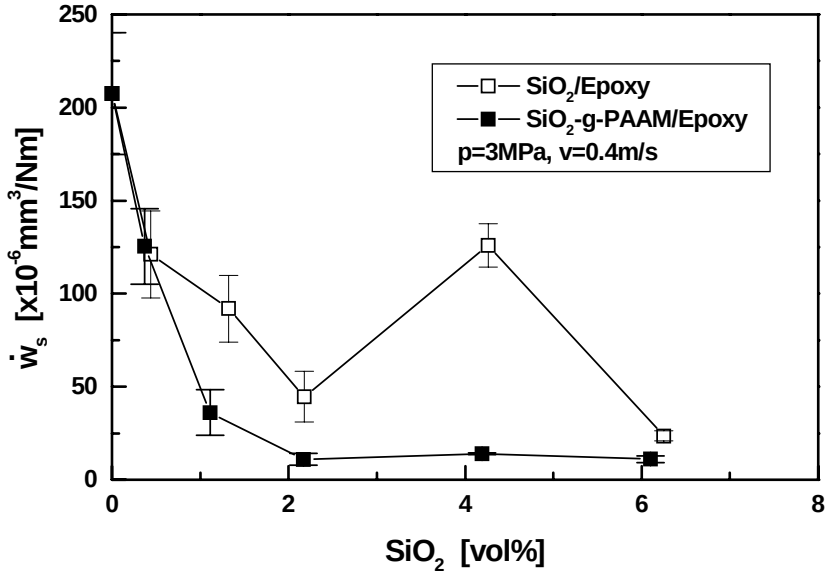

Figure 40. Filler content dependence of specific wear rate, $\dot{w}_s$, of epoxy and its composites.

As manifested by ref.[68], nanoparticles are able to significantly reduce the wear rate of epoxy because the wear mechanism changes from severe abrasive wear to mild sliding wear. A further improvement of the tribological performance of SiO_2-g-PAAM/epoxy composites may be caused by the excellent interfacial coupling between SiO_2 nanoparticles and epoxy resulting from reactions of amide groups of PAAM grafted on the particulates with epoxy groups of the matrix. In addition, the remarkably reduced material removal due to wearing (Fig.40) and the lubricating effect provided by the nanoparticles tightly embedded in the

matrix [69] should account for the low frictional coefficient characteristics of SiO_2-g-PAAM/epoxy composites over the filler range examined (Fig.39). Comparatively, lack of the above-mentioned interfacial chemical bonding between untreated SiO_2 nanoparticle agglomerates and matrix resin results in higher wear rates and higher μ values of SiO_2/epoxy composites. The epoxy splinters due to severer materials loss entrapped at the interface between the steel counterpart and the composite pin might form a three-body abrasive wear situation, and thus counteract the lubricating effect of the nanoparticles, leading to μ values of SiO_2/epoxy composites similar to that of unfilled resin when SiO_2 content ≤ 4vol%.

In addition to the examination of the filler content dependence of the tribological performance at constant pressure and sliding velocity, effect of pressure should also be investigated. Fig.41 gives the coefficient of friction of epoxy and its composites determined at the pressures 3MPa and 5MPa under a constant sliding velocity v=0.4m/s. It is seen that the frictional coefficient of epoxy keeps almost unchanged when the pressure increases from 3 to 5MPa. This coincides with the results reported in ref.[70]. The frictional coefficients of nanosilica filled composites are lower than that of unfilled epoxy and decrease with increasing pressure. The lowest value of μ is recorded at a load of 5MPa for SiO_2-g-PAAM/epoxy composites. These phenomena imply that nanosilica can improve the friction-reducing ability of the composites especially under higher load [24]. The introduction of grafting PAAM further enhances the role of the particles.

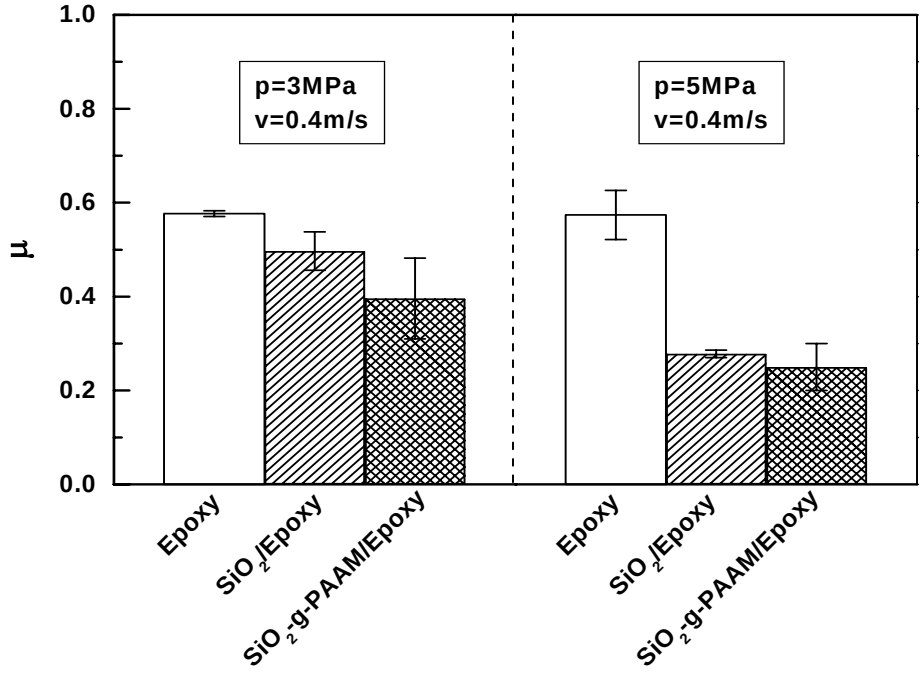

Figure 41. Frictional coefficient, μ, of epoxy and its composites at 2.17vol% nanosilica content.

The specific wear rates of the materials are exhibited in Fig.42. By comparing Fig.42 with Fig.41, it is seen that the decrement of wear rate is greater than that of frictional

coefficient when other conditions being equal. Silica nanoparticles seem to be more effective for improving the anti-wear property of the composites. Moreover, in the same way as it was observed for the materials' frictional coefficient μ, the additional surface modification of the nanoparticles helps to further decrease the wear rare of the composites. On the other hand, Fig.42 shows different pressure dependencies of the wear rate. With a rise in testing pressure, the wear loss of epoxy is increased but that of the composites is decreased. This phenomenon reflects that different wear mechanisms must be involved.

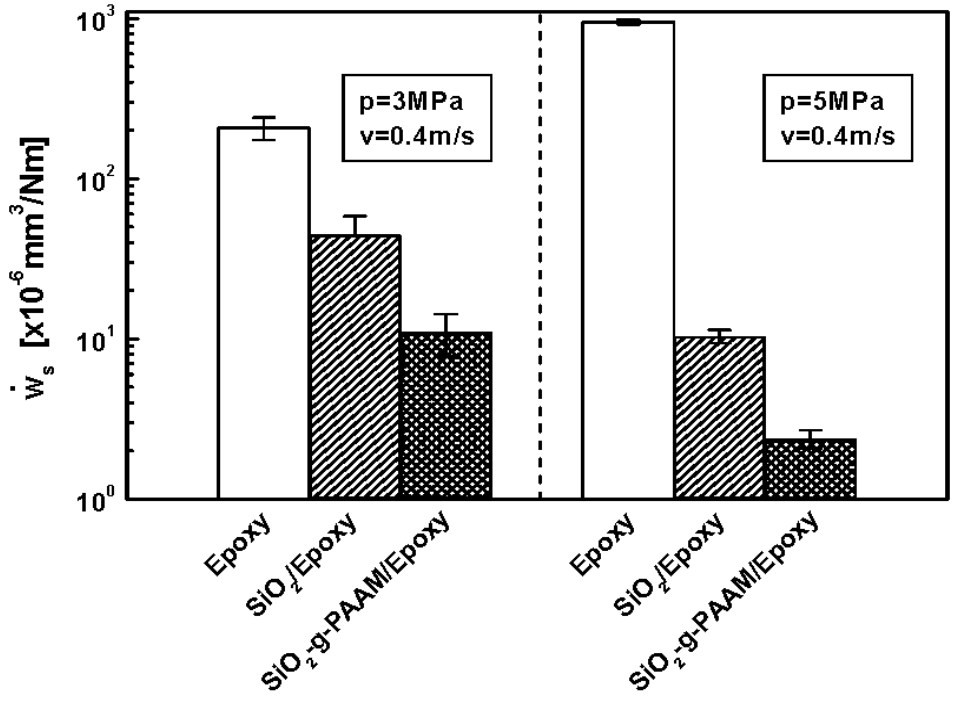

Figure 42. Specific wear rate, $\dot{w}_s$, of epoxy and its composites at 2.17vol% filler content.

Fatigue wear has been regarded as a main mechanism responsible for the sliding of epoxy against a hard counterpart [24, 71]. The model is based on the sub-surface crack nucleation and coalescence due to shear deformation of the softer surface induced by the traction of the harder asperities [64]. As shown in Fig.43(a), scale-like removal of materials has left traces on the worn surface of unfilled epoxy. Clearly it is indicative for fatigue-delamination generated under repeated loading during sliding. When a higher load was applied, large cracks appear on the surfaces (Fig.43(b)). The reason is that the fatigue mechanism of wear, which strongly depends on the load, plays a more and more important role. It gives rise to a substantial increase in the specific wear rate of epoxy (Fig.42). For SiO_2 reinforced composites, the basic wear patterns (Fig.43(c~f)) are characterized by mild fatigue wear, resembling that of the matrix tested at 3MPa (Fig.43(a)). A careful examination of the wear grooves manifested that the flaws' distribution produced on the worn surface change from a discontinuous mode (Fig.43(a)) to a continuous mode (Fig.43(c~f)). In particular, the uneven stress concentration built up inside epoxy might have been homogenized to some extent in the

composites due to the effect of dispersion strengthening of the nanoparticles [68, 69]. This is certainly beneficial for reducing the amount of material loss.

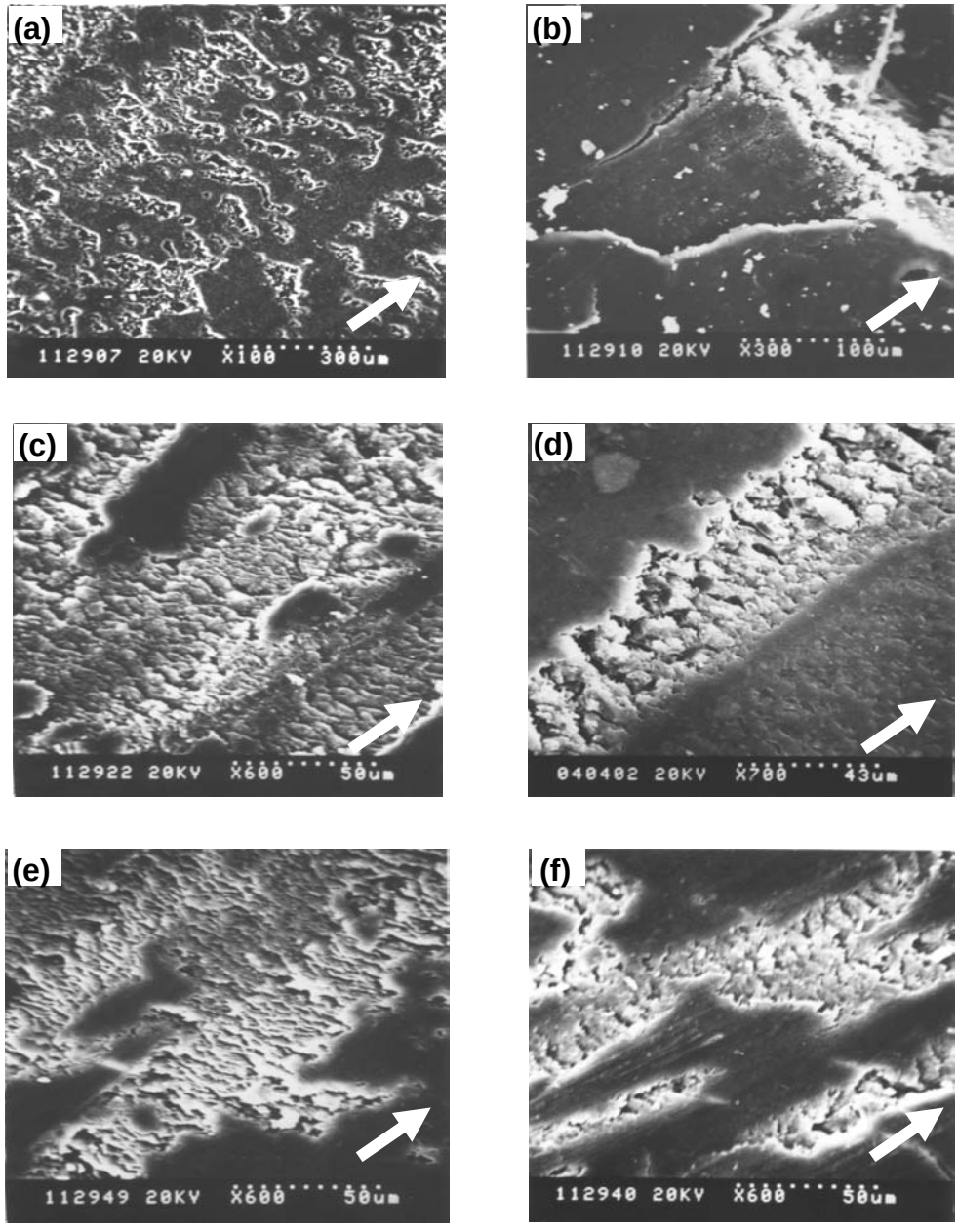

Figure 43. SEM micrographs of the worn surface of (a, b) epoxy, (c, d) SiO_2/epoxy composites and (e, f) SiO_2-g-PAAM/epoxy composites. Nanosilica content: 2.17vol%. Conditions of the sliding wear tests: (a, c, e) p=3MPa, v=0.4m/s; (b, d, f) p=5MPa, v=0.4m/s. The arrows indicate the sliding direction.

Studying the tribological behavior of epoxy sliding against inox steel, Bassani and co-workers [70] suggested that the nominal pressure controls the interfacial stress between the counterparts involved in the contacts and hence the stability of transfer films. Considering

that the addition of inorganic nanoparticles into polymers may increase the adhesion strength of a transfer film on the counterface [23, 72], it can be deduced that nanometer SiO_2 not only acts as a load carrier in the composites but also helps to improve the bonding between the transfer film and the steel counterface. Moreover, the stability of the transfer film might be increased with the applied pressure. As a result, the wear rates of the composites are remarkably lower than that of the unfilled resin, and decrease with increasing load, as observed in this work. Further studies on the nature of the transfer film are required to have a better understanding of the above analysis.

It should be noted that it occurred very difficult to detect large differences in the characteristics of the wear traces between the composites filled with treated and untreated particles (e.g. Fig.43(c) and (d), Fig.43(e) and (f)). According to the experimental results plotted in Fig.42, however, it is believed that an increased interfacial interaction between SiO_2 nanoparticles and epoxy favors the aforesaid positive effects. These interactions result from reactions of the amide groups in PAAM grafted on the particles with the epoxy groups of the matrix. The SiO_2-g-PAAM/epoxy composites have therefore the highest wear resistance. Besides, the remarkably reduced material removal (Fig.42) and the lubricating effect provided by the nanoparticles tightly embedded in the matrix [69] should account for the low frictional coefficient characteristics of SiO_2-g-PAAM/epoxy composites.

3.4. Friction and Wear Properties of Nano-Si_3N_4/Epoxy Composites

In general, epoxy is not an ideal material used in sliding wear applications due to its three-dimensional network structure as compared with thermoplastics. As shown in Fig.44, both frictional coefficient and specific wear rate of unfilled epoxy is quite high. The situation is changed greatly when nano-Si_3N_4 is incorporated. It is seen that there is a significant reduction in the values of μ and $\dot{w}_s$ at filler content as low as 0.27vol%. With a rise in the concentration of the nanoparticles, the declining trend becomes gentle and is replaced by a slight increase from 1.38vol% on. It means the nanometer Si_3N_4 particles are very effective in improving the tribological performance of epoxy.

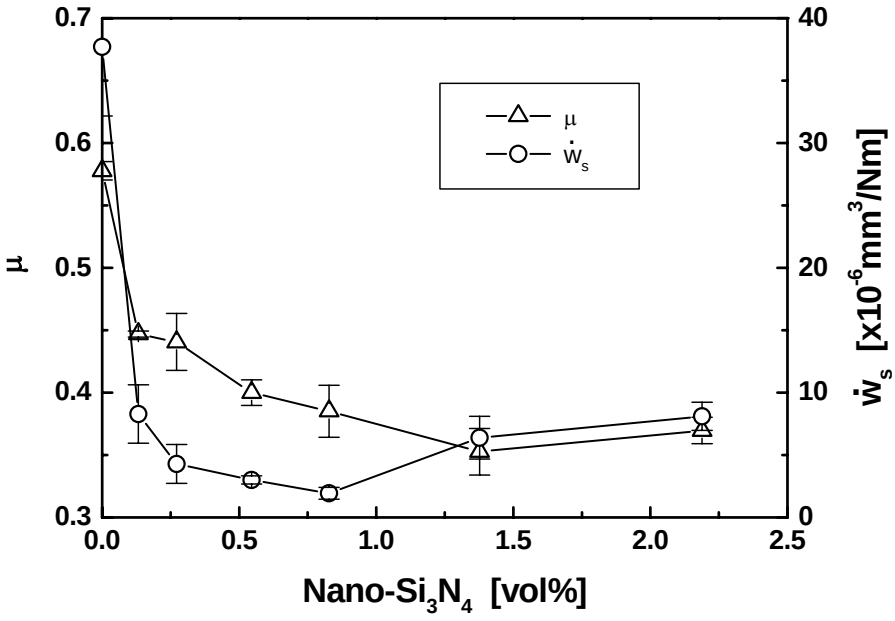

Figure 44. Frictional coefficient, μ, and specific wear rate, $\dot{w}_s$, of nano-Si_3N_4/epoxy composites as a function of filler content.

Fig.45 exhibits the SEM micrographs of the worn surfaces of epoxy and the composites. The wear scars on the epoxy pin are characterized by obvious scale-like traces (Fig.45(a)). A close view (Fig.45(b)) shows that micrometer size blocks of epoxy resin have left the materials surface. This is indicative for fatigue-delamination generated under repeated loading during sliding. Fatigue wear has been regarded as a main mechanism responsible for the sliding of epoxy against a hard counterpart [70, 71]. The model is based on the sub-surface crack nucleation and coalescence due to shear deformation of the softer surface induced by the traction of the harder asperities [64]. For filled composites, the worn surfaces are full of smoothly polished grooves (Fig.45(c), (e), (g) and (i)). This is particularly evident in the case of V_f=0.83vol% (Fig.45(e)), which corresponds to the lowest $\dot{w}_s$ as shown in Fig.44. When the surfaces are observed at high magnification (Fig.45(d), (f), (h) and (j)), they still look quite smooth besides the thin resin sheets to be removed (Fig.45(d), (j)), tiny cracks several nanometers wide and hundreds nanometers long (Fig.45(f), (h)), and the exposed nanoparticle agglomerates dozens of nanometer in diameter (Fig.45(f)). Naturally, the transition from severe wear mode of unfilled epoxy to mild one of the composites results from the addition of nano-Si_3N_4 particles.

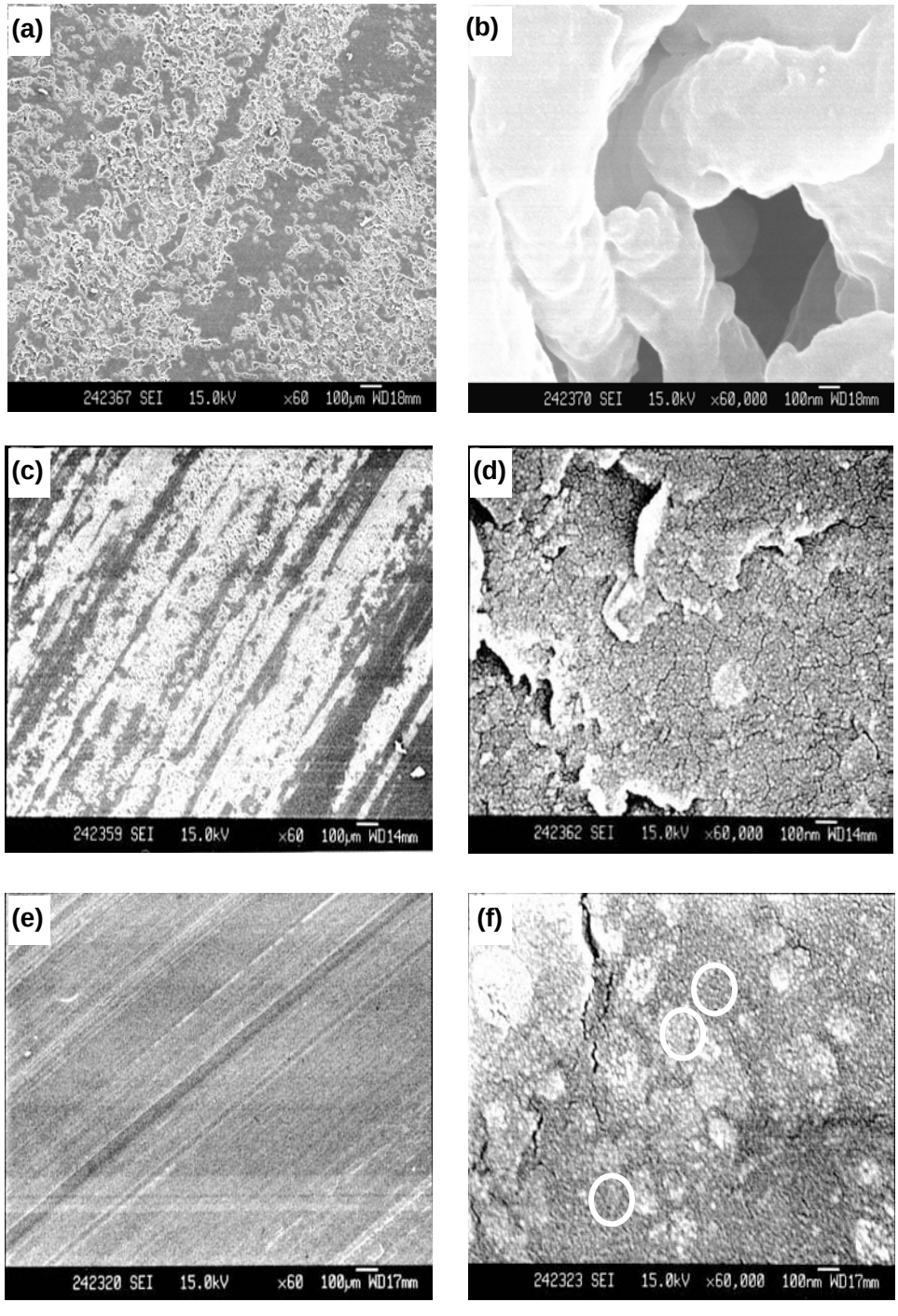

Figure 45. SEM images of the worn surfaces of (a, b), epoxy, (c, d) nano-Si_3N_4/epoxy composites (V_f=0.27vol%), (e, f) nano-Si_3N_4/epoxy composites (V_f=0.83vol%), (g, h) nano-Si_3N_4/epoxy composites (V_f=1.38vol%), and (i, j) nano-Si_3N_4/epoxy composites (V_f=2.19vol%). To ensure equal observation conditions, all the surfaces are examined at two magnifications. The white circles on Fig.45(f) indicate the agglomerated nanoparticles.

As surface hardness is generally taken as one of the most important factors that govern the wear resistance of materials, Vickers microhardness, H_v, of the composites is measured (Fig.46). Evidently, the surface hardness of the composites keeps almost unchanged until the filler content reaches 2.19vol%. In fact, the size of the micro-indenter is much larger than that of the nanoparticles. For the composites with lower nanoparticles concentration and better dispersion, the measured H_v values cannot reflect the true hardening effect around the particles but the performance of the matrix resin itself. In the case of higher particulate content (2.19vol%, for instance), agglomeration of the particles is rather severe, resulting in higher microhardness with considerable testing error, which also characterizes the uneven distribution of the nanoparticles [69].

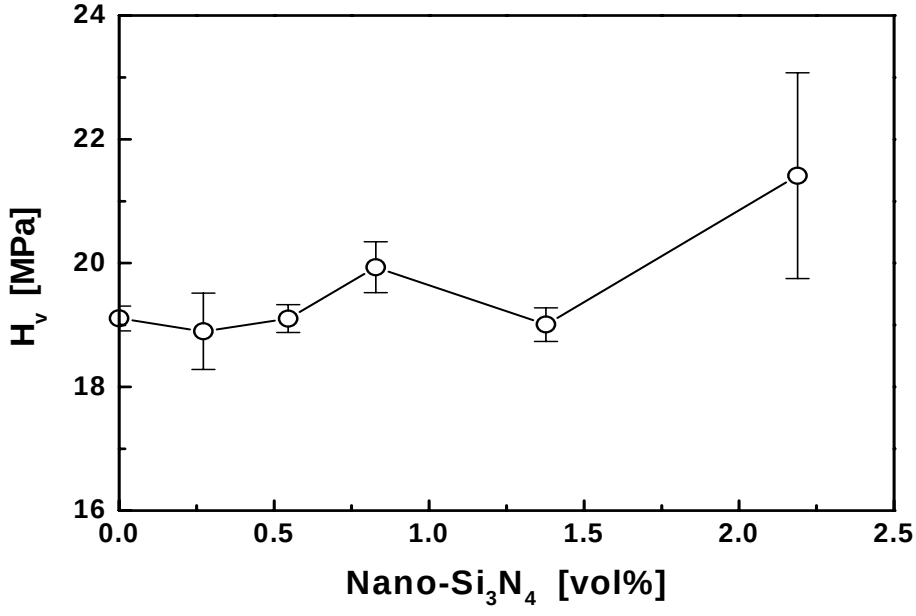

Figure 46. Vickers microhardness, H_v, of nano-Si_3N_4/epoxy composites as a function of filler content.

Since the measured microhardness is not qualified for analyzing the causes for the reduction of frictional coefficient and wear rate of the composites, the dynamic mechanical responses of the materials (Fig.47) are studied in correlation with the frictional property as follows. This is done also because of the viscoelastic nature of polymer composites that might influence the tribological behavior of the composites through hysteretic motion of the macromolecular chains. Considering that the transient surface temperature at rubbing surface is rather high, frictional coefficient of the composites is plotted as a function of the area under the α-transition peak in Tanδ~temperature (Fig.48). It is obvious that the relationship follows exponential growth, which is analogous to Arrhenius equation implying the frictional process is closely related to thermally activated motion of the molecular segments of epoxy. Since frictional coefficient increases with a rise in damping of the composites, the ability of the

materials to transform mechanical energy into heat contributes to the frictional behavior. In other words, the stiffer the composites, the lower the frictional coefficient, so that the stick-and-slip phenomenon can be prevented [73]. Fig.49 shows the results of thermomechanical analysis (TMA) of the materials. The comparative measurements manifest that the thermally induced deformation of epoxy is decreased after the addition of the nanoparticles, especially when the filler content is high. It means dimensional stability of the composites is superior to that of unfilled epoxy when the specimens are heated up due to the repeated friction, which favors the reduction of frictional coefficient as concluded from Fig.48.

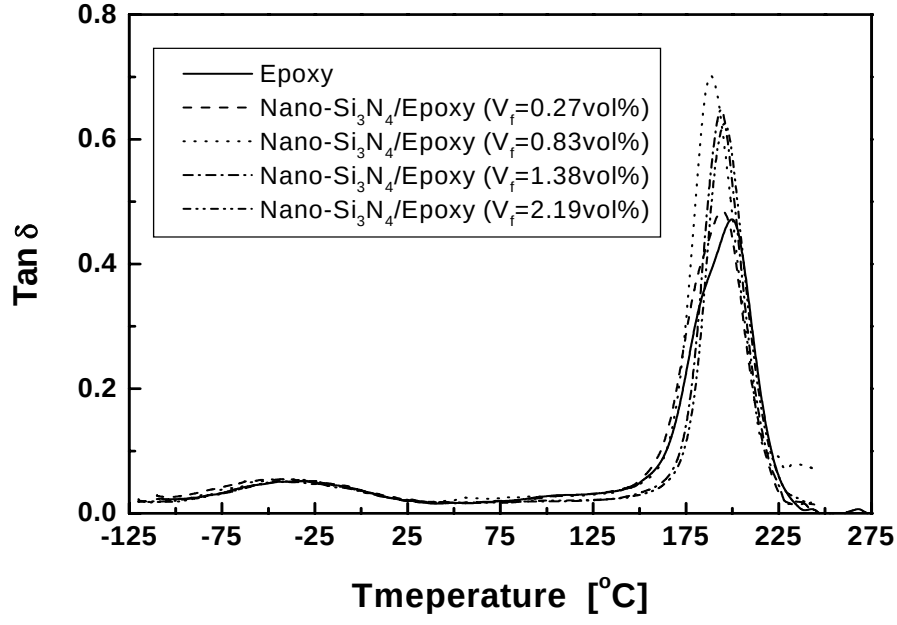

Figure 47. Temperature dependence of internal friction, Tanδ, of nano-Si_3N_4/epoxy composites measured at 1Hz.

It is worth noting that when the curve in Fig.48 is extrapolated to the position at which the α-peak area=0, the corresponding μ doesn't equal 0. Therefore, mechanical damping is not the only influencing factor. Fig.50 shows the microhardness values of the surfaces of epoxy and its composites before and after wear testing. Although no obvious variation can be seen in the case of nano-Si_3N_4/epoxy composites, microhardness of the worn surface of epoxy pin decreases significantly, suggesting structural decay of the top resin layer in the scale range of micrometer. On the basis of this finding, thermogravimetric analyses (TGA) of the surface layers of the same samples are carried out to check whether surface chemistry is involved. From Fig.51 it is seen that both unworn epoxy and nano-Si_3N_4/epoxy composites have similar pyrolytic behavior so that their TGA curves almost overlap. When the specimens had undergone sliding wear tests, however, the residual weights of the materials surface layers are much greater than those from the unworn specimens. The disproportional increase

in the residual weight strongly suggests transfer from the steel counterpart to the specimen pins besides variation of chemical structures of the components. It is thus necessary to further study the tribochemistry of the worn specimens in the following section.

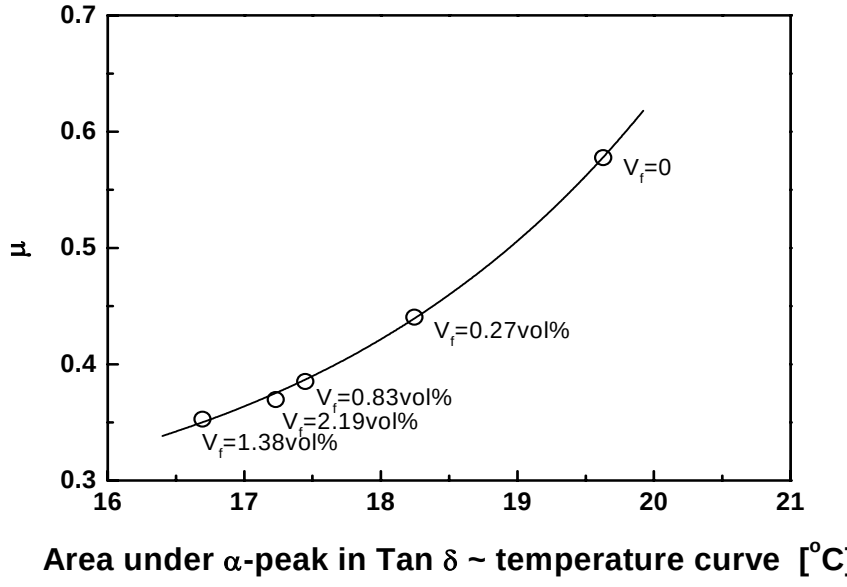

Figure 48. Frictional coefficient, μ, versus area under the α-transition peak in Tanδ~temperature curve shown in Fig.47.

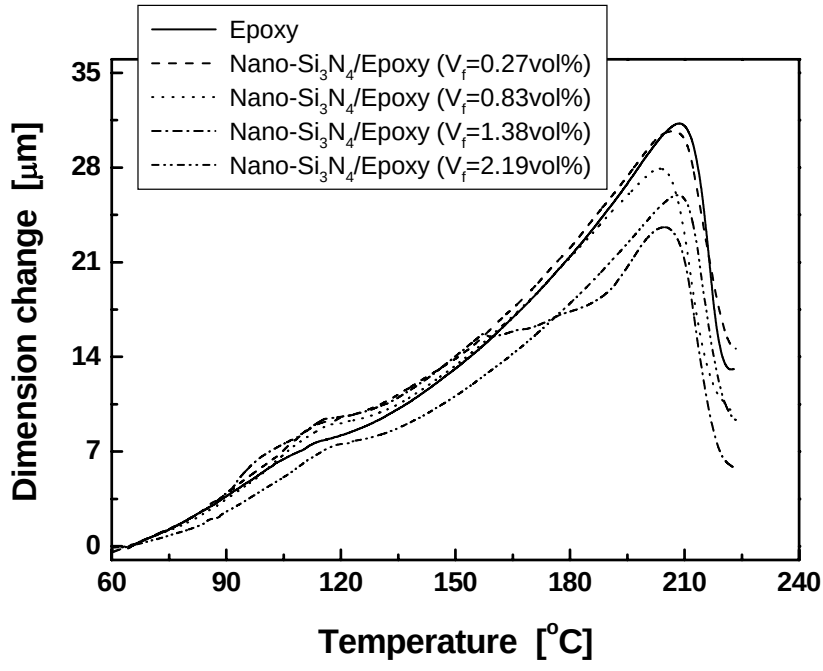

Figure 49. Thermomechanical curves of epoxy and nano-Si_3N_4/epoxy composites.

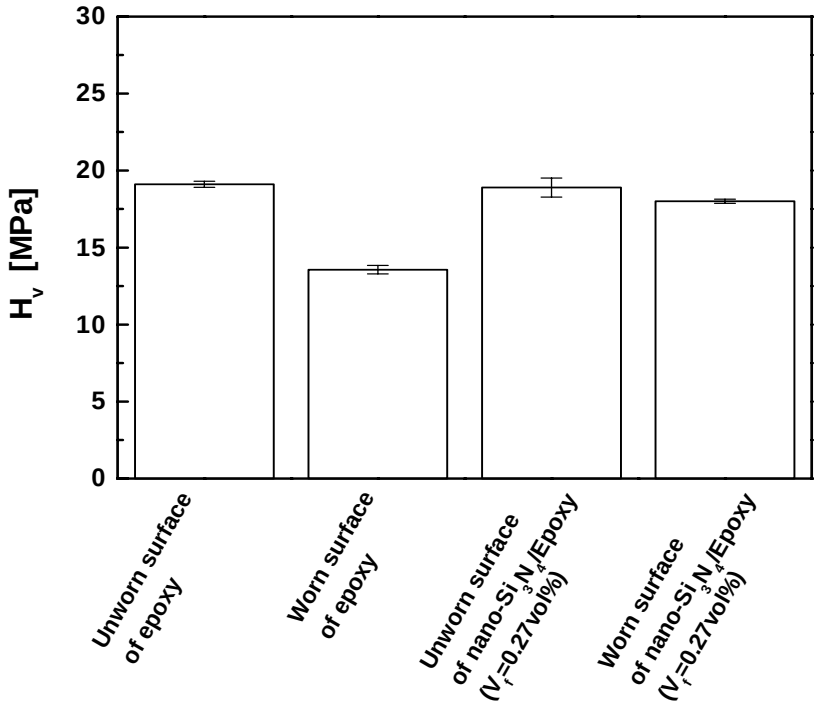

Figure 50. Vickers microhardness, H_v, of pin surfaces of epoxy and nano-Si_3N_4/epoxy composites before and after the wear tests.

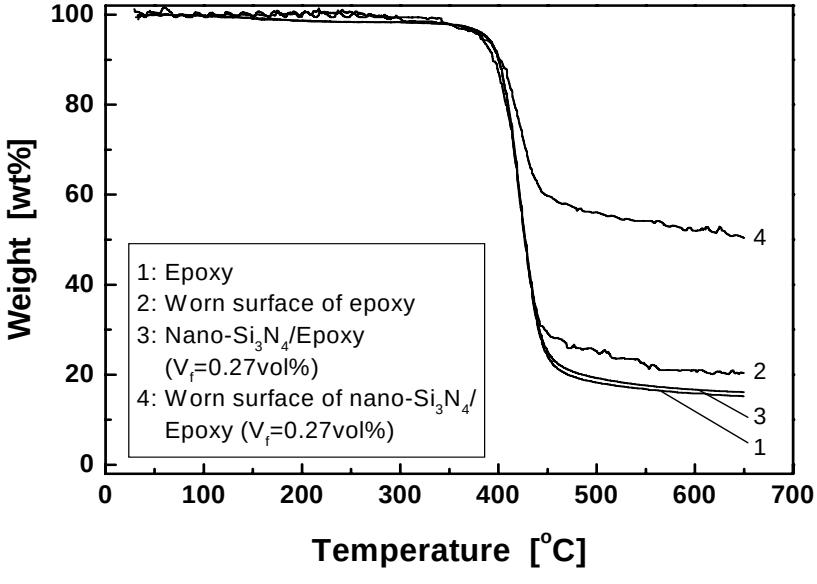

Figure 51. Thermogravimetric curves of pin surfaces of epoxy and nano-Si_3N_4/epoxy composites before and after the wear tests.

As friction and wear takes place between a pair of counterparts, examination of the surface of the steel ring would be a reasonable starting point. Table 11 records the EDS results of the steel rings before and after rubbing with epoxy and its composites. Having undergone the wear tests, the surface atomic ratios are changed. In the case of epoxy pin, for example, element S appears on the surface of the steel ring. Moreover, the addition of nano-$S_{i3}N_4$ into epoxy brings about the rise in the content of Si on the surface of the steel ring. Hence the above results (Fig.51, Table 11) evidence the mutual transfer between the specimen pins and the steel rings. To have a clearer image of the tribochemical reaction involved, XPS spectra from the surfaces of epoxy and the nanocomposites should be carefully analyzed.

Table 11. EDS analytical results of the surface of the steel counterpart

	Elements and content (%)		
	S	Si	Fe
Steel ring before wear test	0	0.22	98.65
Steel ring rubbed against epoxy pin	0.42	0.21	98.55
Steel ring rubbed against nano-Si_3N_4/epoxy composite pin (V_f=0.83%)	0.46	1.08	97.82

The low resolution XPS spectra of the pin surfaces of epoxy and nano-Si_3N_4/epoxy composites before and after the wear tests demonstrate that the atomic ratios of C/O have changed (Fig.52). The increased C/O ratios is indicative of carbonization, as evidenced by the decreased surface microhardness (Fig.50), manifesting partial chain scission and reorganization of epoxy macromolecules at the surface of the specimen pins during wearing. In consideration of the fact that the frictional surface temperature could be as high as several hundred degrees centigrade in the case of polymer/steel sliding pair [74, 75], tribochemically induced structure variation on top layers of the specimens has to take place inevitably [76].

Fig.53 illustrates the C1s spectra collected from the unworn and worn surfaces of virgin epoxy and its composites with 0.83vol% nano-Si_3N_4. It can be seen that the C1s peaks from the two worn surfaces (Figs.53(b), (d)) are somewhat broadened and shift slightly towards high binding energy regime as compared to those of the unworn surfaces of the materials (Figs.53(a), (c)). These phenomena suggest that the carbon atoms become electron-poor. Similar to the C1s spectra, the O1s spectra of the samples (Fig.54) also become broader and shift to high binding energy after sliding wear tests. As a result, it can be estimated that oxidation and carbonization are the main mechanochemical processes that had occurred on the specimen surfaces during wearing driven by the high frictional temperature and contact pressure.

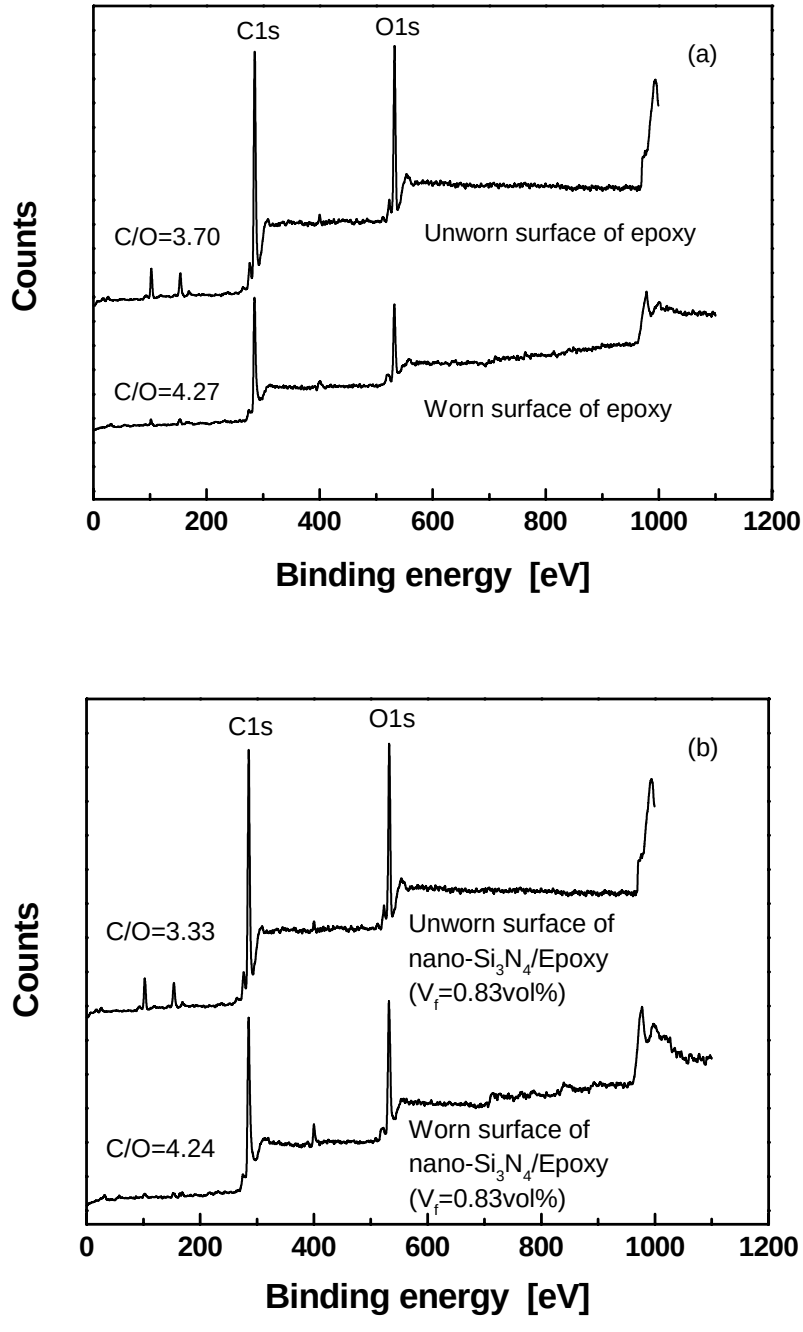

Figure 52. Low resolution XPS spectra of pin surfaces of (a) epoxy and (b) nano-Si_3N_4/epoxy composites before and after the wear tests.

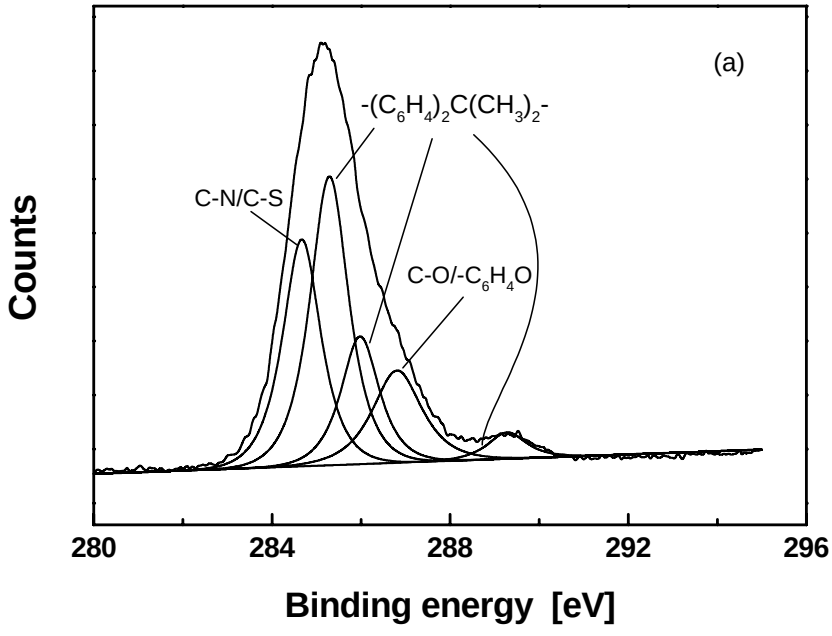
(a)
-(C6H4)2C(CH3)2-
C-N/C-S
C-O/-C6H4O
Counts
280
284
288
292
296
Binding energy [eV]

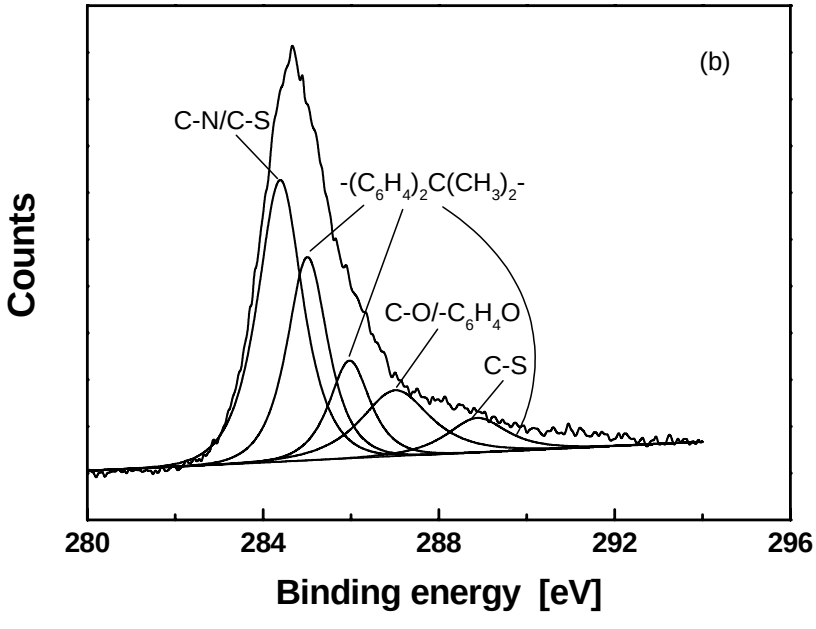
(b)
C-N/C-S
-(C6H4)2C(CH3)2-
C-O/-C6H4O
C-S
Counts
280
284
288
292
296
Binding energy [eV]

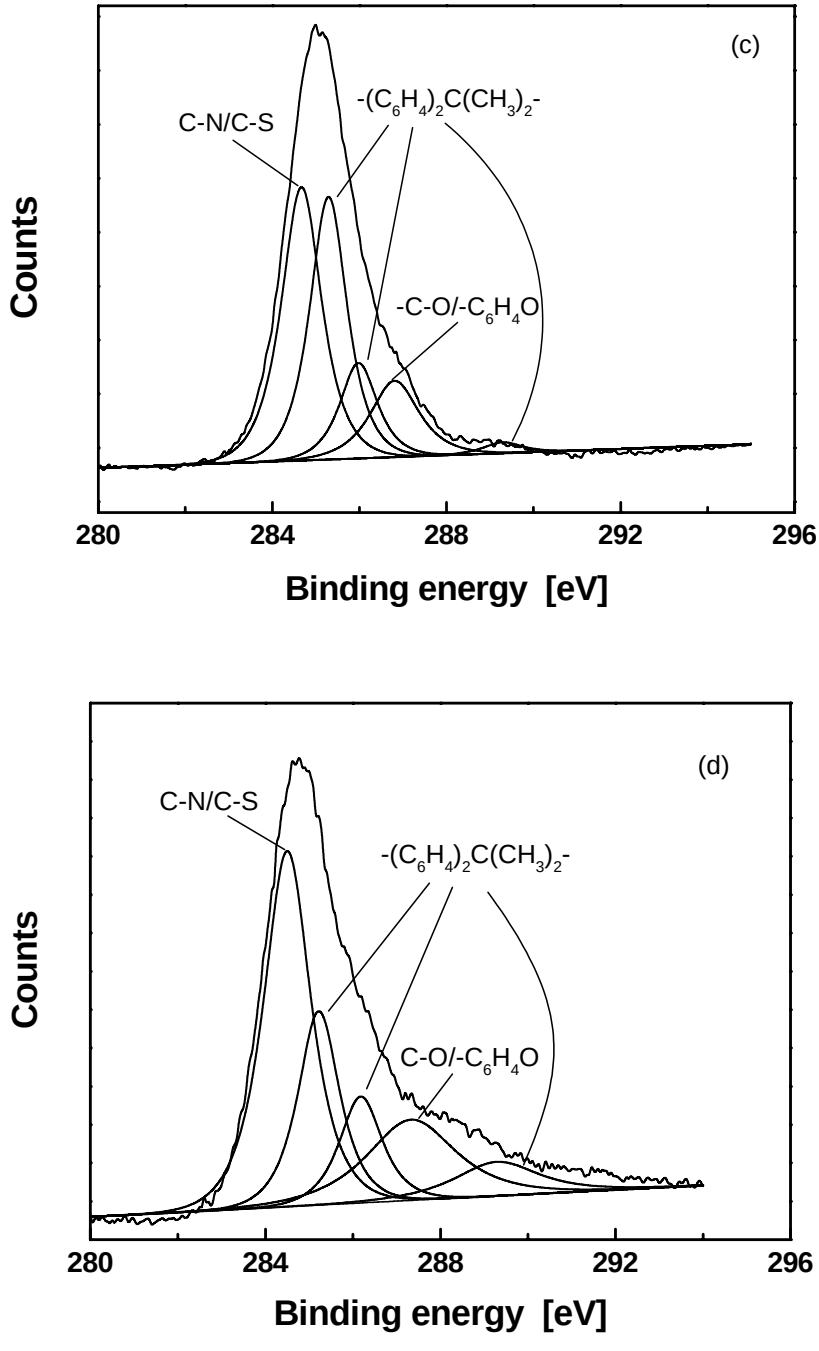

Figure 53. C1s spectra of pin surfaces of (a) unworn epoxy, (b) worn epoxy, (c) unworn nano-Si_3N_4/epoxy composites (V_f=0.83vol%), (d) worn nano-Si_3N_4/epoxy composites (V_f=0.83vol%).

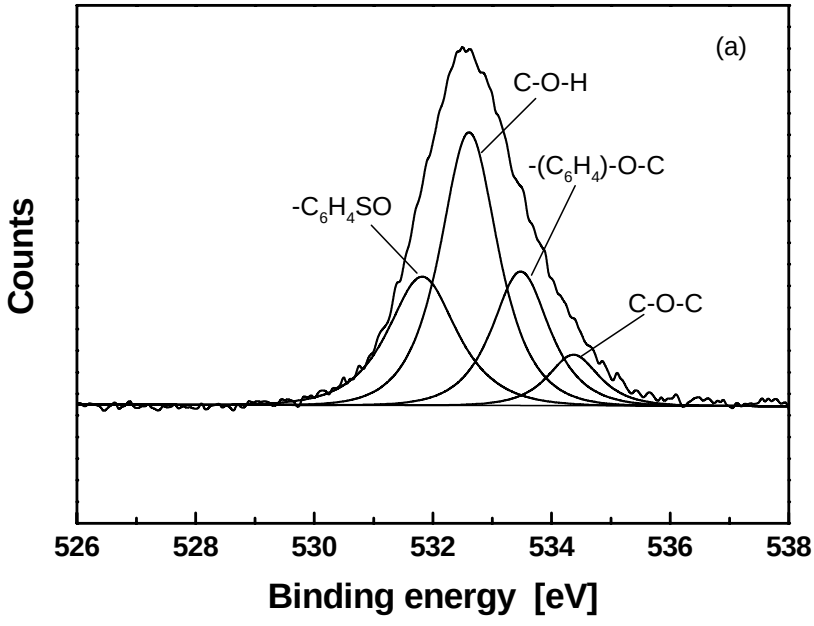
(a)
C-O-H
-(C6H4)-O-C
-C6H4SO
C-O-C
Counts
526
528
530
532
534
536
538
Binding energy [eV]

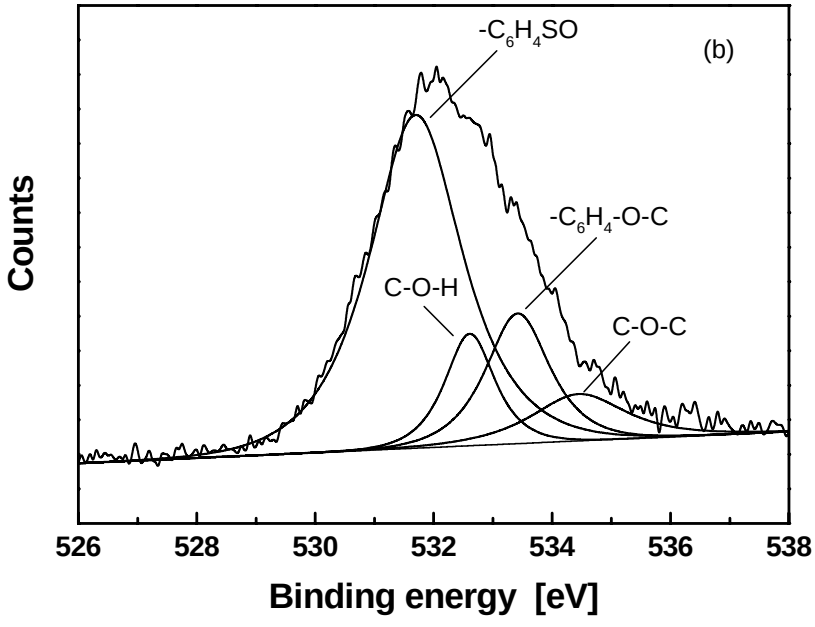
(b)
-C6H4SO
-C6H4-O-C
C-O-H
C-O-C
Counts
526
528
530
532
534
536
538
Binding energy [eV]

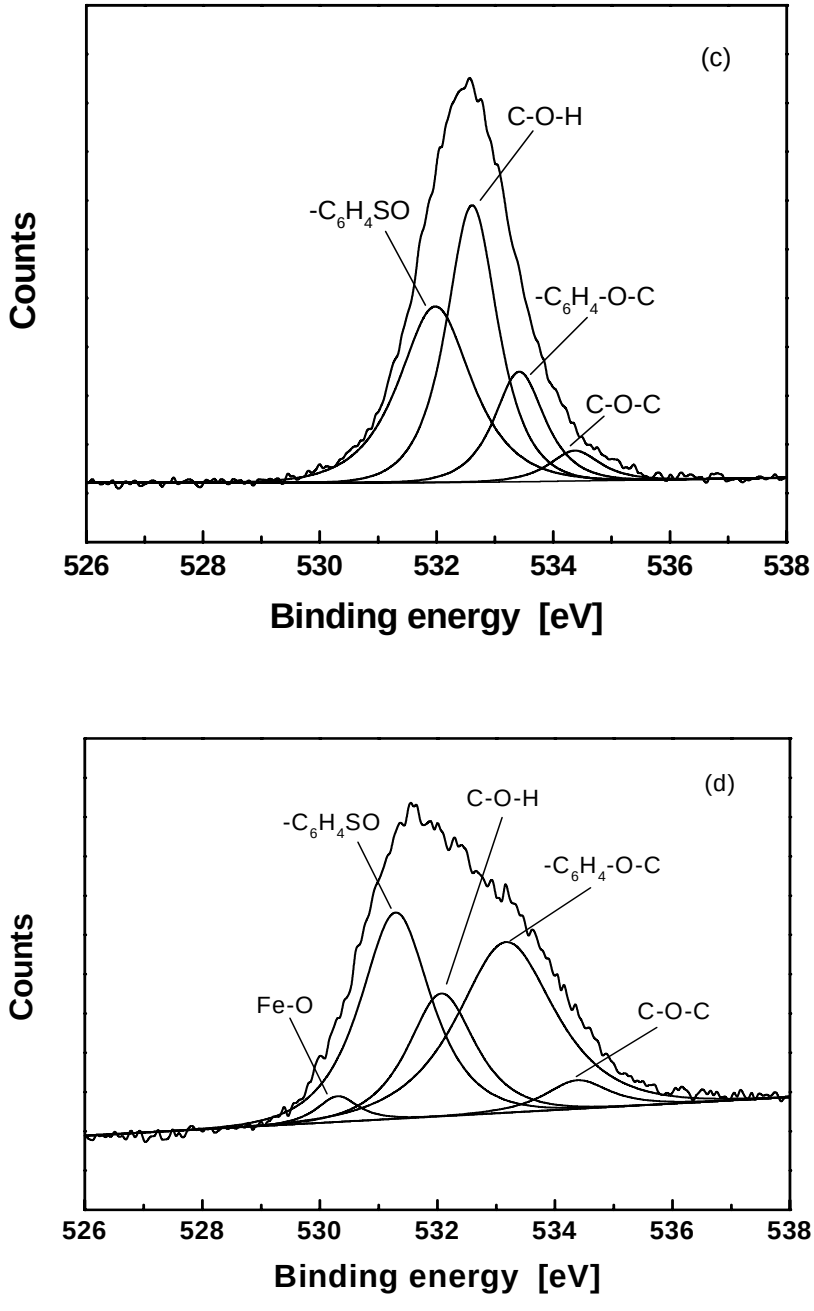

Figure 54. O1s spectra of pin surfaces of (a) unworn epoxy, (b) worn epoxy, (c) unworn nano-Si_3N_4/epoxy composites (V_f=0.83vol%), (d) worn nano-Si_3N_4/epoxy composites (V_f=0.83vol%).

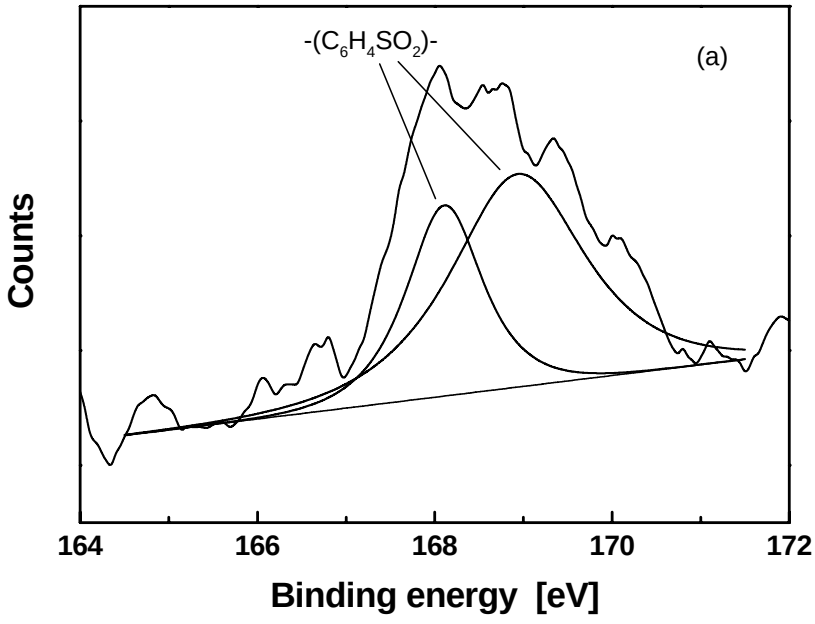
-(C6H4SO2)-
(a)
Counts
164
166
168
170
172
Binding energy [eV]

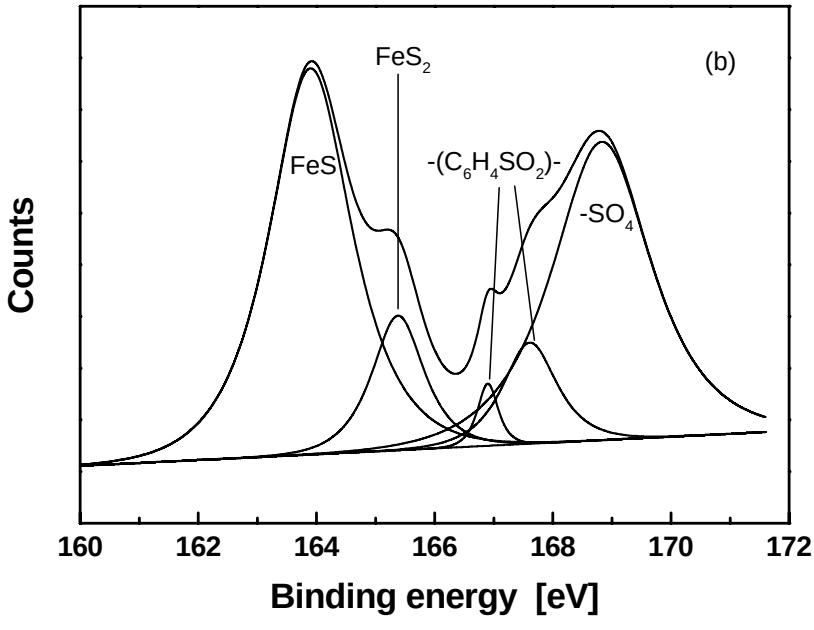
FeS2
(b)
FeS
-(C6H4SO2)-
-SO4
Counts
160
162
164
166
168
170
172
Binding energy [eV]

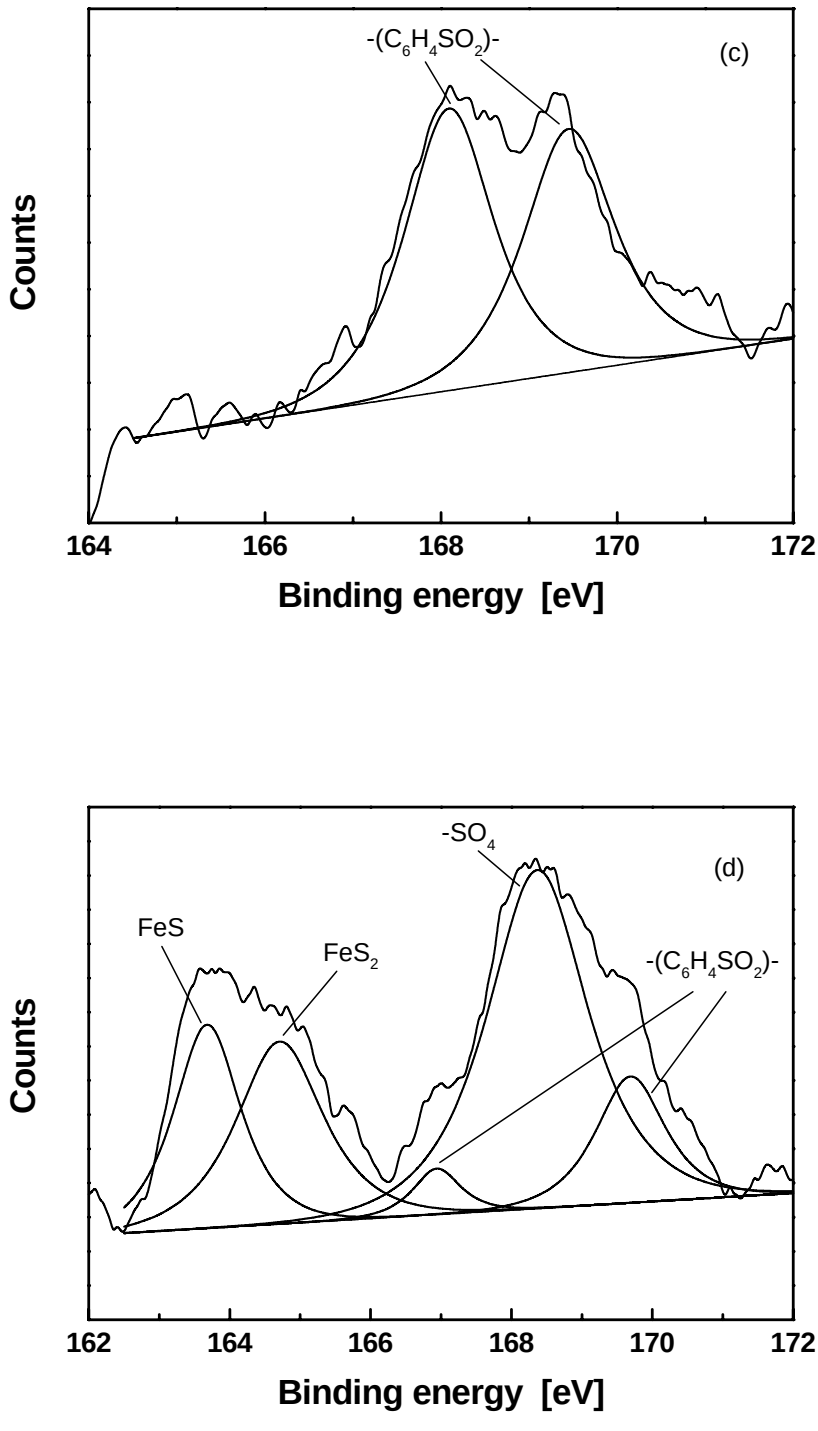

Figure 55. S2p spectra of pin surfaces of (a) unworn epoxy, (b) worn epoxy, (c) unworn nano-Si_3N_4/epoxy composites (V_f=0.83vol%), (d) worn nano-Si_3N_4/epoxy composites (V_f=0.83vol%).

S2p spectra are given in Fig.55. The S atom comes from the curing agent in epoxy. Deconvolution of the spectra indicates that a few new peaks appear on the spectra of the worn surfaces, meaning the generation of some S-containing compounds. According to the investigation in ref.[77], the new compounds are assigned to be FeS, FeS_2 and $FeSO_4$. That is, in the course of sliding wear the S atoms in epoxy react with Fe atoms at the metallic counterface and environmental water vapor under high contact temperature and pressure conditions. Then, the new products are attached to both counterfaces, as the trace of S atoms has been found on the steel ring surface (Table 11).

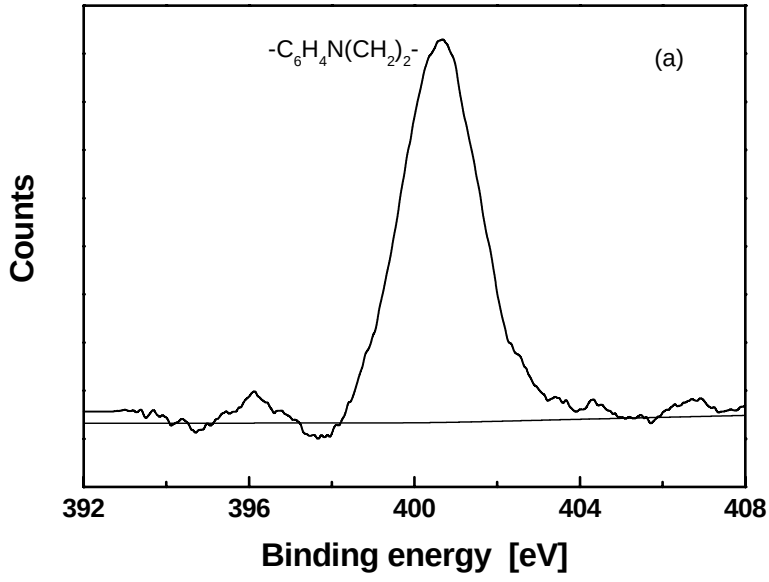

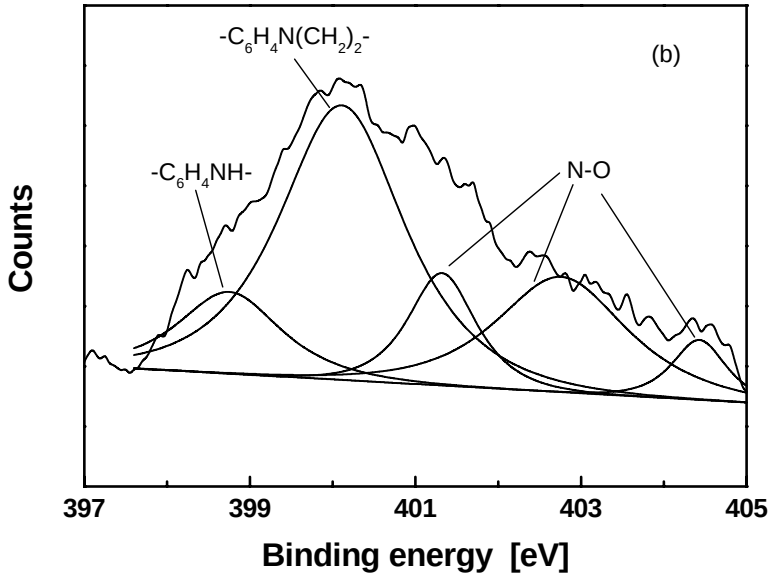

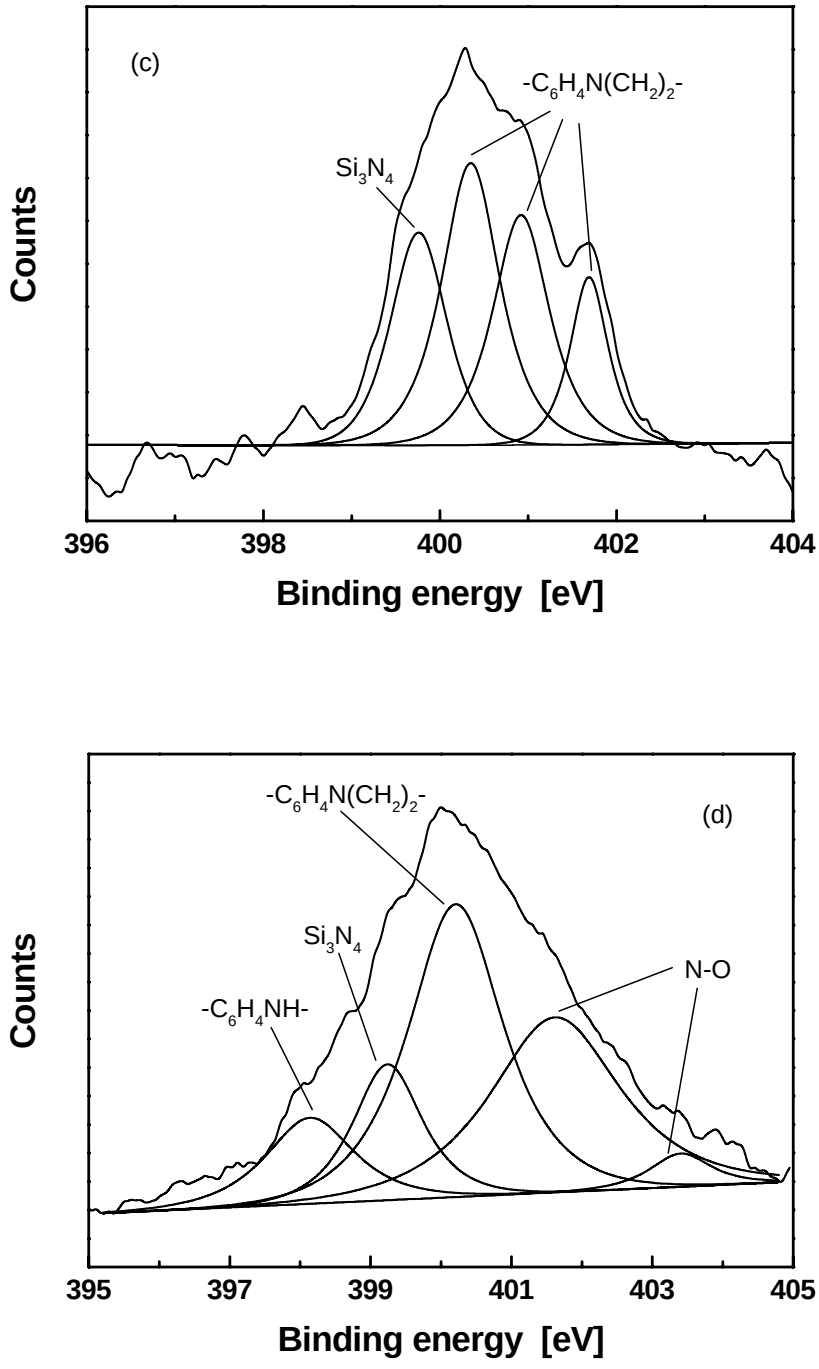

Figure 56. N1s spectra of pin surfaces of (a) unworn epoxy, (b) worn epoxy, (c) unworn nano-Si_3N_4/epoxy composites (V_f=0.83vol%), (d) worn nano-Si_3N_4/epoxy composites (V_f=0.83vol%).

Fig.56 exhibits the N1s spectra collected from the sample surfaces. The N atom comes from the curing agent in epoxy and nanometer Si_3N_4 particles in the composites. The spectra collected on the worn surfaces have different profiles from their virgin materials. Besides, the

peaks from the worn specimens slightly shift to high binding energy regime, and some new sub-peaks appear. All these imply that the chemical environment of N atoms also becomes more oxidative. The N atoms might react with atmospheric O_2 under sliding wear condition.

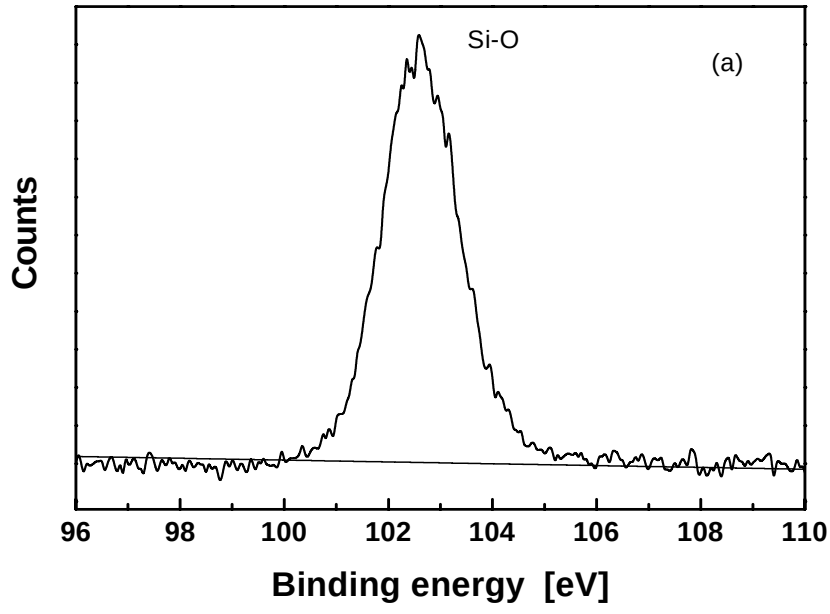

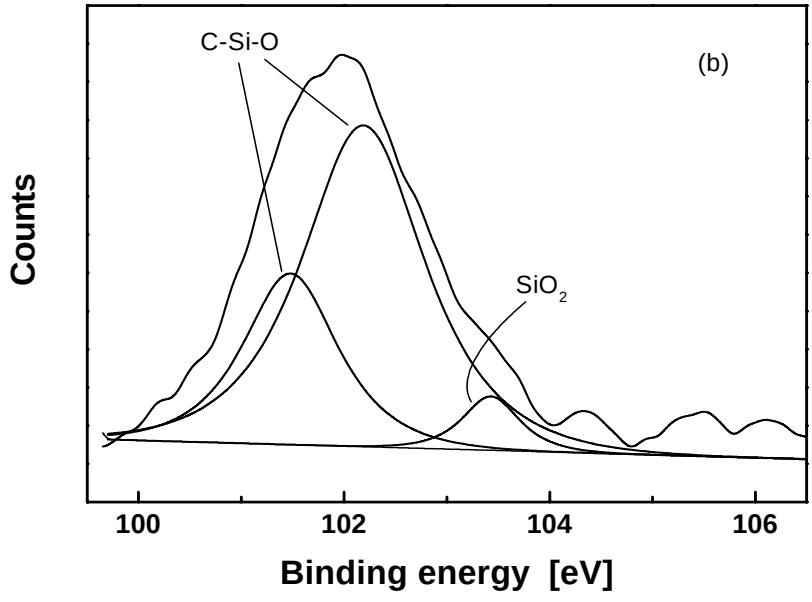

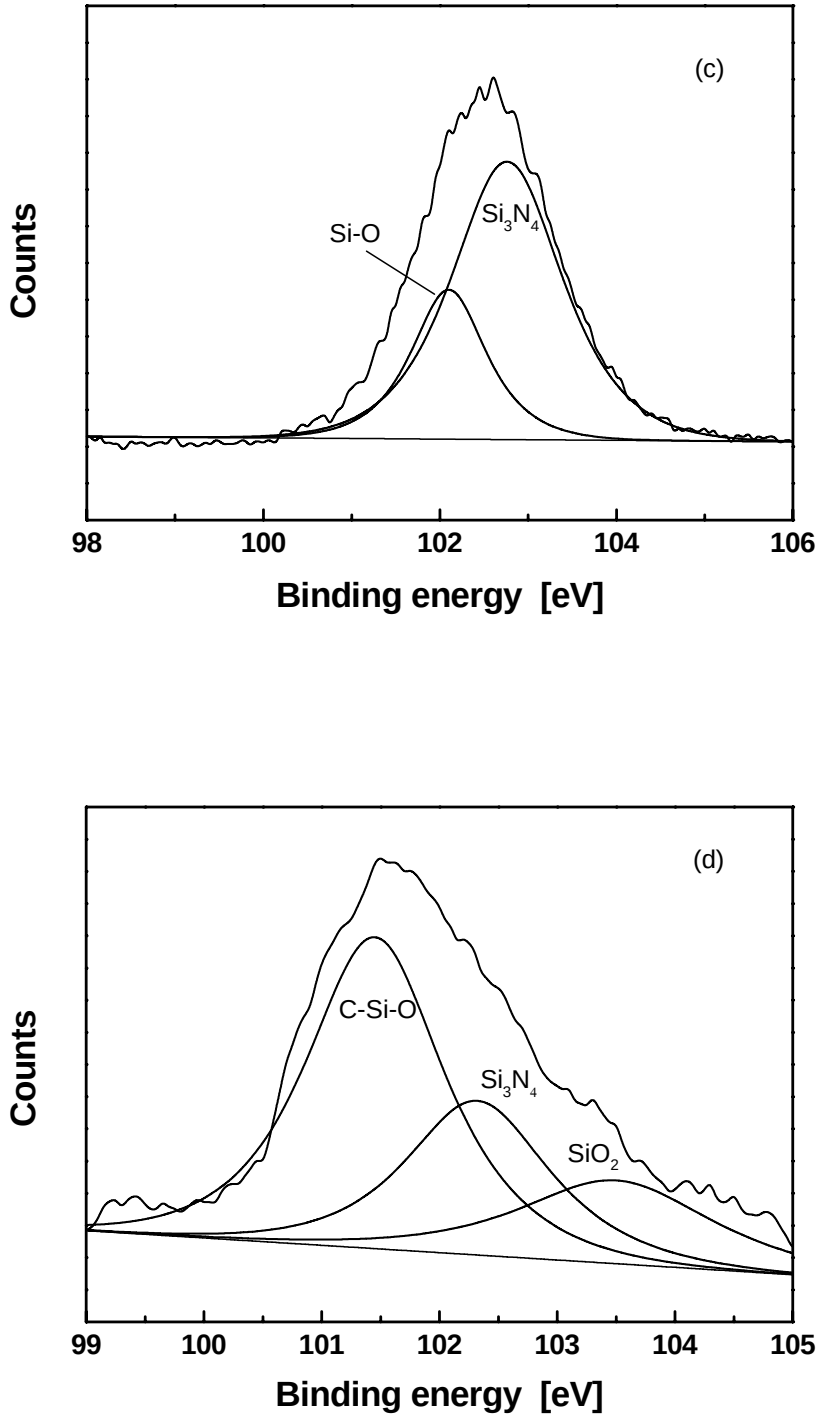

Figure 57. Si2p spectra of pin surfaces of (a) unworn epoxy, (b) worn epoxy, (c) unworn nano-Si_3N_4/epoxy composites (V_f=0.83vol%), (d) worn nano-Si_3N_4/epoxy composites (V_f=0.83vol%).

Fig.57 gives the Si2p spectra of the specimen surfaces. The Si atoms mainly come from the nanometer Si_3N_4 filler in the composites, but those transferring from the polishing paper to the materials' surfaces during samples preparation and from the steel counterpart during wear testing can also contribute to the spectra. The most distinct information yielded from the spectra before and after wear tests lies in the formation of SiO_2. It represents a tribochemical way of wear in which material is removed molecule to molecule, instead of the classic removal of fragments by fracture [78, 79]. In addition, the tribofilm of SiO_2 protects the specimens and the steel counterpart, providing friction reducing ability [80].

Since no Fe peak can be found on the spectra from the pin surfaces of unworn epoxy, worn epoxy and unworn Si_3N_4/epoxy composites, Fig.58 only shows the Fe2p spectrum collected from the worn surface of the composites. Besides the reactions between the Fe atoms from the metal counterface, the S atoms from epoxy and Si_3N_4, the Fe atoms can also be oxidized, forming FeO and Fe_3O_4. Kong et al. reported on the effect of surface oxide layers on wear behavior [81]. FeO or Fe_3O_4 layers show a significant reduction in friction and wear, while Fe_2O_3 layer promotes the wear. Therefore, the decreasing of μ and $\dot{w}_s$ of epoxy with the addition of Si_3N_4 nanoparticles can be partly attributed to the appearance of FeO and Fe_3O_4 on the counterfaces [82].

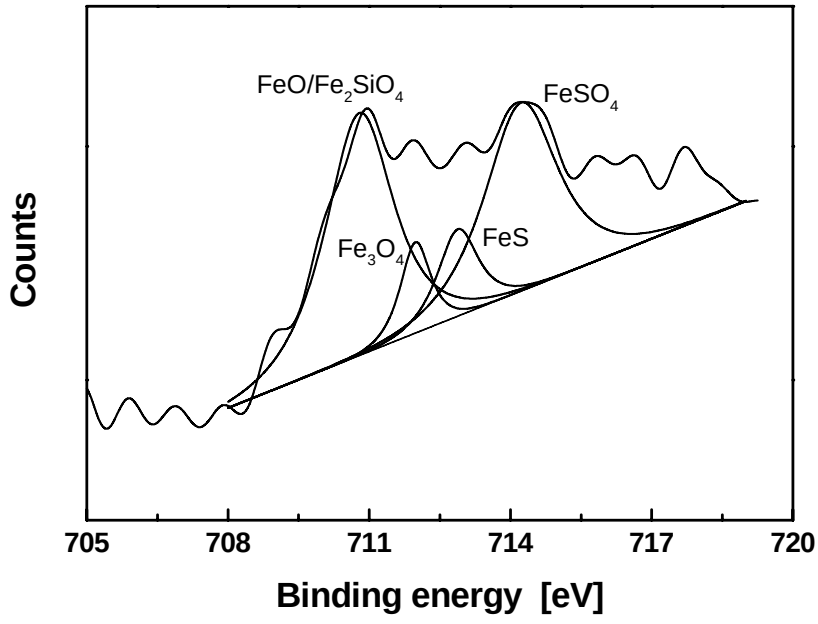

Figure 58. Fe2p spectrum of pin surface of worn nano-Si_3N_4/epoxy composites (V_f=0.83vol%).

To conclude the tribochemical reactions of epoxy and its composites, and those between the materials and the counterface metal Fe, the following Scheme I is given according to the

above discussion, which might help to have an overview of the role of the nanocomposites operating under sliding wear conditions.

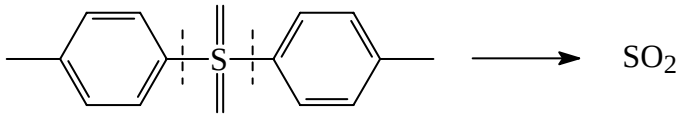

$O_2 + \cdot NH—CH_2— \rightarrow ON—CH_2—$

$SO_2 + Fe + O_2 \rightarrow FeSO_4$

$Fe + H_2O + O_2 \rightarrow Fe_3O_4$

$Fe + O_2 + H_2O \rightarrow FeO$

$Fe + S \rightarrow FeS$

$Si_3N_4 + O_2 + H_2O \rightarrow SiO_2$

$Si_3N_4 + Fe + H_2O + O_2 \rightarrow Fe_2SiO_4$

Scheme I

4. CONCLUSIONS

1. Modification of inorganic nanoparticle agglomerates through grafting polymerization represents an attractive route to give full play to the nanoparticles in improving performance of polymer composites by enhancing the interfacial interaction between the particles and the matrix through chemical bonding. The addition of inorganic nanoparticles into epoxy can reduce wear rate and frictional coefficient of the matrix at low filler loading, but a further improvement of the tribological properties is obtained by incorporating the grafted nanoparticles. The mechanism for this improvement is ascribed to the matrix enhancement rather than the nanoparticles themselves. The key effects of the grafting polymers lie in the strengthening of the loose nanoparticle agglomerates besides the increase of the filler/matrix interfacial adhesion.
2. Grafting of PAAM onto the nanoparticles can establish covalent bonding between the particles and epoxy during the subsequent curing process, while the presence of PS as grafting polymer improves the interfacial compatibility between the hydrophilic nanoparticles and the hydrophobic matrix. Comparatively, the composites filled with PAAM grafted nanoparticles receive higher enhancement of sliding wear performance than those with PS grafted particles.
3. Unlike micrometer particles, nanoparticles can simultaneously provide epoxy with friction and wear reducing functions at rather low filler content. This provides the basis of utilizing the nanocomposites as coating materials for wear resisting and friction reducing applications in industries.
4. The untreated nanoparticles have either accelerating effect on the curing kinetics of epoxy because of their surface hydroxyl groups, or decelerating effect due to the increased viscosity of the composite system (before curing) and/or the strong interaction between the nanoparticles and the matrix polymer that hinders the

molecular motion of epoxy. The ultimate result is a competition of the two opposite factors. For PAAM grafted nanoparticles, the curing behavior of epoxy is promoted as a result of the catalytic effect via hydrogen bonding of the hydroxyl group in amide of PAAM to the oxygen of the glycidyl ether in the transition state. On the whole, the incorporation of either untreated or treated nanoparticles don't change the curing mechanism of epoxy.

5. Basically, the surface micro-hardness data reflect the particles dispersion status and coincide with the wear performance improvement of the composites, but the relationship between the micro-hardness and the wear data is not straightforward enough. Furthermore, it is hard to estimate the wear performance of the nanocomposites from their mechanical properties.

ACKNOWLEDGEMENTS

The financial support by the Volkswagen-Stiftung, Federal Republic of Germany (Grant No.I/76645), for the cooperation between the German and Chinese institutes on this subject is gratefully acknowledged. Further thanks are due to the Natural Science Foundation of China (Grants: 50273047 and 50133020), the Team Project of the Natural Science Foundation of Guangdong, China (Grant: 20003038), the Key Project of the Natural Science Foundation of Guangdong, China (Grants: 2003C50107 and 2004A10702001) and the project of Guangdong Economic & Trade Commission, China (Grant: 20040112) for supporting some parts of the chemical works involved in this project.

REFERENCES

[1] Bahadur, S. & Gong, D. (1992). The action of fillers in the modification of the tribological behaviour of polymers. *Wear*, 158, 41-59.

[2] Duand, J. M., Vardavoulias, M. & Jeandin, M. (1995). Role of reinforcing ceramic particles in the wear behaviour of polymer-based model composites. *Wear*, 181-183, 826-832.

[3] Lancaster, J. K. (1972). Polymer-based bearing materials: The role of fillers and fiber reinforcement. *Tribol. Int.*, 5, 249-255.

[4] Evans, D. C. & Lancaster, J. K. The Wear of polymers. In: Scott, D. editor. *Treatise on Materials Science and Technology*, vol.13. New York: Academic Press; 1979; 85-139.

[5] Tanaka, K. Effects of various fillers on the friction and wear of PTFE-based composites. In: Friedrich, K. editor. *Friction and Wear of Polymer Composites*. Amsterdam: Elsevier; 1986; 152-173.

[6] Briscoe, B. J. (1981). Wear of polymers: An essay on fundamental aspects. *Tribol. Int.*, 14, 231-243

[7] Cadman, P. & Gossedge, G. M. (1979). The chemical nature of metal-polytetrafluoroethylene tribological interactions as studied by X-ray photoelectron spectroscopy. *Wear*, 54, 211-215.

[8] Bahadur, S. & Gong, D. (1992). The role of copper compounds as fillers in the transfer and wear behaviour of polyetheretherketone. *Wear*, 154, 151-165.

[9] Voort, J. V. & Bahadur, S. (1995). The growth and bonding of transfer film and the role of CuS and PTFE in the tribological behavior of PEEK. *Wear*, 181-183, 212-221

[10] Bahadur, S., Gong, D. & Anderegy, J. W. (1993). The investigation of the action of fillers by XPS studies of the transfer films of PEEK and its composites containing CuS and CuF_2. *Wear*, 160, 131-138.

[11] Bahadur, S. & Gong, D. (1994). The effect of reinforcement and the synergism between CuS and carbon fiber on the wear of nylon. *Wear*, 178, 123-130.

[12] Zhao, Q. & Bahadur, S. (1999). The mechanism of filler action and the criterion of filler selection for reducing wear. *Wear*, 225-229, 660-668.

[13] Vishvanath, B., Verma, A. P. & Kameswara Rao, C. V. S. (1993). Effect of reinforcement on friction and wear of fibric reinforced polymer composites. *Wear*, 167, 93-99.

[14] Ei-Tayeb, N. S. & Gadebrab, B. M. (1996). Friction and wear properties of E-glass fiber reinforced epoxy composites under different sliding contact conditions. *Wear*, 192, 112-117.

[15] Symonds, N. & Mellor, B. G. (1999). Polymeric coatings for impact and wear resistance I: *Wear*, 225-229, 111-118

[16] Bely, V. A., Sviridenok, A. I., Petrokovets, M. I. & Savkin, V. G. *Friction and Wear in Polymer-Based Materials*. Oxford: Pergamon Press Ltd.; 1982.

[17] Yamaguchi, Y. Improvement of lubricity. In: Yamaguchi, Y. editor. *Tribology of Plastic Materials*, Tribology Series, vol.16. Amsterdam: Elsevier; 1990; 143-202.

[18] Sekiguchi, I., Kubota, K., Oyanagi, Y., Kasaka, K. & Sone, Y. (1992). Tribological properties of COPNA resin. *Wear*, 158, 171-183.

[19] Friedrich, K. Wear of reinforced polymers by different abrasive counterparts. In: Friedrich, K. editor. *Friction and Wear of Polymer Composites*. Amsterdam: Elsevier; 1986; 233-287.

[20] Song, J., Maertin, Cl. G. & Ehrenstein, G. W. The effect of self-reinforcement on the tribological behavior of thermoplastics. *Proc. ANTEC* 88, SPE, Atlanta (Society of Plastics Engineers, Brookfield, 1988)

[21] Song, J. & Ehrenstein, G. W. Friction and wear of self-reinforced thermoplastics. In: Friedrich, K. editor. *Advances in Composite Tribology*. Amsterdam: Elsevier; 1993; 19-63.

[22] Giannelis, E. P. Polymer layered silicate nanocomposites. (1996). *Adv. Mater*., 8, 29-35.

[23] Wang, Q., Xu, J., Shen, W. & Liu, W. (1996). An investigation of the friction and wear properties of nanometer Si_3N_4 filled PEEK. *Wear*, 196, 82-86.

[24] Wang, Q., Xu, J. & Shen, W. (1997). The friction and wear properties of nanometer SiO_2 filled polyetheretherketone. *Tribol. Int*., 30, 193-197.

[25] Wang, Q., Xu, J., Shen, W. & Zhang, J. (1998). The friction and wear properties of nanometer ZrO_2 filled polyetheretherketone. *J. Appl. Polym. Sci*., 69, 135-141.

[26] He, J. L., Wang, L. D., Li, W. Z. & Li, H. D. (1998). Experimental observations on the mechanical properties of nanoscale ceramic/Teflon multilayers. *Mater. Chem. Phys*., 54, 334-337

[27] Schadler, L. S., Laul, K. O., Smith, R. W., & Petrovicova, E. (1997). Microstructure and mechanical properties of thermally sprayed silica/nylon nanocomposites. *J. Therm. Spray Technol*., 6, 475-485.

[28] Novak, B. M. (1993). Hybrid nanocomposite materials-between inorganic glasses and organic polymers. *Adv. Mater*., 5, 422-433.

[29] Kojima, Y., Usuki, A., Kawasumi, M., Okada, A., Fukushima, Y., Kurauchi, T. & Kamigaito, O. (1993). One-pot synthesis of nylon 6-clay hybrid. *J. Polym. Sci., Part A, Polym. Chem*., 31, 1755-1758.

[30] Yano, K., Usuki, A., Okada, A., Kurauchi, T. & Kamigato, O. (1993). Synthesis and properties of polyimide-clay hybrid. *J. Polym. Sci., Part A: Polym. Chem*., 31, 2493-2498.

[31] Zilg, C., Thomann, R., Mülhaupt, R. & Finter, J. (1999). Polyurethane nanocomposites containing laminated anisotropic nanoparticles derived from organophilic layered silicates. *Adv. Mater*., 11, 49-51.

[32] Zilg, C., Mülhaupt, R. & Finter, J. (1999). Morphology and toughness/stiffness balance of nanocomposites based upon anhydride-cured epoxy resins and layered silicates. *Macromol. Chem. Phys*., 200, 661-670.

[33] Carrotenuto, G., Nicolais, L., Kuang, X. & Zhu, Z. (1995). A method for the preparation of PMMA-SiO_2 nanocomposites with high homogeneity. *Appl. Comp. Mater*., 2, 385-393.

[34] Gonsalves, K. E., Carlson, G., Chen, X., Gayen., S. K., Perez, R. & Jose-Yacaman, M. (1995). Surface functionalized nanostructured gold/polymer composites. *Polym. Mater. Sci. Eng*., 73, 298-299.

[35] Xu, W., Huang, R., Cai, B. & Fan, W. (1998). Nano-$CaCO_3$ filled HDPE composite. *Chin.Plast*., 12(6), 30-34 (in Chinese).

[36] Sumita, M., Tsukuma, Y., Miyasaka, K. & Ishikawa, K. (1983). Tensile yield stress of polypropylene composites filled with ultrafine particles. *J. Mater. Sci*., 18, 1758-1764.

[37] Rong, M. Z., Zhang, M. Q., Zheng, Y. X. & Zeng, H. M. *Surface treatment of inorganic nanoparticles by irradiation grafting of polymers*. Chinese Patent (Application No.: CN99116017), 1999.

[38] Rong, M. Z., Zhang, M. Q., Zheng, Y. X., Zeng, H. M., Walter, R. & Friedrich, K. (2001) Structure-property relationships of irradiation grafted nano-inorganic particle filled polypropylene composites. *Polymer*, 42, 167-183.

[39] Hayashi, S., Takeuchi, Y., Eguchi, M., Iida, T. & Tsubokawa, N. (1999). Graft polymerization of vinyl monomers initiated by peroxycarbonate groups introduced onto surface by Michael addition. *J. Appl. Polym. Sci*., 71, 1491-1497

[40] Oosterling, M. L. C. M., Sein, A. & Schouten, A. J. (1992). Anionic grafting of polystyrene and poly(styrene-block-isoprene) onto microparticulate silica and glass slides. *Polymer*, 33, 4394-4400.

[41] Espiard, P. & Guyot, A. (1995). Poly(ethyl acrylate) latexes encapsulating nanoparticles of silica: 2. Grafting process onto silica. *Polymer*, 23, 4391-4395.

[42] Baraton, M. I., Chancel, F. & Merhari, L. (1997). In-situ determination of the grafting on nanosized ceramic powders by FT-IR spectrometry. *Nanostruct. Mater*., 9, 319-322.

[43] Liu, Q., Wijn, J. R. D., Groot, K. D. & Blitterswijk, C. A. V. (1998). Surface modification of nano-apatite by grafting organic polymer. *Biomaterials*, 19, 1067-1072.

[44] Tsubokawa, N. & Yoshikawa, S. (1995). Grafting of polymer with controlled molecular weight onto silica surface. J. Polym. Sci., Part *A Polym. Chem*., 33, 551-586.

[45] Rong, M. Z., Zhang, M. Q., Zheng, Y. X., Zeng, H. M., Walter, R. & Friedrich, K. (2000). Irradiation graft polymerization on nano-inorganic particles: An effective means to design polymer based nanocomposites. *J. Mater. Sci. Lett*., 19, 1159-1161.

[46] Rong, M. Z., Zhang, M. Q., Zheng, Y. X., Zeng, H. M., & Friedrich, K. (2001). Improvement of tensile properties of nano-SiO_2/PP composites in relation to percolation mechanism. *Polymer*, 42, 3301-3304.

[47] Yu, T. Y. *Experimental Techniques of Polymers*. Shanghai: Fudan University Press; 1983 (in Chinese).

[48] Odian, G. *Principle of Polymerization*. New York: John Wiley; 1981.

[49] Lin, B. P., Gu, X. Y., Wang, G. L. & Yang, L. (1996). Study on polymerization of acrylamide aqueous solution. *Mod. Chem. Eng*., (1), 29-31 (in Chinese).

[50] Shim, M.-J. & Kim, S.-W. (1998). Effect of zeolite filler on the cure and thermal characteristics of diglycidyl ether of bisphenol A/4,4"-methylene dianiline system. *Polym. J*., 30, 73-77.

[51] Kissinger, H. E. (1957) Reaction kinetics in differential thermal analysis. *Anal. Chem*., 29, 1702-1706.

[52] Crane, L. W., Dynes, P. J. & Kaelble, D. H. (1973). Analysis of curing kinetics in polymer composites. *J. Polym. Sci. Polym. Lett. Ed*, 11, 533-540.

[53] Rong, M. Z., Ji, Q. L., Zhang, M. Q. & Friedrich, K. (2002). Graft polymerization of vinyl monomers onto nanosized alumina particles. *Eur. Polym. J*., 38, 1573-1582.

[54] Ji, Q. L., Rong, M. Z., Zhang, M. Q. & Friedrich, K. (2002). Graft polymerization of vinyl monomers onto nanosized silicon carbide particles. *Polym. Polym. Compos*., 10, 531-539.

[55] Shechter, L., Wynstra, J. & Kurlziy, R. P. (1956). Glycidyl ether reactions with amines. *Ind. Eng. Chem*., 48, 94-97.

[56] Chua, P. S. (1987). Dynamic mechanical analysis studies of the interphase. *Polym. Compos*., 8, 308-313.

[57] Wu, H. F., Gu, W., Lu, G.-Q. & Kampe, S. L. (1997). Non-destructive characterization of fibre-matrix adhesion in composites by vibration damping. *J. Mater. Sci. Lett*., 32, 1797-1798.

[58] Rong, M. Z., Zhang, M. Q., Liu, Y., Yan, H. M., Yang, G. C. & Zeng, H. M. (2002). Interfacial interaction in sisal/epoxy composites and its influence on impact performance, *Polym. Compos*., 23, 182-192.

[59] Kubat, J., Rigdahl, M. & Welander, M. (1990). Characterization of interfacial interactions in high density polyethylene filled with glass spheres using dynamic-mechanical analysis, *J. Appl. Polym. Sci*., 39, 1527-1539.

[60] Heux, L., Halary, J. L., Lauprêtre, F. & Monnerie, L. (1997). Dynamic mechanical and 13C n.m.r. investigations of molecular motions involved in the β relaxation of epoxy networks based on DGEBA and aliphatic amines. *Polymer*, 38, 1767-1778.

[61] Pogany, G. A. (1970). Gamma relaxation in epoxy resins and related polymers. *Polymer*, 11, 66-78.

[62] Rong, M. Z., Zhang, M. Q., Shi, G., Ji, Q. L., Wetzel, B. & Friedrich, K. (2003). Graft polymerization onto inorganic nanoparticles and its effect on tribological performance improvement of polymer composites. *Tribol. Int*., 36, 697-707.

[63] Yan, H.-X., Shi, L.-P., Shen, H.-P. (2000). Friction and wear properties of nanocrystalline Al_2O_3 filled-PTFE composites. *Tribol*., 20(2), 153-155 (in Chinese).

[64] Suh, N. P. (1973). The delamination theory of wear. *Wear*, 25, 111–124.

[65] Eliezer, Z., Schulz, C. J. & Barlow, J. W. (1978). Friction and wear properties of an epoxy-steel system. *Wear*, 46, 397-403.

[66] Lancaster, J. K. (1968). The effect of carbon fibre reinforcement on the friction and wear of polymers. *Brit. J. Appl. Phys*., 1, 549-559.

[67] Zhang, M. Q., Rong, M. Z., Yu, S. L., Wetzel, B. & Friedrich, K. (2002). Improvement of tribological performance of epoxy by the addition of irradiation grafted nano-inorganic particles. *Macromol. Mater. Eng*., 287, 111-115.

[68] Wetzel, B., Haupert, F., Friedrich, K., Zhang, M. Q. & Rong, M. Z. Mechanical and tribological properties of microparticulate and manoparticulate reinforced polymer composites. *Proc. ICCM-13*, Zhang, Y. editor. Beijing: Wan Fang Digital Electr. Publish.; 2001; ID1021.

[69] Rong**,** M. Z., Zhang, M. Q., Liu, H., Zeng, H. M., Wetzel, B. & Friedrich, K. (2001). Microstructure and tribological behavior of polymeric nanocomposites. *Ind. Lubr. Tribology*, 53(2), 72-77.

[70] Bassani, R., Levita, G., Meozzi, M. & Palla, G. (2001). Friction and wear of epoxy resin on inox steel: Remarks on the influence of velocity, load and induced thermal state. *Wear*, 247, 125-132.

[71] Bonfield, W., Edwards, B. C., Markham, A. J. & White, J. R. (1976). Wear transfer films formed by carbon fibre reinforced epoxy resin sliding on stainless steel. *Wear*, 37, 113-121.

[72] Schwartz, C. J. & Bahadur, S. (2000). Studies on the tribological behavior and transfer film-counterface bond strength for polyphenylene sulfide filled with nanoscale alumina particles. *Wear*, 237, 261-273

[73] Shimbo, M., Ochi, M. & Ohoyama, N. (1983). Frictional behavior of cured epoxide resins. *Wear*, 91, 89-101.

[74] Zhang, M. Q., Song, L., Zeng, H. M., Friedrich, K. & Karger-Kocsis, J. (1997). Frictional surface temperature determination of high temperature resistant semicrystalline polymers by using their double melting features. J. *Appl. Polym. Sci*., 63, 589-593

[75] Zhang, M. Q., Lu, Z. P. & Friedrich, K. (1997). Thermal analysis of the wear debris of polyetheretherketone. *Tribol. Internl*., 30, 103-111.

[76] Li, T. Q., Zhang, M. Q., Song, L. & Zeng, H. M. (1999). Friction induced mechanochemical and mechanophysical changes in high performance semicrystalline polymer. *Polymer*, 40, 4451-4458.

[77] Yu, L., Bahadur, S. & Xue, Q. (1998). An investigation of the friction and wear behaviors of ceramic particle filled polyphenylene sulfide composites. *Wear*, 214, 54-63.

[78] Tomizawa, H. & Fischer, T. E. (1987). Friction and wear of silicon nitride and silicon carbide in water: Hydrodynamic lubrication at low sliding speed obtained by tribochemical wear. *ASLE Trans*., 30 (1), 41-46.

[79] Fischer, T. E. & Tomizawa, H. (1985). Interaction of tribochemistry and microfracture in the friction and wear of silicon nitride. *Wear*, 105, 29-45.

[80] Gao, Y.-M., Fang, L., Su, J.-Y., Xu, X.-W. (1997). An investigation on component and formation of tribochemical film in Si_3N_4-white iron sliding pair lubricated with distilled water. *Tribol. Int*., 30, 693-700.

[81] Kong, H., Yoon, E.-S. & Kwon, O. K. (1995). Self-formation of protective oxide films at dry sliding mild steel surfaces under a medium vacuum. *Wear*, 181-183, 325-333.

[82] Nakamura, M., Hirao, K., Yamauchi, Y. & Kanzaki, S. (2002). Tribological behaviour of uni-directionally aligned silicon nitride against steel. *Wear*, 252, 484–490.

In: Nanomaterials: New Research
Editor: B.M. Caruta, pp. 81-113
ISBN: 1-59454-369-0

Chapter 2

USE OF ION BEAMS TO PRODUCE OR MODIFY NANOSTRUCTURES IN MATERIALS

J.C. Pivin
CSNSM, CNRS-IN2P3, Bâtiment 108, 91405 Orsay Campus, France

ABSTRACT

The mechanisms of structural transformations occuring in ion irradiated solids are summarized and an overview of the different types of nanostructures which can be obtained is presented. They are sorted on basis of the slowing down regime of ions and bonds nature in the material. Typical examples are given, instead of an exhaustive list.

1. INTRODUCTION

Nanostructured materials are presently the topics of many conferences and publications because their extremely small size and large surface-to-volume ratio lead to differences in their chemical and physical properties compared to bulk materials of the same chemical composition or to molecular clusters. The critical size range of the nano-domains with particular properties are quite well defined on basis of relevant dimensions in each field of physics, such as the Bohr radius of excitons in semiconductors or the correlation length of spins in magnets.

Ions penetrating in a solid lose their energy in collisions with nuclei and in electronic excitations. The latter induce no significant deflection of the ion path and, in the absence of collision cascades, the perturbed tracks are cylinders of radii ranging from 1 to 20 nm, depending on the target structure (organic, metal, semiconductor....) and on the ion nature. The spatial extension of cascades is significantly broader because of their subdivision by secondary projectiles. The mean size of nano-domains created by ions is correlated to those of tracks and secondary cascades. These parameters can be varied via a proper choice of the ion mass and energy, which determine the densities $S_e(r,t)$ ans $S_n(r,t)$ of energy transferred by the

ion to electrons and nuclei. The system perturbation lasts a very short time, typically of 10^{-13} s for the cascade and of 10^{-12} 10^{-10} s for the relaxation of the lattice and electron gas. Transient melting or vaporization of the target material may occur beyond a threshold of energy transfer to the electronic system and, for this reason, such events are more characteristic of swift heavy ion irradiation (S.H.I.). On the contrary, the displacements number density decreasing with the ion velocity, low energy ion beams are generally used for producing topography changes resulting from the sputtering of surface atoms and for disordering superficial layers (disorder leading in some cases to the target amorphization). Changes of local composition are also induced by the migration of displaced atoms and by electronic spikes. A radiation-induced diffusion of atomic defects over distances limited to the cascade extent occurs during the ballistic perturbation, then a radiation-enhanced diffusion occurs when the defects are mobile at the temperature of the experiment. These two types of diffusion have for effect a variety of chemical and structural changes, which are often similar to those obtained by thermal treatments, such as the mixing of overimposed layers, the segregation and precipitation of some species in metastable systems. However, the synergic effects of displacements and lattice excitations induce also some modifications which are specific to ion beam processing.

These considerations of general nature give good reasons for believing that ion irradiation is a suitable means to synthesize nanostructures with well controlled sizes and metastable phases. Ion beam induced modifications of materials are localized either in a controlled range of depth, correlated to the ion implantation depth, or in a defined number of cylindrical tracks. In addition, the nano-patterning of thin films can be achieved by scanning a focused and pulsed beam. On the other hand, the major drawback of ion beam treatments is their cost. Therefore, most of the examples given in this overview of nanostructures produced by ion beams are the results of researches performed for fundamental purpose or for fabricating sophisticated devices and biomaterials. After a short summary of the ion-solid interaction physics, structures will be sorted on basis of the slowing down regime and of the bonds nature in the material. Ballistic disorder can for instance lead to the amorphization of metals, semiconductor or covalent compounds while ionic crystals are more sensitive to high densities of electronic excitations. Effects of electronic excitations in dielectrics will be emphasized because these materials absorb little the energy of visible laser beams and consequently an ion beam treatment constitutes an alternative route.

2. PHYSICAL BASES

The purpose of this paragraph is to provide general concepts of ions interaction with solids useful to the understanding of phenomena described hereafter. Fine reviews already exist on the subject of energy loss and fundamental expressions can be found in handbooks [1-3]. They are briefly summarized in the appendix.

2.1. The Slowing Down Process

First let me start with tutorial definitions and description of the stopping process. Ions lose their energy in a series of elastic collisions with nuclei, screened by their electron shells, and inelastic collisions with electrons in various localized orbitals and in the conduction band. The nuclear and electronic stopping powers of the target are average values of energy transfers, T, occuring for different impact conditions, weighted by the probability $d\sigma$ of these events. This probability has the dimension of a section because it is determined by the distance p of the atom or electron at rest projected upon the ion path, called impact parameter. For simplifying the problem of summing the energy lost to various atoms in compound targets, the travelled thickness (range R) is generally defined under the form of a number of target atoms per unit area and the unit of energy loss is a number of eV/atoms/cm^2. The advantage of this unit is that the Bragg rule can be applied to calculated or measured stopping powers of elements (under different physical states), without having to assume a density value for compound targets.

An important simplification made for solving the transport equations consists in considering nuclear and electronic stopping as independent processes. This hypothesis is justified by the fact that the slowing down of the projectile due to electronic excitations is similar to the friction of an electron gas (with local fluctuations of gas density, which can be modelized by a Hartree Fock Slater distribution). The interest of this simplification can be easily understood when remembering that, although the electronic stopping is always substantial, the projectile loses little energy in each electronic collision and does not deviate significantly from its original path. On the contrary, its trajectory and residual energy vary stochastically during each nuclear collision, depending on the impact parameter p. The energy transfer $T(E_0, p)$, for a given impact parameter and projectile energy E_0 before the collision, is determined by the screened repulsion potential $V(r, E_0, Z_1, Z_2)$ of colliding atoms, which has the simple form of a Coulomb potential for short distances of cloasest approach r. A universal expression of this potential for any r value has been established for solving transport equations or performing Monte Carlo simulations of binary collisions in solids (basis of the Stopping and Range of Ion in Matter program [1]).

The expressions of T, scattering angle in a nuclear collision and stopping powers S_n, S_e, as a function of the ion energy E_0 before it penetrates in the target, atomic numbers and masses of ion (1) and target atom (2) are given in the appendix. Typical variations of S_n and S_e as a function of E_0 are shown in figure 1. Schematically, the electronic stopping power S_e increases as the product of the ion velocity by the cube root of the electron gas density up to the Bohr velocity v_B ($e^2/\hbar$, corresponding to an energy of 25 keV/amu) [2,3], then more steeply between v_B and $2Z_1v_B$, then it decreases as $1/E_0$ when the ion becomes stripped from its electrons (referred as Bethe in Fig. 1). When using the reduced energy unit ε (see appendix), $S_n(\varepsilon)$ goes through a maximum at a same ε value of 0.3 keV for all combinations of ions and targets. This optimal energy for the atomic damaging corresponds to E_0 values of 1 to 400 keV for ion masses M_1 in the range 1 to 200 penetrating in a silica target, chosen as example. Whatever the ion and target, this energy of maximum nuclear stopping is 2 to 3 orders of magnitude smaller than the energy of maximum electronic stopping.

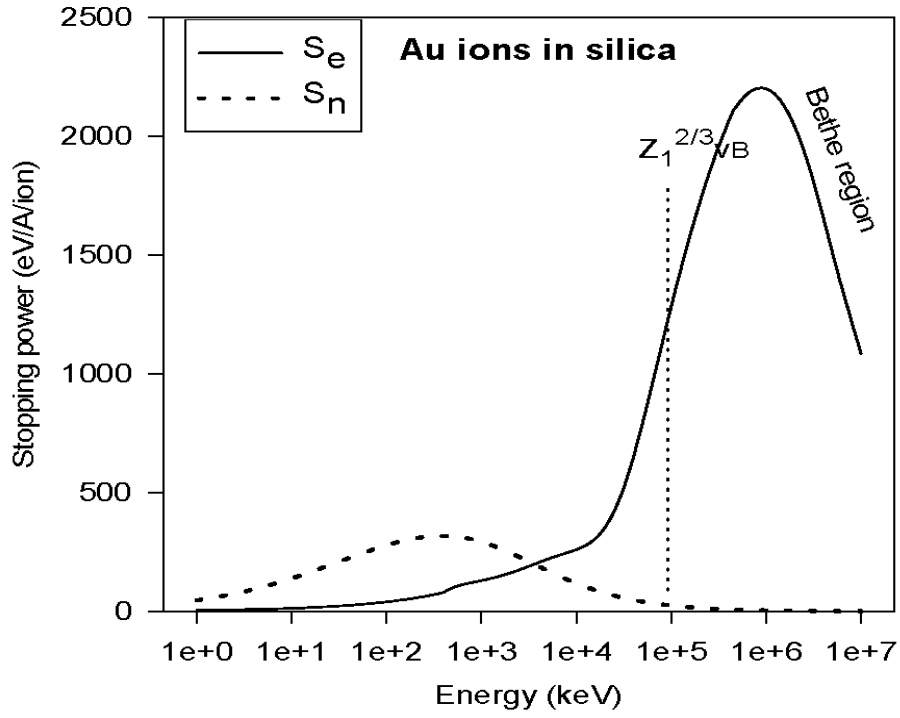

Figure 1. variations of electronic (S_e) and nuclear (S_n) stopping power of Au ions in silica as a function of their energy

2.2. Spatial Distribution of Damages in Collisional Regime

In most cases the atom set in motion during a primary collision with the incident ion (primary recoil) produces secondary collisions, which don't interfere with those resulting from other primary collisions. This regime of linear cascade, i.e. of independent sub-cascades (which is the basic assumption of SRIM calculations), takes place when the density of moving atoms is much lower than the atomic density. In such a case, the depth distribution of secondary recoils is roughly the same as the distribution of primary recoils because of the short mean free path of the formers. When the collisions density exceeds a threshold, either because of the low incident energy or high ion mass, a collision spike occurs instead of a linear cascade [4]. Atoms which do not collide with the ion or a recoil acquire nevertheless a momentum under the effect of electronic interactions with moving neighbors. These ballistic spikes have some common features with the thermal spikes produced by high densities of electronic excitations under the impact of swift ions (with a velocity $v_0 > Z_1^{2/3} v_B$, above which the charge state of the ion increases when it penetrates in the target) or by illumination with a laser, in this respect that they are modelled by using the same transport equations of heat (see paragraph 2.4). However, the expressions of the concentration of atoms set in motion and of the temperature at the end of the energy impulse are different and the heat is dissipated for a part by a transfer from phonons to the electronic system in the case of ballistic spikes, instead of the reverse in electronic spikes [4, 5].

The basic quantity defining the concentration of displaced atoms $N_d(R)$ and the threshold value for the occurence of a collision spike is the ratio of the density of nuclear energy transfer to the displacement energy E_d. The latter is the minimal energy which a recoil must receive in order that the formed Frenckel pair is not annihilated by direct recombination with the associated vacancy, located at a few interatomic distances, or by relaxation of the lattice. E_d depends on the crystallographic orientation of the displacement, because replacement collisions are favored along dense atomic rows and the binding energy is anisotropic (on the average it is correlated to the cohesion energy of the crystal). This anisotropy contributes to various phenomena, such as the preferential sputtering and disordering of some crystals in a polycrystalline target. Since nuclear collisions don't necessarily lead to effective displacements, the part of the primary energy, E_0, which is converted in defects energy, $F_d(E_0)$, amounts to only 20 to 50% (according to the used model) of the energy transferred to nuclei over the whole ion path, $\nu(E_0)$. According to the earliest estimate by Kinchin-Pease [6], the number of stable Frenkel pairs created by each ion is:

$$N_d = \nu(E_0)/2E_d \tag{1}$$

The most probable ranges of ions, $<R_1>$ and of defects, $<R_d>$, can be derived directly from mean values of energy losses given in tables by writing:

$$<R_1> = \int_0^{E_0} \frac{1}{N_{at}} \frac{dE}{S_n + S_e} \tag{2}$$

$$\text{and } <R_d> = \int_{E_d}^{E_0} \frac{1}{N_{at}} \frac{dE}{S_n} \tag{3}$$

where N_{at} is the atomic density of the target.

Due to the stochastic nature of the nuclear stopping process, the depth distributions of implanted atoms and of energy transferred to nuclei, $f_1(E_1, R)$ by ions having a residual energy E_1 at depth R (which is the derivative of $\nu(E_0)$ also labelled $F_1(E_0)$), can be approximated by Gaussian functions in the case of amorphous or polycrystalline targets. These distributions are however estimated more accurately by using transport equations defined by Lindhart [1] and computing Monte Carlo simulations of binary collision cascades with the SRIM code. Molecular dynamics simulations attract more and more interest with the increasing speed of computers for their ability to simulate spikes and crystallographic effects which are randomized in Monte Carlo simulations.

2.3. Cooperative Effects of Cascades

The overlap of cascades produces a random walk of target atoms called radiation induced-diffusion (RID also called ballistic diffusion, cascade mixing). Note that the anisotropic relocation of primary recoils must be distinguished from this RID in the analysis

of transport processes such as the mixing of overimposed layers, especially when these layers are composed of atoms with very different masses [7]. In addition to RID, a migration of point defects occurs after the cascade when the temperature is sufficiently high (radiation-enhanced diffusion, RED in abbreviated form). RID and RED lead in some cases to the segregation of an atomic species (one of the target components or the implanted ions), either due to its lower mass or its lower binding energy or its tendency to form complexes with defects [8-10]. Another factor to take into account in the analysis of diffusion fluxes is that a vacancy-rich zone is formed in the core of cascades and interstitials are more numerous at their periphery. As a result, a given atomic species diffuses towards R_d or interfaces, depending on its stability and mobility on interstitial and substitutional sites, and point defects segregate into dislocation loops.

Another effect of the cascade overlap is the progressive change of surface geometry and composition related to sputtering. Let's just give here Sigmund analytical expression of the sputtering yield Y [11], obtained by applying Boltzman transport equation to describe the flux of particles. Sigmund equation is less accurate but more useful than simulations to outline the effects of the mass and binding energy of target atoms and of the beam orientation with respect to the surface normal on the yield Y and on surface modifications. An overview of these effects was given in [12] and a compilation of experimental data in [13]. The sputtering yield is proportional to the fraction F_d of the ion energy used to displace atoms in outermost layers (which includes displacements by all projectiles) and to the probability Λ that these displaced atoms escape to the surface. F_d differs from the energy deposited by the ion in the escape depth range R_e (close to zero, so that $F_1(R_e) \approx S_n$) by a factor α. This factor represents the influences of the mass ratio M_2/M_1 and of the incidence angle θ on the anisotropy of ion scattering in outer layers of an amorphous or polycrystalline target. Its value α_N for a normal incidence is a slowly varying function of M_2/M_1, increasing from 0.2 to 1, and the exponent f of the angular factor $\cos \theta^{-f}$ is equal to 5/3 for not too heavy target atoms. The escape probability is inversely proportional to the Born-Mayer screening factor of the interaction potential C_0 ($3/4\pi^2 C_0 = 0.0420$) for slow recoil atoms and to the surface energy barrier U_s (half the binding energy of target atoms).

$$Y = \Lambda\, F_d(R_e) = \frac{3}{4\pi^2}\frac{1}{C_0 U_s}\,\alpha_N \cos\theta^{-f}\, S_n(E_0) \qquad (4)$$

Y presents the same periodic variation with Z_2 in elemental targets as does the surface binding energy, with the result that volatile elements (H_2, O_2, N_2..) are preferentially sputtered from compound targets. When the binding energies of target components are comparable, a superficial impoverishment in the lighter element is usually observed. The escape depth R_e of sputtered atoms is of the order of 2 atomic distances [6], but the target composition is modified from the surface to the mean range of defects <Rd>. The surface topography changes progressively, due to statistical fluctuations in the number of atoms ejected in each point and to the differential sputtering of dislocation loops, or of precipitates in composite targets. Cones topped with precipitates are formed when their sputtering yield is lower than that of the matrix and the precipitates number density changes in all cases.

The depth profile of implanted atoms also changes with the implanted fluence, under the combined effects of lattice swelling and sputtering (disregarding the casualty of a

segregation). Schematically, the surface moves outward at a rate proportional to the ion fluence ϕ for keeping approximately constant the target atomic density when ions come at rest on substitutional sites, while sputtering induces an inward motion of the surface. The concentration profile becomes an error function with a plateau value equal to $\tilde{\phi}N_{at}(1+Y)$ close to the surface.

At this point, mention must be made of the channeling phenomenon, which consists in a slighly oscillating path of ions and considerably increased penetration depth when their incident direction is parallel to dense packing planes and rows of a crystal. The lessening of scattering cross section is related to a large and constant impact parameter on the average. Channeling affects not only the depth profiles of implanted ions and defects in single crystals, but also their sputtering yield. In polycrystalline targets, the different sputtering yields of grains according to their orientation induces a surface relief.

In some cases, residual defects segregate under the form of amorphous clusters instead of dislocation loops, because the configuration energy over short distance is lower in the amorphous state. This process is particularly efficient in all semiconductors and covalent compounds (such as quartz). The amorphization occurs locally when the amount of disorder exceeds a threshold value, either in the core of subcascades, when their density is sufficiently high, or by a statistical process of cascades overlap. On the contrary, ionic crystals are amorphized with difficulty because displacements produce two types of charged Frenckel pairs, which exhibit a stronger tendency to recombine than in covalent systems for minimizing the space charge.

2.4. Electronic Damaging in Isolated Tracks Produced by Swift Heavy Ions

Beside the linear density of energy transferred to the electronic system (product of S_e by the atomic density), another parameter to take into account in the damaging process is the radial distribution of this energy in tracks, as long as they don't overlap. One generally distinguishes two regions: a high density of electronic excitations is produced in the track core extending over 1-3 nm and the energy is transported by fast secondary electrons (δ-electrons) in a track halo with a radius of some hundreds nm. For a same S_e value, the energy deposition is smeared out into a larger radius for high velocity projectiles [14]. The reason for this velocity effect is that the the maximum energy transferred to δ electrons is $T_{max}= 2\ m_e\ v_{ion}^2$. The swifter the ion is, the higher is the fraction of the ion energy swept away from the core by these electrons for a given S_e value. Polymers are sensitive essentially to ionizations produced in the core, while damaging in metals results from lattice vibrations induced by elastic collisions of δ electrons outside the core. The damaging mechanisms of semiconductors and inorganic insulators are more intricate, since they involve various processes of electron-hole recombination and charge transfer.

For most inorganic materials, there exist a threshold value of S_e above which the damaging of crystalline targets increases dramatically (Figure 2) or on the contrary crystalline order is reconstructed in some amorphous targets [15-17]. The threshold effect is particularly clear for metals, in which electronic excitations cause a partial annihilation of the defects created by atomic collisions at low energies. Two different mechanisms have been proposed for the steep increase of damaging: ion explosion spikes and thermal spikes.

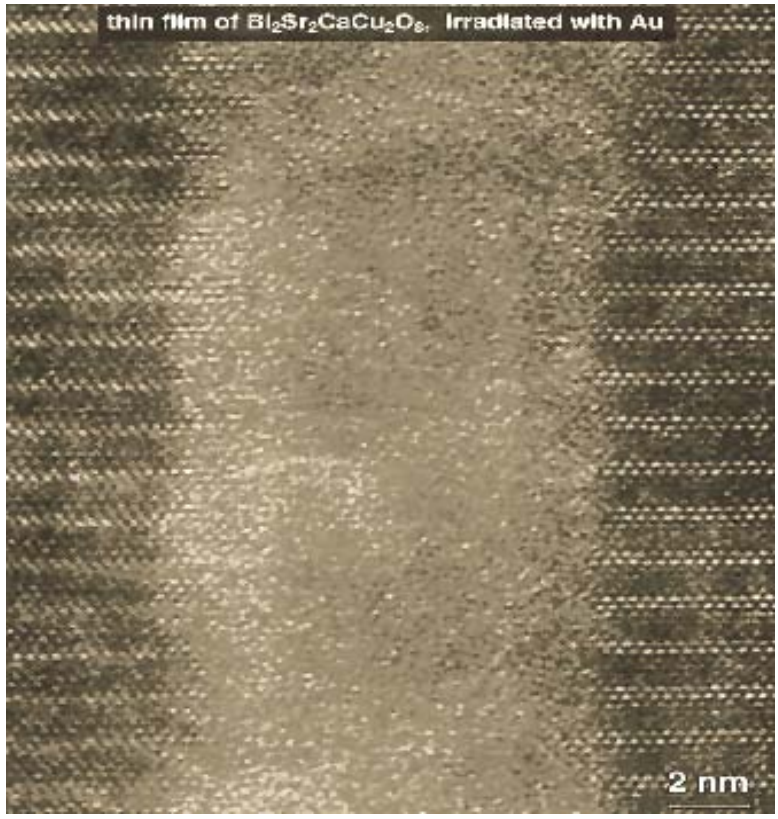

Figure 2. amorphous track in $Bi_2Sr_2CaCu_2O_8$ irradiated with swift Au ions (by courtesy of J. Wiesner et al [17]

In the ion explosion spike theory one considers that the ion creates in its wake a cylinder of highly ionized matter which is very unstable due to Coulomb repulsion between electrostatic charges. Several models were derived from this theory, being the core-plasma model, the shock-wave model, and the modified lattice potential model [18)]. In fact, damage creation via electronic excitations in metals was considered during some time as unrealistic due to the high mobility of conduction electrons, which rapidly smear out the deposited energy and very efficiently screen the atoms that were ionized in the ion wake. However, a shock-wave mechanism is pertinent in the case of metals with a low phonon frequency. Moreover, even if the charge neutrality is re-established in the track core, the interatomic potentials remain during some time different from the equilibrium potentials, setting atoms into motion and producing an athermal melting of the track. On the other hand, mainly insulators are sensitive to Coulomb explosion spikes in the strict sense of the term [19]. Their effect may be annealed by thermal spikes occuring thereafter in the same material, because the returning time of electrons expelled from the track core in a Coulomb explosion is of 10^{-14} to 10^{-13} s and the spreading of the energy in a thermal spike is much slower (10^{-13} to 10^{-12} s depending on the electron mobility).

In the thermal spike model the transfer of energy from the bombarding ion to the lattice is a two-step process [20, 21] : thermalisation of the energy deposited in the electronic system via electron-electron interaction and transfer of this energy to the lattice via electron-phonon

interaction. Since the electronic system and the lattice are not in thermal equilibrium with each other, their temperatures, Te and Ta , respectively, are governed by a set of coupled nonlinear differential equations:

$$C_e(T_e)\frac{\partial T_e}{\partial t}=\frac{1}{r}\frac{\partial}{\partial r}\left[rK_e(T_e)\frac{\partial T_e}{\partial r}\right]-g(T_e-T_a)+E(r,t) \quad (5)$$

$$C_a(T_a)\frac{\partial T_a}{\partial t}=\frac{1}{r}\frac{\partial}{\partial r}\left[rK_a(T_a)\frac{\partial T_a}{\partial r}\right]+g(T_e-T_a) \quad (6)$$

where $T_{(e,a)}$, $C_{(e,a)}$, and $K_{(e,a)}$ are the temperature, the specific heat, and the thermal conductivity for the electronic ($_e$) and lattice ($_a$) subsystem, respectively. E(r,t) is the radial density of energy transferred to electrons. The electron-phonon coupling constant g is directly linked to the electron mean free path λ: $\lambda=K_e/g$. The difference between metals and insulators is that in metals energy can be transferred from the hot lattice back to the electrons when $T_a>T_e$,while this transfer is inhibited in insulators.

The damaging of materials by electronic excitations may lead to their amorphization (Fig. 1), but those which are easily amorphized by collision cascades (such as Si) are little sensitive to electronic damaging. The reason of this difference of sensitivity is that the transient disordered phase formed within swift ion tracks tends to reconstruct in epitaxy with the surrounding matrix in the case of semiconductors or covalent compounds. The recovery of structural order is less easy in ionic compounds containing charged defects. Moreover, defects on one of the ionic systems may combine to form a gaseous species, as for instance in alkali halides and consequently metal atoms in excess segregate [22]. Note that pure metals (apart Ga, Bi) are disordered but not amorphized [23] and the topological order just changes on short range in metallic glasses.

3.BALLISTIC EFFECTS

3.1. Implantation

Applications of ion implantation to the doping of semiconductors or of other materials (for chemical applications in catalysis, detection of gases,...) are out of the scope of this paper. Beside this undeniable interest of the ion implantation technique, it is also one of the most versatile means to create a supersaturated solid solution in the near-surface region of a solid. With regard to nanostructures, a precipitation may occur under the effect of radiation-induced diffusion during implantation, when the local concentration of implanted atoms is much larger than the solubility limit at equilibrium. It is for instance the case of noble metals in oxides for concentrations over 1 at.% [24, 25] (Figure 3). The radiation-enhanced diffusion of interstitials is also effective in many matrices at room temperature (RT). However that may be, implantations are often followed by annealing treatments at high temperatures (or implantations performed in temperature), in order to induce a maximum yield of precipitation and to eliminate defects in the host lattice. This combination of treatments has been called Ion Beam Synthesis.

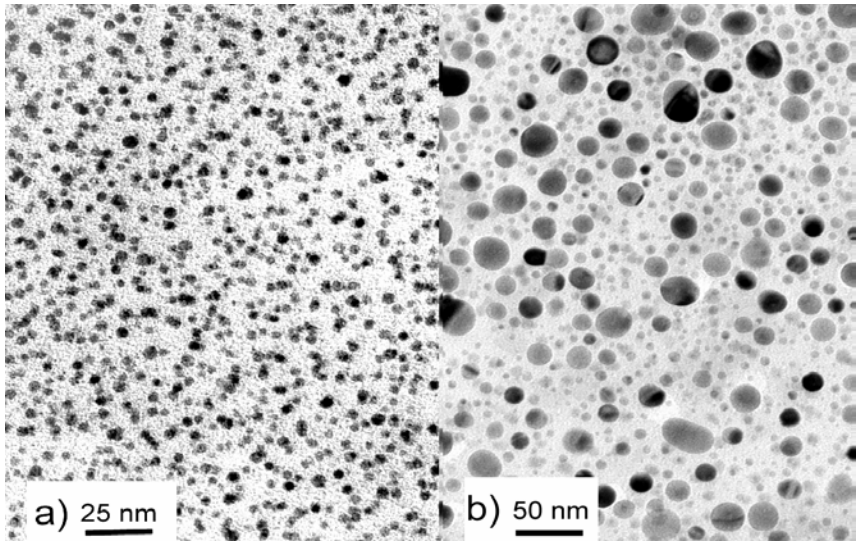

Figure 3. TEM images of silica implanted with 150 keV Ag^+ ions at fluences of (a) 10^{16} and (b) $10^{17}/cm^2$ (3 and 28 at.% at the mean range) [24]

3.1.1. Concentration Gradients in Implantation Layers

In addition to the lattice damaging, the inhomogeneous depth gradient of concentration in implantation layers complicates the interpretation of their properties and may limit their performances. Multi-implantation at several energies permits to overcome this problem, with more or less success because diffusion processes are not taken into account in SRIM simulations. Other programs, such as TRIDYN [26], neglect also the casualty of RED but permit to estimate dynamic changes in the target composition induced by sputtering, ballistic mixing and lattice swelling. Variations in the displacement and binding energies of target atoms with the composition are also considered in the inputs of these simulations.

The narrow depth distribution of ions implanted at a single energy is nevertheless interesting for some applications, as for instance the fabrication of non volatiles memories based on nanocrystals (NCs) embedded in the gate oxide of MOS transistors [27, 28]. By low energy Si^+ implantation, NCs of Si can be formed a few nm above the SiO_2 /Si interface. This allows charging of the NCs by direct electron tunnelling, which is a prerequisite for low operation voltages. Kinetic Monte Carlo Simulations (KMCS) [27] were developped for studying the process of phase separation in these systems. This process involves sequentially the nucleation and growth of particles at the expense of the Si supersaturated solution, then the Ostwald ripening of some of the Si NCs and a spinodal decomposition at higher Si concentrations. The simulations permit to predict the Si concentration threshold of percolation (which process hampers the charging of the NCs) and the optimal temperature range of implantation or post-annealing treatment, in which the trapping of Si solute atoms at the substrate interface together with a controlled growth of the NCs lead to a self alignment suitable for the fabrication of non volatile memories.

An argument put forward by many authors to praise the usefulness of the IBS technique is the obtention of high filling factors of particles close to the surface [29-31]. In fact this characteristics is generally detrimental to the performances of nanocomposite systems, because of the well known effect of dipolar interactions in optics and magnetism. The

plasmon resonance in the visible of Ag particles shown in figure 3 becomes broader with the increasing Ag fluence, under the combined effects of the increase in their size scattering and in their interaction [24]. In current magnetic recording media, the written bits are comprised of an ensemble of weakly interacting magnetic grains, contrarily to what is obtained in insulators implanted with high concentrations of 3d metals (chosen high in fact in order to compensate the shallow range of doping) [30,31]. The confinement of excitons in semiconductors deteriorates also with the gathering of particles.

Beside their usefullness for the charge injection in MOS structures, Si NCs are also interesting for their luminescence or for activating rare earth elements with an excited level at an energy close that of excitons in the NCs [32-35]. Once again, the criterion of quality is a narrow size distribution of the NCs, in the range of 2-3 nm, so that their gap fits the excitation energy of Er^{3+} ions from the $^4I_{15/2}$ to the $^4I_{9/2}$ state for instance. The sensitization of Er ions implanted sequentially with Si ions has been extensively studied and the results constitute a school case of the difficulty to obtain simultaneously: (i) Si clusters with suitable size, (ii) Er atoms in solid solution in the oxide instead of in silicide particles [34], (iii) but at same depth [36]. However, some useful devices seem to have been fabricated [37-39]

3.1.2. Variety of Obtained Structures and IBS Conditions

IBS has been used to create a wide variety of nanocrystals and quantum dots made of a single element or of a compound, by sequential implantation [32, 40-42]. The nature of the precipitation may depend on the implantation order [40, 43]. Implantation of 2 metals, with the aim of obtaining alloyed particles with a controled plasmon resonance energy, results for instance in the formation of core-shell particles after annealing when the 2 elements exhibit a solubility gap [43]. NCs of almost all semiconductors have been synthesized in silica, alumina and silicon [32]. The ionicity of the host affects the crystalline nature of formed phases. As an example, it is possible to produce CdS and CdSe crystals with the hexagonal wurtzite or the cubic zincblende structure in α–Al_2O_3 by modifying the implantation conditions, because this matrix is little sensitice to ballistic damaging. When implantation is carried out at moderate temperature (~600°C), dynamic annealing keeps alumina crystalline and epitaxial relationships favor the formation of NCs with the hexagonal structure. On the contrary, when implantation is carried out at low temperature (LN_2), the near surface region of alumina is amorphized. Upon annealing, the amorphous layer first crystallises with the metastable γ-Al_2O_3 cubic structure embedding NCs with same symmetry (zincblende). Particles with latter structure are formed whatever the implantation temperature in silica. Another example of structure modification correlated to the more or less efficiency of dynamic annealing is that observed during the synthesis of β-$FeSi_2$ in Si single crystals. When implanting Fe atoms in silicon at sufficiently high temperature (about 400°C), precipitates of β-$FeSi_2$ with their [100] axis aligned parallel to the [110] axis of Si are obtained [44]. Randomly oriented particles are formed when Fe is implanted at lower temperature. After further annealing at 800°C or more, the structure of the Si single crystal is restored perfectly in latter case while a large number of dislocation loops remains in the crystal containing particles in epitaxy. Taking that β-$FeSi_2$ is often mentioned as a potential candidate for the solar energy convertion, it may be worth to note that these dislocations are more luminescent than the semiconducting compound and at a close wavelength.

Implantation in channeling conditions permits to increase significantly the ion range and to limit the damaging of the host material. Connectively to the increase in the range, the implanted species undergoes less self-sputtering and is more protected against oxidation. Buried layers of $FeSi_2$ or $ErSi_2$ were grown in such conditions [45].

Rare gas atoms usually form bubbles at high fluences in all materials, which effect is at the origin of the blistering of the walls of ion guns or reactors. These cavities can be used as preferential nucleation sites of particles, formed for instance from layers evaporated thereafter on the surface and mixed by means of a further heat or irradiation treatment. Let's mention for its exotic nature the formation of cubic porosities in MgO crystals, which were used as templates for fabricating cubic Ag and Au particles in this material [46, 47].

3.2. Sputtering

3.2.1. Cleaning, Roughening of Surface for Improving Coatings

The growth of "good quality" films (adherence, homogeneity and eventually epitaxy) owes it success to an appropriate surface cleaning step prior to deposition. Among the few techniques available, sputtering is attractive for its simplicity and insensitivity to the nature of contaminants. However, the damages caused by ions can affect the epitaxy of susbsequently grown films on crystalline substrates and must be repaired by in situ thermal annealing. Technological studies show that the optimal energy of Ar ions, commonly used in sputtering experiments, for removing the native oxide and adsorbed molecules on Si substrates without extensive damaging is of 150-200 eV (while S_n is maximum at 14 keV).

3.2.2. Surface Relief Induced by the Combined Effects of Erosion and Diffusion

The stochastic nature of sputtering makes that the surface roughness would increase monotonously if this statistical effect was not balanced by the local change of ion incidence and by radiation-enhanced diffusion. Experimental studies on amorphous materials and on semiconductors (amorphized by the bombardment) show that off-normal sputtering generates a more significant relief and an anisotropic modulation of the surface. Depending on the ion incidence angle θ, the ripples can be either parallel (θ close to grazing) or perpendicular (θ close to normal) to the projection of the ion beam direction on the surface plane, while for normal incidence (θ=0) a periodic modulation of the topography is generally not observed. These results have been explained, on basis of Sigmund theory, in terms of a linear instability caused by the surface curvature dependence of the sputtering yield (formula 4), which dominates the smoothing due to the thermal surface diffusion [48]. Schematically, the top of crests is eroded faster than the bottom of trenches dug by ions at oblique incidence and the change in the ripple orientation is related to the ratio of interlayer/ superficial diffusion induced by collision cascades. On the contrary, at temperatures where thermal diffusion is noticeable, ion sputtering of single crystal metals produces features that reflect the substrate symmetry, without any relationship with the ion beam direction [49, 50]: square pits have been observed on Cu(001) and Ag(001) or hexagonal ones on Pt(111), Au(111) and Cu(111). This relief is ascribed to the coalescence of vacancies under the surface. In a critical range of temperature and ion flux, interlayer diffusion occurs along preferential directions (<110> in fcc crystals) and ripples are formed parallel to a direction of same family in the surface plane,

independently of the beam orientation with respect to the normal to the surface and to <110> directions in the plane, at least for θ<30°. At lower temperatures, the relief formation is controlled by erosion and depends on θ: ripples of smaller amplitude are formed as on semiconductors. The ripples with a crystalline orientation formed at intermediate temperatures find for example applications in the nano-patterning of epitaxial layers. The magnetic anisotropy of thin Co layers can be forced to be parallel to the <100> axis by modulation of the film thickness perpendicular to this direction [51].

Arrays of asperities with a conical or sinusoidal shape were observed recently at the surface of InP, GaSb, InAs and InSb sputtered at normal incidence, or at oblique incidence with simultaneous sample rotation [52]. A theory for their formation has not yet been developped. They are characterized by a uniform size distribution (around 100 nm) and a large degree of spatial ordering. They self-organize in hexagonal or square close-packed patterns, depending on the incidence angle and temperature (in the range of 280 to 330 K).

3.3. Ion Beam Assisted Deposition (Ibad)

Similar effects of diffusion occur during the vapor deposition of thin films. Adatoms diffuse faster along dense directions at moderate temperatures and interlayer diffusion takes place at high substrate temperatures. Shadowing of hollows for the atom flux plays the same role as for ions in sputtering experiments. As a result, different regimes of deposition can be distinguished as a function of the temperature, T: (i) at low T where the grains growth is controlled by the transport geometry, the coating exhibits a columnar structure and porosities; (ii) at intermediate T, the structure densifies and the columnar grains become coarser, with their axis oriented preferentially parallel to the dense packing direction; (iii) a fully dense and equiaxed structure is formed at high T [53, 54].

Now, ion beams can be used to modify this texture through the effect of ion channeling. Molecular dynamics simulations predict the preferential growth of crystals with channeling directions parallel to the beam, due to the reduced sputtering and damaging [55]. The energy stored under the form of lattice defects leads to a migration of grain boundaries, towards the most damaged grains. This effect can be used to favor the epitaxial growth of some coatings or to alter their natural growth anisotropy. For instance, an ion bombardment at normal incidence of a fcc metal film will cause a shift from a <111> texture favored by surface energy considerations to a <110> texture, because the sputtering decreases by 2 to 5 times when the beam is parallel to <110> directions of easiest channeling in fcc crystals. MgO films, which naturally grow under the form of islands with a <001> axis perpendicular to the surface, can be forced to grow with, in addition to the <001> texture, a preferential orientation of one of their <110> axes parallel to the ion beam if θ=45° [56].

The ion bombardment tends also to improve the film density and adhesion [57-59]. The adhesion improvement may be due for a part to the mixing of interfacial layers or in other cases to the formation of precipitates anchoring the coating. Indeed, huge increases of resistance to indentation cracking and wear of diamond-like carbon coatings are obtained for instance by pre-implantation of C in the substrate, having for result the formation of carbide nanoparticles, or by irradiation throughout the coating thickness (taking care to not destroy the diamond-like pilling of atoms by cascades) [60, 61].

When implantation is performed at very low energy (some 100 eV to a few keV), the concentration of implanted atoms tends progressively towards 100%, if their coefficient of self-sputtering is lower than 1. Their segregation by RED at the surface is facilitated by the shallow implantation depth when their solubility in the host material is limited. This ion beam deposition technique (IBD), shows common features with IBAD, in this respect that in both cases the structure of deposited layers is affected by erosion and diffusion effects. However, the ratio of ion/deposited atom fluxes in IBD experiments is of 1, so that outermost layers are strongly shaken and eventually frozen in an out of equilibrium state with ultimate properties. Films of pure amorphous diamond, with a proportion of sp_3 bonds larger than 80% and a hardness close to 100 GPa, were grown by this method [62,63]. There is no upper limit to their thickness (apart a reasonable implantation time) and they are found indestructible in friction tests [60].

3.4. Cluster Beams

Beside other interests which are out of the scope of this paper, the use of a cluster beam allows an easier control of the kinetic energy of atoms impinging a target than that of monoatomic ions. Indeed, the energy of cluster ions is shared betwen the atoms when they break during the collision with the target atoms. If the energy per atom is below the cohesion energy, the clusters can be deposited on the surface without destroying their structure. Nanostructured silicon films with controlled particle size obtained by cluster beam deposition (CBD) show a higher photoluminescence yield than porous silicon [64]. The proportion of sp^2 rings in C clusters is intrinsically connected to their size, so that the size selection of cluster beams permits to grow coatings with various degrees of diamond-like hybridization [65]. The formation of composite materials characterised by a monodisperse size and an homogeneous spatial distribution of particles, which constitute quality criteria for applications in opto-electronics and magnetism, were also obtained by combining CBD with an evaporation of matrix atoms [66, 67]. $B_{10}H_{14}$ clusters were used to fabricate shallow junctions (of 7 nm) in p-type Si, which cannot be obtained by atom beam implantation due to boron enhanced diffusion. [68]

3.5. Mixing

The ion beam mixing of superimposed layers of different materials under the effects of RID and RED deserves a place in the synthesis of nanostructures by the fact that the thickness of formed alloys or compounds is often nanometric (when the target is not made of multiple layers). One can put forward several advantages of using mixing instead of ion implantation for synthesizing compound layers:

- Alloying to high concentration by ion implantation is time consuming and uneconomical.
- The maximum concentration that can be reached in the surface region is generally limited by sputtering.

- Ion implantation is not well suited to obtain flat concentration profiles, even when using multi-energy implantation, and to form alloys over thicknesses larger than a few hundreds of nanometers
- Implantation also requires to make use of a different ion source in each case.

These limitations are in principle overcome by using the alternative route of ion beam mixing. A good illustration is the mixing of metal/silicon systems, which was extensively studied in the 80th because of the technological interest for the fabrication of electronic components. Making simply use of noble gas ions selected for their mass, Xe, with an energy of the order of 100 keV, about 10^{17} atoms/cm^2 can be mixed with Xe fluences as low as 10^{15}/cm^2. The indicated value of mixing yield corresponds to a silicide thickness of 20nm and in many cases the composition of the formed silicide is homogeneous, because the enhanced-diffusion of Si atoms in metals is efficient at room temperature [69-72]. In the case of a metal implantation in Si at same energy, the sputtering yield is of same order of magnitude as the implanted dose.

An advantage of mixing over fast anneal by laser or electron beams may come from the fact that ions transfer kinetic energy to target atoms without necessarily involving melting. Thus, one may expect to form metastable alloys with zero solubility in the liquid state. In fact, numerous experiments have shown that the concentrations of crystalline solid solutions formed from overimposed layers of two metals are generally extended to the detriment of intermetallic phases and the result of mixing is the formation of a metallic glass when the metals are not miscible at high T [73]. Several authors argued that in many metal-metal or metal-silicon systems mixing occurs during the thermalizing stage of the ion-solid interaction after the cascade (for a comprehensive review of models see [74]). Indeed, they estimated the mean kinetic energy of atoms during the time wherein mixing occurs to kT_{eff} = 1-2 eV, from a fit a experimental diffusion rates [75]. If this was true, there should not be much advantage over laser or electron beam heating (apart that transparent materials cannot be heated with a laser beam) since ion mixing would involve melting. However, other experiments give evidence of a dependency of the mixing rate on the temperature of the experiment or of a diffusion anisotropy which may be explained by the occurence of RED or of recoil implantation, but certainly not by thermal spikes.

Whatever the collisional regime, linear cascades, localized or global spikes all along the ion path [74], the mixing extent is correlated to the heat of alloying in most systems. This phenomenological law was verified as well for silicides [76] as for metals in covalent compounds and insulators [77]. The metal silicide formed by mixing of a single metal layer on silicon is generally the stable phase that lies near an eutectic composition and its composition is forced by the ratio of layers thicknesses in multilayers. In a regime of low displacements density (linear cascades), the mixing rate may be controlled by recoil implantation, diffusion or an interfacial reaction, according to the system. A diffusion controlled kinetics is characterized by a variation of the number of mixed atoms N and a widening of interfaces $W=\sqrt{2Dt}$ as $\phi^{1/2}$ (D being the effective diffusion coefficient and t the equivalent time, ratio of the fluence ϕ to the flux), while in the two other cases N and W vary as ϕ (examples are given in [72]).

The above mentioned enthalpy rule is of little use to predict the mixing efficiency in the most insulating materials, such as alumina, because the charged defects which are formed in

the oxide are unstable, so that displaced atoms tend to move back to the interface [77, 78]. On the other hand, when insoluble metal atoms are pushed in an insulator with a sufficient velocity (by primary collisions with ions of comparable mass), they migrate over short range before precipitating under the form of nanoparticles. Taking that, when the interface energy of metal layers embedded in oxides or on their surface is high, they spheroidize under irradiation as they do during heat treatments, complex structures are obtained, made of large particles surrounded by a halo of smaller particles created by the mixing-reprecipitation process (Figure 4). Particles of noble metals with this bimodal distribution of sizes in silica exhibit a plasmon-related resonance peak in the visible which is abnormally narrow, compared to a same ensemble of particles that are apart from each other. The effect is ascribed to a screening by nanoparticles arranged in a halo around each large particle of the polarization induced by other large particles (nanoparticles contributing directly to the absorption for less than 10%). The strong dipolar interaction between particles in implantation systems of same nature has an opposite effect because of their random distribution of size and spatial arrangement [24, 79].

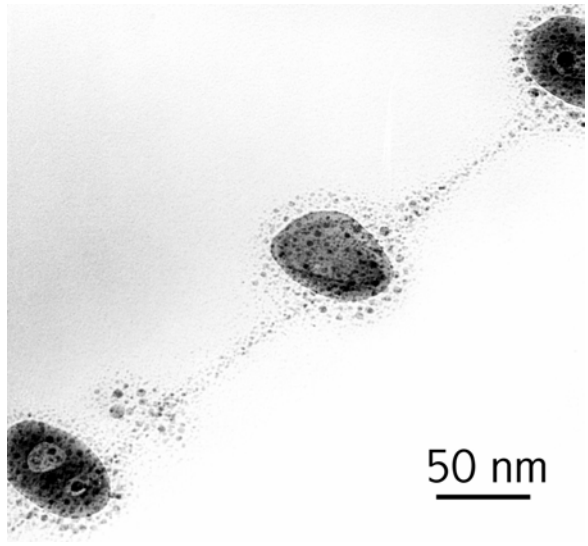

Figure 4. TEM image the cross section of a 50 nm SiO_2/ 8 nm Ag / bulk SiO_2 sample irradiated with 10^{16} Au ions/cm^2 of 4.5 MeV

3.6. Amorphization and Recrystallization

A discussion of amorphization and recrystallization mechanisms under ion irradiation may appear irrelevant in a review concerning nanostructures. It finds its justification by the fact that amorphization is the most probable change of structure in semiconductors and insulators and it proceeds from the coalescence of amorphous nuclei. This particular type of precipitation was studied first and most others obey same kinetic laws. On the other hand, the recrystallization of semiconductors after implantation treatments is a topics of major importance for applications in electronics and an understanding of the recrystallization

mechanism of bulk semiconductors under irradiation (IBIEC) is needed for applying the same principles to the formation of heterostructures.

Experiments on semiconductors and metallic compounds presenting an amorphous counterpart (like Ni_3B, NiAl, NiTi) showed that amorphization can occur by two different mechanisms, depending on the energy density deposited in nuclear collisions. In the case of a displacements spike regime, amorphous clusters are formed under the impact of each ion, while the number of displacements per atom (dpa) must be accumulated until it reaches locally a critical value in a linear cascade regime. Consequently, the amorphization kinetics is a linear function of the fluence in the former case and presents a sigmoidal shape in the latter, described by the following law [80, 81]:

$$\alpha = \sum_{nc}^{\infty} P_n = \sum_{nc}^{\infty} \frac{(\sigma\phi)^n}{n!} \exp(-\sigma\phi) \qquad (7)$$

The probabililty P_n of cluster formation is proportional to that for an area of the target σ to be perturbed by n impacts and n_c is the critical number of impacts to obtain a stable nucleus. In fact σ is the cross section of damaging, product of the stopping power by its efficiency. The same law applies to many precipitation processes in regimes of nuclear or electronic stopping.

Ion implantation of high ion fluences in pure metals has also been used for synthesizing amorphous alloys, generally of same nature as those obtained by quenching from the melt but interesting for their high purity [82] . The study of amorphization kinetics has shown that the decisive parameter is the chemical ordering in the amorphous phase, which lessens the configuration energy on short range [80, 83]. At low T, where the implanted atoms are not mobile, clusters are formed where the local concentration of implanted atoms exceeds a theshold value and the amorphization kinetics obeys the Poisson law given above (equation 7). At higher T, the short range diffusion of implanted atoms favors the formation of clusters for very low concentrations of implanted atoms, so that the kinetics is a linear function of the fluence.

Epitaxial recrystallization of amorphous implantation layers may be promoted by ion irradiation at lower T than purely thermal recrystallization (called solid phase epitaxial regrowth). The ion-beam-induced epitaxial crystallization (IBIEC) is not an effect of beam heating and numerous experiments have demonstrated that only the defects which are created at the a-c interface contribute to the process [84]. Each ion produces in the vicinity of the interface the amorphization of some atoms and in the meanwhile king-like defects (along [110] ledges connecting two (111) terraces in Si). IBIEC and ion-beam-induced interfacial amorphization (IBIIA) are competing processes and the direction and rate of the a-c interface motion depend on the temperature and ion flux: (i) at low T and/or at high flux, a planar layer-by-layer amorphization occurs; (ii) IBIIA and IBIEC are in balance at a critical temperature T_r and (iii) the IBIEC rate increases above T_r. A residual amorphous layer often remains close to the surface and planar growth is blocked at too high temperatures by the formation of crystallites inside the amorphous layer [85]. Dopants such as B, P and As enhance the IBIEC rate while C, O, F produce a retardation by pinning interfacial defects. The recrystallization of implanted layers can be obtained by subsequent irradiation with an energetic ion beam having an implantation range well beyond the a-c interface or by a proper

choice of implantation flux and T (self-annealing process). Beside the technological interest of IBIEC for lowering the crystallization temperature of implanted layers in Si, it found applications in the fabrication of epitaxial heterostructures [84]. The maximum thickness of strained layers free of dislocations networks is increased and the interface is more planar than by crystallization in a furnace. Higher temperatures must also be used for growing films of same composition by molecular beam epitaxy.

3.7. Patterning

A number of patterning methods have been used, for instance to obtain single magnetic domains with as small sizes as possible but exhibiting no spontaneous reversal of magnetization. The principle, when using irradiation through a mask for patterning a magnetic film, consists to create arrays of soft regions with a longitudinal magnetization in a film of higher coercivity, with a perpendicular anisotropy. However a coupling remains between strongly magnetized bits and noise in disordered regions. The ideal material is one where magnetism is either created or destroyed upon exposure to a low ions fluence. A technique consists in creating discrete islands of a magnetic phase by digging trenches with a focused ion beam (FIB) in a continuous thin film and, in addition, to poison the magnetic order in the trenches by incorporation of implanted ions or by mixing of an overcoating [86]. Collimators of diameter smaller than 100 nm are commonly available for this purpose.

Focused ion beams provide also a means to fabricate channel waveguides and laser gratings by localized mixing of semiconductors multilayers [87].

4. ELECTRONIC EFFECTS

4.1. Radiolysis and Conversion of Polymers

Polymers are the most sensitive of all materials to radiation damaging, so that photons, electrons or ions may be used as well for promoting the crosslinking or decomposition of thin polymeric films. One of the interests of using ion beams for this purpose lies in the much higher radiolytic efficiency of ions [88-90]. The short range order in amorphous ceramic films obtained by ion irradiation is also very different from that in polymers converted into ceramics by means of other processes. Moreover, irradiation with low ion fluences permits to pattern the surface with isolated cylindrical tracks, which may thereafter be etched and filled with other materials. This use of tracks as templates is discussed in a next paragraph. Unetched tracks constitute also interesting nanostructures with particular chemical properties which will first be summarized.

4.1.1.Organic Polymers

The final product of the crosslinking process is a three-dimensional amorphous network composed principally of C, O and N atoms. The bond scission under the effect of nuclear collisions is supposed to favor the formation of a network where C atoms exhibit a high degree of sp^2 hybridization [88-91]. However, collision cascades do not affect significantly

the physical properties of this network, as long as ions lose as much energy in electronic excitations than in collisions (because useful fluences are so low that few atoms are displaced). This has been shown by performing experiments with ions of energy in the range of 20 to 100 keV/nucleon on polymers with alliphatic or cyclic structures [92, 93]. The measured values of optical gap E_g (larger than 0.5 eV) and of hardness H (5 times that of turbostratic graphite) of polymer films irradiated in such conditions indicate that they exhibit a noticeable degree of diamond-like hybridization, contrarily to heat treated films. In addition, variations of E_g, H [92] and of other properties [88-90] show that the efficiency of ionizations in crosslinking the structure increases with S_e, most probably because the ability of formed radicals to combine increases.

Let's get down to tracks formed in the purely electronic stopping regime by saying that fullerenes clusters seem to be formed in the core of tracks when the electronic LET exceeds a threshold value. This fact suggests the occurence of thermal spikes since this allotrope of C is stable at high T [94-97]. In milder conditions of irradiation, phenyl rings (even in alliphatic polymers) and other types of unsaturated bonds are formed before C clusters at low fluences [98, 99]. The nature of observed moieties differs in many cases from those formed in polymers submitted to other types of ionizing radiations. They constitute grafting sites for other macromolecules or inorganic ions, which attract the interest of chemists [100]. It is also worth to note that the linearity of swift ions tracks facilitates the diffusion of dopants and tracks decorated with alcaline or halogen elements can be used as nanometric electric contacts.

4.1.2. Semi-Organic Polymers and Gels

Taking that ion irradiation of organic polymers produces carbon-rich amorphous phases (at high fluences) with more interesting physical properties than those of pyrolyzed polymers, as also with less change in the content of other elements than hydrogen, experiments were carried out on semi-organic polymers and gels . These materials made of an inorganic backbone and organic side groups are particularly useful as precursors of ceramic coatings, foams and fibers. Experiments on silicon-based polymers and gels with various ions show that, like in organic polymers, hydrogen is released selectively [101], with same kinetic laws [102], and the molecular structure is crosslinked then transformed into a glassy ceramics. Physical properties such as the density and hardness increase with same slope as a function of the transferred energy $Se\times\phi$ as do the amount of H release. Nuclear collisions appear once again to play no significant role in the conversion process and don't affect the chemical order in the fluence range useful for the conversion into ceramics.

The C content in the ceramics generally exceeds the maximum value in homogeneous glasses $SiO_{2-x}C_{x/2}$ ($x\leq 2$) and the C excess segregates in polysiloxanes with a Si-O- backbone as well as in polycarbosilanes with a Si-CH_2- backbone. Energy filtered TEM images of the C distribution in cross sections of the irradiated films put into evidence that C atoms or CH_x radicals migrate in the structure to form clusters with a diameter of 3 to 7 nm, depending on the C content and S_e value (Figure 5) [103]. In the case of phenyl-substituted precursors, clusters are also supposed to form on the spot of the radiolytic reaction [104]. C clusters are aligned along tracks or exhibit a more random distribution when ions undergo also nuclear scattering. Assuming that continuous wires may be obtained above a threshold of S_e or C concentration, they would find applications as field emission tips or electric contacts with a well defined and nanometric section. Raman analyses show that, whatever their arrangement,

isolated C particles formed at low ion fluences exhibit a noticeable degree of tetragonal hybridization, while C clusters which are also formed in films of same nature by annealing in vacuum are made of turbostratic graphite. The semiconducting particles formed under irradiation emit a yellow-green luminescence, contrarily to those formed in annealed films. The PL emission wavelength and yield is the same for spherical, randomly distributed, clusters and for discontinuous cylinders obtained at high energy, for a given value of energy transfer $S_e \times \phi$. The PL peak shows a red shift and broadening with the increasing $S_e \times \phi$, ascribed to the growth of part of the clusters (in matrices where a percolation is unlikely, due to the low C excess). Rings of C atoms with a sp^2 hybridization state are known to form at the periphery of C clusters when their size increases and this graphitic state is the one stable at equilibrium (which factor explains the nature of clusters in annealed samples). Beside interesting optical properties, the tetragonal hybridization of C clusters afford irradiated films hardness 2-3 times higher than that of heat-treated films, as shown by nanoindentation tests: the hardness of irradiated polycarbosilanes reaches that of bulk SiC [101].

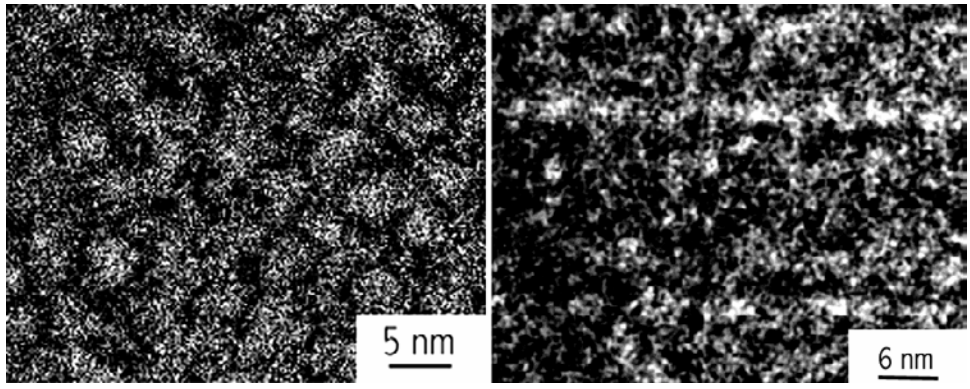

Figure 5. Energy filtered images of cross sections of methyltriethoxysilane gel films ($[Si(OH)(CH_3)-O]_n$) irradiated with 3 MeV and 100 MeV Au ions at fluences of 10^{15} and 10^{13} /cm^2 respectively [103]

Similarly to C in gels and polymers containing C in excess, Si precipitates under irradiation in the suboxide with stoichiometry $SiO_{1.5}$ derived from the triethoxysilane gel (the ethoxide precursor has for formula $SiH(OC_2H_5)_3$) and the semiconducting clusters show a red luminescence, at a wavelength which is correlated to the particles size (~1 nm) [105]. When the same gel is mixed with metal salts, SiH hydrido group react with the metal ions for forming metal nanoparticles [106]. Their distribution is relatively narrow (of Gaussian type with a standard deviation/mean size ratio of 25%) contrarily to that of particles formed in films heat-treated in vacuum. Another drawback of heat treatments is that the evolution of gases leads to the formation of ovoid porosities and the particles are segregated on the pore walls. An investigation of the precipitation kinetics, by means of electron spin resonance in the case of magnetic metals or of optical absorption for noble metals, shows that the driving force is the formation of $Si^{\bullet}$ free radicals under the effect of ionizations and clusters are formed when the number of neutralized metal atoms exceeds locally a threshold value for the building of a stable nucleus. The volume of metal phase therefore increases as the cumulative

of a Poisson distribution function (formula 7), like that of amorphous clusters which are formed in semiconductors or metals in the ballistic regime of slowing down.

4.2. Formation of Composites and Phase Changes in other Materials

4.2.1. Demixion of out of Equilibrium Solid Solutions

Irradiation of metastable solid solutions, such as silicate glasses containing noble metals, at energies below the threshold of matrix damaging by electronic excitations, may lead to a precipitation. By varying the ratio of electronic to nuclear energy transfer, for instance via the mass of ions, it has been demonstrated that displacements contribute to the precipitation only when the dissipated power is high enough to induce a substantial target heating [107]. Otherwise the nucleation yield varies in proportion to the energy transferred to electrons $S_e \times \phi$ [108, 109]. The kinetic law of precipitation may be the cumulative of a Poisson distribution when tracks must overlap to form nuclei with a stable size [109] or a linear function of $S_e \times \phi$ when stable nuclei are very small [108]. Their size remains constant as long as the source of metal ions in solid solution is not exhausted and the clusters can be as small as 0.5 nm. Particles with such a size undergo a very high compressive stress due to their interface energy. Contractions of the order of 10% of the lattice parameter a were calculated for Ag particles in silica on basis of the observed blue shift of their plasmon resonance.

4.2.2. Growth of Particles

When pursuing the irradiation of same targets, or irradiating composites containing very few atoms of noble metal in solid solution obtained by means of another technique, a growth of the particles is observed when the energy density S_e is not too high [110]. The linear increase of the particle size with the fluence indicates that the rate controlling process is the desorption of the noble metal atoms from the surface of pre-existing particles. These desorbed atoms diffuse over a short distance and are adsorbed at another particle surface. Thus, some particles grow at the expense of others as long as the density of excitations remains low.

Above a given S_e value, in the range of 5 to 10 keV/nm, the size of same particles decreases. A detailed investigation of the density effect is still needed for defining if the critical parameter is the ratio of the desorption/adsorption rates or the threshold of matrix damaging. On the contrary, a growth of Co particles formed by ion implantation in silica has been observed when they were submitted subsequently to electronic excitations with an as high density (of about 20 keV/nm) [111]. Taking that the particles became elongated parallel to the beam direction and the density of energy transfer was 10 times larger than the threshold of silica damaging, the authors ascribed the structural transformation to a thermal spike effect. However the increasing elongation of the particles which was observed with the track overlap seems to indicate that the relaxation of energy in the transient disordered phase was so fast that a thermal equilibrium could not be reached. The occurence of Coulomb explosions or an increase in the readsorption /desorption rates ratio in the case of a particle ensemble with a very high filling factor (compared to ion exchanged glasses and other colloids studied in [110]) cannot be excluded. On a practical point of view, the Co particles elongation had for interesting effect to tilt their easy magnetization axis perpendicular to the film surface.

4.3. Latent Tracks

Since tracks in some materials can be chemically revealed, the initial damage is also called latent track. Fission fragments from nuclear accelerators are sometimes used instead of ion beam accelerators for producing tracks. Latent tracks are formed in most materials above a S_e threshold. This threshold is one order of magnitude larger in crystalline metals than in quartz and tracks have been observed only in pure metals with a low phonons frequency and exhibiting a displacive transformation (of martensitic type) such as Fe, Ti, Zr [18]. The formation threshold is also much higher in Si or Ge than in compound semiconductors and the ions must have a low velocity (together with a high stopping power, which combination is possible for cluster beams), probably because the crystalline order is more easily restored after melting of the track core when atoms are of same nature and the core diameter small. In other terms, monoatomic semiconductors of type IV are probably not amorphized as long as the rate of power dissipation dE_e/dt in the track core does not exceeds that of epitaxial reconstruction [15]. The quantity dE_e/dt may be more significant than the linear density S_e (dE_e/dR) in the modeling of transformations since these transformation depend on the lifetime of the transient disorder and on structural parameters above mentioned. The track morphology is however correlated to the magnitude of S_e. Close to the S_e threshold, the track consists of extended spherical defects. Increasing S_e leads to the percolation of these defects under the form of a discontinuous cylinder of the same radius, then to the homogenization of the damaged radius.

4.3.1. Changes in Magnetic Ordering

Latent tracks have a wide range of applications linked to their anisotropy. The radial stress in magnetic oxides leads to an anisotropic orientation of the magnetic internal field. This orientation can be parallel or perpendicular to the track axis, depending on the sign and strength of the magnetostriction effect [112-114]. The same effect is observed for magnetic colloids in an amagnetic matrix, as shown by the change in the magnetic anisotropy of iron particles embedded in a silica film after irradiation with 100 MeV Au ions in figure6. Before irradiation (spectrum labelled n.i.) the anisotropy of magnetization is determined by the shape factor (demagnetizing field) and the easy axis is parallel to the surface. After irradiation with 10^{13} Au ions/cm^2, the minimum resonance field is measured for a tilt angle φ of 90°, indicating that the easy axis is perpendicular to the surface [115].

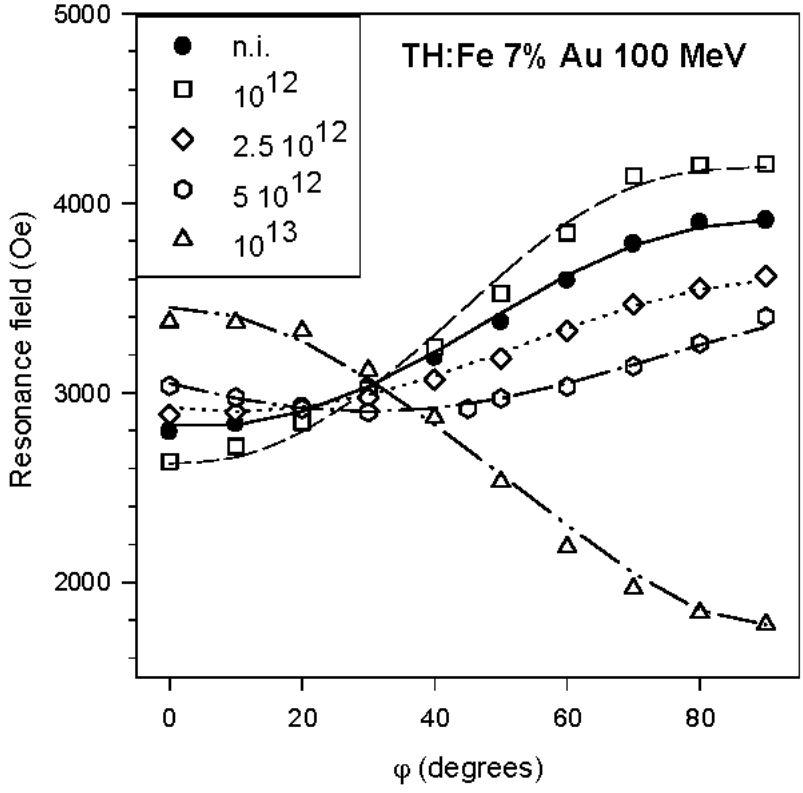

Figure 6. variation of the resonance field, in electron spin resonance experiments, as a function of the angle φ between the applied static field and the surface, for films of SiO_2:7% Fe 400 nm thick, before (n.i.) and after irradiation with 100 MeV Au ions at fluences indicated in the frame. The lines are fits

with equation: $\frac{\omega_0^2}{\gamma^2}=H_0^2=(H_{res}+H_i\cos 2\varphi)\times(H_{res}-H_i\sin^2\varphi)$,

where H_0 is the precession effective field, ω_0 the angular frequency of the cavity, γ the gyromagnetic factor and H_i the internal field, sum of the demagnetizing field and of the magnetostriction field

Paramagnetic phases may exhibit a permanent magnetization after irradiation, due to their disordering and related either to site exchanges between cations ($ZnFe_2O_4$, $NiFe_2O_4$) [116,117] or to the localization of d electrons in the amorphized structure such as in the case of YCo_2 [118]. Amorphous tracks are insulating in high T_c superconductors and, since their size is comparable to the coherence length of spins, they pin lines of magnetic flux [119], leading to an increase of the critical current by more than one order of magnitude. The pinning of walls by amorphous tracks also tends to increase the coercitivity of the matrix in other magnetic materials [120]. As well as carbon cylinders formed in polymers, conducting cylinders formed by damaging diamond like carbon film [121] may be useful as nanometric field emitters.

4.3.2. Filters and Templates

Chemical etching becomes very efficient whatever is the material when track radii are larger than 2-3 nm. To date commercial ion track membranes made of polymers, crystalline insulators (micas) and glasses with calibrated pore diameters between 15 nm and several µm are available [122, 123]. Research activities aim at even smaller pore opening (around 2 nm). They find many applications as biosensors, filters for controlling drug delivery on wounds [123] or filters with pores sizes changing as a function of the external conditions, T and P (intelligent materials) .

Using electrochemical or electroless deposition, pores can be filled with metals or semiconductors in order to fabricate micro or nanometric needles, wires or tubes [122, 124-133] (Figure 7). This replication technique is very simple and the wires or tubes can be removed from the membranes (by chemical etching or using a scotch tape) or used as an ensemble protuding from the membrane surface as the bristles of a brush. The template synthesis requires very low ion fluences (of the order of 10^6 to 10^8/cm^2). Nanostructures with extraordinary low and monodisperse diameters are obtained, which are difficult to manufacture using lithographic techniques. In the case of galvanic deposition, one has control over the filled length of the pores and can fabricate axially structured wires, consisting for instance of Co/Cu multilayers with a giant magnetoresistance perpendicular to the membrane plane [133] or of Cu/Se resonant tunneling diodes [129]. Radially structured tubes and wires can also be fabricated by electrochemical or electroless deposition with a catalyst on the pores walls. CdSe/CdTe nanodiode arrays obtained by this technique act as retinal photocells, resembling those in the human eye [127]. Metal tubes may be used as microchannel plates or anodes in batteries.

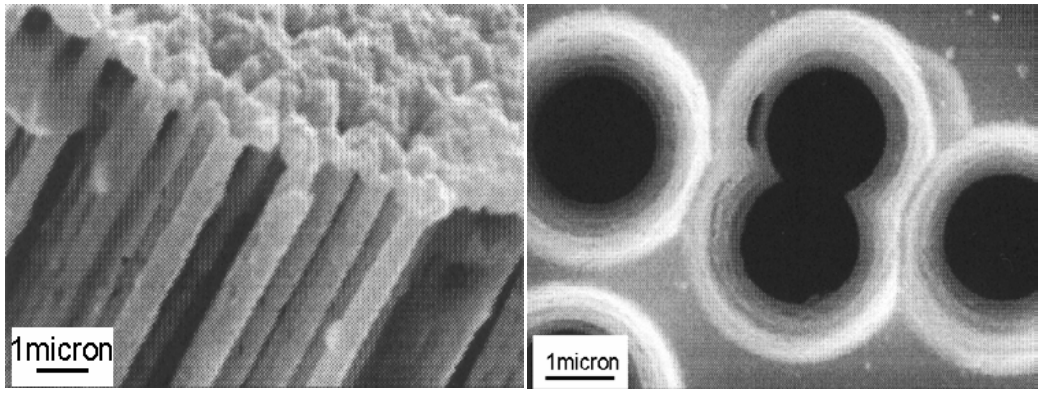

Figure 7. example of structure obtained by filling tracks with a metal: left Ag nanowires and right Cu-Ni concentric tubes , by courtesy D. Fink [127, 128]

5. CONCLUSION

During their very short passing through the target, ions induce stochastic atoms displacements and/or electronic excitations within tubular tracks of nanometric radius, depending on their velocity. The two processes of energy transfer may lead to a redistribution

of atomic species and structural transformations by mechanisms involving either solid state diffusion or relaxation of kinetic energy in a liquid-like, of short life, phase.

Ballistic effects are localized within a given depth range and the displacements density can be varied by means of the ion mass and velocity. In addition, other parameters such as the damaging resistance of the matrix, epitaxy relationships, ion channeling, ion flux and irradiation temperature may be used to modify the dynamic annealing of damage. Provided that these irradiation conditions are judiciously chosen, on basis of empirical studies and Monte Carlo dynamic simulations, the nature and the nucleation and growth rate of nanoparticles synthesized by ion implantation can be predicted and controlled. Ion beam mixing of heterostructures constitutes an interesting alternative for getting rid of implantation physical limitations (sputtering, depth gradients) and for decreasing the ion fluences needed to obtain compound layers and colloids. One can also take advantage of the crystallographic anisotropy of atomic displacements and sputtering for modifying the surface topography and the texture of PVD films.

Electronic excitations in swift ion tracks permit to localize the energy deposition along the transverse direction (with respect to ballistic interactions) and the electron-lattice coupling to create cylindrical structures. Some are obtained directly through the migration of radicals and secondary ions in materials particularly sensitive to electronic excitations, such as polymers and out of equilibrium solid solutions in insulators. Atomic rearrangements during the lattice relaxation produce also changes of density or crystalline structure with interesting effects on the magnetization anisotropy of thin films. Finally, latent tracks can be easily etched in many materials to obtain pore filters and templates for the fabrication of nanowires and tubes of various natures by a chemical deposition process. This use of tracks is particularly attracting for the extraordinarly low and monodisperse diameter of the pores and for their controlled density.

A large variety of planar or cylindrical structures have been synthesized by using ion beams, with applications as waveguides, nanodiode arrays, magnetic memories, electric contacts, field emitters, transparent metallic structures, gas sensors and separators, mimics of biological systems.

6. REFERENCES

[1] J. F. Ziegler, J. P.Biersack, , and U. Littmark, *The stopping and Range of Ions in Solids*, ed. J.F. Ziegler, (Pergamon Press, New York, 1985)

[2] J.W. Mayer, E. Rimini, *Ion Beam Handbook for Material Analysis*, , (Academic Press, New York, 1977).

[3] W.K. Chu, in *Materials Chacracterization Using Ion Beams* , eds. J.P. Thomas and A. Cachard , (1976) , p 3

[4] P. Sigmund and C. J. Claussen, *Appl. Phys*. 52(1981) 990

[5] Z.G. Wang, C. Dufour, E. Paumier, and M J. Toulemonde, *Phys. Condens. Matter*. 6(1994) 6733

[6] P. Sigmund, *Rad Effects* 1 (1969) 15

[7] P. Sigmund, and A. Gras-Marti, *Nucl. Instr. and Methods* 182-183(1981) 25.

[8] J.C. Pivin, and J.P. Riviere, in *Compte Rendus Congres National Société Française de Physique*, (les Editions de Physique1985), p 199.
[9] R.C. Piller and A.D. Marwick, *J. Nucl. Mat.* 83 (1979) 42
[10] R.C. Piller and A.D. Marwick, *Rad. Effects* 47 (1980) 195
[11] P. Sigmund, *Phys. Rev*. 184 (1969) 383
[12] J.C. Pivin, *J. Mat. Sci*., 18 (1983) 1267 .
[13] R. Behrisch, *Sputtering by Particle Bombardment*, (Springer Verlag, Heidelberg,1981).
[14] Meftah, F. Brusard, J.M. Constantini, M. Hage-Ali, J.P. Stoquert, F. Studert and M. Toulemonde, *Phys. Rev. B48* (1993) 920.
[15] L.T. Chadderton, *Rad Measurements* 36 (2003) 13
[16] M. Levalois, and P. Marie, *Nucl; Instr. and Meth*. B156 (1999) 64
[17] J. Wiesner, C. Traeholt, J.G. Wen, H.W. Zandbergen, G. Wirth and H. Fuess, *Physica C* 268 (1996) 161.
[18] D. Lesueur, and A. Dunlop, *Rad Effects* 126 (1993) 163
[19] R.L. Fleischer,.P.B. Brice, and R.M. Walker, *J. Appl. Phys*. 36 (1965) 3645
[20] Z.G. Wang, C. Dufour, E. Paumier, and M. Toulemonde, *J. Phys. Condens. Matter*. 6 (1995) 2525
[21] M. Toulemonde, C. Trautmann, E. Balanzat, K. Hjort, and A. Weidinger, *Nucl; Instr. and Meth. in Phys. Res*. B216 (2004) 1.
[22] F. Beneu, *Nucl. Instr. and Meth. in Phys. Res*. B141 (1998) 241
[23] Audouard, R. Mamy, M. Toulemonde, G. Szenes, and L. Thomé, *Europhys Lett*. 40 (1997) 557
[24] J.C. Pivin, M.A. Garcia, J. Llopis, and H. Hofmeister, *Nucl. Instr. and Meth. in Phys. Res*. B 191 (2002) 794
[25] P. Mazzoldi , L. Tramontin , A. Boscolo-Boscoletto, G., Battaglin, , and G.W. Arnold, *Nucl. Instr. and Meth. in Phys. Research* B80/81 (1993) 1192
[26] W. Möller and W. Eckstein, *Nucl. Instr. and Meth*. B 2 (1984) 814
[27] T. Müller, K.H. Heinig and W. Möller,. *Appl. Phys. Lett*. 81 (2002) 3049
[28] P. Normand , E. Kapetanakis and P. Dimitrakis, *Nucl. Instr. and Meth. in Phys. Res.* B216 (2004) 355.
[29] N. Kishimoto, Y. Takeda, M. Umeda , V.T. Gritsyna, C.G. Lee, and T. Saito, *Nucl. Instr. and Meth. in Phys. Res.* B 166-167 (2000) 840
[30] T. Isobe, S.Y. Park, R.A. Weeks, and R.A. Zuhr, *J. Non-Crystal. Solids* 189 (1995) 173
[31] R.I. Khaibullin, V.N. Popok, V.V. Bazarov, E.P. Zheglov, B.Z. Rameev, C. Okay, L.R. Tagirov, and B. Aktas, *Nucl.Instr. and Meth. in Phys. Res*. B 191 (2002) 810
[32] C.W. White , J.D. Budai, S.P. Withrow, J.G. Zhu, E. Sonder, R.A. Zuhr, A. Meldrum, D.M. Hembree, D.O. Henderson, and S.Prawer, *Nucl. Instr. and Meth. in Phys. Res*. B 141 (1998) 228
[33] P.G. Kik, and A. Polman, *J. Appl. Phys*. 88 (2000) 1992
[34] J.C. Pivin, M. Jimenez de Castro, H. Hofmeister and M. Sendova-Vassileva, *Mat. Sci. Engineer*. B97 (2003) 13
[35] D.I. Tetelbaum, O.N. Gorshkov A.P. Kasatkin, V.A. Burdov, S.A. Trushin, A.N. Mikhaylov, and D.M. Gaponova, *Surf. Coat. Technol*. 158-159 (2002) 1
[36] M.L. Brongersma, A. Polman, K.S. Min, , and H.A. Atwater, *J. Appl. Phys.* 86 (1999) 759
[37] P.G. Kik and A. Polman, *J Appl Phys*. 91 (2002) 534

[38] G. Franzo, F. Iacona, V.Vincigueiro and F. Priolo, *Mat.Sci. Engineer*. B69 (2000) 335
[39] Garrido, M. Lopez, A. Perez-Rodiguez, C. Garcia, P. Pellegrino, R. Ferre, J.A.Z.Moreno, J.R. Morante, C. Bonafos, M. Carrada, A. Claverie, J. de la Torre and A. Souifi, *Nucl. Instr. and Meth. in Phys. Res*. B216 (2004) 213.
[40] Ila, *Nucl. Instr. and Meth*. B 141 (1998) 289
[41] S. Nakao, *Nucl. Instr. and Meth. in Phys. Res*. B 141 (1998) 246
[42] G. Battaglin, *Nucl. Instr. and Meth. in Phys. Research* B141 (1998) 252 and 274
[43] G. Battaglin, E. Cattaruzza, C. de Julian Fernandez, G. De Marchi, F. Gonella, G. Mattei, P. Maurizio, A. Miotello, C. Sada, and F. D'Acapito, *Nucl. Instr. and Meth. in Phys. Res.* B175-177 (2001) 410
[44] Y. Gao, S.P. Wong, W.Y. Cheung, G. Shao, and K. P. Homewood, *Nucl. Instr. and Meth. in Phys. Res.* B 206 (2003) 317
[45] Vantomme, *Nucl. Instr. and Meth. in Phys. Res*. B120 (1996) 190
[46] M.A. Van Huis, A.V. Fedorov, A. van Veen , P.J.M. Smulders, B.J. Kooi and De J.T.M. Hosson, *Nucl. Instr. and Meth. in Phys. Res*. B 166-167 (2000) 225
[47] M.A. Van Huis, A.V. Fedorov , A. van Veen , C.V. Falub , S.W.H. Eijt , B.J. Kooi , J.T.M. De Hosson , T. Hibma , and R.L. Zimmerman, *Nucl. Instr. and Meth. in Phys. Res*. B 191 (2002) 442
[48] R. Cuerno, H. A. Makse, S. Tomassone, S. T.Harrington and H. E. Stanley, *Phys. Rev. Lett.* 75 (1995) 4464
[49] S. Rusponi, C. Boragno and U. Valbusa, *Phys. Rev. Lett*. 78 (1997) 2795.
[50] S. Rusponi, G. Costantini, C. Boragno, and U. Valbusa, *Phys Rev. Lett.* 81 (1998) 2735
[51] Sekiba, R. Moroni, G. Gonella, F. Buatier de Mongeot, C. Boragno, L. Mattera and U. Valbusa, *Appl. Phys. Lett*. 84 (2004) 762
[52] Frost, B. Ziberi, T. Höche, and B. Rauschenbach, *Nucl. Instr. and Meth. in Phys. Res*. B216 (2004) 9
[53] J.A. Thornton, J. *Vac. Sci. Technol*. 11 (1974) 866.
[54] K.H. Müller, *J. Appl. Phys.* 58 (1985) 2573.
[55] L. Dong, D.J. Srolovitz, *J. Appl. Phys*. 84 (1998) 5261
[56] L. Dong, L.A. Zepeda-Ruiz, and D.J.Srolovitz, *J. Appl. Phys*. 89 (2001) 4105
[57] M. Ektessabi, *Nucl. Instr. Meth. in Phys. Res*. B 127/128 (1997) 1008
[58] A. Schmidt, *Int. Mater. Rev*. 35 (1990) 61
[59] J.E. Greene, S.A. Barnett, J.E. Sundgreen, A. Rockett, in *Ion Beam Assited Film Growth* ed. T. Itoh, , (Elsevier, 1989), pp 101
[60] J.C. Pivin, *J. Mat. Sci*. 27 (1992) 6735.
[61] J.C. Pivin, and T.J. Lee, *Nuc. Instr. and Meth. in Phys. Res*. B80-81 (1998) 1499
[62] J.C. Pivin, M. Allouard and G. Rotureau, *Surf. and Coat. Technol*.47 (1991) 433
[63] S.N. Shamin, J.C. Pivin, and E.Z. Kurmaev, *J. Appl. Phys*. 73 (1993) 4605
[64] Perez , P.Melinon, , and V. Dupuis, *J. Phys. D: Appl. Phys*. 30(1997) 709
[65] P. Milani, A. Podesta, and P. Piseri, *Diamond and Rel. Mat*. 10 .(2001) 240
[66] J.M. Meldrim, Y. Qiang, Y. Liu, H. Haberland, D.J. Sellmyer, *J. Appl. Phys.* . 87.(2000)7013
[67] Dupuis, V. Tuaillon, B. Prevel, A. Perez, and P Z. Melinon, *Phys.* D 40 (1997) 155
[68] Yamada Matsuo, *J. Mat. Sci. Semicond. Proc*. 1 (1998) 27
[69] S.S. Lau, B.X. Liu, and M.A. Nicolet, *Nucl. Instr. and Meth*. 209-210 (1983) 97

[70] J.W. Mayer, B.Y. Tsaur, S.S. Liau, and L.S. Hung, *Nucl. Instr. and Meth*. 182-183 (1981) 1
[71] D.L. Santos, J.P. de Souza, L. Amaral, and H. Boudinov, *Nucl. Instr. and Meth. in Phys. Res.* B103 (1995) 56
[72] J.C. Pivin, D. Dimova-Malinovska, M. Sendova-Vassileva, and M. Nikolaeva, *Nucl. Instr. and Meth. in Phys. Res.* B174 (2001) 453
[73] R.J. Gaboriaux, and M.A. Nicolet, *Ann. Phys. Fr*. 8 (1983) 563
[74] D. Averbach, *Nucl. Instr. and Meth. in Phys. Res*. B 15 (1996) 675
[75] Y.T. Cheng, *Matter. Sci. Rep*. 5 (1990) 45
[76] S.S. Lau, B.X. Liu and M.A. Nicolet, *Nucl. Instr. and Meth. in Phys. Res*. 209-210 (1982) 125
[77] C.J. McHargue, D.L. Joslin, and C.W. White, *Nucl. Instr. and Meth. in Phys. Res* B91 (1994) 549
[78] J.C. Pivin, *Mater. Sci. Engineer*. A293 (2000) 30
[79] J.C. Pivin, M.A. Garcia, H. Hofmeister, A. Martucci, , M. Sendova-Vassileva, M. Nikolaeva, O. Kaitasov, , and J. Lllopis, *European Physical Journal* D 20 (2002) 251.
[80] Cohen, A. Benyagoub, H. Bernas, J. Chaumont, L. Thomé, M. Berti and A.V. Drigo, *Phys. Rev*. B31 (1986) 5
[81] J.F. Gibbons, Proc. *IEEE* 60 (1972) 1062
[82] J.C. Pivin, *Ann. Chim. Fr*. 11 (1985) 45
[83] L. Thomé, F. Pons, J.C. Pivin, and C. Cohen, *Nucl. Instr. Meth. in Phys. Res*. B 15 (1986) 269
[84] Priolo and E. Rimini, *Mat. Sci. Reports* 5 (1990) 319
[85] E. Glaser, T. Bachmann, R. Sculz, S. Schippel, and U. Richter, *Nucl. Instr. and Meth. in Phys. Res*. B 106 (1995) 281
[86] J. Lohau, A. Moser, C.T. Retner, M.E. Best, and B.D. Terris, *Appl. Phys. Lett*. 78 (2001) 990
[87] P. Chen, A.J. Steckl, *J. Appl. Phys*. 77 (1995) 5616
[88] J. Davenas, *Solid State Commun*. 30-31 (1993) 317
[89] T. Venkatesan, L. Calcagno, B.S. Elman and G. Foti, in *Ion Beam Modification of Insulators* eds. P. Mazzoldi and G.W. Arnold, (Elsevier, Amsterdam, 1987), pp 301
[90] T. Venkatesan, *Nucl. Instr. and Meth*. B7-8 (1985) 461.
[91] E.H. Lee, G.R. Rao, M.B. Lewis, and L.K. Mansur, *J. Mat. Res*. 9 (1994) 1043
[92] J.C. Pivin, P. Viel, G. Zalczer, and G. Marletta, *Nucl. Instr. and Meth. in Phys. Res*. B105 (1995) 185
[93] J.C. Pivin, *Thin Solid Films* 263 (1995) 185
[94] L.T. Chadderton, D. Fink, H.J. Möcker, K.K. Dwivedi, and A. Hammoudi, *Rad. Eff. and Def. in Solids* 127 (1993) 163
[95] Fink, M. Mueller, L.T. Chadderton, P.H. Canning D.C. Ellinman, and D.C. McDonald, *Nucl. Instr. and Meth. in Phys. Res*. B32 (1988) 125
[96] J. Davenas, G. Boiteaux, X.L. Xu , and E. Aden, *Nucl. Instr. and Meth. in Phys. Res*. B32 (1988) 136
[97] Y.Q. Wang, R.E. Giedd, and L.B. Bridwell, *Nucl. Instr. and Meth. in Phys. Res*. B79 (1993) 659
[98] Balanzat, M. Betz, and S. Bouffard, *Nucl. Instr. and Meth. in Phys. Res*. 105 (1995) 46
[99] Marletta, F. Iacona and A. Toth, *Macromolecules* 25 (1992) 319

[100] N. Betz, *Nucl. Instr. and Meth. in Phys. Res*. 105 (1995) 55
[101] J.C. Pivin, and P. Colombo *J. Mat. Sci.* 32 (1997) 6163 and 6175
[102] S.K. Srivastava, D.K. Avasthi and J.C. Pivin, *Nucl. Instr. and Meth.* B 191 (2002) 7185
[103] J.C. Pivin, E. Pippel , J. Woltersdorf, D.K. Avasthi, S.K. Srivastava, Z. *Metallkd.* 92 (2001) 7
[104] J.C. Pivin, P. Colombo and G.D. Soraru, *J. Am. Ceram. Soc*. 83 (2000) 713
[105] J.C. Pivin, P. Colombo, A. Martucci, G.D. Soraru, E. Pippel, and M. Sendova-Vassileva, *J. Sol-Gel Sci. and Technol*. 26 (2003) 251
[106] J.C. Pivin, *Nucl. Instr. and Meth. in Phys. Res*. B216 (2004) 239
[107] G. De Marchi, F. Gonella, P. Mazzoldi, G. Battaglin, E.J. Knytautas, and C. Meneghini, *J. Non-Cryst. Solids* 196 (1996) 79
[108] J.C. Pivin, G. Roger, M.A. Garcia, F. Singh and D.K. Avasthi, *Nucl. Instr. and Meth. in Phys. Res.* B 215 (2004) 373.
[109] Valentin, H. Bernas, C. Ricolleau, and F. Creuset, *Phys. Rev. Lett.* 86 (2001) 99
[110] J.C. Pivin, *Nucl. Instr. and Meth. in Phys. Res*. B195 (2002) 302
[111] D'Orleans, J.P. Stoquert, C. Estournès, C. Cerutti, J.J. Grob, J. L. Guille, F. Haas, D. Muller and M. Richard-Plouet, *Phys. Rev*. B67 (2003) 220101
[112] M. Toulemonde, G. Fuchs, N. Nguyen, F. Studer, D. Groult Phys. Rev. B 35 (1987) 6560
[113] Fnidiki and H. Pascard, *Eur. Phys. J*. B 24 (2001) 291
[114] S. Meillon, F. Studer, M. Hervieu, and H. Pascard, *Nucl. Instr. and Meth. in Phys. Res*. B107 (1996) 363
[115] J.C. Pivin, S. Esnouf, D.K. Avasthi, *Nucl Instr. and Meth*., submitted for publication
[116] Dogra, M. Singh , N. Kumar, P. Sen and R. Kumar, *Nucl. Instr. and Methods in Phys. Res.* 212 (2003) 190
[117] Studer, C. Houpert, D. Groult, J.Y. Fan, A. Meftah and M. Toulemonde, *Nucl. Instr. and Meth. in Phys. Res.* B82 (1993) 91
[118] M. Ghidini, J. P. Nozières, D. Givord , and B. J. Gervais, *Magn. and Magn. Mat*. 140-144 (1995) 483
[119] Wiesner, C. Traeholt, J. G. Wen, H. W. Zandbergen, G. Wirth , and H. Fuess, *Physica* C268 (1996) 161
[120] N.M. Dempsey, *Phys Rev Lett* 81-25 (1998) 5652
[121] Krauser, J.H. Zollondz, A. Weidinger, and C.Trautmann, *J. Appl. Phys.* 94 (2003) 1959
[122] R. Spohr, in *Ion Tracks and Microtechnology. Basic Principles and Applicatio*ns ed. K. Bethge, (Vieweg ,1990)
[123] D.K. Avasthi, *Current Science* 78 (2000) 1299
[124] E. Ferain, and R. Legras, *Nucl. Instr. Meth. in Phys. Res.* B174 (2001) 116
[125] M. E. Toimil Molares, E. M. Hohberger, C. Schaeflein, R. H. Blick, R. Neumann, and C. Trautmann, *Appl. Phys. Lett*. 82 (2003) 2139
[126] S.K. Chakarvati, and J. Vetter, *J. Rad. Measur*. 29 (1998) 149.
[127] Fink, *J. Phys*. 25 (1995) 54
[128] Fink, *Rad. Eff. and Def. in Solids* 140 (1997) 263
[129] Biswas, D.K. Avasthi, B. K. Singh, . S. Lotha, J.P. Singh, D. Fink, B.K. Yadav, B. Bhattacharya, and S.K. Bose, *Nucl. Instr. and Meth. in Phys. Res*. B 151 (1999) 84.
[130] Vetter, and D. Dobrev, *Nucl. Instr and Meth. in Phys. Res*. B62 (1999) 109
[131] M.S. Gudiksen, J. Wang, and C.M. Lieber, *J. Phys. Chem.* B106 (2002) 4036

[132] J.D. Klein, R.D. Herrick, D. Palmer, M.J. Sailor, C.J. Brumlik, and C.R. Martin, *Chem. of Mat.* 5 (1993) 902

[133] Piraux, J. M. George, J. F. Despres, C. Leroy, E. Ferain, R. Legras, K. Ounadjela and A. Fert , *Appl. Phys. Lett*. 65 (1994) 2484.

APPENDIX : BASIC FORMULA OF ION STOPPING

1- The energies of recoil E_2 and scattered particle E_1 after an elastic collision in laboratory frame are given by following formula:

$$E_2 = \frac{4M_1M_2}{(M_1+M_2)^2} E_0 \cos^2\zeta = \gamma E_0 \cos^2\zeta \quad (8)$$

$$E_1 = \frac{M_1^2}{(M_1+M_2)^2} \left[\cos\psi + \left(\frac{M_2}{M_1}\right)^2 - \sin^2\psi\right]^2 E_0 \quad (9)$$

$$\sin\zeta = \left(\frac{M_1E_1}{M_2E_2}\right)^{1/2} \sin\psi \quad (10)$$

where ζ is the recoil angle and ψ the scattering of the projectile The scattering factor k, useful for instance in Rutherford backscattering formula, is defined as the ratio of E_1/E_0 and $E_2=(1-k)E_0$

2-Calculation of the nuclear scattering cross section:

Assuming that the force between the 2 particles act only along the line joining them, the use of center of mass (CM) coordinates reduces the problem to a one-body problem, namely the interaction of a particle with mass M_{CM} (or μ) and velocity v_{CM} with a static potential field V(r) centered at the origin of the CM coordinates. This is because the total linear momentum of the particles is always zero in this frame.

$$\frac{1}{\mu} = \frac{1}{M_1} + \frac{1}{M_2} \quad (11)$$

$$E_{CM} = \frac{1}{2}\mu v_0^2 = E_0 \frac{M_2}{M_1+M_2} \quad (12)$$

The scattering angle of the projectile in this frame is a function of the impact parameter p (projected offset of the original path of the projectile (1) from the atom at rest (2)):

$$\theta = \pi - 2\int_{r_{min}}^{\infty} \frac{pdr}{r^2\left[1-\frac{V(r)}{E_{CM}}-\frac{p^2}{r^2}\right]^{1/2}} \quad (13)$$

The transferred energy E_2, also noted T, is equal to :

$$T = \gamma E_0 \sin^2 \frac{\theta}{2} \tag{14}$$

The choice of a proper interaction potential V(r) during the collision is needed for calculating values of θ(p) and T(p) used in transport equations or Monte Carlo simulations of ion impacts and the value of energy transferred per unit length of the ion path, S_n, averaged over all impact parameters p. This potential is of the form:

$$V(r) = \frac{Z_1 Z_2 e}{r} \Phi(\frac{r}{a}) \tag{15}$$

where Φ(r) is a screening function and a is a characteristic screening lenght . The unscreened potential of Rutherford collisions is valid for short r (energetic collisions). The earliest screening functions proposed by Bohr and Thomas-Fermi are:

$$\Phi_B = \exp(-x) \qquad \text{and } \Phi_{TF} = [1+(\frac{x^3}{144})^{1/3}]^{-2.4} \tag{16}$$

x being a reduced approach radius =r/a , with

$$a_B = \frac{a_0}{Z} = \frac{\hbar^2}{me^2}\frac{1}{Z} \text{ and } a_{TF} = \frac{1}{2}(\frac{3\pi}{4})^{2/3} a_0 \frac{1}{Z} \tag{17}$$

In these expressions Z is the charge of the quasi-molecule formed during the overlap of electron shells and a_0 (0.0528 nm) is the Bohr radius. Different averaging were proposed by Bohr and Thomas-Fermi:

$$Z_B = (Z_1^{2/3} + Z_2^{2/3})^{1/2} \text{ and } Z_{TF} = (Z_1^{1/2} + Z_2^{1/2})^{2/3} \tag{18}$$

Lindhard used the a_{TF} expression with the Bohr equation for Z. On basis of Hartree-Fock-Slater calculations for a large number of quasi molecules, a universal potential is now used in most calculations:

$$\Phi_u = 0.1818\, e^{-3.2x} + 05099\, e^{-0.9423x} + 0.2802\, e^{-0.4028x} + 0.0282\, e^{-0.202x} \tag{19}$$

$$\text{with } a_u = \frac{0.8854\, a_0}{(Z_1^{0.23} + Z_2^{0.23})} \tag{20}$$

For being able to give universal expressions of the scattering angle θ as a function of the impact parameter p, it is useful to normalize p to a, as also the center of mass energy E_{CM} and the range R of the projectile:

$b=p/a$, (21a)

$$\varepsilon=E_{CM}\frac{a}{(Z_1 Z_2 e^2)} \quad (21b)$$

$$\rho = \quad N \pi a_U^2 \gamma R_. \quad (21c)$$

N being the atomic density. Finally, the nuclear stopping power (energy lossed by the projectile per unit depth in nuclear collisions), $S_n(\varepsilon)$, is the integrated product of the transferred energy $T(E_0, p)$ in each collision by the probability $d\sigma(p)$ for a collision with an impact parameter p. σ is the impact cross section πp^2:

$$S_n(E_0) = \int_0^\infty T d\sigma = \int_0^\infty T(E_0, p)\, 2\pi p\, dp = 2\pi\, T_{max}\, E_0 \int_0^{p\,max} \sin^2\frac{\theta}{2}\, p\, dp \quad (22a)$$

or in reduced units:

$$S_n(\varepsilon) = \varepsilon \int_0^\infty \sin^2\frac{\theta}{2} d(b^2) \quad (22b)$$

Calculations with the universal potential were fitted by an analytic expression with the form:

$$S_n(\varepsilon) = \frac{Ln(a + b\varepsilon}{2(\varepsilon + c\varepsilon^d + e\varepsilon^{0.5})} \quad (23)$$

in which a=1, b=1.14, c=0.01, d=0.21, e=0.20 for $\varepsilon<30$, a=0, b=1.0, c=d=e=0 for $\varepsilon>30$ (i.e. case of unscreened stopping)

3- Calculation of the electronic stopping power $S_e(\varepsilon$ or E):

The earliest expression proposed in the 1930's for the energy loss per unit lenght of slow particles in an electron plasma is the product of the ion velocity, v, by the cube root of the electronic density of the medium, N_e. Lindhard introduced a stopping interaction function $I(v,N_e)$ taking into account local density fluctuation of ρ_e and the perturbation of this density by the ion (individual and collective excitations):

$$S_e = \int I(v, \rho_e)\, Z_1^2\, N_e \quad dV \quad (24)$$

V being the volume of each element of the target. S is a flat function when the ion is going much faster than the mean electron density and it decreases almost linearly with N_e when $v<v_F$, $v_F$being the Fermy velocity:

$$v_F = (\frac{\hbar}{m_e})\,(3\pi^2 N_e)^{1/3} \quad (25)$$

Low velocity ions are neutralized when penetrating in the target and their stopping power is:

$$S_e = 8\pi N e^2 a_0 Z_1^{1/6} \frac{Z_1 Z_2}{(Z_1^{2/3} + Z_2^{2/3})^{3/2}} \frac{v_0}{v_B} \quad (26)$$

which is proportional to $N_e^{1/3}$ as v_0. High velocity ions ares stripped of all electrons whose classical orbital velocities are less than the ion velocity. Their effective charge is γZ_1 with:

$$\gamma = 1 - \exp - \frac{v_0}{v_B Z_1^{2/3}} \quad (27)$$

where v_B is the Bohr velocity of H electrons. For $v_0 >> v_B Z_1^{2/3}$, S_e is proportional to $1/E_0$ and Z_2. The Bethe expression for S_e corrected for the partial stripping of electrons at intermediate energies and for the change of density and mass at relativistic energies is:

$$S_e = \frac{4\pi Z_2 Z_1^2 e^4}{m_e v_0^2} \left[\mathrm{Ln}\left(\frac{2 m_e v_0^2}{I}\right) - \mathrm{Ln}\left(1 - \frac{v_0^2}{c^2}\right) - \frac{v_0^2}{c^2} - \frac{c}{Z_2} - \frac{\delta}{2} \right] \quad (28)$$

with a mean ionization and excitation energy I of target atoms: $I \approx 10\mathrm{eV} \times Z_2$

In: Nanomaterials: New Research
Editor: B.M. Caruta, pp. 115-128
ISBN: 1-59454-369-0

Chapter 3

NANOSTRUCTURED SnO_2: TiO_2 COMPOSITE AND BILAYERED THIN FILMS: HUMIDITY SENSOR

Weon-Pil Tai
Institute of Advanced Materials, Inha University,
Yonghyun-dong, Nam-ku, Inchon 402-751, South Korea

ABSTRACT

The nanostructured SnO_2:TiO_2 composite and bilayered thin films are prepared using a sol-gel process by spin coating onto the alumina substrate and the humidity sensitive properties of the films are investigated. The nanostructured films possess the grain size of nanometer order and have porous structures with capillary nanopores. The nanostructured films facilitate the adsorption of water vapors due to the large surface area and capillary nanopores. The TiO_2-20 wt.% SnO_2 composite film shows high sensitivity over three orders change in the resistance during the relative humidity variation from 30 to 90%. The SnO_2/TiO_2 bilayered film exhibits a better linearity with narrower hysteresis loop in the resistance variation for relative humidity than the SnO_2 and TiO_2 monolayered films. The humidity sensing properties in the nanostructured SnO_2:TiO_2 composite and bilayered films are discussed.

1. INTRODUCTION

Humidity sensors have found increasing application with the advancement of automation systems. Materials as humidity sensors include ceramic, polymer and composite. The ceramic humidity sensors based on porous and sintered oxides compared with other materials have received much attention due to their chemical and physical stability [1-4]. Furthermore, the humidity sensors of thin film types having the nano-sized grains and nanoporous structure have attracted considerable interest because the miniaturization of the sensing devices is

possible [5, 6]. Nanostructured films are optimal candidates for humidity sensing because of the high surface area of sensing element that facilitates the adsorption of water molecules.

SnO_2 and TiO_2 thin films have been fabricated using a variety of techniques, such as, sputtering [7], chemical vapor deposition [8, 9], pulsed laser deposition [10, 11], laser molecular-beam epitaxy method [12], spray pyrolysis technique [13], ion implantation [14], and sol-gel process [15-18], etc. The sol-gel process has distinct advantages over the other techniques due to excellent compositional control, homogeneity on the molecular level due to the mixing of liquid precursors, and lower crystallization temperature. Moreover, the microstructural properties, i.e., the pore size, pore volume and surface area of the thin film can be tailored by the control of sol-gel processing variables [19]. In this regard, the TiO_2 thin films prepared by sol-gel process have been found to be extremely wide and important applications in many fields, such as humidity sensors, gas sensors, photocatalysis and dye-sensitized solar cells [20-24]. The addition of alkali ions to TiO_2 improved the performance of humidity sensors, in which charge carriers were alkali ions instead of surface protons [25, 26]. SnO_2 is a well-known material exhibiting exceptional gas sensing property as well as the humidity sensing behavior [4, 17, 18, 27]. Thus, nanocrystalline and nanoporous SnO_2:TiO_2 composite and bilayered thin films are prepared by sol-gel process and the composite and bilayered thin films have been tried to be applied as a new humidity sensor.

In this paper, nanostructured SnO_2:TiO_2 composite and bilayered thin films were prepared using a sol-gel process by spin-coating onto the alumina substrate. Nanostructured SnO_2 and TiO_2 monolayered thin films were also prepared in identical manner for direct comparison. The humidity sensitive properties of the nanostructured SnO_2:TiO_2 composite and bilayered thin films were investigated. The variation of resistance was studied as a function of relative humidity (RH).

2. EXPERIMENTAL DETAILS

2.1. Synthesis

SnO_2 coating solution was prepared by the following procedure. Tin chloride pentahydrate ($SnCl_4 \cdot 5H_2O$, Wako pure chemical) was dissolved in ethanol (0.4 M). The solution was stirred and then refluxed for 3h. The solution was finally aged at room temperature for 10 days. In order to synthesize SnO_2 colloidal solution for the composite films, an 5.5 M aqueous ammonia solution (Wako pure chemical, 25~27.9%) was added dropwise to a refluxed solution and the resulting precipitate was washed thoroughly with deionized water. Finally, SnO_2 colloidal solution was prepared by adding deionized water.

TiO_2 colloidal solution was prepared as follows. 150 ml of titanium tetraisopropoxide ($Ti(C_3H_7O)_4$, Wako pure chemical, 95%) was rapidly added to 270 ml of deionized water. The resulting precipitate was washed with deionized water. The precipitate cake was transferred into a well-sealed autoclave vessel containing 0.5 M tetramethylammonium hydroxide solution ($(CH_3)_4NOH$), Aldrich). Peptization occurred after heating at 110°C for 6h. The suspension which resulted from peptization was treated hydrothermally in the autoclave at 190°C for 6h. TiO_2 coating solution was prepared as follows. TiO_2 colloidal solution of 6g (18.1 wt% TiO_2) and commercial TiO_2 (Nippon Aerosil, P25) of 0.08g was

ground in a mortar. A detergent (Triton X-100) of 20 μ L was added to facilitate the spreading of the colloid on an alumina substrate. Polyethylene glycol(PEG 20000) of 0.35g was added to make porous film, which facilitate the adsorption of water molecules. Finally, the colloid was diluted by the addition of ethanol (3mL). TiO_2-SnO_2 composite coating solutions were prepared by adding SnO_2 colloidal solution to TiO_2 colloidal solution for each ratio.

2.2. Preparation of Thin Films

The inter-digital Ag electrodes are screen printed on polycrystalline alumina (Al_2O_3) substrate of 10 mm x 10 mm x 0.5mm. TiO_2-SnO_2 composite thin films were deposited by spin coating onto the inter-digital Ag electrodes for humidity sensing measurement, and the schematic diagram is shown in Fig. 1. The spin coating was performed at room temperature, with a rate of 3000rpm. TiO_2/SnO_2 (T/S, SnO_2 on TiO_2) and SnO_2/TiO_2 (S/T) bilayered thin films were deposited in identical manner. After deposition, the films were annealed in air at 500°C for 30min, at a heating rate of 5°C /min. SnO_2 (S) and TiO_2 (T) monolayered thin films were also prepared in identical manner for direct comparison with the composite and bilayered films.

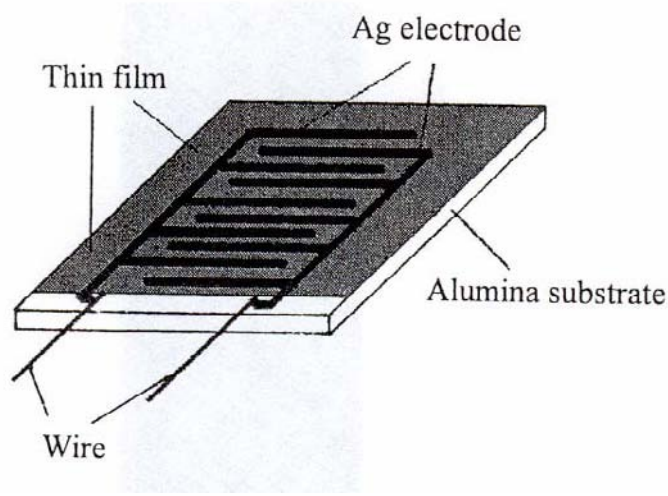

Figure 1. Schematic diagram of humidity sensor.

2.3. Measurements and Analyses

The surface and cross section of thin films were observed by scanning electron microscope (SEM, Hitachi S-4200). The thickness of the films was evaluated from SEM images of the cross section of the films. X-ray diffraction (XRD, Philips X-PERT-MPP, DY 616) analyses of the films were conducted using CuK_α radiation to determine the phases and the crystallite size. The crystallite size was calculated from the full width at half maximum (FWHM) of the first peak using the Scherrer formula [28].

To measure the relative humidity characteristics, the sensor element was placed into a 2 neck glass flask, partially filled with water. The relative humidity inside the glass flask was varied using an ice-salt mixture placed outside the glass flask, which was placed in a chamber and the basic measurement was performed using the two temperature method [29]. The relative humidity value was calculated from the saturated vapor pressure, i.e., the sample and water noted during experimental process. The values of saturated vapor pressure were obtained from CRC handbook [30]. The electrical resistance of the films was measured using a programmable Keithley 617 electrometer at room temperature.

3. RESULTS AND DISCUSSION

3.1. TiO_2-SnO_2 Composite Thin Films

3.1.1. Characteristics of Composite Films

Nanostructured TiO_2-SnO_2 composite thin films were prepared using sol-gel process by spin coating on polycrystalline alumina substrate. All the films were annealed at 500°C for 30min. The films were transparent and semiconducting in nature. Fig. 2 shows the SEM images of TiO_2 and TiO_2-SnO_2 thin films. The SEM image reveals that the surfaces of TiO_2-SnO_2 composite films are more rough than that of TiO_2 monolayered film, which may be due to a slight agglomeration by mixtures of both SnO_2 and TiO_2 colloids. The films possess nano-sized grains and nanoporous structure. It means that such nanostructured films are likely to facilitate the adsorption process of water vapors because of the capillary nanopores and large surface area.

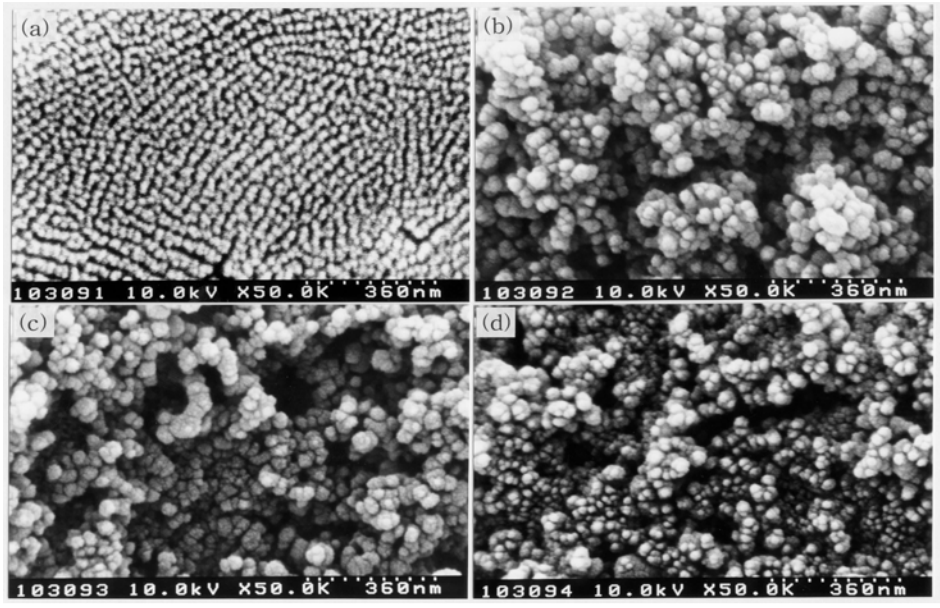

Figure 2. SEM micrographs for TiO_2-SnO_2 films: (a) TiO_2, (b) TiO_2-5 wt.% SnO_2, (c) TiO_2-20 wt.% SnO_2 and (d) TiO_2-40 wt.% SnO_2.

XRD studies were carried out on the TiO_2-SnO_2 thin films to characterize the film crystal structure. Subsequently, the crystallite size was calculated from the Scherrer formula [28]:

$$D = k \lambda /(B \cos \theta)$$

where D is the crystallite size, k, a fixed number of 0.9, λ, the X-ray wavelength, θ, the Bragg's angle in degrees, and B, the full width at half maximum of the first peak.

The average size of crystallites for the TiO_2-SnO_2 composite films with 5, 20 and 40 wt.% SnO_2 content is 13.1, 12.5, and 11.6 nm, respectively. While, it is 10.8 nm for the pure TiO_2 film. The crystallite size for the TiO_2-SnO_2 composite films is nearly same, which have no large change by adding SnO_2 and exhibits a similar tendency as obtained from SEM micrographs shown in Fig. 2. The TiO_2 phase in the TiO_2-SnO_2 composite films measured by XRD technique is anatase, containing a small amount of rutile. Further, no second phases formed in the TiO_2-SnO_2 composite films except TiO_2 and SnO_2.

The thickness of the TiO_2 and TiO_2-SnO_2 films on alumina substrate was measured by identifying the cross section in the SEM images. The films were deposited well on the alumina substrate without any microcracks. The thickness of the TiO_2-SnO_2 films with 0, 5, 20 and 40 wt.% SnO_2 content was 480, 460, 540 and 560 nm, respectively.

3.1.2. Humidity Sensing Properties of Composite Films

Fig. 3 shows the variation of resistance as a function of the relative humidity for the TiO_2-SnO_2 composite thin films. The resistance of the films slightly decreases with increasing SnO_2 content over almost all relative humidity range. The resistance variation on the relative humidity shows almost similar behavior, i.e., the resistance of the films decreases linearly with increasing relative humidity with about three orders change in the resistance during the relative humidity variation of 30 to 90%, exhibiting a good exponential relationship. In particular, the resistance of TiO_2-20 wt.% SnO_2 composite film decreases largely with increasing 30 to 90% in the relative humidity, showing very high sensitivity.

In the electrical properties for the relative humidity, the nanostructured TiO_2-SnO_2 thin films responded quickly to exposure of the water vapor atmosphere. The response time for the TiO_2-SnO_2 films with 0, 5, 20 and 40 wt.% SnO_2 content was 5, 6, 15 and 20 seconds, respectively, at 70% relative humidity. The shorter response time in the films with decreased SnO_2 content, i.e., increased TiO_2 content seems due to hydrophilic property of TiO_2 [31-33]. The ceramic humidity sensors consisting of nano-sized grains and nanopores were found to be quite stable for about 3h at 60% relative humidity atmosphere.

A large decrease in resistance with increasing relative humidity in the nanostructured ceramic films is related to the adsorption of water vapors on the film surfaces with large surface area and capillary nanopores. All the films have nano-sized grains and nanopores. The addition of SnO_2 to TiO_2 produces more rough surfaces with the capillary nanopores of wide distribution. The nano-sized grains having more rough surfaces result in a larger surface area. The nanoscaled grain size leads to many more grain boundaries and nanopores, leading to more active sites available for condensed water to react [34]. The higher surface area provides

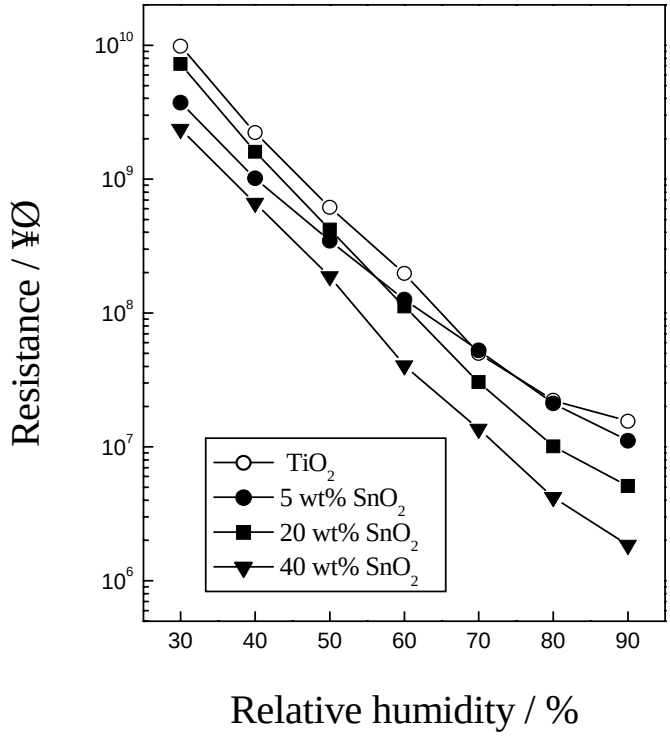

Figure 3. Humidity sensing properties for TiO_2-SnO_2 composite thin films.

more sites for water adsorption [35]. Fig. 4 shows the adsorption-desorption behaviors for the TiO_2 and TiO_2-40 wt.% SnO_2 films. The TiO_2-40 wt.% SnO_2 composite film exhibited narrower hysteresis loop than TiO_2 film. The narrower hysteresis loop indicates the facility of adsorption and desorption process of water vapor.

The TiO_2-SnO_2 composite films show a linearly large decrease in resistance with relative humidity. It is very likely that the increased conduction phenomenon with increasing relative humidity is due to an increase in the number of adsorbed water vapors in the nanostructured films with the capillary nanopores of wide distribution. Gusmano et al. [20] observed in compact and low-porosity TiO_2 film prepared by sol-gel process that the resistance variation was small during the relative humidity variation of 5% to 50%, whereas it exhibited a good exponential relationship for the higher relative humidity range of 50 - 85%. Porous materials with a wide pore-size distribution exhibit a better sensitivity even at low relative humidity [36]. The water vapors can be occupied more easily on nano-sized grain than large-sized grain. The water vapors adsorbed on the nanostructured film surface enhance electrolytic conduction as well as protonic conduction by permitting capillary condensation of water within the pores [37, 38]. The high humidity sensitivity of TiO_2-SnO_2 composite films at low and high relative humidity seems due to the protonic and electrolytic conduction between hydroxyl ions and water molecules adsorbed on the film surfaces with nano-sized grain and capillary nanopores.

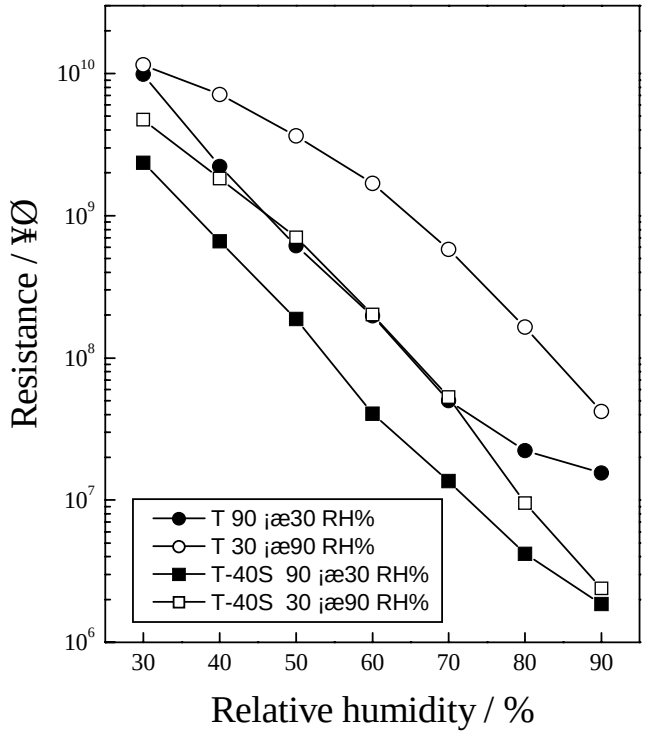

Figure 4. Adsorption and desorption behaviors for TiO_2 and TiO_2-40 wt.% SnO_2 Films.

3.2. SnO_2:TiO_2 Bilayered Thin Films

3.2.1. Characteristics of Bilayered Films

Nanostructured SnO_2:TiO_2 bilayered thin films were prepared using sol-gel process by spin coating on polycrystalline alumina substrate. Fig. 5 shows the SEM micrographs for TiO_2/SnO_2 and SnO_2/TiO_2 bilayered thin films. Here, the SnO_2/TiO_2 bilayered film indicates a upper TiO_2 layer on a lower SnO_2 layer. The films possess the grain size of nanometer order and have nanoporous structure. The films also have capillary nanopores connected by nanopores. Such structure of films facilitates the adsorption of water vapors due to the large surface area and capillary nanopores.

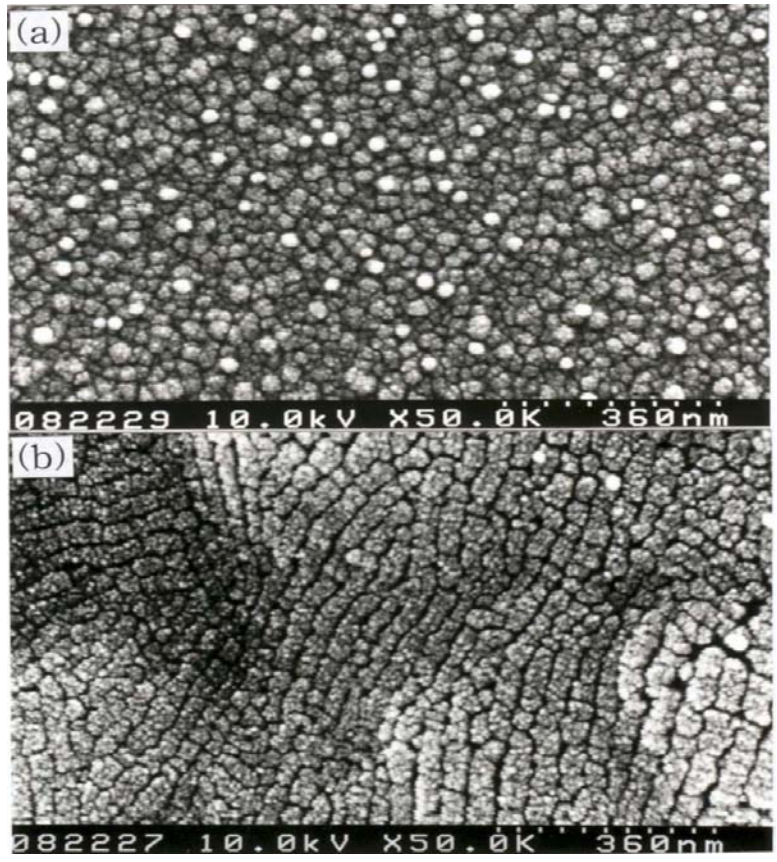

Figure 5. SEM micrographs for bilayered thin films: (a) TiO_2/SnO_2 and SnO_2/TiO_2.

The crystallite size for the TiO_2/SnO_2 and SnO_2/TiO_2 bilayered films calculated from the Scherrer formula [28] was 7.6 and 11.5 nm, respectively. While, it was 7.9 and 10.8 nm for the SnO_2 and TiO_2 monolayered films. The crystallite size of same surface phases in the monolayered and bilayered films was nearly same and exhibits a similar tendency as obtained from SEM micrographs shown in Fig. 5. The phases in the SnO_2 and TiO_2 monolayered films measured by XRD technique were polycrystalline SnO_2 and anatase TiO_2 having tetragonal structure. The phases in the TiO_2/SnO_2 bilayered films were SnO_2, containing a small amount of anatase TiO_2. The phases in the SnO_2/TiO_2 bilayered films were anatase TiO_2, containing a small amount of SnO_2.

The thickness of the SnO_2:TiO_2 monolayered and bilayered films on alumina substrate was measured by identifying the cross section in the SEM images, as shown in Fig. 6. The films were deposited well on the alumina substrate. The thickness of the SnO_2 and TiO_2 monolayered films was 500 and 480 nm, respectively. While, the thickness of the TiO_2/SnO_2 and SnO_2/TiO_2 bilayered films was 620 and 635 nm, respectively. The thickness for each monolayered and bilayered films is nearly same, respectively.

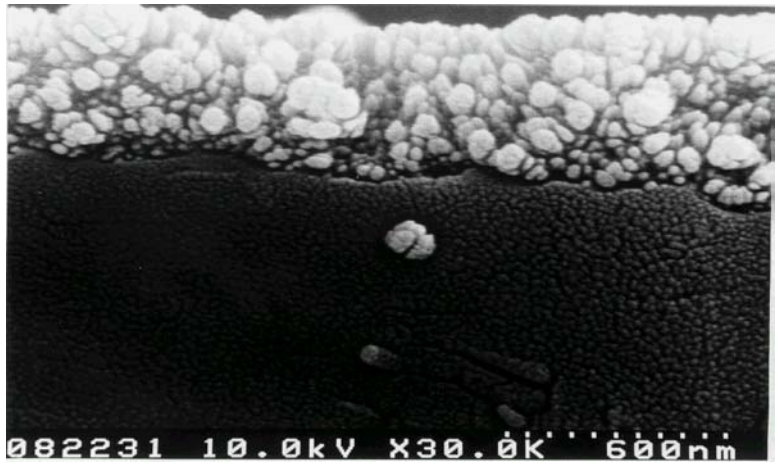

Figure 6. Cross sectional view for SnO_2 film.

3.2.2. Humidity Sensing Properties of Bilayered Films

Fig. 7 shows the variation of resistance as a function of the relative humidity for the SnO_2(S), TiO_2(T), TiO_2/SnO_2(T/S) and SnO_2/TiO_2(S/T) thin films. The resistance of TiO_2 film was higher than that of SnO_2 film in the relative humidity range from 30 to 60% and a reversed behavior was observed for the higher relative humidity. The resistance of the bilayered films decreased almost linearly with increasing relative humidity as compared to the monolayered films, exhibiting a good exponential relationship. In particular, the SnO_2/TiO_2 bilayered film showed high sensitivity with nearly three orders change. Further, the TiO_2/SnO_2 bilayered film exhibited a better linearity in the resistance variation for relative humidity than monolayered SnO_2 film. In the SnO_2 monolayered film, the resistance-relative humidity variation showed low sensitivity with a nonlinearity in the relative humidity range from 60 to 90%.

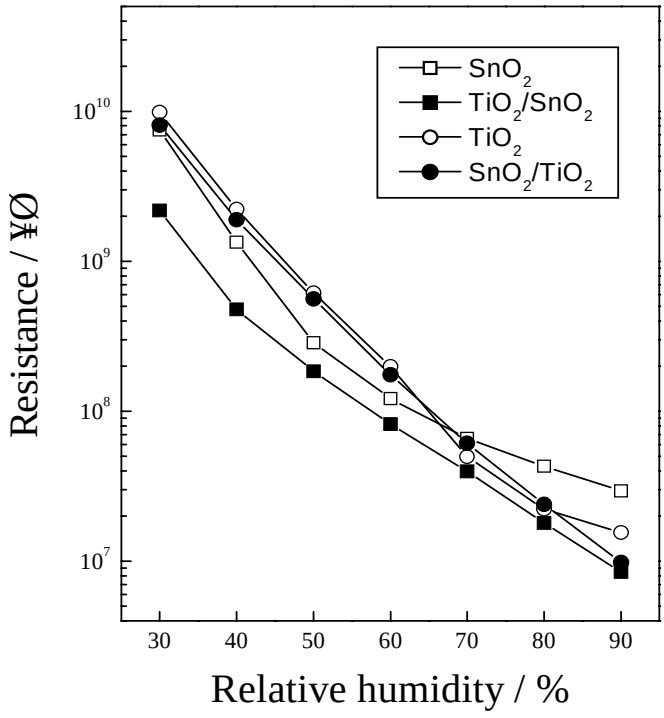

Figure 7. Humidity sensing properties for SnO_2:TiO_2 mono- and bi-layered films.

Fig. 8 shows the adsorption-desorption behaviors for SnO_2 and TiO_2/SnO_2 films. The TiO_2/SnO_2 bilayered film exhibited narrower hysteresis loop than SnO_2 monolayered film. The improved linearity with narrower hysteresis loop means the facility of adsorption and desorption process of water vapors and hence the sensitivity is increased. The hysteresis loop of SnO_2/TiO_2 bilayered film also was narrower than that of TiO_2 film. The SnO_2:TiO_2 humidity sensors consisting of nano-sized grains and nanopores were stable for minimum 3 h at 60% relative humidity.

The SnO_2/TiO_2 and TiO_2/SnO_2 bilayered films showed improved linearity and larger decrease in resistance with increasing relative humidity than the SnO_2 and TiO_2 monolayered films. The large decrease in resistance with increased relative humidity is related to the adsorption of water vapors on the nanostructured film surfaces having the nano-sized grains and capillary nanopores. The water vapors are adsorbed on the grain surface and in the nanopores. The water vapors also can be occupied more easily on nano-sized grains than large-sized grains. The nanoscaled grains lead to many more grain boundaries and nanopores, thus leading to more active sites available for condensed water to react [34]. The higher surface area provides more sites for the adsorption of water vapors and produces more charge

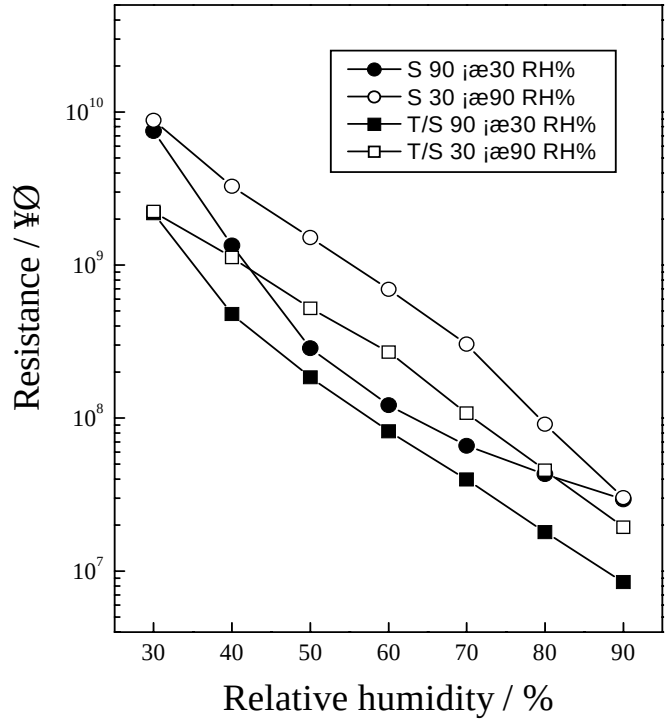

Figure 8. Adsorption and desorption behaviors for SnO_2 (S) monolayered and TiO_2/SnO_2 (T/S) bilayered films.

carriers for electrical conduction [35]. Further, TiO_2 have hydrophilic property [31, 32]. Thus, the resistance of TiO_2 film with relative humidity is lower than that of SnO_2 film at higher relative humidity, even though the resistivity of TiO_2 is higher than that of SnO_2. Moreover, the SnO_2/TiO_2 bilayered film was first deposited SnO_2 on alumina substrate containing Ag electrode and then TiO_2 was deposited on a lower porous SnO_2. Thus, the bilayered SnO_2/TiO_2 film of different chemical compositions may have more porous with capillary nanopores than monolayered SnO_2 and TiO_2 films, in which the lower film layer acts as a buffer layer. It means that the adsorption-desorption process of water vapors occurs more easily in the SnO_2/TiO_2 bilayered film. Niranjan et al. [39] showed that a tandem of nanoscale thin film of ZrO_2 on SnO_2 film minimises the hysteresis loop. The nanostructured SnO_2/TiO_2 and TiO_2/SnO_2 bilayered films exhibited improved linearity with narrower hysteresis loops compared to the SnO_2 and TiO_2 monolayered films, due to the large surface area and capillary nanopores. At higher relative humidity, the water vapors adsorbed on the nanostructured-bilayered film having nano-sized grains and capillary nanopores enhance the electrolytic conduction as well as the protonic conduction by permitting capillary condensation of water molecules within the pores [37, 38, 40].

4. CONCLUSIONS

Nanostructured SnO_2:TiO_2 composite and bilayered thin films were prepared using a sol-gel process by spin coating onto the alumina substrate and investigated for the application as a new humidity sensor. Nanostructured SnO_2 and TiO_2 monolayered thin films were also synthesized in identical manner for direct comparison. The films possess nano-sized grains and nanoporous structure, which facilitate the adsorption process of water vapors. The TiO_2-20 wt.% SnO_2 composite film exhibits the highest sensitivity for the humidity, which shows over three orders change in the resistance during the relative humidity variation of 30 to 90%. The SnO_2:TiO_2 bilayered films exhibit better linearity with narrower hysteresis loop in the resistance variation for relative humidity than the SnO_2 and TiO_2 monolayered films. In particular, the SnO_2/TiO_2 bilayered film shows high sensitivity with nearly three orders change in the resistance during the relative humidity variation of 30 to 90%. A humidity sensor with high sensitivity and good linearity could be developed from low-cost SnO_2:TiO_2 composite and bilayered films prepared by sol-gel spin-coating method.

REFERENCES

[1] Nitta, T., Terada, Z., & Hayakawa, S. (1980). Humidity-sensitive electrical conduction of $MgCr_2O_4$-TiO_2 porous ceramics. *J.Am.Ceram.Soc*., 63, 295-300.

[2] Shimizu, Y., Shimabukuro, M., Arai, H., & Seiyama, T. (1985) Enhancement of humidity sensitivity for perovskite types oxides having semiconductivity. *Chem.Lett*., 7, 917-920.

[3] Yeh, Y.-C., Tseng, T.-Y., & Chang, D.-A. (1990) Electrical properties of TiO_2-$K_2Ti_6O_{13}$ porous ceramic humidity sensor. *J.Am.Ceram.Soc.*, 73, 1992-98.

[4] Fagan, J.G., & Amarakoon, V.R.W. (1993) Reliability and reproducibility of ceramic sensors: Part III, Humidity sensors. *Am.Ceram.Soc.Bull*., 72 119-130.

[5] Wu, Q., Lee, K.M., & Liu, C.C. (1993) Development of chemical sensors using microfabrication and micromachining techniques. *Sensors and Actuators* B, 13, 1-6.

[6] Rittersma, Z.M. (2002) Recent achievements in miniaturised humidity sensors- a review of transduction techniques. *Sensors and Actuators A*, 96, 196-210.

[7] Chow, L.L.W., Yuen, M.M.F., Chan, P.C.H., & Cheung, A.T. (2001) Reactive sputtered TiO_2 thin film humidity sensor with negative substrate bias. *Sensors and Actuators B*, 76, 310-315.

[8] Tuan, A., Yoon, M., Medvedev, V., Ono, Y., Ma, Y., & Rogers Jr, J.W. (2000) Interface control in the chemical vapor deposition of titanium dioxide on silicon(100). *Thin Solid Films*, 377-378. 766-771.

[9] Kang, B.-C., Lee, S.-B., Boo, & J.-H. (2000) Growth of TiO_2 thin films on Si(100) substrates using single molecular precursors by metal organic chemical vapor deposition. *Surface and Coatings Technology*, 131, 88-92.

[10] Liu, X., Yin, J., Liu, Z.G., Yin, X.B., Chen, G.X., & Wang, M. (2001) Structural characterization of TiO_2 thin films prepared by pulsed laser deposition on GaAs(100) substrates. *Applied Surface Science* ,174, 35-39.

[11] Suda, Y., Kawasaki, H., Ueda, T., & Ohshima, T. (2004) Preparation of high quality nitrogen doped TiO_2 thin films as a photocatalyst using a pulsed laser deposition method. *Thin Solid Films*, 453-454, 162-166.

[12] Ong, C.K., & Wang, S.J. (2001) In situ RHEED monitor of the growth of epitaxial anatase TiO_2 thin films. *Applied Surface Science*, 185, 47-51.

[13] Abou-Helal, M.O., & Seeber, W.T. (2002) Preparation of TiO_2 thin films by spray pyrolysis to be used as a photocatalyst. *Applied Surface Science*, 195, 53-62.

[14] Zheng, S.K., Wang, T.M., Hao, W.C., & Shen, R. (2002) Improvement of photocatalytic activity of TiO_2 thin film by Sn ion implantation. *Vacuum*, 65, 155-159.

[15] Tang, H., Prasad, K., Sanjines, R., & Levy, F. (1995) TiO_2 anatase thin films as gas sensors, *Sensors and Actuators B*, 26-27, 71-75.

[16] Garzella, C., Comini, E., Tempesti, E., Frigeri, C., & Sberveglieri, G. (2000) TiO_2 thin films by a novel sol-gel processing for gas sensor application, *Sensors and Actuators B*, 68, 189-196.

[17] Rella, R., Serra, A., Siciliano, P., Vasanelli, L., De, G., & Licciulli, A. (1997) CO sensing properties of SnO_2 thin films prepared by the sol-gel process, *Thin Solid Films*, 304, 339-343.

[18] Racheva, T.M., & Critchlow, G.W. (1997) SnO_2 thin films prepared by the sol-gel process, *Thin Solid Films*, 292, 299-302.

[19] Brinker, C.J., & Scherer, G.W. *Sol-Gel Science: The Physics and Chemistry of Sol-Gel Processing, Academic press*, New York, 1990.

[20] Gusmano, G., Montesperelli, G., Nunziante, P., Traversa, E., Montenero, A., Braghini, M., Mattogno, G., & Bearzotti, A. (1993) Humidity-sensitive properties of titania films prepared using the sol-gel process, *J.Ceram.Soc.Jpn*., 101, 1095-1100.

[21] Li, Y., Wlodarski, W., Galatsis, K., H.Moslih, S., Cole, J., Russo, S., & Rockelmann, N. (2002) Gas sensing properties of p-type semiconducting Cr-doped TiO_2 thin films. *Sensors and Actuators B*, 83, 160-163.

[22] Guillard, C., Beaugiraud, B., Dutriez, C., Herrmann, J.-M., Jaffrezic, H., Jaffrezic-Renault, N., & Lacroix, M. (2002) Physicochemical properties and photocatalytic activities of TiO_2-films prepared by sol-gel methods. *Applied Catalysis B: Environmental*, 39, 331-342.

[23] O'Regan, B., & Gratzel, M. (1991) A low-cost, high-efficiency solar cell based on dye-sensitized colloidal TiO_2 films. *Nature*, 353, 737-739.

[24] Tai, W.-P., Inoue, K., & Oh, J.-H. (2002) Ruthenium dye-sensitized SnO_2/TiO_2 coupled solar cells, *Solar Energy Mat. & Solar cells*, 71, 553-557.

[25] Traversa, E., Gnappi, G., Montenero, A., Gusmano, G. (1996) Ceramic thin films by sol-gel processing as novel materials for integrated humidity sensors. *Sensors and Actuators B*, 31, 59-70.

[26] Gusmano, G., Bianco, A., Montesperelli, G., & Traversa, E. (1996) An EIS study of the humidity-sensitive electrical conduction of alkali-doped TiO_2 films. *Electrochimica Acta*, 41, 1359-1368.

[27] Arndt, J., Ceramics and Oxides. In: Gopel, W., Hesse, J., Zemel, J.N. In: Grandke, T., Ko, W.H., *Sensors, Fundamentals and General Aspects*. Vol.1, VCH; 1989; p.248.

[28] Cullity, B.D., *Elements of X-ray diffraction.* Addison-Wesley Publishing Company, Inc., London, 1978.

[29] Seiyama, T., Yamazoe, N., & Arai, H. (1983) Ceramic humidity sensors. *Sensors and Actuators*, 4, 85-96.
[30] *Handbook of chemistry and physics*, 60th edition, CRC press, 1979-1980.
[31] Yu, J., Zhao, X., Zhao, Q., & Wang, G. (2001) Preparation and characterization of super-hydrophilic porous TiO_2 coating films. Mater.*Chem.Phys*., 68, 253-259.
[32] Nakamura, M., Makino, K., Sirghi, L., Aoki, T., & Hatanaka, Y. (2003) Hydrophilic properties of hydro-oxygenated TiO_2 films prepared by plasma enhanced chemical vapor deposition. *Surface and Coating Technology*, 169-170, 699-702.
[33] Guan, K., Lu, B., & Yin, Y. (2003) Enhanced effect and mechanism of SiO_2 addition in super-hydrophilic property of TiO_2 films. *Surface and Coating Technology*, 173, 219-223.
[34] Chauhan, P., Annapoorni, S., & Trikha, S.K. (1999) Humidity-sensing properties of nanocrystalline haematite thin films prepared by sol-gel processing. *Thin Solid Films*, 346, 266-268.
[35] Chou, K.-S., Lee, T.-K., & Liu, F.-J. (1999) Sensing mechanism of a porous ceramic as humidity sensor. *Sensors and Actuators B*, 56, 106-111.
[36] Gusmano, G., Montesperelli, G., Nunziante, P., & Traversa, E. (1993) Microstructure and electrical properties of $MgAl_2O_4$ and $MgFe_2O_4$ spinel porous compacts for use in humidity sensors. *Br.Ceram.Trans*., 92, 104-108.
[37] Kulwicki, B.M. (1984) Ceramic sensors and transducers, *J.Phys.Chem.Solids*, 45, 1015-1031.
[38] Kulwicki, B.M. (1991) Humidity sensors, *J.Am.Ceram.Soc*., 74, 697-708.
[39] Niranjan, R.S., Sathaye, S.D., & Mulla, I.S. (2001) Bilayered tin oxide: zirconia thin films as a humidity sensor. *Sensors and Actuators B*, 81, 64-67.
[40] Tai, W.-P., & Oh, J.-H. (2002) Preparation and humidity sensing behaviors of nanocrystalline SnO_2/TiO_2 bilayered films. *Thin Solid Films*, 422, 220-224.

In: Nanomaterials: New Research
Editor: B.M. Caruta, pp. 129-167
ISBN: 1-59454-369-0

Chapter 4

SYNTHESIS OF ZNO NANOPOWDER BY SOLUTION COMBUSTION METHOD AND ITS PHOTOCATALYTIC CHARACTERISTICS

Sung Park*, Jae-Chun Lee and Ju-Hyeon Lee[1]
Department of Materials Science and Engineering, Myongji University,
382 San, Nam-dong, Yongin, Kyunggi-do 449-728, Korea
[1]Department of Electronic Materials Engineering,
SunMoon University, Asan, Choongnam 336-708, Korea

ABSTRACT

The main objectives of the present work were to synthesize zinc oxide powder, to investigate its photocatalytic activity and to compare its activity with that of the present day state-of-the-art commercial semiconductor oxide photocatalyst powders. The work was focused mainly on the synthesis of zinc oxide powder for the degradation of organic and inorganic pollutants. Commercial zinc oxide powder shows low photocatalytic activity for degradation of organic and inorganic pollutants as it contains many defect structures, which enhance the recombination rate of generated electron-hole pairs responsible for redox reactions during photocatalytic experiments.

To obtain high purity zinc oxide powder free of defects, a new self-propagating process initiated at low temperature using redox compounds and mixtures in solution was investigated. The process makes use of highly exothermic redox chemical reactions between metals and non-metals. The method is referred to as the "solution-combustion method (SCM). Different zinc oxide powders were synthesized using a number of oxidants and fuels (reductants) in various proportions using the SCM. The formed zinc oxide powders were analyzed using different powder characterization techniques such as SEM, TEM, BET, XRD, and PL spectra measurements. SEM and TEM revealed the formation of uniform particle size in the nanometer range. As-synthesized primary particles were as small as 30 nm in size and the specific surface area of the nanopowder

* Corresponding Author : spark@mju.ac.kr

was about 120 m^2/g. Single phase was confirmed by XRD and PL spectra revealed the defect-free nature and high UV light absorption capacity of the synthesized nanopowder.
The photocatalytic performance of the synthesized nanopowder was evaluated to remove organic pollutants and metal ions from aqueous solutions in a batch-type reactor. Other photocatalyst powders such as state of the art commercial ZnO (Junsei, Japan), commercial titanium dioxide powder (P-25 TiO_2, Degussa, Germany) and titanium dioxide powder prepared by homogeneous precipitation process at low temperature (HPPLT TiO_2) were also used in duplicate experiments to compare their degradation and removal rates. In all cases, the SCM ZnO nanopowder showed a much higher rate of degradation of phenol and removal rate of metal ions than that other photocatalyst powders.
Photocatalysis is a surface phenomena and the method of preparing the photocatalyst powder determines its efficiency. Here, all the characteristics of the obtained powder such as nanometer size, very high surface area, defect-free nature, and high UV absorption capacity have played a positive role in enhancing its efficiency in photocatalytic reactions.

1. INTRODUCTION

1.1. Zinc Oxide

Zinc oxide (ZnO) is a wide direct bandgap II-VI semiconductor that has a Wurtzite structure. Its significant applications include varistors, phosphors, pigment material, rubber additive, gas sensor, photocatalyst, etc. [1,2]. It is optically transparent in the visible region and electrically conductive with appropriate dopants. Therefore, this material is used as transparent conducting electrodes for displays and solar cells [3,4]. With a particle size in the nanometer range, it has proven to be an excellent UV absorbing material that can be used in sunscreen lotions [5].

The minimum value of bandgap energy stated in literatures is 3.1 to 3.3 eV [6]. This high bandgap makes ZnO highly suitable for optical applications. The recent development of thin-film fabrication techniques now allows the growth of large single crystals, which, essential for optical devices, demands high quality materials. There have been reports on the construction of blue laser diodes based on ZnO and of electrodes for solar cells and flat panel displays [7, 8]. The reactivity of the surfaces for methanol synthesis and other catalytic processes has been utilized on an industrial scale.

1.2. Crystal Structure of Zinc Oxide

ZnO crystallizes in a hexagonal wurtzite structure in which the oxygen atoms are arranged in a hexagonal close-packed (HCP) type of lattice with zinc atoms occupying half the tetrahedral sites. The Wurtzite structure in figure 1.1 can be described as two HCP lattices, which are inserted into each other. The O-lattice is displaced a fraction 0.38 of the unit cell height in the c-direction with respect to the Zn- lattice. All atoms in ZnO have tetrahedral coordination with four nearest neighbors of the opposite type. This means that

close packed planes of Zn- and O- are stacked along the c-axis in the cell, forming a polar crystal with the polarization in this direction. The mean lattice constants are a = 3.250 Å and c = 5.206 Å, which depend slightly on stoichiometry deviation. The c/a ratio of 1.602 is a little less than the ideal value of 1.633. The Zn-O distance is 1.992 Å parallel to the c-axis and 1.973 Å in the other three directions of the tetrahedral arrangement of the nearest neighbors [6].

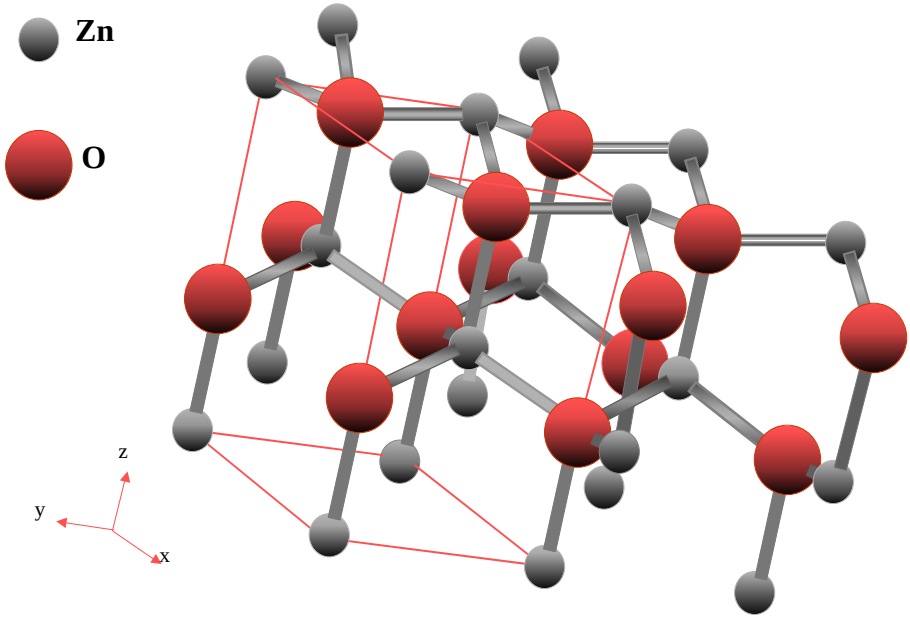

Figure 1. The unit cell of ZnO (hexagonal wurtzite).

1.3. Electronic Structure of Zinc Oxide

The Zn-atoms in ZnO to a large extent have donated its two 4s-valence electrons to their neighboring O-atoms; however, there is a significant delocalized charge between the atoms, consequently giving ZnO a mixed ionic-covalent character. According to the Phillips ionicity scale, ZnO is therefore on the borderline between an ionic and a covalent crystal. This mixed ionic-covalent character is probably one reason for the difficulties that have occurred in determining the electronic structure of ZnO. The bandstructure of the Wurtzite-phase of ZnO has been investigated [6]. ZnO has a wide direct optical band gap at near 3.3 eV.

1.4. Scope of This Work

The main scope of the present work was:

1. to investigate a new method of synthesizing oxide powders referred to as the 'solution-combustion method'
2. to synthesize zinc oxide (ZnO) powder by the solution-combustion method
3. to determine the effectiveness of the synthesized powder in the photocatalytic oxidation of organic pollutants in aqueous solution
4. to determine the effectiveness of the synthesized powder in the photocatalytic reduction of metal ions in aqueous solution, and
5. to compare the photocatalytic activity of the synthesized powder with that of other state-of-the-art photocatalyst powders like titanium dioxide powder (P-25 TiO_2; Degussa, Germany)

2. SYNTHESIS OF ZNO NANOPOWDER

2.1. Background

When ZnO is irradiated with UV light of appropriate energy greater than its bandgap, highly mobile electron-hole pairs can be generated. These carriers then migrate to the surface and in turn are trapped by reactants adsorbed on the surface, giving rise to powerful redox chemistry [9]. Therefore, ZnO has attracted interest as a photocatalyst, especially, in the degradation of environmental pollutants [10-12]. It has almost the same bandgap energy as titanium dioxide (TiO_2). Thus its photocatalytic activity is predicted to be similar to that of TiO_2. But the research carried out to realize its full potential as a semiconductor photocatalyst is limited [13-17].

Chemical methods have shown several distinct advantages for the synthesis of nanophase particles [18]. Several chemical methods for the synthesis of zinc oxide have been reported (e.g., preparations of fine zinc oxide by means of spray pyrolysis, sol-gel technique, vapor method and thermal decomposition [19-23]). The synthesis of zinc oxide through precipitation of organic solutions has also been reported [24]. However, the characteristics of zinc oxide synthesized by these methods revealed that it was not good enough to used as a photocatalyst compared to other materials such as TiO_2. That is the reason for the use of TiO_2 as a photocatalyst.

One innovative technique for synthesizing fine ceramic powders with good homogeneity is 'combustion synthesis'. This technique offers added advantages over alternatives, such as a simple experimental set-up, the surprisingly short time between preparing the reactants and obtaining the final product, and the savings in external energy consumption [25-31]. The combustion synthesis technique begins with combining reactants that oxidize easily, (eg., nitrates) and a suitable organic fuel (like glycine, urea, carbohydrazide) that acts as a reducing agent. The mixture is brought to boil until it ignites and a self-sustaining and rather fast combustion reaction occurs, resulting in a dry, crystalline and unagglomerated, fine oxide

powder. The large amount of gases formed can result in the appearance of flames, which can reach temperatures that exceed 1500^0C.

In combustion synthesis, the energy released from the exothermic reaction between the nitrates and the fuel, which is usually ignited at a temperature much lower than the actual phase transformation temperature, can rapidly heat the system to a high temperature and sustain it long enough for the synthesis to occur, even in the absence of an external heat source.

The combustion synthesis technique is based on the thermochemical concepts used in the field of propellants and explosives. Self-propagating combustion reaction occurs when explosives are ignited.

The need for a clear indication of the effective constitution of a fuel-oxidizer mixture led Jain et al. to devise a simple method of calculating the oxidizing to reducing character of the mixture [32]. Stoichiometry of the metal nitrate and fuel mixture can be calculated based on the total oxidizing and reducing valency of the oxidizer and the fuel, which serves as a numerical coefficient for the stoichiometric balance so that the equivalence ratio (φ_e) is equal to unity and the energy released is maximum. As an example, the oxidizing valence of zinc nitrate is –10, while the reducing valence of carbohydrazide is +8 and that of glycine is +9. Hence, 1 mole of zinc nitrate requires 1.25 moles of carbohydrazide or 1.11 moles of glycine to keep the equivalence ratio (φ_e) unity.

In a typical combustion synthesis, a pyrex dish containing an aqueous redox mixture of stoichiometric amounts of zinc nitrate and glycine is heated on a hot plate inside a chamber. The solution boils and froths, followed by the appearance of flame yielding a voluminous product.

2.2. Experiment

Zinc hydroxide powder [$Zn(OH)_2$, Junsei (Japan)] or zinc nitrate powder [$Zn(NO_3)_2$ $6H_2O$, 3N, High purity chemicals lab.(Japan)] was used as the starting material. Glycine [H_2NCH_2COOH, Yakuri pure chemicals co. Ltd (Japan)] or carbohydrazide [$H_2NNHCONHNH_2$, Aldrich (USA)] was used as the fuel. Here, the zinc hydroxide powder was dissolved in nitric acid before use, forming zinc nitrate. The starting material (zinc nitrate or zinc hydroxide dissolved in nitric acid) was dissolved in distilled water in a beaker, and fuel (glycine or carbohydrazide) was added to the starting material solution. The solution mixture was then heated on a hot plate while being stirred. As the distilled water evaporated, the solution became viscous and generated small bubbles. The viscous solution was then transferred to another stainless steel beaker and heated inside a chamber for ignition (fig. 2). The nitrate group (NO_3^-) reacted with the fuel and formed highly explosive $CO(N_3)_2$ [33]. At this point, the temperature rose to 1500–1800°C instantaneously with flame and combustion. This intense heat resulted in instantaneous high pressure, which led to an explosion. The ZnO powder was formed in this high temperature and pressure environment. At this point the powder was gathered by the collector, and placed above the beaker. The powder was annealed for one hour at 400^0C.

X-ray diffractometer (XRD) was used to confirm the crystalline phase of the synthesized ZnO powder. A scanning electron microscope (SEM) was used to investigate the average particle size and shape. Specific surface area of the powder was measured by the brunauer

emett teller (BET) method. Fluorospectrometer (SIM-AMINCO) was used to measure photoluminescence (PL) emission values as a function of wavelength. Different ZnO powders were synthesized, changing the amount of carbohydrazide.

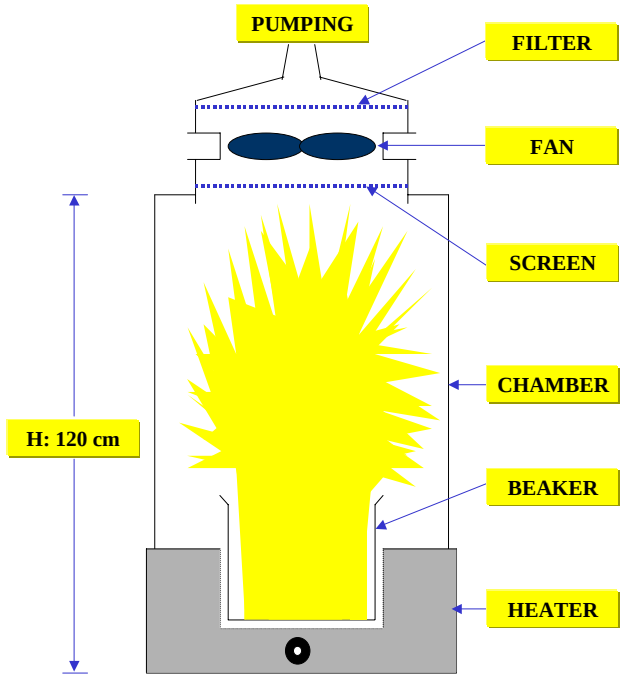

Figure 2. Schematic diagram of the SCM ZnO synthesis apparatus

2.3. Results and Discussion

The crystalline phases of the powders were confirmed by the XRD patterns shown in fig.3. When the molar ratio of fuel (carbohydrazide) to oxidant (zinc hydroxide dissolved in nitric acid) was 0.8 or 1.0, XRD patterns showed that the synthesized ZnO powders were not single phase ZnO but a mixture of materials including the remainders of an incomplete combustion. XRD patterns showed that peaks of single phase ZnO started to form only when the molar ratio of fuel to oxidant was higher than 1.2. At the molar ratio of 1.333, single

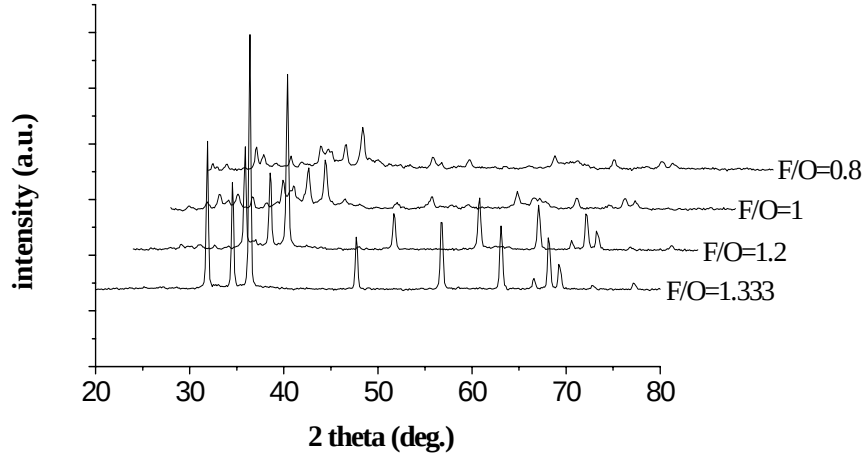

Figure 3. XRD patterns of ZnO powders synthesized using carbohydrazide and zinc hydroxide (dissolved in nitric acid) with different molar ratios (F: fuel and O: oxidizer).

phase ZnO was completely formed. The ratio of 1.333 is the ratio in which the reaction formula forms complete $CO(N_3)_2$ from the reaction between nitrate group and carbohydrazide. Similar results were obtained up to the molar ratio of 1.6, a case of fuel excess. During the combustion reaction in the reaction chamber, the degree of explosion appeared to be similar even though the ratio was increased. However, it showed a slightly higher degree of explosion when the molar ratio exceeded 1.4. When the molar ratio was lower than 1.2, carbohydrazide was completely consumed with the nitrate group partially remaining. This resulted in a mixture of materials rather than single phase ZnO. The intensity of the peaks was inconsiderable even though the peaks of single phase ZnO were detected. At the molar ratio of 1.333, the fuel (carbohydrazide) and oxidant (nitrate group) were completely consumed to form highly explosive $CO(N_3)_2$. In the case of fuel excess(molar ratio higher than 1.4), the remaining fuel decomposed and evaporated in the air.

Figure 4 shows XRD peaks of ZnO powders synthesized using glycine instead of carbohydrazide as a fuel. Generally, using glycine as a fuel, oxide powders are synthesized adding the fuel in equilibrium (oxidant: fuel = 1), fuel lean or fuel rich states considering the degree of explosion during self-combustion, based on the calculation of oxidation number for oxidant and fuel. Five different ZnO powders were synthesized with varying fuel/oxidant molar ratios (F/O=0.75~1.3). It is easy to obtain single-phase ZnO powder regardless of the

fuel/oxidant ratio. Especially the ZnO powder with a fuel/oxidant molar ratio of 0.8 showed highest XRD peaks that indicate best crystalline quality.

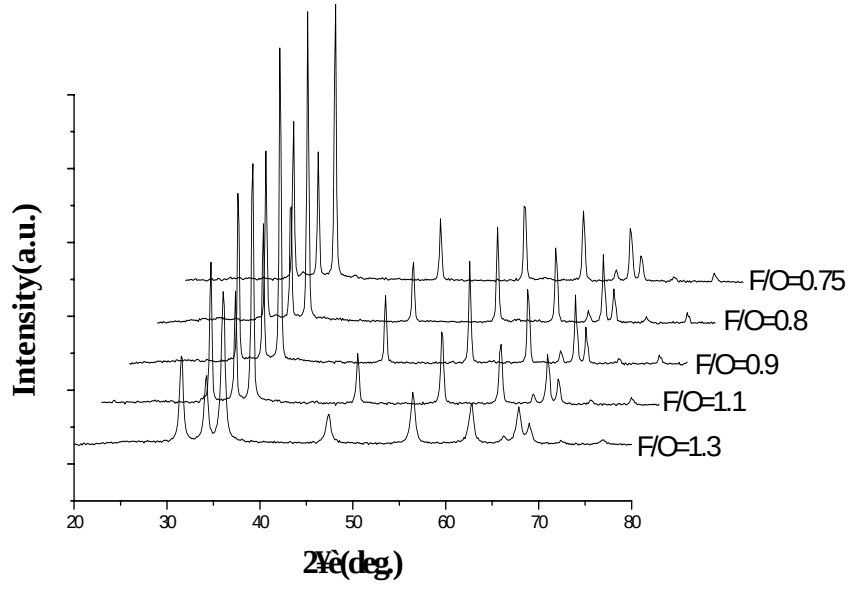

Figure 4. XRD patterns of ZnO powders synthesized using glycine and zinc hydroxide (dissolved in nitric acid) with different molar ratios (F: fuel and O: oxidizer).

Table 1 shows the average size of ZnO particles synthesized by SCM with various starting materials and fuels. The average particle size determined from SEM images is shown in fig. 5 and 6. Here, the particle size was greatly depended on the types of oxidants and fuels used during synthesis.

Table1. Average Particle Size of ZnO Powders Synthesized by SCM Using Various Starting Materials and Fuels

Starting Materials Fuels	$Zn(NO_3)_2 \cdot 6H_2O$	$Zn(OH)_2$
Carbohydrazide	320 nm	110 nm
Glycine	125 nm	30 nm

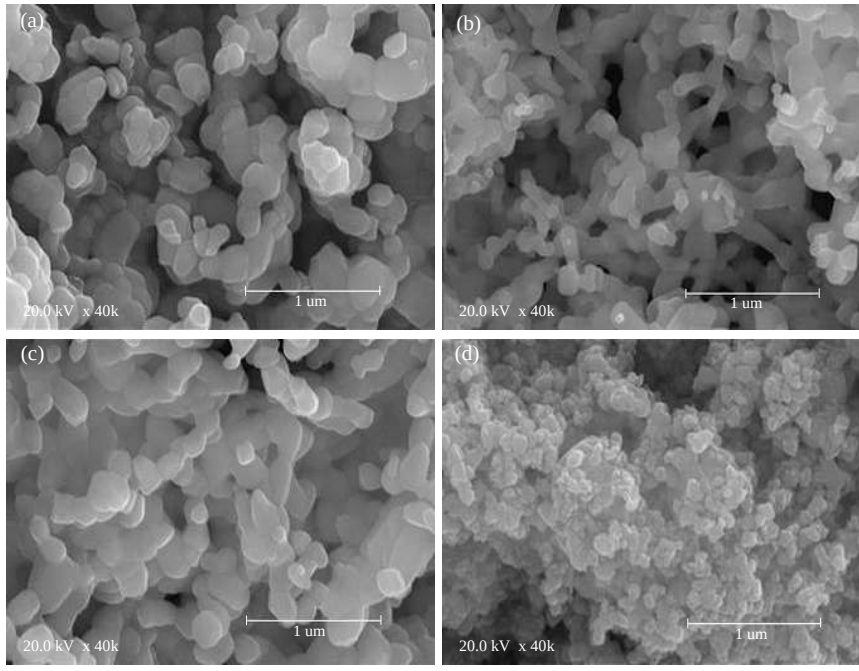

Figure 5. SEM photographs of ZnO powders synthesized by SCM using (a) $Zn(NO_3)_2 \cdot 6H_2O$ and carbohydrazide, (b) $Zn(OH)_2$ and carbohydrazide, (c) $Zn(NO_3)_2 \cdot 6H_2O$ and glycine and (d) $Zn(OH)_2$ and glycine.

The difference in particle size was more than four fold depending on the oxidants and fuels used. Plate-like particles were obtained when carbohydrazide was used as a fuel. On the other hand, when using glycine as a fuel, the shape of the particles was spherical and their size uniform. The finest particles (30 nm), as shown in fig. 6, were obtained when $Zn(OH)_2$ and glycine (molar ratio: F/O=0.8) were used. In this case, $Zn(OH)_2$ was dissolved in nitric acid solution to form zinc nitrate. There would have been more NO_3^- groups in the solution than the case of using zinc nitrate as the starting material. The NO_3^- group acts as an igniter for the combustion. This probably means that more igniter is available for the combustion process. At this point it is not clear, but it may be considered that this is conductive to finer particle size.

Table 2 shows the specific surface areas of the synthesized ZnO powders. The specific surface area depended on the types of oxidants and fuels. The largest specific surface area of the powder (120 m^2/g) was obtained when glycine and zinc hydroxide at a molar ratio of 0.8 were used to synthesize the ZnO powder. The difference in surface area depending on oxidants and fuels was about five fold. This result is consistent with the average particle size data. This confirms that smaller particle size results in larger specific surface area.

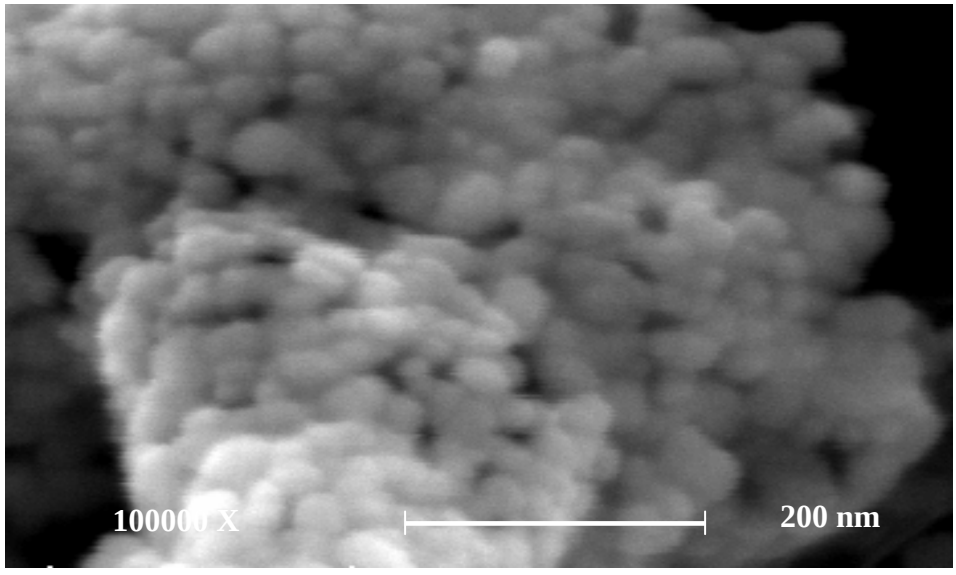

Figure 6. High magnification SEM photograph of fig.5(d)

Table 2. Specific Surface Area of ZnO Powders synthesized by SCM Using Various Starting Materials and Fuels

Starting Material Fuel	$Zn(NO_3)_2 \cdot 6H_2O$	$Zn(OH)_2$
Carbohydrazide	19 m^2/g	32m^2/g
Glycine	27m^2/g	120 m^2/g

Figure 7 shows photoluminescence (PL) spectra of commercial ZnO powder (Junsei, Japan) and ZnO powders synthesized by SCM with different glycine/zinc hydroxide molar ratios. As shown in the figure, commercial ZnO powder showed two peaks: one is in the vicinity of 500 nm, and the other one is near 400 nm. The peak near 500 nm was probably from the energy transition between oxygen vacancy level and Zn vacancy level. The UV peak near 400 nm might be from band to band transition. However, ZnO powder synthesized by SCM showed only one sharp peak near 390 nm that was slightly shifted to UV side. This peak is equivalent to the energy gap of ZnO (~ 3.2 eV). These results indicate that the ZnO powder synthesized by SCM did not show defect energy levels inside the energy gap. The defects were probably annealed out as a result of the high temperature during the synthesis process. Again, the powder showed higher PL intensity at UV than the commercial ZnO powder. Especially, ZnO powder with the fuel/oxidant molar ratio of 0.8 showed highest PL intensity

at UV. The intensity was almost three fold higher than that of the commercial ZnO powder given the same wavelength. This suggests that SCM ZnO powder absorbs much more UV light than the commercial ZnO powder.

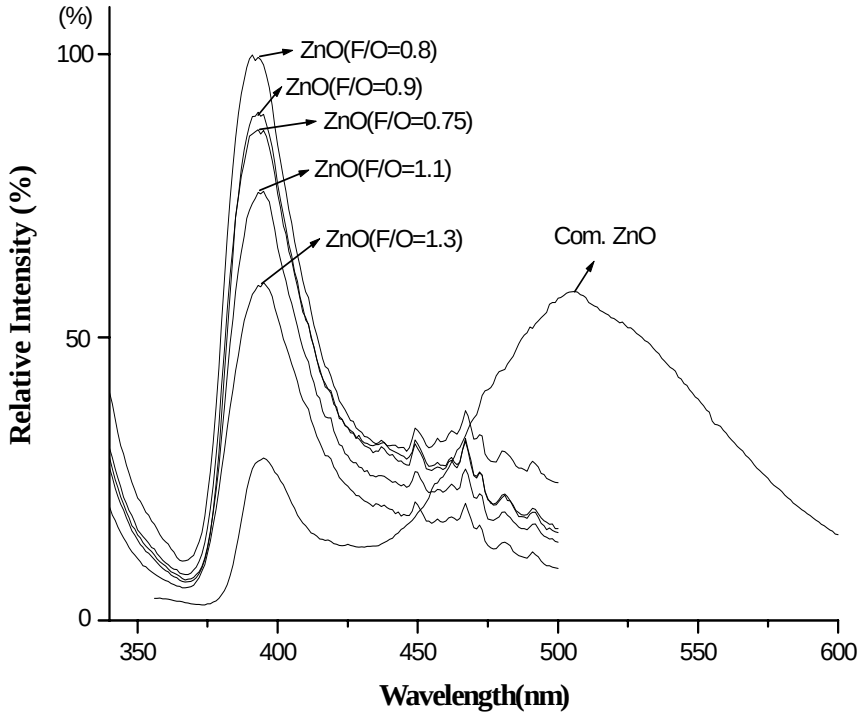

Figure 7. Photoluminescence (PL) spectra of commercial ZnO (Junsei, Japan) and ZnO nanopowders synthesized by solution combustion method with different molar ratios of glycine and zinc hydroxide (F/O)

2.4. Summary

Nano-sized single-phase ZnO powders could be easily obtained using SCM regardless of starting materials and fuels. However, the particle size of the synthesized ZnO powders greatly varied, depending on the selection of oxidants and fuels. The particle size difference was more than four fold. Especially, the use of glycine and zinc hydroxide (molar ratio: F/O=0.8), the synthesized ZnO powder showed the best powder characteristics, such as an average particle size of 30 nm and specific surface area of 120 m^2/g.

Preparation methods affect surface properties such as surface defect levels. Generally, it is known that the smaller particle size results in more surface defects. In the above case (SCM ZnO), however, the level of surface defects seemed to be minimized even though the powder was synthesized in nano-size. The surface defects might have been annealed out on short exposure at high temperature, which reaches up to 1500- 1800 ^0C during synthesis.

3. REMOVAL OF METAL IONS FROM WASTEWATER

3.1. Recovery of Ag ions from wastewater

3.1.1. Background

Photocatalytic processes involving aqueous suspensions of semiconductors have received considerable attention in view of solar energy conversion [34, 35]. Recent studies mainly concentrate on environmental problems such as purification of contaminated water or air [36-38]. Semiconductors for photocatalytic reactions should have conditions such as high photoactivity, high photostability, high sensitivity for UV-visible light and low fabrication cost. There is an ample interest in wide band gap oxide semiconductors and ease of handling [39-43].

ZnO is an important material in various fields of applications. For photocatalysts, ZnO is an n-type semiconductor that has a wide band gap of 3.2 eV. When ZnO is irradiated by light with greater energy than the ZnO band gap, electron-hole pairs are generated in the conduction and valence bands of the semiconductor, respectively. These charge carriers migrate to the semiconductor surface and have suitable redox potentials.

It is known that nano-particles have different physical and chemical properties compared to bulk materials. High catalytic activity is expected from their large surface area and different surface properties such as surface defects [44, 45].

In this work, synthesis of ZnO powder was investigated to obtain semiconductor particles smaller than 30 nm for photocatalytic applications. Two methods, a vapor method and a sol-gel method, are generally being used to obtain ZnO nanopowders. In the case of the vapor method, the resulting powders are agglomerated rather than separated because it is very difficult to control the reaction condition during the process. Therefore, this method is not recommended for obtaining nano-sized ZnO powders. In contrast, the sol-gel method results in uniform ZnO powders. However, strict control of the reaction condition is necessary because of its violent hydrolysis reaction in air during synthesis. In addition, the material cost for this method is high. For this reason, the sol-gel method is not commercialized but is utilized in small laboratory scale only [46, 47].

Park et al. proposed the SCM for preparing of ceramic powders [48-50]. In this process, by heating mixture solution containing the oxidant (source material) and fuel, there is an ignition, instantaneously producing high temperature and pressure by explosion. This instantaneous high temperature and pressure lead to the formation of very fine sized and high quality oxide ceramic powders. In this work, ZnO nanopowders were synthesized by this SCM process and used to recover Ag ions from wastewater.

3.1.2. Experiment

Photocatalytic activity of the synthesized ZnO powder was then confirmed by removing Ag ions from a waste development solution that contained them. Ag recovery rate was measured as photocatalytic efficiency. For this, water was used as a solvent for the waste development solution. The light source for the photocatalytic reaction was a UV lamp (6 W, maximum energy at 365 nm). The remaining Ag ion concentration was determined by atomic absorption spectrophotometer (Model 5100 PC, Perkin-Elmer).

3.1.3. Results and Discussion

Figure 8 shows photoluminescence (PL) spectra of state of the art, commercial ZnO (Junsei, Japan), HPPLT (Homogeneous Precipitation Process at Low Temperature) TiO_2, commercial state of the art TiO_2 (P-25 Degussa, Germany) and ZnO powders synthesized by SCM with different glycine/$Zn(OH)_2$ ratios. Figure 9 represents the energy band diagram of the commercial, state of the art ZnO powder. The peak near 500 nm can be attributed to the energy transition between O vacancy level and Zn vacancy level. The UV peak near 400 nm might be from band to band transition. However, the SCM ZnO nanopowder showed only one sharp peak near 390 nm that was slightly shifted to the UV side. This peak is equivalent to the energy gap of ZnO (~ 3.2 eV). These means that the SCM ZnO nanopowder did not show defect energy levels inside the energy gap. The defects were probably annealed out from the high temperature during the synthesis process. The SCM ZnO nanopowder showed a UV absorption that is threefolds than that of other ZnO and TiO_2 powders.

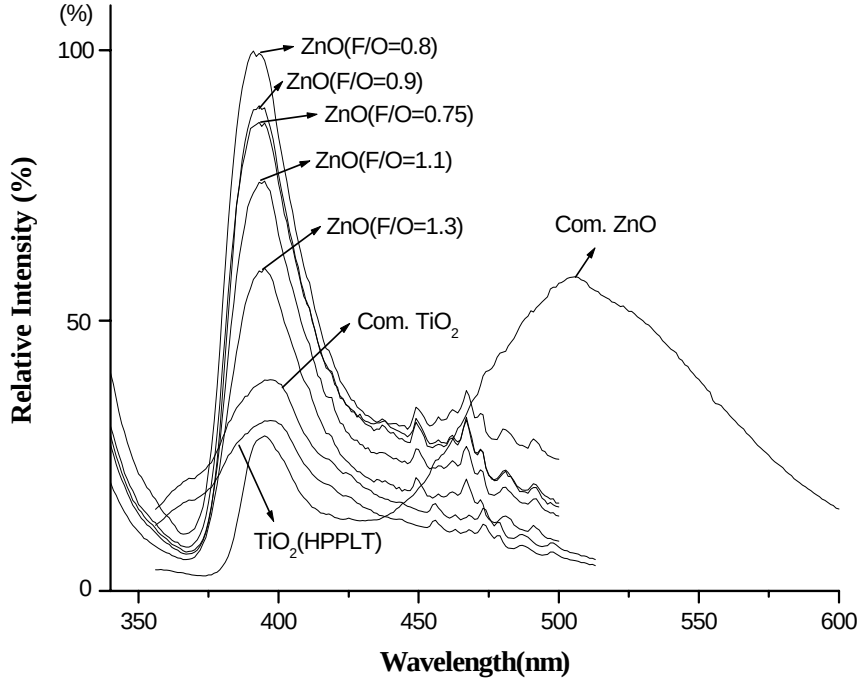

Figure 8. Photoluminescence (PL) spectra of commercial state of the art ZnO (Junsei, Japan), HPPLT TiO_2, commercial state of the art TiO_2 (P-25 Degussa, Germany) and the SCM ZnO powders synthesized with different glycine/$Zn(OH)_2$ ratios.

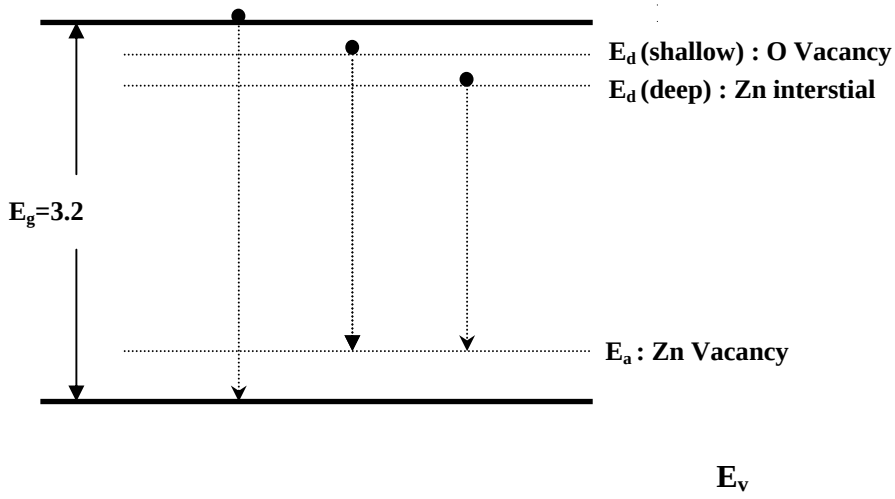

Figure 9. Schematic diagram of ZnO energy band gap and defect energy levels.

As mentioned above, results from XRD (fig. 4) and PL measurements led to select the ZnO powder with glycine/$Zn(OH)_2$ ratio of 0.8 for this Ag recovery experiment. To confirm the photocatalytic characteristics, there were attempts to remove Ag ions from waste development solution. Figure 10 shows the Ag recovery rate of commercial state of the art ZnO (Junsei, Japan), HPPLT TiO_2, commercial state of the art TiO_2 (P-25 Degussa, Germany) and ZnO powders synthesized by SCM. Here, state of the art commercial ZnO powder did not show detectable photocatalytic reaction while ZnO powders synthesized by SCM showed remarkable photocatalytic reactions. Especially, the powder synthesized using $Zn(OH)_2$ and glycine completely removed the Ag ions within 15 min. This Ag recovery rate is at least 3 folds higher than that of photocatalytic powders including HPPLT TiO_2 and commercial state of the art TiO_2 (P-25 Degussa, Germany). These results were strongly supported by the PL measurement data as mentioned above.

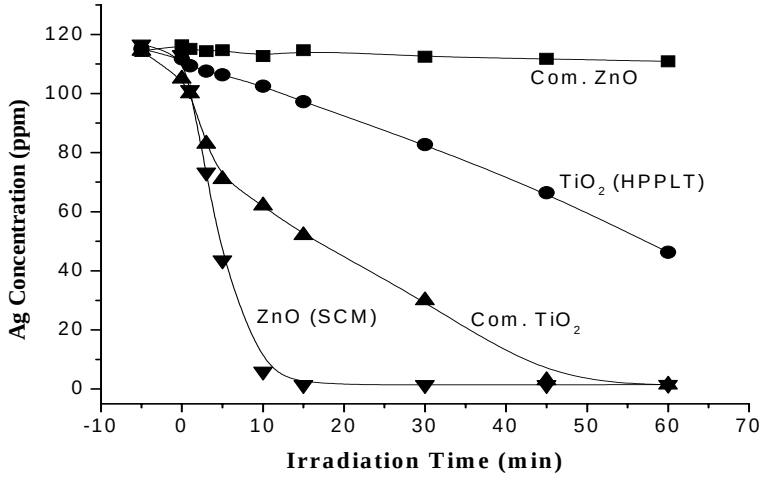

Figure 10. Ag recovery rate by photocatalytic reaction of commercial state of the art ZnO (Junsei, Japan), HPPLT TiO_2, commercial state of the art TiO_2 (P-25 Degussa, Germany) and the SCM ZnO powders synthesized with glycine/$Zn(OH)_2$ ratio of 0.8.

3.1.4. Summary

Surprisingly, the Ag ions in the waste development solution were completely removed within just 15 mins when the ZnO powder was used for photocatalytic reaction. This result confirms the outstanding photocatalytic characteristics of ZnO powder synthesized using SCM. The Ag recovery rate with the ZnO powder was at least 3 times higher than that of commercial state of the art photocatalytic powders including ZnO and TiO_2. This result strongly correlated with PL measurement data showing that the PL intensity of the ZnO powder was 3 times higher than that of the commercial state of the art TiO_2 powder. The high quality of the ZnO powder might be due to the fact that the high temperature, generated during SCM removed any defects.

To the author's knowledge, photocatalytic Ag removal from actual waste development solution (not simulated solution) has not been reported. The ZnO powder synthesized by SCM could be utilized for high efficiency photocatalytic reaction, UV-blocking cosmetics and other UV-related areas.

3.2. Removal of Cu^{++} Ions from Aqueous Cu-EDTA Solution

3.2.1. Background

Heterogeneous photocatalysis has been under extensive research not only for the removal of non-degradable organic chemicals like phenol [51-55] and its derivatives, but also for the recovery of heavy metal ions from waste water. The process has many advantages like simple system, lower operating cost and formation of more stable byproducts in the environment as compared to the conventional processes such as precipitation, carbon adsorption, ion exchange, membrane separation, air stripping, etc.used for degradation of organics, and for either disposal or recovery of metal ions in waste water [56].

Metal ions are generally non-degradable. They have infinite lifetimes, and build up their concentrations in food chains to toxic levels. In recent years, an array of industrial activities has disrupted the geological equilibrium of metal ions through release of large quantities of toxic metal ions into the environment. Again, the demand for metals increases significantly with the development of industry. Thus, waste metal recovery has the potential simultaneously to resolve two issues: metal pollution prevention and resource conservation.

The reduction of metal ions with semiconductor photocatalysis couples low-energy UV light with semiconductor particles acting as catalyst and is based on the reduction by photogenerated electrons. The metals are deposited onto the surface of semiconductor photocatalyst powder, and can be extracted from the slurry by physical and/or chemical means.

If the size of the photocatalyst powder decreases and reaches nano level, then its surface properties change as the ratio of the surface molecules with the bulk molecules increases simultaneously. This leads to the easy diffusion of the conduction band electrons and valence band holes through the surface to rapidly react with decomposing materials [57]. When the particle size is smaller than the wavelength of the incident light, light scattering is negligibly small. Thus, the nano-sized photocatalyst particles have the additional advantage of providing a transparent solution for efficient photoredox processes.

Titanium dioxide is the most used semiconductor photocatalyst powder these days and it has become nearly synonymous to the best photcatalyst powder. Our group is investigating

the substitute of titanium dioxide and working on zinc oxide, another potential semiconductor photocatalyst. In this work, we report the comparative results of the reduction rates of copper ions in aqueous solution using the zinc oxide photocatalyst powder prepared in our laboratory and two different titanium dioxide photocatalyst powders.

3.2.2. Experiment

ZnO nanopowder was synthesized by the solution-combustion method as described above. For the purpose of comparing photocatalytic removal rates, P-25 titanium dioxide powder (Degussa, Germany) was purchased while the TiO_2 powder using homogeneous precipitation process at low temperature (HPPLT) was prepared following the synthesis method given in reference [58].

XRD and TEM were used to confirm the crystalline phase and particle size and shape respectively. The powder was then used as a photocatalyst for the removal of metal ions from aqueous solution. The reaction was carried out in a 100 ml batch-type quartz reactor with a diameter of 37 mm and height of 120 mm. A high-pressure mercury arc lamp was used as an external UV source. 52 ppm aqueous Cu-ethylenediaminetetraacetic acid (EDTA) solution was prepared by complexing 1:1 molar Na_2EDTA (Aldrich), the sacrificial donor agent [59-61] and reagent grade copper nitrate [$Cu(NO_3)_2$] (Aldrich) in distilled water. 3.0 g/L of the photocatalyst powder was mixed in the Cu^{++} solution and mixed ultrasonically for 5 minutes and left for half an hour in the dark for adsorption/ desorption equilibrium, stirring it magnetically. Then the UV light was turned on for the photocatalytic reaction. The concentrations of Cu^{++} ions remaining in the solution during different time intervals were detected with an AA spectrophotometer (Perkin-Elmer 5100 PC). Before the metal ions were dectected, the solution was passed through a syringe filter having pore size of 0.2μm for the removal of photocatalyst particles. TEM (JEOL JEM-4010, 200 kV) equipped with an energy-dispersive x-ray spectrometer (EDS) was used for analyzing the composition and shape of the respective photocatalyst-metal complexes containing metal that had been removed by the photoreduction reaction from the aqueous solutions.

3.2.3. Results and Discussion

Single-phase zinc oxide powder was obtained from the above experiment. Authors had selected two other semiconductor photocatalyst powders for the purpose of evaluating their efficiency in removing Cu^{++} ions from its aqueous solution in similar conditions and comparing the efficiency with the SCM prepared ZnO nanopowder. P-25 TiO_2 powder and HPPLT TiO_2 powder were selected for this purpose. P-25 powder is a commercially available photocatalyst powder and it has become one of the standard powders in photocatalytic experiments. In fact, many researchers have tried to compare other photocatalyst powders using it as a standard photocatalyst powder [62]. Lee et al. [58] has claimed that the HPPLT TiO_2 powder had 1.5 folds faster removal rate of Cu^{++} ions and Pb^{++} ions than P-25 powder.

The P-25 TiO_2 powder was a mixture of 70% anatage and 30% rutile phases having specific surface area of 55 m^2/g. The HPPLT TiO_2 powder was purely rutile phase powder with the specific surface area of 180-200 m^2/g, while the SCM ZnO powder was a single phase powder having the specific surface area of ~120 m^2/g.

Figure 11 shows the results of removal of Cu^{++} ions using different photocatalyst powders (SCM ZnO, P-25 TiO_2, and HPPLT TiO_2) from the aqueous metal-EDTA solution

with an initial Cu^{++} concentration of 52 ppm. For convenience, the concentrations at 0 and 1 minutes of irradiation indicate the initial concentration and the equilibrium concentration of Cu^{++} ions after stirring the solution magnetically in the dark for half an hour, respectively. Complete removal of Cu^{++} ions from the solution was observed within the UV irradiation time of 90 minutes using SCM ZnO powder. As for the other two powders, however, complete removal of the ions could not be observed within the reaction time of 180 minutes. From this result, we could confirm that the Cu^{++} ions removal efficiency of SCM ZnO powder was at least twice the efficiency of other photocatalyst powders investigated.

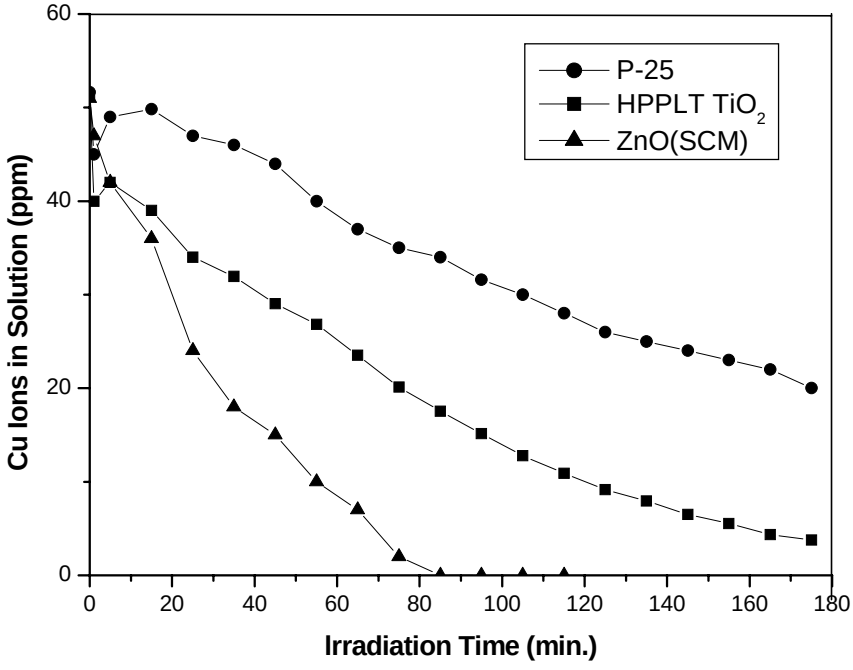

Figure 11. Comparison of Cu^{++} ions removal effeciency of differentphotocatlayst powders from the aqueous Cu-EDTA solution.

Figure 12 shows the TEM images of all the photocatalyst powders investigated after the photcatalysis experiments. In the images copper lumps can be clearly seen in SCM ZnO powder and on the surface edges, of HPPLT TiO_2 powder, but the lumps are larger in the former case. On the other hand, the copper lumps are small and sparse in the agglomerated P-25 powder. These results are also in agreement with the above results. The highest efficiency of the SCM ZnO powder among the above-investigated powders is attributed to its highest UV absorption capacity, which could be confirmed by the PL spectra.

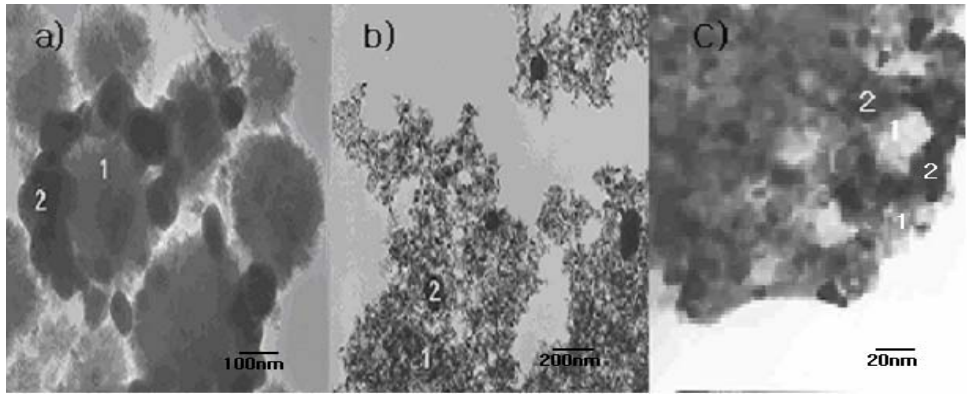

Figure 12. TEM images of different photocatalyst powders, showing lumps of copper on their surfaces, taken after the experiment. (a) HPPLT TiO_2 powder, (b) P-25 TiO_2 powder, and (c) SCM ZnO powder, in the figures: number1 represents the respective powder while number 2 represents the copper lumps.

3.2.4. Summary

To the best of our knowledge, this is the first time that such a fast removal of Cu^{++} ions from aqueous solution using photocatalyst powder has been reported. Zinc oxide nanopowder seems far more efficient than other photocatalyst powders like P-25 TiO_2 powder for removing toxic metal ions from solutions.

3.3. Removal of Pb^{++} Ions from Aqueous Wastewater

3.3.1. Background

Heterogeneously dispersed semiconductor surfaces provide an environment for influencing the chemical reactivity of a wide range of molecules and serve as a means to initiate light-induced redox reactivity in these molecules. The semiconductor surfaces basically are of the oxides of titanium, zinc, and tin. Upon photoexcitation of such surfaces, simultaneous oxidation and reduction reactions occur. The incident light that initiates this sequence is in the visible or low-energy ultraviolet regions of the spectrum. Investigations in the field began in order to develop photochemical and photocatalytic methods for utilizing the solar energy, widening the applications in chemical and environmental technologies [63]. Recent studies mainly focus on environmental problems such as purification of contaminated water and air [64, 65].

At a certain concentration, lead is a health hazard to both humans and animals and exerts its most toxic effects on the nervous system and kidneys. It is not biodegradable and cannot be decontaminated chemically in an aquatic environment. However, it can be removed by photocatalytic methods [66-68]

Titanium dioxide is the most widely used semiconductor photocatalyst powder as of now. Our research group is investigating the substitute of titanium dioxide and working on zinc oxide, another potential semiconductor photocatalyst. In this work, we report the comparative results of the reduction rates of lead ions in aqueous solution using SCM ZnO powder and two other different titanium dioxide photocatalyst powders.

3.3.2. Experiment

ZnO nanopowder was prepared by the solution-combustion method described above. Other photocatalyst powder, titanium dioxide (TiO_2, P-25), was purchased from Degussa, Germany and rutile TiO_2 powder was prepared by HPPLT.

XRD spectra of all the photocatalyst powders were taken to confirm their crystalline phases. At the same time, SEM images of the two synthesized powders were captured to observe their particle shape and size. The powders were then used as photocatalysts for removing metal ions from the aqueous solution. The reaction was carried out in a 100 ml batch-type quartz reactor with the diameter of 37 mm and height of 120 mm (fig.13.). A high-pressure mercury arc lamp was used as an external UV source. 150 ppm aqueous lead-ethylenediaminetetraacetic acid (Pb-EDTA) solution was prepared by complexing 1:1 molar Na_2EDTA (Aldrich, USA), the sacrificial donor agent [69] and reagent grade lead nitrate [$Pb(NO_3)_2$] (Aldrich, USA) in distilled water. 3.0 g/L of the above-prepared ZnO nanopowder was mixed in the Pb-EDTA solution and it was mixed ultrasonically for 5 minutes. The mixture was then stirred magnetically in the dark for half an hour for adsorption/ desorption equilibrium. UV light was then turned on for the photocatalytic reaction. The concentration of Pb^{++} ions remaining in the solution during different time intervals was detected with an AA spectrophotometer (Perkin-Elmer 5100 PC). Before the metal ions were dectected, the solution was passed through a syringe filter having a pore size of 0.2μm to remove photocatalyst particles. The same experiment was repeated for two types of photocatalyst powders (P-25 TiO_2 and HPPLT TiO_2). TEM (JEOL JEM-4010, 200 kV) equipped with an energy dispersive x-ray spectroscope (EDS) was used to analyze the composition and shape of the respective photocatalyst-metal/ metal oxide complexes after the photoreduction of lead (II) ions from the aqueous solutions.

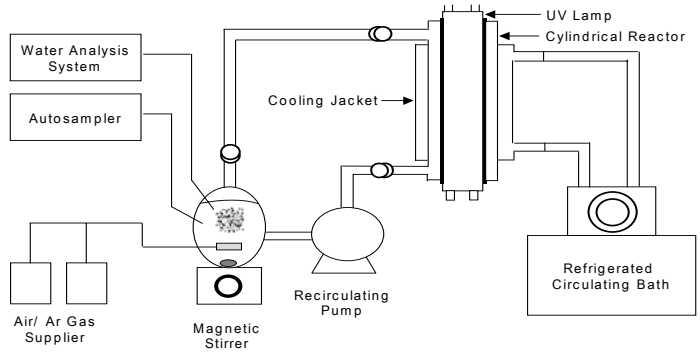

Figure 13. Schematic diagram of recirculating-cylindrical batch type reactor

3.3.3. Results and Discussion

As shown in fig. 14, the XRD patterns of P-25 TiO_2 showed anatage and rutile phases; however, the HPPLT TiO_2 powder showed only the rultile phase. Figure 15 shows the TEM image of HPPLT TiO_2 powder. It shows the chestnut burr shaped powder having a grain size of 200-400 nm. The grains are made up of needle-shaped primary particles having a diameter of 3-7 nm and length of 20-30 nm.

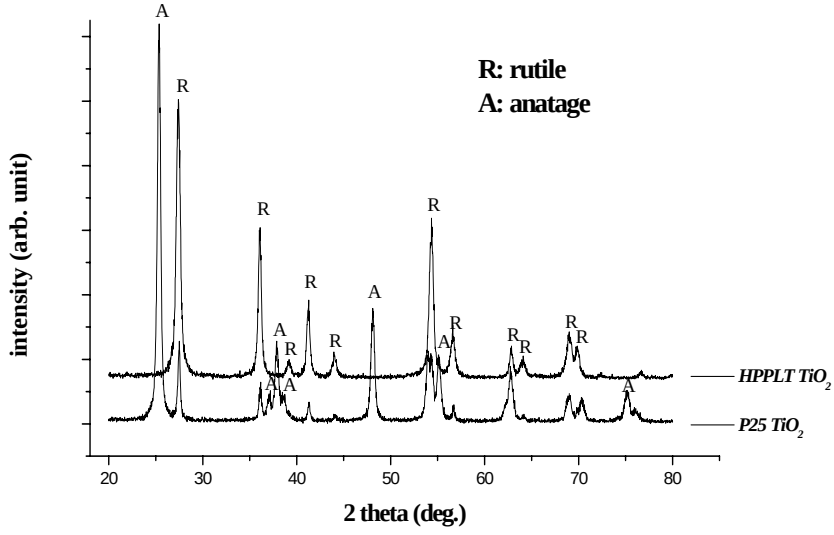

Figure 14. XRD spectra of HPPLT TiO_2 and P-25 TiO_2 powders

The ZnO powder was then subjected to a photocatalytic experiment, which aims to remove heavy metal ions. Other two powders, P-25 TiO_2 and HPPLT TiO_2 were also subjected to similar experiments for the purposes of evaluating their efficiency in removing Pb^{++} ions from its aqueous solution in similar conditions and comparing the efficiency of the SCM prepared ZnO nanopowder. P-25 TiO_2 is a commercially available photocatalyst powder and has become a standard photocatalyst powder in photocatalytic experiments. In fact, many researchers have tried to compare other photocatalyst powders by using it as a standard powder [62]. As mentioned above, the HPPLT TiO_2 powder was claimed to have 1.5 folds faster removal rate of Cu^{++} ions and Pb^{++} ions than P-25 powder.

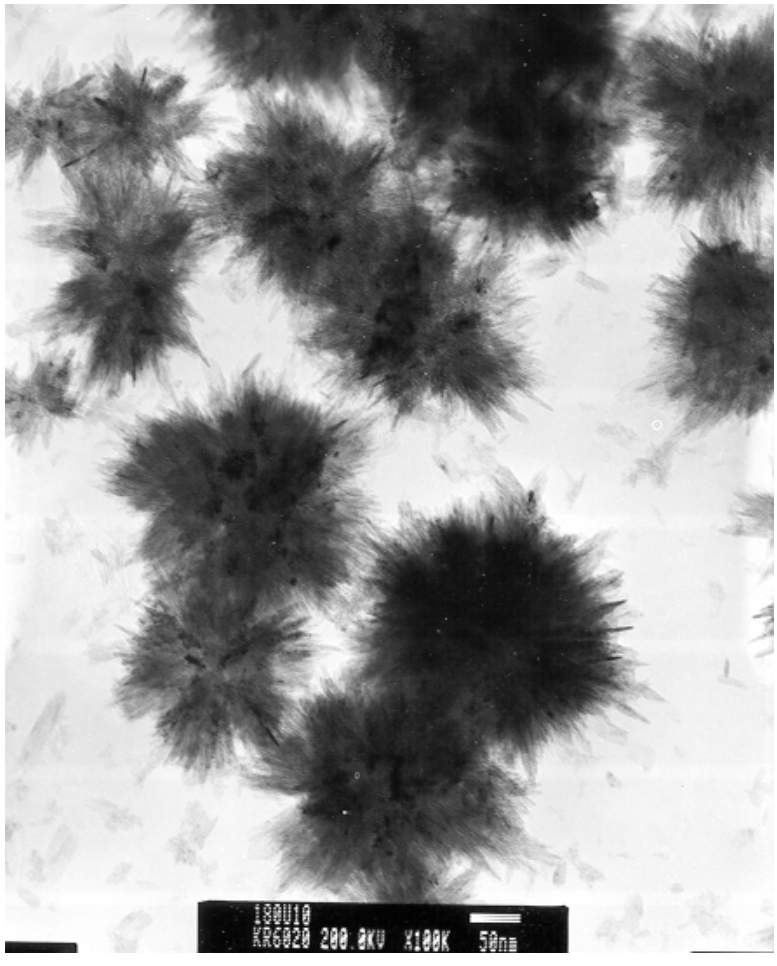

Figure 15. TEM image of HPPLT TiO_2 powder

Figure 16 shows the results of remaining Pb^{++} ions using different photocatalyst powders (SCM ZnO, P-25 TiO_2, and HPPLT TiO_2) from the aqueous Pb-EDTA solution with an initial Pb^{++} concentration of 150 ppm. For convenience, the concentrations at 0 and 1 minutes of irradiation indicate the initial concentration and the equilibrium concentration of Pb^{++} ions after stirring the solution magnetically in the dark for half an hour, respectively. Complete removal of Pb^{++} ions from the solution was observed within the UV irradiation time of 20 minutes using SCM ZnO powder. For the other two powders, however, it took almost 60 minutes in similar conditions to completely remove the lead ions with P-25 TiO_2 . The HPPLT TiO_2 took almost 40 minutes for the same. From this result, we could confirm that the Pb^{++} ions removal efficiency of SCM ZnO powder is at least twice the efficiency of other photocatalyst powders investigated.

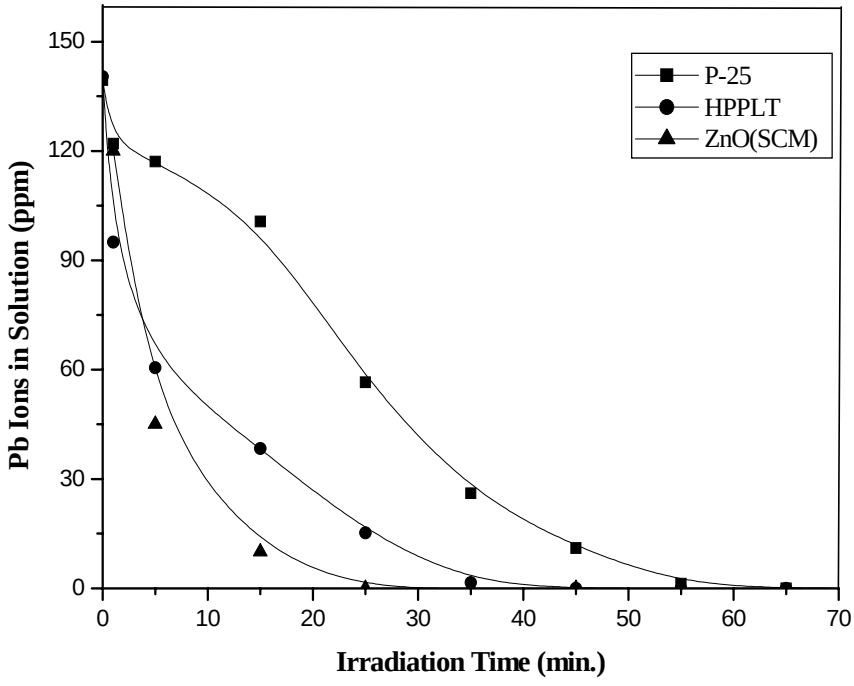

Figure 16. Comparison of Pb^{++} ions removal effeciency of different photocatlayst powders from the aqueous Pb-EDTA solution

Figure 17 shows TEM images of all the photocatalyst powders used after the photcatalysis experiments. In the images, platelet-shaped lead lumps (assigned with number 2 in the figure) can be clearly seen in SCM ZnO powder and HPPLT TiO_2 powder on the surface, with the lumps being larger in the former case. On the other hand, the lead lumps are small and sparse in the agglomerated P-25 powder. These results are also in agreement with the above results. The highest efficiency of the SCM ZnO nanopowder among the above-investigated powders is attributed to its highest UV absorption capacity, which could be confirmed by the PL spectra.

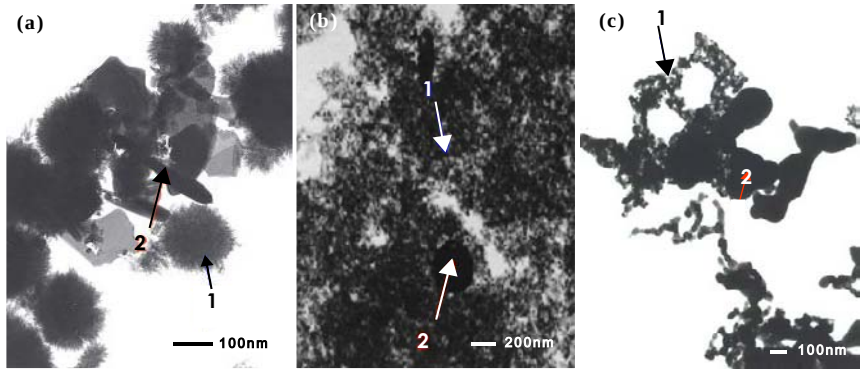

Figure 17. TEM images of different photocatalyst powders, showing lumps of lead on their surfaces, taken after the experiment. (a) HPPLT TiO_2 powder, (b) P-25 TiO_2 powder, and (c) SCM ZnO powder, in the figures: number 1 represents the respective powder while number 2 represents the lead lumps

3.3.4. Summary

ZnO nanopowder (~30 nm) was synthesized and the powder used in the photocatalytic removal of lead ions. Its removal capacity was compared with that of another commercially available photocatalyst powder, P-25 TiO_2. In our investigation, the zinc oxide nanopowder was far more active in removing lead ions from the aqueous lead-EDTA solution than the commercially available photocatalyst powder. The powder could be used in the efficient removal of heavy metal ions from aqueous waste.

3.4. Recovery of Au Ions from Wastewater

3.4.1. Background

Conventionally, precipitation has been the method most often used to remove heavy metals. Of the few precipitation methods, hydroxide precipitation is the most widely used one. However, this method is problematic, since all metal hydroxides do not completely precipitate at a single pH. This means that all of the various metals present in the wastewater cannot be accounted for. This limitation makes researchers study photocatalysts.

Photocatalysts have the unique capability of not only seperating and converting heavy metal ions from aqueous solution to their less toxic, readily recoverable metallic forms, but also destroying the toxic organic contaminants. Photocatalysis using titanium dioxide (TiO_2) has been extensively studied for oxidation and is known to be effective in the destruction of organics. Work on photocatalytic metal removal has been much less extensive. A process that can remove metals and destroy organics at the same time would represent a significant breakthrough for the treatment of heavy-metal-contaminated waters. In addition, metals

deposited on the photocatalyst particle surface could be recovered. The particular aspect of being able to recover the heavy metals in metallic form minimizes the heavy metal toxicity and reduces the number of steps required for recovery. It was reported that metal ions such as lead, chromium, copper, silver and mercury could be removed/recovered from dilute aqueous solutions using TiO_2. [70-100] However, few studies have been conducted to recover metal ions using ZnO since it is well-known that TiO_2 is the best photocatalyst. [101]

In this study, ZnO nanopowder was prepared by a new "solution-combustion method (SCM)". To confirm its applicability, our attempts to recover gold metal ions took place in real plating wastewater, not simulated wastewater.

3.4.2. Experiment

ZnO nanopowder was synthesized by the solution-combustion method as reported earlier. For the purpose of comparing photocatalytic recovery rates, TiO_2 nanopowder (Degussa, Germany) was purchased. The powder was then used as a photocatalyst for removing metal ions from the aqueous solution. The reaction was carried out in a 100 ml batch-type quartz reactor with a diameter of 37 mm and height of 120 mm (fig.13). A high-pressure mercury arc lamp was used as an external UV source. Plating wastewater containing 60 ppm of gold ions was. 3.0 g/L of the photocatalyst powder was mixed in plating wastewater, and mixed ultrasonically for 5 minutes and left for 15min in the dark for adsorption/desorption equilibrium, stirring it magnetically. Then the UV light was turned on for the photocatalytic reaction. The concentrations of gold ions remaining in the plating wastewater during different time intervals were detected with an AA spectrophotometer (Perkin-Elmer 5100 PC). Before the detection of metal ions, the solution was passed through a syringe filter having pore size of 0.2 um to remove photocatalyst particles. A scanning electron microscope (SEM) was used to investigate the remaining materials after evaporation of water. An EDX (Energy Dispersive X-ray Spectrometer) was used to confirm the composition of the recovered materials. An optical microscope was also used to examine the recovered gold after removing the ZnO powder.

3.4.3. Results and Discussion

As shown in fig. 18, the photocatalytic reaction using SCM ZnO nanopowder shows that the gold ions were completely recovered after 45min of UV irradiation. However, the photocatalytic reaction using the state of the art commercial TiO_2 (P-25 Degussa, Germany) shows that only 17% of the gold ions were recovered after identical treatment. The photocatalytic gold recovery efficiency of SCM ZnO nanopowder is about 6 fold higher compared to that of the state of the art commercial TiO_2 nanopowder. Furthermore, when 10% of methanol (CH_3OH) was added to the solution, the gold ions were completely recovered after 30min of UV irradiation. Here the methanol acts as hole scavenger. This hole scavenger improved the photocatalytic efficiency by 33%. This is a surprising result. As well-known, TiO_2 is the best photocatalyst of its kind.

As shown in fig. 19, large particles were observed after the photocatalytic reaction, but no particle was observed before it. Furthermore, the color difference was also observed. It was gold and gray before photocatalytic reaction. However, it showed a pure gold color after photocatalytic reaction. Figure 20 shows the schematic representation of above photocatalytic reaction. At first, the gold ions and ZnO nanopowders were mixed together (fig. 20(a)). Then the gold ions were adsorbed on the ZnO nanopowder surfaces (fig. 20(b)). Eventually, the

positive gold ions were reduced to neutral gold metal by receiving electrons that were generated on ZnO nanopowder surfaces by UV irradiation (fig. 20(c)). The SEM photograph of fig. 19(a) represents the state in which the gold ions and ZnO nanopowder were mixed together as shown in fig. 20(a). The SEM photograph of fig. 20(b) represents the state in which the gold ions were neutralized to gold metal on ZnO nanopowder surfaces as shown in fig. 20(c).

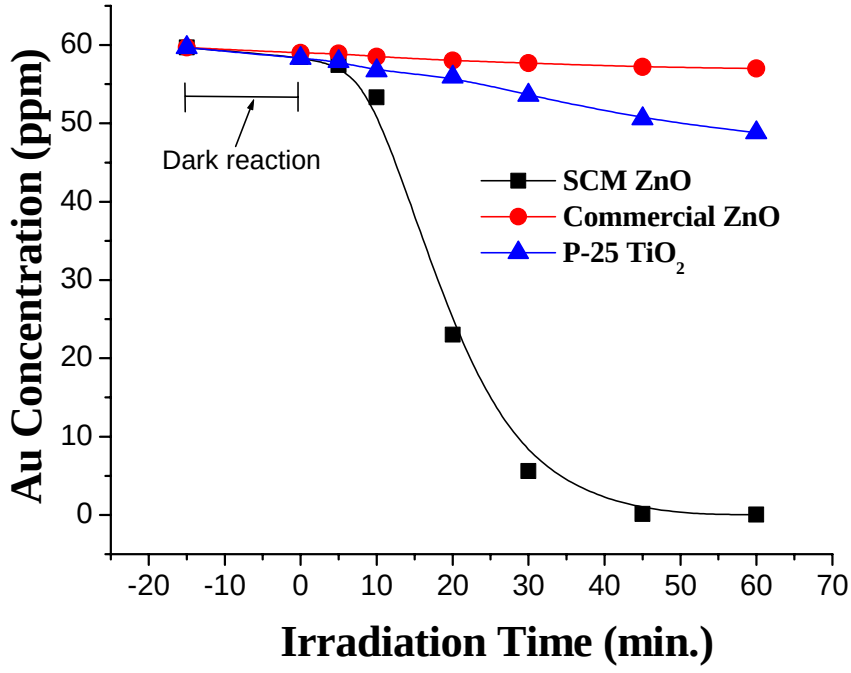

Figure 18. Au recovery rate by photocatalytic reaction of commercial ZnO (Junsei, Japan), commercial TiO_2 (P-25 Degussa, Germany) and the SCM ZnO powders synthesized in this study.

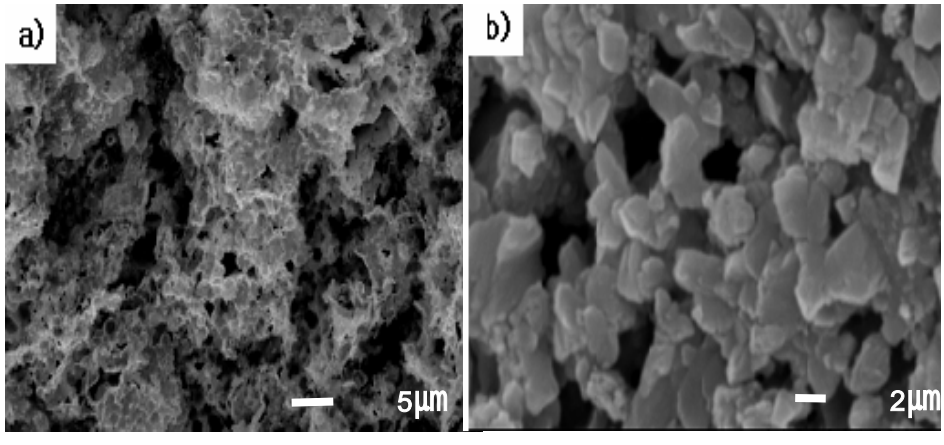

Figure 19. SEM photographs (a) before and (b) after photocatalytic reaction

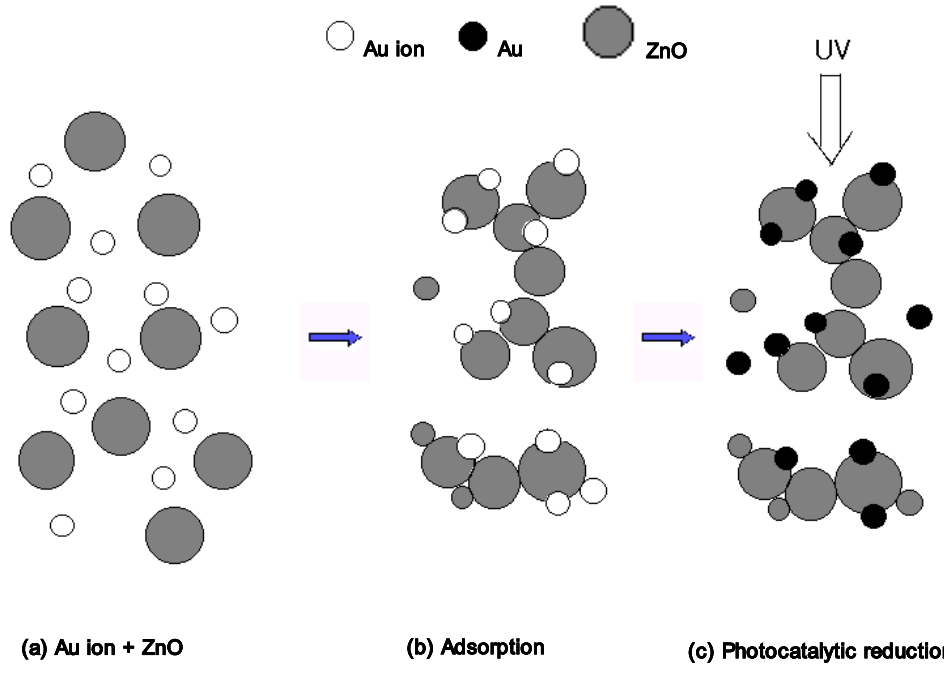

Figure 20. Schematic representation of photocatalytic reaction

EDX measurement was performed to confirm if this recovered metal was gold. Figure 21 showed weak gold peaks before photocatalytic reaction; however, it showed strong and sharp gold peaks after photocatalytic reaction. This suggests that photocatalytic reaction by SCM ZnO nanopowder produces gold particles from gold ions in solution. The calculation based on EDX measurement data showed that the purity of recovered gold was about 99.6% in weight% and 98.8% in atomic%.

Finally, the optical photograph of the recovered gold powder was obtained. Figure 22 clearly shows the recovered gold powders. The color is that of pure gold.

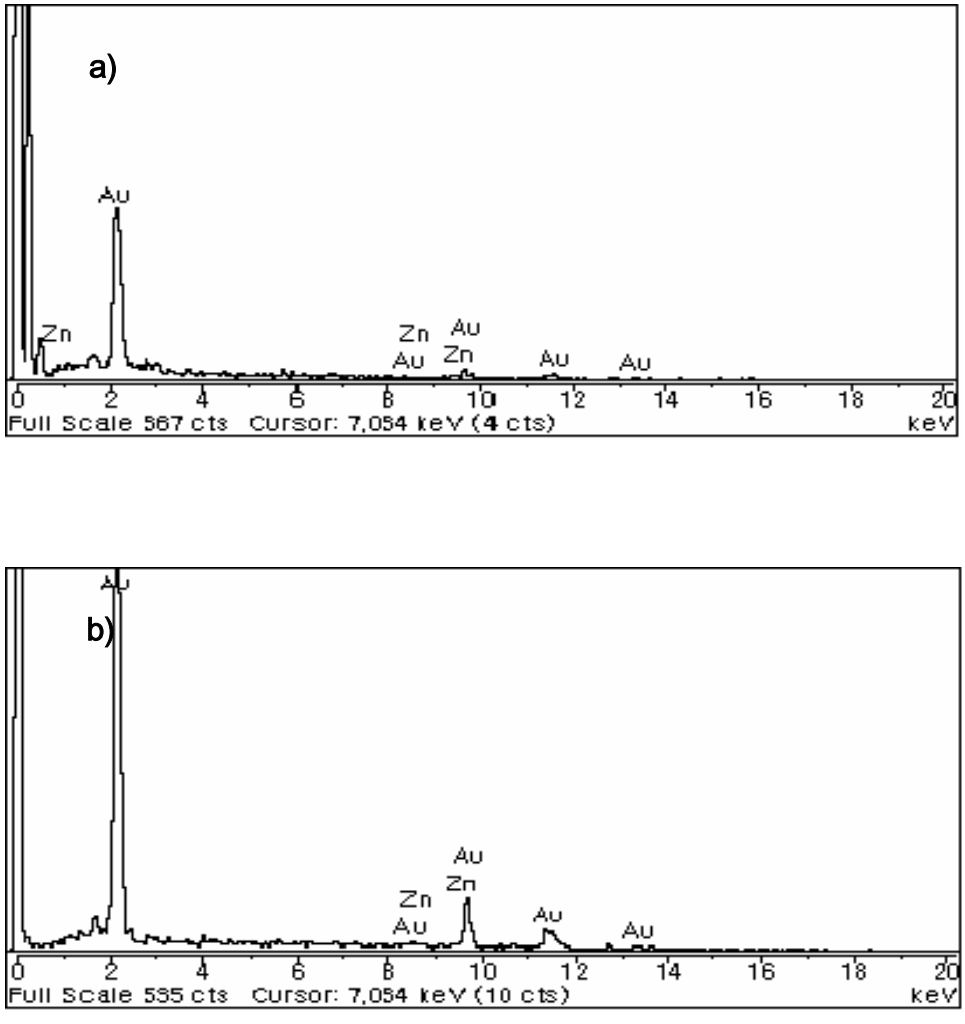

Figure 21. EDX patterns (a) before and (b) after photocatalytic reaction

Figure 22. Optical photograph of recovered Au after photocatalytic reaction

3.4.4. Summary

In this study, ZnO nanopowders were synthesized by SCM. The photocatalytic gold recovery efficiency of this SCM ZnO nanopowder was about 6 fold higher compared to that of state of the art commercial TiO_2 nanopowder.

The purity of recovered gold was about 99.6% in weight% and 98.8% in atomic%. Furthermore, the ZnO nanopowder method of synthesis and gold recovery process are very cost-effective. This technology is very viable in obtaining high purity gold from plating wastewater.

Photocatalytic reactivity seems to depend on the preparation method of photocatalytic powders rather than the crystalline phase, specific surface area or even kinds of material. Preparation methods affect surface properties such as surface defect levels. Generally it is known that smaller particle size results in more surface defects. In the present SCM ZnO case, however, the level of surface defects seemed to be minimized even though the powder was synthesized in nano-size. This might be due to the high synthesis temperature that reaches about 1500-1800^{o}C.

4. DESTRUCTION OF ORGANIC POLLUTANTS IN WASTEWATER

4.1. Background

The term ‘heterogeneous photocatalysis’ is associated with the process occurring in the intrinsic absorption band of semiconductor oxide catalyst, basically the oxides of titanium,

zinc and tin. [103-105]. Investigations in the field began as a result of the demand for the development of photochemical and photocatalytic methods for utilizing solar energy, widening the application of photoinduced reactions in chemical and environmental technologies. Recent studies mainly concentrate on environmental problems such as purification of contaminated water and air. Semiconductors for photocatalytic reactions should have conditions such as high photoactivity, high photostability, and high sensitivity for UV-visible light and low cost for manufacture. Oxide semiconductors are getting much attention as they have a wide band gap energy and are easy to handle.

These days nanoparticles are getting considerable attention, as they possess different physical and chemical properties compared to their bulk counterparts. Improved catalytic efficiency of the semiconductor system can be expected as the surface area and modified surface sites in such particles increase.

In this work, the photocatalytic characteristics of the SCM ZnO nanopowder were investigated through the attempts at removing the total organic carbon (TOC) content from the aqueous phenol solution.

4.2. Experiment

ZnO nanopowder was synthesized by the solution-combustion method as reported earlier. The powder was then used as a photocatalyst to remove the total organic carbon (TOC) from aqueous phenol solution using a batch reactor as shown in the schematic diagram of fig.13. It consisted of a tubular cylindrical reactor with a centrally mounted UV lamp. A jacketed cooling system was used for temperature control. The aqueous phenol solution was mixed with the ZnO nanopowder using a magnetic stirrer and the solution mixture was circulated in the reactor where the reaction took place. The removal rate of TOC using the above-prepared ZnO nanopowder was compared with other photocatalytic powders to measure its catalytic efficiency.

4.3. Results and Discussion

The average particle size of the above prepared powder was calculated from TEM images shown in fig. 23. Finest particles (30 nm) were obtained when $Zn(OH)_2$ and glycine as an oxidant and fuel (F/O=0.8) were used, respectively. Here, the powder had a uniform nanometer size and was spherical in shape. At the same time, the specific surface area of the powder was $120 m^2/g$. To prepare this powder, $Zn(OH)_2$ was dissolved in nitric acid solution to form zinc nitrate. Therefore, there would be excess nitrate (NO_3^-) groups in the solution. The (NO_3^-) group acts as an igniter for combustion, which presumably would be helpful for the fine particle size.

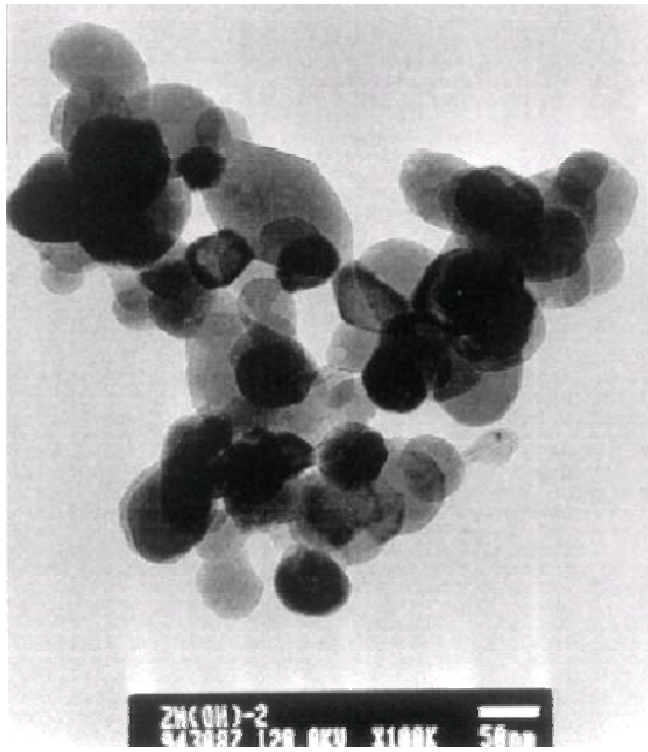

Figure 23. TEM image of the prepared ZnO nanopowder using glycine and $Zn(OH)_2$ (at the ratio of 0.8)

For the experiment, phenol was selected as a typical organic pollutant in water. Aqueous phenol solution of known concentration(~100ppm) was taken. We tried to degrade the phenol completely using the above mentioned ZnO nanopowder. Then its reaction rate was compared with other phtocatalysts to evaluate photocatalytic efficiency. The rates of reaction of different photocatalysts are shown in fig. 24. Here, ZnO nanopowder showed rapid photocatalytic reactions. When there was 300min of UV light irradiation, the nanotube type TiO_2 destroyed just 30% of phenol, P-25 TiO_2 nanopowder destroyed 50%, HPPLT TiO_2 nanopowder 60% and SCM ZnO nanopowder 80%. Therefore, SCM ZnO nanopowder shows 1.6 fold higher destruction rates of organic pollutants than P-25 TiO_2 nanopowder.

Here, small particle size might have led to greater photocatalytic efficiency. But the particle size may not be the only reason behind such a fast reaction rate. It might be strongly dependent on the UV absorption sensitivity of the prepared powder, which is supported by the PL measurement data.

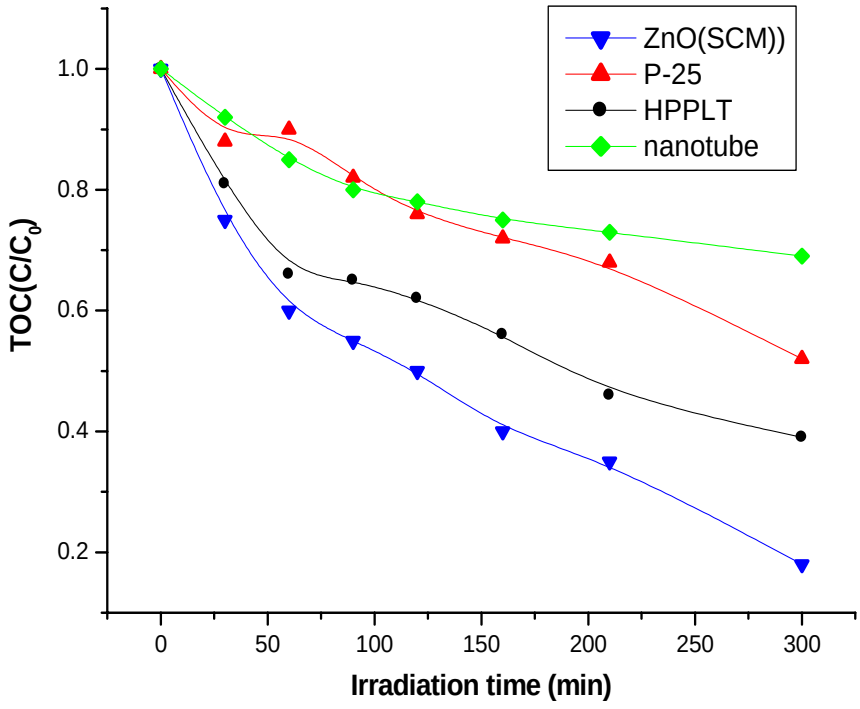

Figure 24. Comparison of TOC removal efficiency of the above prepared ZnO nanopowder with other powders and nanotube in the photocatalytic process

4.3. Summary

When SCM ZnO nanopowder was used as a photocatalyst to remove TOC from an aqueous phenol solution, the level of TOC in the solution decreased faster than other commercially available powders. This result confirms the outstanding photocatalytic characteristics of ZnO nanopowder synthesized using the solution combustion method. This result was strongly supported by the PL measurement data showing that the PL intensity of the ZnO powder was much higher than that of the commercial TiO_2 and ZnO powders. The high quality of the ZnO powder might be due to the defect removal by the high temperature generated during the synthesis process.

5. Summary and Conclusions

Zinc oxide is a large band-gap semiconductor having a bandgap energy of ~3.2 eV, which is similar to the bandgap energy of titanium dioxide, another prominent semiconductor photocatalyst used commercially in the removalof environmental pollutants. This study

mainly focused on the synthesis of zinc oxide powder having high photocatalytic activity. Commercial zinc oxide powder shows low photocatalytic activity for degradation of organic and inorganic pollutants as it contains many defect structures, which enhance the rate of recombination of the generated electron-hole pairs responsible for redox reactions during photocatalytic experiments.

To obtain defect free and high purity zinc oxide powder, a novel self-propagating process initiated at low temperature using redox compounds and mixtures in solution was investigated. The process makes use of highly exothermic redox chemical reactions between metals and non-metals. The method is referred to as the "solution-combustion method (SCM). The process is simple, fast, and cost-effective and yields high purity products compared to the conventional methods used to prepare the same material.

Two different fuels (reductants), glycine and carbohydrazide were used in varying proportions with oxidant precursors (zinc nitrate hexahydrate or zinc hydroxide dissolved in nitric acid to form zinc nitrate solution) to synthesize different powders. The fuel was mixed with a precursor dissolved in water and the mixture was heated to a temperature between 100-200^{0}C whereby a highly exothermic reaction took place with the formation of pure oxide powder of very fine morphology.

The formed zinc oxide powders were characterized using different powder evaluation techniques such as SEM, TEM, BET, XRD, and PL spectra measurements. SEM and TEM revealed the formation of uniform particle size in the nanometer range. Finest particles were obtained at the fuel: oxidant molar ratio of 0.8 when glycine and zinc hydroxide dissolved in nitric acid was used as a fuel and an oxidant, respectively. The finest particles were 30 nm and the surface area of the nanopowder was measured to be 120m^2/g. XRD measurement showed single-phase zinc oxide particles. PL spectra of the above-prepared nanopowder was taken and compared with the PL spectra of the commercial zinc oxide powder. The spectra revealed the defect free nature and high UV absorption capacity of the synthesized nanopowder.

To confirm photocatalytic activities of the synthesized ZnO powder, we tried to remove Ag ions from waste development solution. The Ag ions were completely removed within 15 min. This Ag recovery rate is at least 3 fold higher than that of commercial state of the art TiO_2.

The removal of copper ions from the aqueous solution of Cu-EDTA and lead ions from Pb-EDTA was carried out and the removal efficiency of the SCM ZnO nanopowder was again compared with the removal efficiencies of the P-25 TiO_2 and HPPLT TiO_2 powders. Here the removal efficiency of the SCM ZnO was at least 1.5 fold higher than the other photocatalyst powders.

The photocatalytic gold recovery efficiency by this SCM ZnO nanopowder was about 6 fold higher compared to the state of the art commercial TiO_2 nanopowder. The purity of the recovered gold was about 99.6% in weight% and 98.8% in atomic%. Furthermore, the ZnO nanopowder synthesizing method and gold recovery process are very cost-effective. Our attempts to recover gold metal ions took place in real plating wastewater, not simulated wastewater. This technology is therefore very viable in obtaining high purity gold from plating wastewater.

The synthesized nanopowder was then used in aqueous solutions for the degradation of representative organic pollutant, phenol (photocatalytic oxidation process) in aqueous

solution. A comparison of degradation rates shows SCM ZnO nanopowder has 1.6 fold higher destruction rates of organic pollutants than P-25 TiO_2 nanopowder.

Photocatalysis is a surface phenomena and the method of preparing the powder plays a vital role in obtaining efficient photocatalyst powder. Such a high photocatalytic efficiency of the SCM ZnO nanopowder was probably due to the same reason. The powder size was in the nanometer range and had a high surface area, which would have enhanced the adsorption of the substrate molecules. From the PL spectra, the powder showed no defect levels inside the bandgap region thus decreasing the recombination rate of the formed electron-hole pairs. As the PL intensity in the UV region was almost 3 fold higher than other photocatalyst powders, the SCM ZnO nanopowder would have absorbed more UV light, forming more electrons and holes in the conduction and valence band, which could either reduce or oxidize the substrate molecules having suitable redox potentials. All those favorable characteristics of the ZnO powder enhanced its photocatalytic efficiency and showed the highest efficiency for the degradation of organic contaminants and removal of heavy metal ions from aqueous solution.

Photocatalytic reaction using SCM ZnO nanopowders could be very valuable technology in view of the following two applications. Expensive noble metals such as silver and gold could be economically recovered using this technology while simultaneously removing toxic heavy metal ions and organic pollutants from wastewater for environmental purposes.

REFERENCES

[1] Levinson L. M. (Editor) (1988) *Electronic Ceramics - Properties, Devices, and Applications* (Marcel Dekker, Inc., New York).

[2] Wada K., Yoshida K., Takatani T.& Watanabe Y. “Selective photo-oxidation of light alkanes using solid metal oxide semiconductors.” (1993) *Appl. Catal. A- Gen.*, 99 (1) 21.

[3] Zin Z. C., Hamberg I. & Granqvist C. G. “Optical properties of sputter-deposited ZnO:Al thin films.” (1988) *J. Appl. Phys.*, 64, 5117.

[4] Li Y., Thompa G. S., Liang S., Gorla C., Lu Y.& Doyle J. “ Transparent and conductive Ga-doped ZnO films grown by low pressure metal organic chemical vapor deposition.” (1997) *J. Vac. Sci. Technol. A*, 15, 1063.

[5] Brown H. E. (1976) *Zinc oxide* (International Lead Zinc Research Organization, Inc., New York).

[6] Hirschwald W. H. et al. (1981) *Current Topics in Materials Science*, 7, Chapter 3, 143.

[7] Bagnall D. M., Chen Y. F., Zhu Z. Q., Yao T., Koyama S, Shen M. Y.& Goto T. “Optically pumped lasing of ZnO at room temperature.” (1997) *Appl. Phys. Lett.*, 70, 2230.

[8] Bagnall D. M, Chen Y. F., Zhu Z. Q., Yao T., Shen M. Y.& Goto T. “High temperature excitonic stimulated emission from ZnO epitaxial layers.” (1998) *Appl. Phys. Lett.*, 73, 1038.

[9] Mills A. & Hunte S. L. “An Overview of semiconductor photocatalysis.” (1997) *J. Photochem. Photobiol.*, 108, 1.

[10] Sehili T., Boule P.& Lemaire J. “Photocatalysed transformation of chloroaromatic derivatives on zinc oxide III: Dichlorobenzenes.” (1989) *J. Photochem. Photobio. A*, 50, 103.

[11] Villasenor J., Reyes P.& Pecchi G. “Photodegradation of pentachlorophenol on ZnO.” (1998) *J. Chem. Technol. Biotechnol.*, 72, 105.

[12] Driessen M. D., Miller T. M. & Grassian V. H. “Photocatalytic oxidation of trichloroethylene on zinc oxide : characterization of surface-bound and gas-phase products and intermediates with FT-IR spectroscopy.” (1998) *J. Mol. Catal. A: Chem.*, 131, 149.

[13] Khalil L. B., Mourad W. E. & Rophael M. W. “Photocatalytic reduction of environmental pollutant Cr(VI) over some semiconductors under UV/visible light illumination.” (1998) *Appl. Catal. B: Environ.*, 17, 267.

[14] Poulios I., Kositzi M. & Kouras A. “Photocatalytic decomposition of triclopyr over aqueous semiconductor suspensions.” (1998) *J. Photochem. Photobio. A:Chemistry* 115, 175.

[15] Mansilla H. D., Yeber M. C., Freer J., Rodriguez J. & Baeza J. “Homogeneous and heterogeneous advanced oxidation of a bleaching effluent from the plup and paper industry.” (1997) *Wat. Sci. Tech.*, 35 (4) 273.

[16] Sakthivel S., Neppolian B., Shankar M. V., Arabindoo B., Palanichamy M. & Murugesan V. “Solar photocatalytic degradation of azo dye: comparison of photocatalytic efficency of ZnO and TiO_2.” (2003) *Sol. Energy Mat. & Sol. Cells*, 77, 65.

[17] Li D. & Haneda H. “Morphologies of zinc oxide particles and their effects on photocatalysis.” (2003) *Chemosphere*, 51, 129.

[18] Muhammed M. “Gas phase synthesis and mechanical properties of nanomaterials.” (1996) *Analusis*, 24, M12.

[19] Liu T., Sakurai O., Mizutani N. & Kato M. “Preparation of spherical fine ZnO particles by the spray pyrolysis method using ultrasonic atomization techniques.” (1986) *J. Mater. Sci.*, 21, 3698.

[20] Westin G. & Nygren M. “On the formation of M^{2+}-Sb^{3+}-alkoxide precursors and sol-gel processing of M-Sb oxides with M=Cr,Mn,Fe,Co,Ni,Cu and Zn.”(1992) *J. Mater. Sci.*, 27, 1617.

[21] Westin G., Ekstrand A., Nygren M., Osterlund R. & Merkelbach E.A. “Preparation of ZnO-based varistors by the sol-gel technique.” (1994) *J. Mater. Chem.*, 4, 615.

[22] Meulenkamp E.A. “Synthesis and Growth of ZnO Nanoparticles.” (1998) *J. Phys. Chem. B*, 102, 5566.

[23] Chiou B., Tsai Y. J. & Duh J. “Thermal evolution in synthesized ZnO varistors by the urea process.” (1988) *J. Mater. Sci. Lett.*, 7, 785.

[24] Costa M. E. V. & Baptista J. L. “Characteristics of zinc oxide powders precipitated in the presence of alcohols and amines.”(1993) *J. Eur. Ceram. Soc.*, 11, 275.

[25] Sekar M. A. & Patil K. C. “Combustion synthesis and properties of fine-particle dielectric oxide materials.”(1992) *J. Mater. Chem.*, 2, 739.

[26] Dhas A & Patil K. C. “Combustion synthesis and properties of Zircornia-Alumina powders.” (1994) *Ceram. Int.*, 20, 57.

[27] Fumo D. A., Morelli M. R. & Segadaes A. M. “Combustion synthesis of Calcium Aluminates.” (1996) *Mater. Res. Bull.*, 31 (10) 1243.

[28] Park S., Lee K. R., Jung C. H., Kim S. J. & Shin H. C. "Preparation of $La_{0.84}Sr_{0.16}CrO_3$ powders by pH-controlled glycine-nitrate process."(1996) *Jpn. J. Appl. Phys.*, 35, L996.

[29] Park S., Park I. S., Kim S. J. & Lee B. H. "Sintering and electrical properties of $(CeO_2)_{0.9}(Gd_2O_3)_{0.1}$ powders prepared by glycine-nitrate process for solid oxide fuel cell applications." (1997) *Jpn. J. Appl. Phys.*, 36, 6426.

[30] Aruna S. T., Ghosh S. & Patil K. C. "Combustion synthesis and properties of $Ce_{1-x}Pr_xO_{2-\delta}$ red ceramic pigments." (2001) *Int. J. Inorg. Mater.*, 3, 387.

[31] Anuradha T. V., Ranganathan S., Mimani T. & Patil K. C. "Combustion synthesis of nanostructured Barium Titanate." (2001) *Scripta Mater.*, 44, 2237.

[32] Jain S. R., Adiga K. C. & Verneker V. R. P. "A new approach to thermochemical calculations of condensed fuel-oxidizer mixtures." (1981) *Combust. Flame*, 40, 71.

[33] Budavari S., O'Neil M. J., Smith A., Heckelman P. E. & Kinneary J. F. (1996) *The Merck Index, 12th ed.* (Merck & Co., Inc, New Jersey, p.1849).

[34] Parmon V. N. "Photocatalysis as a phenomenon : Aspects of terminology." (1997) *Catalysis Today*, 39, 137.

[35] Krasnovsky A. A. & Nikandrov V. V. "The Photobiocatalytic system : Inorganic semiconductors coupled to bacterial cells." (1987) *FEBS Letters*, 219 [1] 93.

[36] Farrauto R. J. & Heck R. M. "Environmental catalysis into the 21st century." (2000) *Catalysis Today*, 55, 179.

[37] Fujishima A. & Rao T. N. "Interfacial photochemistry: Fundamentals and applications." (1998) *Pure & Appl. Chem.*, 70, 2177.

[38] Lee S. H. & Lim H. S. "TiO_2-The principles and applications of photocatalytic reaction." (1999) *Ceramist*, 2 [2] 79 (in Korea).

[39] Zou Z., Ye J., Sayama K. & Arakawa H. "Direct splitting of water under visible light irradiation with an oxide semiconductor photocatalyst." (2001) *Nature*, 414, 625.

[40] Bahnemann D. W., Kholuiskaya S. N., Dillert R., Kulak A. I. & Kokorin A. I. "Photodestruction of dichloroacetic acid catalyzed by nano-sized TiO_2 particles." (2002) *Appl. Catal. B: Environ.*, 36, 161.

[41] Volodin A. M. "Photoinduced phenomena on the surface of wide-band-gap oxide catalysts." (2002) *Catalysis Today*, 58, 103.

[42] Chatterjee D. & Mahata A. "Demineralization of organic pollutants on the dye modified TiO_2 semiconductor particulate system using visible light." (2001) *Appl. Catal. B: Environ.*, 33, 119.

[43] Wilcoxon J. P., Thurston T. R. & Martin J. E. "Applications of metal and semiconductor nanoclusters as thermal and photo-catalysts." (1999) *Nanostructured Materials*, 12, 993.

[44] Carnes C. L. & Klabunde K. J. "Synthesis, isolation and chemical reactivity studies of nanocrystalline zinc oxide." (2000) *Langmuir*, 16, 3764.

[45] Wang L. & Muhammed M. "Synthesis of zinc oxide nanoparticles with controlled morphology." (1999) *J. Mater. Chem.*, 9, 2871.

[46] Vanheusden K., Seager C. H., Warren W. L., Tallant D. R., Caruso J., Hampden-Smith M. J. & Kodas T. T. "Green photoluminescence efficiency and free-carrier density in ZnO phosphor powders prepared by spray pyrolysis." (1997) *J. Lumin.*., 75, 11.

[47] Chu S. Y., Yan T. M. & Chen S. L. "Characteristics of sol-gel synthesis of ZnO-based powders." (2000) *J. Mater. Sci. Lett.*, 19 [4] 349.

[48] Park S., Kim S. J., Lee B. H. & Park I. S. "Sintering and electrical properties of $(CeO_2)_{0.9}(Gd_2O_3)_{0.1}$ powders prepared by glycine-nitrate process for solid oxide fuel cell applications." (1997) *Jpn. J. Appl. Phys.*, 36, 6426.

[49] Park S., Lee H. W., Song J. S., Kim W. W. & Lee C. R. "Synthesis and Ag recovery of nanosized ZnO powder by solution combustion process for photocatalytic applications." (2001) *Journal of Materials Synthesis and Processing*, 9 [5] 281.

[50] Park S., Song J. S. & Lee K. R. "Characteristics of $La_{0.7}Ca_{0.3}MnO_3$ powders prepared by solution combustion method and solid state reaction method for CMR applications." (2002) *Journal of Materials Synthesis and Processing*, 10 [1] 47.

[51] Ilisz, Laszio Z.& Dombi A., "Investigation of the photodecomposition of phenol in near-UV-irradiated aqueous TiO_2 suspensions. I: Effect of charge-trapping species on the degradation kinetics." (1999) *Appl. Catal. A: Gen*., 180, 25.

[52] Chen D. & Ray A.K. "Photocatalytic kinetics of phenol and its derivatives over UV irradiated TiO_2." (1999) *Appl. Catal. B: Environ*., 23, 143.

[53] Li X., Cubbage J. W., Tetzlaff T. A.& Jenks W. S. "Photocatalytic degradation of 4-chlorophenol: 1. The hydroquinone pathway." (1999*) J. Org. Chem*., 64 (23) 8509.

[54] Li X., Cubbage J. W., Tetzlaff T. A. & Jenks W. S. "Photocatalytic Degradation of 4-chlorocatechol: 2. The 4-Chlorocatechol Pathway." (1999) *J. Org. Chem.*, 64 (23) 8525.

[55] Mills A. & Sawunyama P. "Photocatalytic degration of 4-chlorophenol mediated by TiO_2: a comparative study of the activity of laboratory made and commercial TiO_2 samples." (1994) *J. Photochem. Photobiol. A: Chem.*, 84, 305.

[56] Serpone N., Boragarello E. & Pelizzette E. (1988) *In M. Schiavelb (Ed.), Photocatalysis and Environment, Trends and Applications*, (Dordrecht: Kluwer p. 527).

[57] Beydoun D., Amal R., Low G. & McEvoy S., "Role of nanoparticles in photocatalysis" (1999) *J. Nanoparticle Res.*, 1 (4) 439.

[58] Lee K. R., Kim S. J., Song J. S., Lee J. H., Chung Y. J. & Park S. "Photocatalytic characteristics of nanometer-sized titania powders fabricated by a homogeneous-precipitation process." (2002) *J. Am. Ceram. Soc.* 85 (2) 341.

[59] Hoffmann M. Z., Prasad D. R., Jones II G. & Malba V. "Formation of photoactive charge-transfer complexes between methyl viologen and sacrifical electron donors. EDTA and triethanolamine." (1983) *J. Am. Chem. Soc.*, 105, 6360.

[60] Ayres J. A. (1970) *Decontamination of Nuclear Reactors and Equipment* (Ronald, New York, p.6)

[61] Loy L. & Wolf E. E. "Photo induced hydrogen evolution from water in the presence of EDTA and a Pt/TiO_2 supported catalyst." (1985) *Sol. Energy* 34 (6) 455.

[62] Matthews R. W. & McEvoy S. R. "A comparison of 254 nm and 350 nm excitation of TiO_2 in simple photocatalytic reactors." (1992) *J. Photochem. Photobiol. A: Chem.*, 66, 355.

[63] Ollis D. F., Pellizetti E. & Serpone N. (1989) *Heterogeneous Photocatalysis in Water Purification* (Wiley, New York).

[64] Fujisima A.& Rao T. N. "Interfacial photochemistry: fundamental and applications" (1998) *Pure & Appl. Chem.*, 70 (11) 2177.

[65] Lee S. H.& Lim H. S. "Principles and applications of TiO_2-photocatalytic reactions" (1999) *Ceramist* 2, 79 (in Korean).

[66] Lawless D., Res A., Harris R., Serpone N., Minero C., Pelizzetti E. & Hidaka H. “Removal of toxic metal from solutions by photocatalysis using irradiated platinized titanium dioxide: removal of lead.” (1990*) Chim. & Ind. (Milan)* 72, 139.

[67] Tennakone & Wijayantha K.G.U. “Heavy-metal extraction from aqueous solution with an immobilized TiO_2 photocatalyst and a solid sacrificial agent.” (1998) *J. Photochem. Photobiol. A: Chem.,* 113, 89.

[68] Muhammad S. V. & Allen P. D., “TiO_2-assisted photocatalysis of lead-EDTA” (2000) *Wat. Res.,* 34 (3) 952.

[69] Loy E.E. Wolf, “Photo induced hydrogen evolution from water in the presence of EDTA and a Pt/TiO_2 supported catalyst.” (1985) *Sol. Energy* 34 (6) 455.

[70] Aguado M. A., Gimenez J. & Cervera-March S. "Continuous photocatalytic treatment of chromium(VI) effluents with semiconductor powders." (1991) *Chem. Eng. Commum.,* 104, 71.

[71] Garcia Gonzalez M. L. & Salvador P. "Titanium dioxide photoetching mechanisms: efficient photocatalytic corrosion of rutile in the presence of dichromate." (1992) *J. Electroanal. Chem.,* 326, no. 1-2: 323.

[72] Prairie M. R., Evans L. R. & Martinez S. L. "Destruction of organics and removal of heavy metals in water via TiO_2 photocatalysis." (1992) *Chemical Oxidation: Technology for the Nineties, Second Int. Symp. Nashville, Tennessee,* 19 February.

[73] Prairie M. R., Evans L. R., Stange B. M., & Martinez S. L. "An investigation of TiO_2 photocatalysis for the treatment of water contaminated with metals and organic chemicals." (1993) *Environ. Sci. Technol.,* 27, no. 9: 1776.

[74] Sabate J., Anderson M. A., Aguado M. A., Gimenez J., Cervera-March S. & Hill Jr. C. G. "Comparison of TiO_2 powder suspensions and TiO_2 ceramic membranes supported on glass as photocatalytic systems in the reduction of chromium(VI)." (1992) *J. Mol. Cat.,* 71, 57.

[75] Yoneyama H., Matsumoto N., Furusawa T. & Tamura H. "Temperature dependence on the rate of heterogeneous reactions on titanium(N) oxide photocatalysts." (1984) *Nippon Kagaku Kaishi,* no. 2 253.

[76] Zhang C., Jiarg Y., Liu W., Yang H., Li T. & Xiao L. "Study of titania ultrafine powder photocatalyst in reducing dichromate(Cr2O72-)." (1991) *Taniyangneng Xuebao 12,* no. 2 176.

[77] Bideau M., Claudel B., Faure L. & Kazouan H. "The photooxidation of propionic acid by oxygen in the presence of titania and dissolved copper ions." (1992) *J. Photochem. Photobiol., A* 67 no. 3, 337.

[78] Butler E. C. & Davis A. P. "Photocatalytic oxidation in aqueous titanium dioxide suspensions: the influence of dissolved transition metals." (1993) *J. Photochem. Photobiol. A: Chem.,* 70, 273.

[79] Reiche H., Dunn W. W. & Bard A. J. "Heterogeneous photocatalytic and photosynthetic deposition of copper on titanium dioxide and tungsten(VI) oxide powders." (1979) *J. Phys. Chem.,* 83, no. 17 2248.

[80] Bideau M., Claudel B., Faure L. & Kazouan H. "The photooxidation of acetic acid by oxygen in the presence of titanium dioxide and dissolved copper ions." (1991) *J. Photochem. Photobiol., A* 61, no. 2 269.

[81] Bideau M., Claudel B., Faure L. & Rachimoellah M. "Photooxidation of formic acid by oxygen in the presence of titanium dioxide and dissolved copper ions: oxygen transfer and reaction kinetics." (1990) *Chem. Eng. Commun.*, 93, 167.

[82] Lawless D., Res A., Harris R., Serpone N., Minero C., Pelizzetti E. & Hidaka H. "Removal of toxic metal from solutions by photocatalysis using irradiated platinized titanium dioxide: removal of lead." (1990) *Chim. Ind.* 72, no. 2 139.

[83] Torres J. & Cervera-March S. "Kinetics of the photoassiated catalytic oxidation of lead(II) in titania suspensions." (1992) *Chem. Eng. Sci.*, 47, no. 15-16, 3857.

[84] Prairie M. R., Pacheco J. & Evans L. R. *"Solar detoxification of water containing chlorinated solvents and heavy metals via TiO_2 photocatalysis."* (1992) Proc. of ASME Int. Sol. Engineering conf. 2 April 1992. Solar Engineering 92, Stein, W., Kreider, J., and Watanabe, K., Eds. New York, NY, ASME 1.

[85] Serpone N., Ah-You Y. K., Tran T. P., Harris R., Pelizzetti E. & Hidaka H. "AM1 simulated sunlight photoreduction and elimination of mercury(+2) and methylmercury (CH3Hg)(+2) chloride salts from aqueous suspensions of titanium dioxide." (1987) *Sol. Energy* 39, no. 6, 491.

[86] Hutchinson B., Cockrum D., Clark C., Pamplin K., Scoggins T., Sloan D. & Reeves P. "Photocatalytic destruction of toxic organic compounds in aqueous solution."(1990) *Sol. 90 Conf.* Austin, Texas, March.

[87] Tennakone K., Thaminimulle C. T. K., Senadeera S. & Kumarasinghe A. R. "TiO_2-catalyzed oxidative photodegradation of mercurochrome: an example of an organo-mercury compound." (1993) *J. Photochem. Photobiol., A* 70, no. 2, 193.

[88] Baciocchi E., Rol C., Rosato G. C. & Sebastiani G. V. "Titanium dioxide photocatalyzed oxidation of benzyltrimethylsilane in the presence of silver sulfate." (1992) *J. Chem. Soc., Chem. Commun.*, no. 1, 59.

[89] Kobayakawa K., Nakazawa Y., Ikeda M., Sato Y. & Fujishima A. "Influence of the density of surface hydroxyl groups on TiO_2 photocatalytic activities." (1990) *Ber. Bunsenges. Phys. Chem.*, 94, 1439.

[90] Ohtani B., Kakimoto M., Miyadzu H., Nishimoto S. & Kagiya T. "Effect of surface-adsorbed 2*propanol on the photocatalytic reduction of silver and/or nitrate ions in acidic TiO_2 suspension." (1988) *J. Phys. Chem.*, 92, 5773.

[91] Ohtani B., Zhang S., Handa J., Kajiwara H., Nishimoto S. & Kagiya T. "Photocatalytic activity of titanium(N) oxide prepared from titanium(N) tetra-2-propoxide: reaction in aqueous silver salt solutions." (1992) *J. Photochem. Photobiol. A: Chem.*, 64, 223.

[92] Ohtsni B. & Nishimoto S. "Effect of surface adsorptions of aliphatic alcohols and silver ion on the photocatalytic activity of titania suspended in aqueous solutions." (1993) *J. Phys. Chem.*, 97, no. 4, 920.

[93] Pelizzetti E., Borgarello M., Minero C., Pramauro E., Borgarello E. & Serpone N. "Photocatalytic degradation of polychlorinated dioxins and polychlorinated biphenyls in aqueous suspensions of semiconductors irradiated solar light." (1988) *Chemosphere 17*, no. 3, 499.

[94] Sakata T., Kawai T. & Hashimoto K, "Heterogeneous photocatalytic reactions of organic acids and water. New reaction paths besides the photo-Kolbe reaction." (1984) *J. Phys. Chem.* 88, 2344.

[95] Sato S. & Kadowaki T. "Photoevolution of oxygen from metal oxide semiconductor suspension in aqueous silver salt solution." (1989) *Denki Kagaku oyobi Kogyo Butsuri Kagaku* 57, no. 12, 1151.

[96] Sato S., Sobczynski A., White J. M., Bard A. J., Campion A., Fox M. A., Mallouk T. E. & Webber S. E. "Photochemical properties of ultrathin titaium dioxide films prepared by chemical vapor deposition." (1989) *J. Photochem. Photobiol., A* 50, no. 2, 283.

[97] Sclafani A., Palmisano L. & Davi E. "Photocatalytic degradation of phenol by TiO_2 aqueous dispersions: Rutile and anatase activity." (1990) *New J. Chem.*, 14, 265.

[98] Sclafani A., Palmisano L. & Davi E. "Photocatalytic degradation of phenol in aqueous polychrystalline TiO_2 dispersions: The influence of Fe(+3), Fe(+2), and Ag(+) on the reaction rate." (1991) *J. Photochem. Photobiol. A: Chem.*, 56, 113.

[99] Sclafani A., Mozzanega M. N. & Pichat P. "Effect of silver deposits on the Photocatalytic activity of titanium dioxide samples for the dehydrogenation or oxidation of 2-propanol." (1991) *J. Photochem. Photobiol. A : Chem.*, 59, no. 2, 181.

[100] Wakoh H., Honda K. & Fujishima A. "Photocatalytic properties of titanium oxide powders." (1989) *Kenkyu Hokoku - Kanagawa - ken Kogyo Shikensho*, no. 60, 68.

[101] Peral J. & Domenech X. "Photocatalytic cyanide oxidation from aqueous copper cyanide solutions over titania and zinc oxide." (1992) *J. Chem. Technol. Biotechnol.* 53, no. 1, 93.

[102] Park S., Lee K. R., Lee K. W. & Lee J. H. “Rapid Ag recovery using photocatalytic ZnO nanopowders prepared by solution combustion method.” (2003) *J. Mater. Sci. Lett.*, 22, 65.

[103] Bickley R. L., (1982) *Catalysis*, (Specialist Periodical Report) Vol 5, The Royal Society of Chemistry, London, 308.

[104] Formenti M. & Teichner S. J. (1978) *Catalysis*, (Specialist Periodical Report) Vol 2, The Chemical Society, London, 87.

[105] Yesodharan E. P., Ramakrishnan V. & Kuriacose J. C. “Photoinduced heterogeneous catalysis” (1976) *J. Sci. Ind. Res.*, 35, 712.

In: Nanomaterials: New Research
Editor: B.M. Caruta, pp. 169-195
ISBN: 1-59454-369-0

Chapter 5

AL-BASED AMORPHOUS AND NANOCRYSTALLINE ALLOYS

Q. Jiang [*] ***and J. C. Li***
Key Laboratory of Automobile Materials (Jilin University),
Ministry of Education, and Department of Materials Science and Engineering,
Jilin University, Changchun 130025, China

ABSTRACT

Aluminum alloys have received considerable attention especially in automobile and aerospace industries due to their high specific strengths. However, the use of these conventional strengthening mechanisms leads to an upper limit of tensile fracture strength of about 600 MPa. To obtain higher tensile strength, new strengthening mechanisms must be utilized. In this chapter, the recent progresses on manufacturing and processing of Al-based amorphous and nanocrystalline alloys with high strength, such as that of AlSi alloys, AlCeMn alloys and AlLaNi alloys, are introduced. In addition, the related microstructures, mechanical and thermal properties of these alloys are also described. Moreover, the considerations on further development for consolidation processes and other possible ways to develop new Al-based alloys with high strength and good toughness are indicated.

1. INTRODUCTION

Considerable efforts have been devoted to the development of novel lightweight engineering materials during the last decades. Al-based alloys have received great attention especially in automobile and aerospace industries due to their high specific strengths. Most works concerned with Al-based alloys are further increase of the specific strengths. It is well

[*] Author to whom all correspondence should be addressed. Fax: +86-431-5095876. E-mail: jiangq@jlu.edu.cn (Q. Jiang)

known that ordinary high strength Al-based alloys have been developed by the use of the following conventional strengthening mechanisms; i.e. solid solution, precipitation, grain size refinement, dispersion, work hardening and fiber reinforcement. However, the uses of these conventional solid solution strengthening and grain size refinement strengthening mechanisms lead to an upper limit of tensile fracture strength of about 600 MPa, and precipitation, work hardening and fiber reinforcement decrease largely the plasticity and toughness of alloys. If a new Al-based alloy with higher tensile strength would be fabricated, new strengthening mechanisms must be utilized.

Since the first synthesis of an amorphous phase in an Au-Si system by rapid solidification in 1960 [1], a great number of amorphous alloys have been synthesized by various preparation methods of rapid quenching from liquid or vapor and of solid-state reactions [2-5]. The formation of Al-based amorphous alloys by liquid quenching has been tried in binary alloys of Al-metalloid and Al-transition metal systems. A co-existing structure of amorphous and crystalline phases in Al-Si [6], Al-Ge [7] and Al-Cu [8], Al-Ni [9], Al-Cr [10] and Al-Pd [11] alloys can be built only near the holes in their thin foils prepared by the gun quenching technique in which the cooling rate is higher than that of the melt spinning method. However, no single amorphous phase was prepared by melt spinning as well as by the gun- and piston-anvil methods. The first formation of a single amorphous phase in Al-based alloys containing more than 50% Al was found in 1981 for Al-Fe-B and Al-Co-B ternary alloys [12]. Subsequently, Al-Fe-Si, Al-Fe-Ge and Al-Mn-Si amorphous alloys were also found by the melt-spun technique [13, 14]. During the last decade, some researchers have paid attention to non-periodic structures such as amorphous and icosahedral phases, with which the tensile strengths of the corresponding alloys exceed 1000 MPa [15-17]. Structure and mechanical properties of Al based alloys developed are summarized in Fig. 1.

For an industrial alloy, Al based alloys must retain their low specific weight, which leads to the requirement of further increase of percentage of Al element in the alloy. In 1987, Al-Ni-Si and Al-Ni-Ge alloys with about 80% Al in amorphous structure with good bending ductility were discovered [18]. The further decrease of metalloid elements in the alloys results in improvement of glass-forming ability and that of mechanical strength [19-22].

Since the limitation of the maximum thickness of amorphous ribbons has prevented a wide extension of application fields, especially for structural materials, great efforts have been devoted to prepare bulk amorphous alloys [23-24]. The bulk amorphous alloys can be made from powders (vapor condensed powders, atomized alloyed powders or mechanically alloyed powders), or melt-spun alloy ribbons, by using various techniques of warm pressing, warm extrusion, explosive compaction etc. [23-24]. These powders or ribbons have metastable structures consisting of amorphous, quasicrystalline and nanocrystalline phases. The subsequent condensation of these raw materials into a bulk form is done at elevated temperatures, leading to a structural change into various nanogranular structures. These bulk nanostructured alloys exhibit good mechanical and physical properties and can be used as structural materials. However, the obtained bulk alloys have lower mechanical, chemical and soft magnetic properties than the corresponding melt-spun amorphous ribbons [25]. Bulk nanocrystalline alloys with a mixed structure of intermetallic compounds embedded fcc-Al or α-Al matrix by the crystallization of Al-based amorphous phase have already been investigated [26]. The bulk nanostructured alloys exhibits high mechanical strength of 700-1000 MPa and have been commercialized with a commercial name of GIGAS [27]. Subsequently, the researched results have been reported that bulk nano-quasi-crystalline

alloys in Al-based system exhibit a good combination of high tensile strength, large elongation, high fatigue strength and high elevated-temperature strength [28].

In this review, recent progresses on manufacturing and processing of Al-based amorphous and nanocrystalline alloys with high strength, such as that of AlSi alloys, AlCeMn alloys and AlLaNi alloys, are introduced. In addition, the related microstructures, mechanical and thermal properties of these alloys are also described. Moreover, the considerations on further development for consolidation processes and other possible ways to develop new Al-based alloys with high strength and good toughness are given.

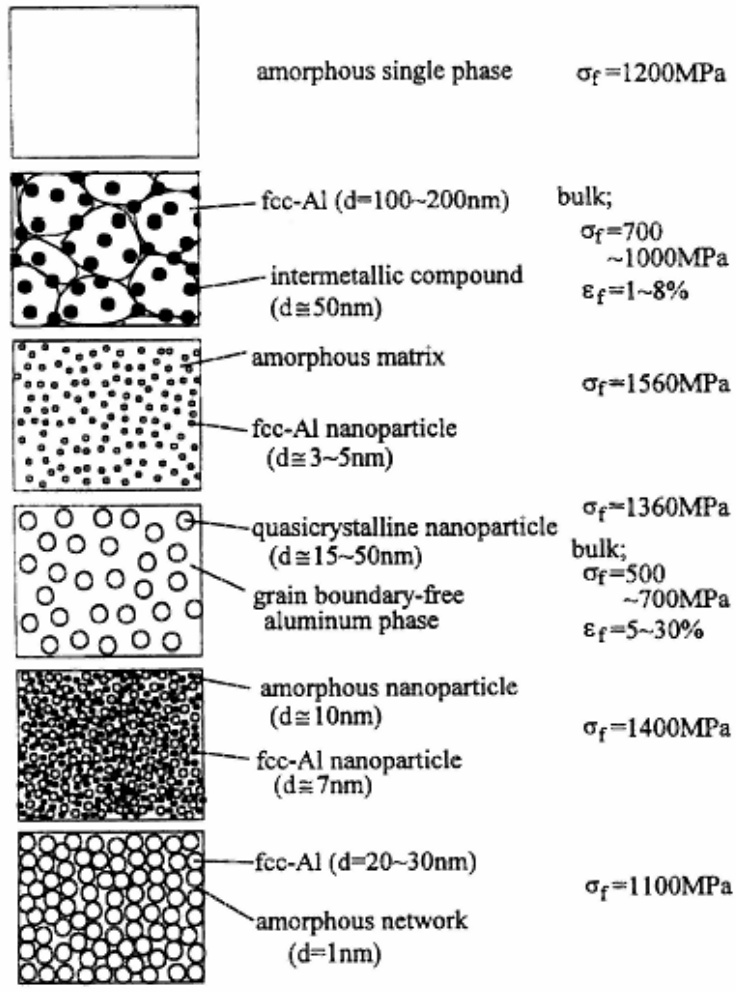

Figure 1. Microstructure and mechanical strength of aluminum base alloys developed for the last decade [18].

2. AL-SI AMORPHOUS ALLOY BY MELT SPINNING METHOD

Although an Al-Si binary alloy has a wide industrial application with lower cost, it has not been paid great attention since the eutectic Al-Si alloy has a bad glass forming ability (GFA) while a eutectic alloy should have the best GFA among the alloy system due to its lowest melting point. Although ternary Al-Fe-Si, Al-Fe-Ge and Al-Mn-Si alloys have amorphous structure by the melt-spun technique [29-30], the structures of binary Al-Si [31] and Al-Ge [7] alloys through a gun quenching technique are mixtures of amorphous and crystalline phases where the amorphous phase is unstable and crystallize even at room temperature. However, according to a polymorphous diagram of Al-Si system, which is schematically shown in Fig. 2, when the composition range of Si% (atom percentage) is located between 25% and 45%, amorphous phases may be formed from liquid with a high cooling rate where the polymorphous crystallization is absent [32-33]. The model predictions for the largest solubility of elemental crystals based on a consideration on a binary chemically random solid solution with local strain instability are also given in the figure with the following equation [34-35],

$$C^*_A \approx 2\lambda R_B^3 / \left| R_B^3 - R_A^3 \right|, \quad (1)$$

$$C^*_B \approx 2\lambda R_A^3 / \left| R_B^3 - R_A^3 \right|, \quad (2)$$

where C^*_A is the maximal solubility of A atom with an atom radius of R_A in a B solution with an atom radius R_B and C^*_B denotes the same meaning for that of the B atom in A solution. λ is a constant. When C_B is located within $C^*_B < C_B < 1 - C^*_A$, the solution becomes topologically unstable and thus has the possibility to form glass. Substituting λ = 0.05 [34], R_{Al} = 0.143 nm and R_{Si} = 0.118 nm [37] into Eqs. (1) and (2), C^*_{Al} = 12.8% and C^*_{Si} = 22.9% are obtained. Thus, there is a possibility to form glasses within the composition range of 22.9% $< C_{Si} <$ 87.2%. When a cooling rate used is not large enough, a structure consisting of amorphous phase and supersaturated nanocrystals should be present [38], which is the case of an $Al_{88}Si_{12}$ eutectic alloy [39]. Note that as C_{Si} increases, the liquidus line of Al-Si system increases quickly due to the large difference of melting temperatures between Al and Si, which is favorable for the primary crystallization of Si during the liquid quenching, C_{Si} should be as low as possible for glass production in the above composition range.

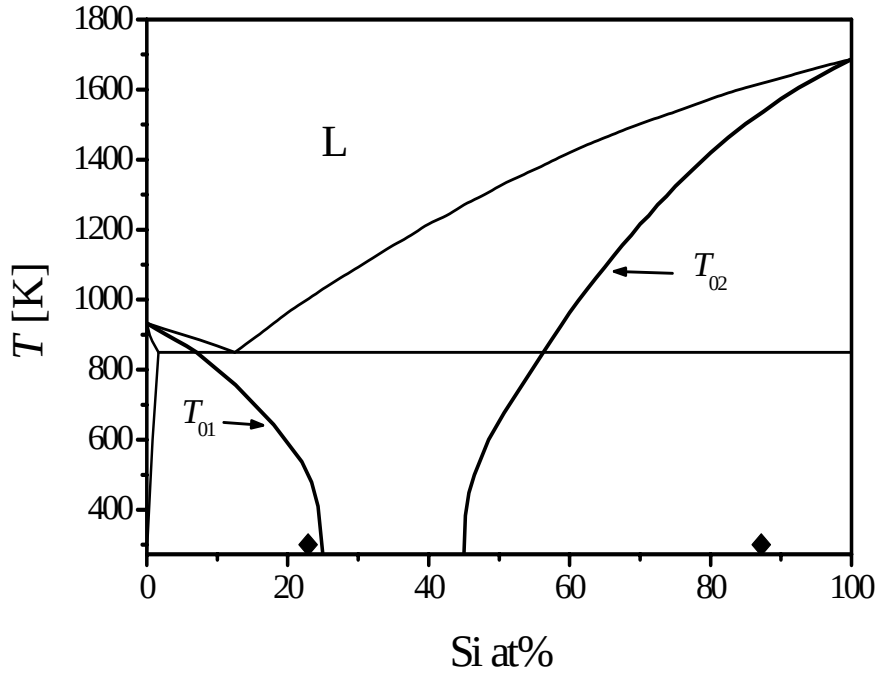

Figure 2. A schematic polymorphous phase diagram of Al-Si system. T_{01} and T_{02} are polymorphous lines for Al and Si solutions [32-33], which are simply plotted in the middle between the solidus lines and the liquidus lines of each component and extended to the solid zone along the original slopes. The symbol ◆ at Si% = 22.9% and Si% = 87.2% denotes the critical solubility determined by Egami's theory [34-35]. The equilibrium binary Al-Si phase diagram is cited from Ref. [36].

Based on the above consideration, $Al_{55}Si_{45}$, $Al_{60}Si_{40}$, $Al_{65}Si_{35}$, $Al_{70}Si_{30}$ and $Al_{75}Si_{25}$ alloys are selected to study GFA of the alloys by the melt spinning technique. It is found that although all alloys consist of embedded supersaturated α-Al nanocrystals, primary Si nanocrystals and amorphous matrix, the relative amounts of them in the alloys are composition dependent.

The alloy ingots with different compositions $Al_{75}Si_{25}$, $Al_{70}Si_{30}$, $Al_{65}Si_{35}$, $Al_{60}Si_{40}$, and $Al_{55}Si_{45}$ were prepared by arc melting of the mixture of Al (99.997%) and Si (99.9%) elements in argon atmosphere. Ribbon samples with 20-30 μm in thickness and 2.0 mm in width were obtained by the melt spinning technique.

TEM micrographs of five kinds of the quenched Al-Si alloys are shown in Fig. 3. The alloys consist of the matrix marked as "A" and the primary Si marked as "B" in micrometer size. The pattern of SAED made by TEM on the primary Si is marked as "B". The primary Si is always present by the melt spinning technique due to the high primary crystallization temperature of the alloy in about 1150 K (see Fig. 2). However, the diffraction ring on Fig. 3a indicates that the primary Si has a fine structure. When the structure of the matrix is further magnified as shown in Fig. 3b, the matrix itself consists of a matrix and uniformly distributed nanoparticles without clear interfaces between them. The pattern of SAED on the matrix

shown in Fig. 3b indicates that the α-Al nanoparticles are embedded in amorphous matrix where the tropism of the α-Al particles is stochastic [40]. Indexing the rings of the diffraction patterns associated to primary Si (Fig. 3a) and Al nanocrystals embedded in amorphous matrix (Fig. 3b) can support the above conclusions on microstructures of the alloys. Note that although the ring patterns taken from diamond structure or fcc structure can look similar, an additional index of (200) of Al can be found in Fig. 3b. This result differs from the early work where no amorphous phases are found in $Al_{70}Si_{30}$ alloy possibly due to different cooling rates during the manufacture of the alloy [41]. The x-ray diffraction result of Fig. 4 shows also a widening of α-Al diffraction peak, which is in agreement with the diffraction pattern of Fig. 3b, both imply that α-Al is in nanometer size range.

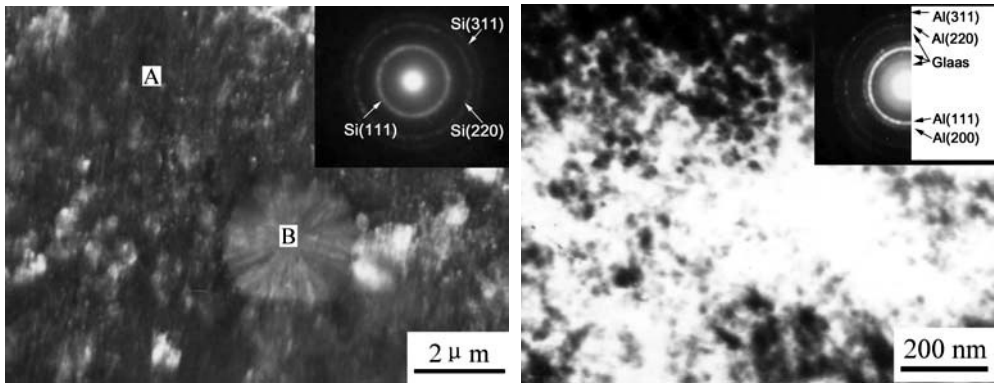

Figure 3. TEM dark field image of the $Al_{60}Si_{40}$ sample and its SAED pattern on the "B" (a), TEM bright field image of the matrix and its SAED pattern (b) where the matrix and the primary Si have marked as "A" and "B" in the (a).

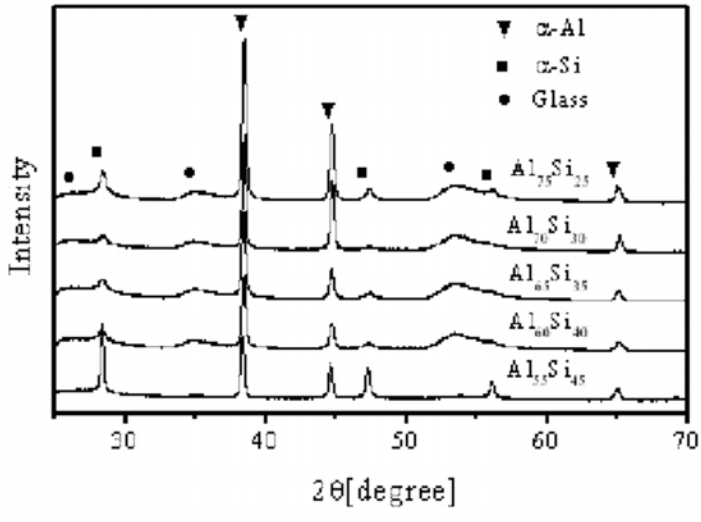

Figure 4. X-ray diffraction curves of the Al-Si alloys

X-ray diffraction curves of five kinds of Al-Si alloys is present in Fig. 4 where the intensity of the Si diffraction peak does not monotonously increase as Si% increases. Integral intensity percentage of each phase is determined based on the XRD curves in Fig. 4, which is shown in Fig. 5. When $30\% \le C_{Si} \le 40\%$, integral intensity percentages of the α-Si or α-Al phases are smaller than that when C_{Si} = 25% and C_{Si} = 45% while the quantities of amorphous phase have a reverse tendency. This result implies that Al-Si alloy in a composition range of $30\% < C_{Si} < 40\%$ has better GFA than that in other composition ranges. Since the solubility of the α-Si or α-Al is limited [34], as C_{Si} increases to 40%, the percentage of Si crystals in the amorphous matrix increases.

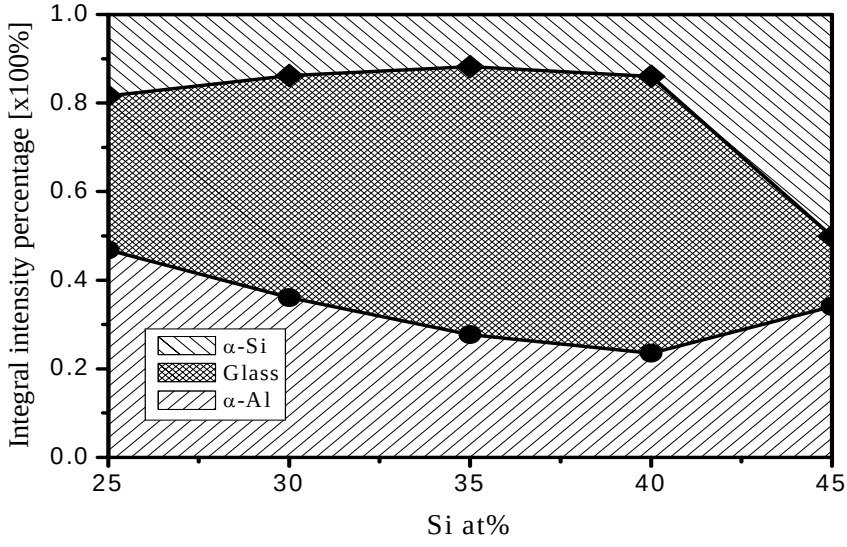

Figure 5. Integral intensity percentage of each phase in the alloys for XRD curves in Fig. 4.

Fig. 6 shows DSC traces of alloys where there are two exothermic peaks in all measured curves. T_{ons} and heat flow (H_{out}) of these peaks are shown in Fig. 7. $H_{out\ 1}$ and $H_{out\ 2}$ denoting the first and the second peaks in the curves have contrary trends as C_{Si} increases where $H_{out\ 1}$ decreases and $H_{out\ 2}$ increases. $T_{ons\ 1} \approx 0.4\sim0.5T_{m\ Al}$ ($T_{m\ Al}$ = 933 K is the melting point of aluminum) and the $T_{ons\ 2} \approx 0.4T_{m\ Si}$ ($T_{m\ Si}$ = 1685 K is the melting point of silicon). Thus, the former peaks should denote the precipitation of α-Al from the amorphous phase and its subsequent growth; the latter should do that of Si both from the amorphous phase and from supersaturated α-Al nanocrystals. In the meantime, crystallization of the amorphous phase may also occur. Since $T_{ons\ 1}$ increases with increasing C_{Si} while $T_{ons\ 2}$ has a reverse tendency, the precipitation and grain growth of α-Al are more difficult with increasing C_{Si} content while that of Si become easier.

Fig. 8 gives microhardness of $Al_{75}Si_{25}$ and $Al_{55}Si_{45}$ alloys annealed at different temperatures. The as quenched $Al_{75}Si_{25}$ and $Al_{55}Si_{45}$ alloys have the highest hardness of 1200 MPa and 2100 MPa, which imply that the content increase of Si% leads to evident enhancement of alloys. When the alloys are annealed, as the annealing temperature increases,

the hardness gradually drops. This drop may be related to the internal stress relaxation and the growth of the α-Al nanocrystals. Since there are two hardening peaks in the curves, which are similar to that of the DSC results, it seems that after the nanoparticles have just precipitated from the amorphous phase, the hardness of the alloys increases since the nanocrystalline crystals have higher hardness than that of amorphous phase [42]. As the grain growth occurs, the hardness decreases again.

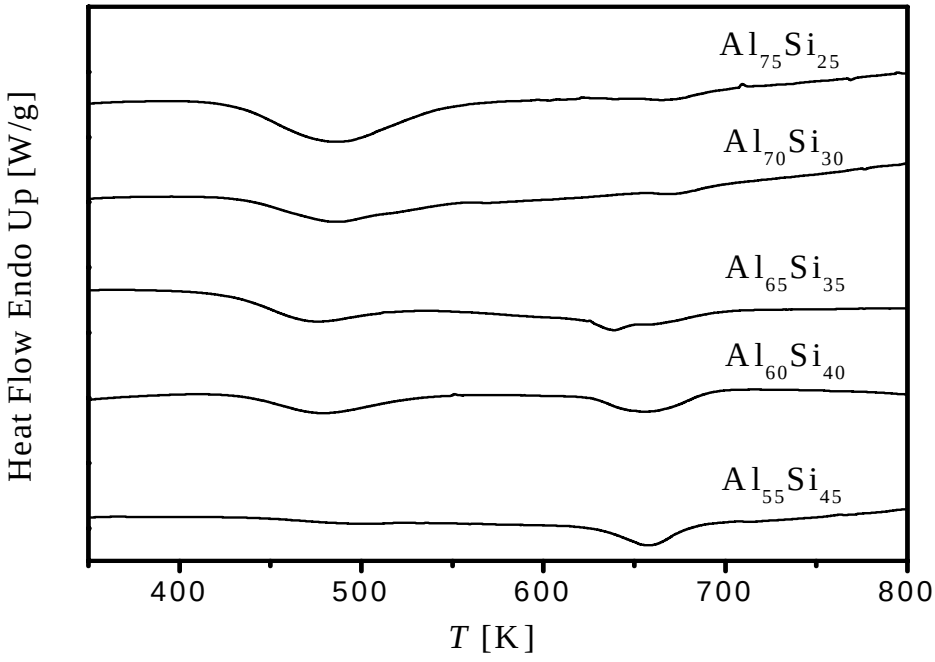

Figure 6. DSC curves of the Al-Si alloys.

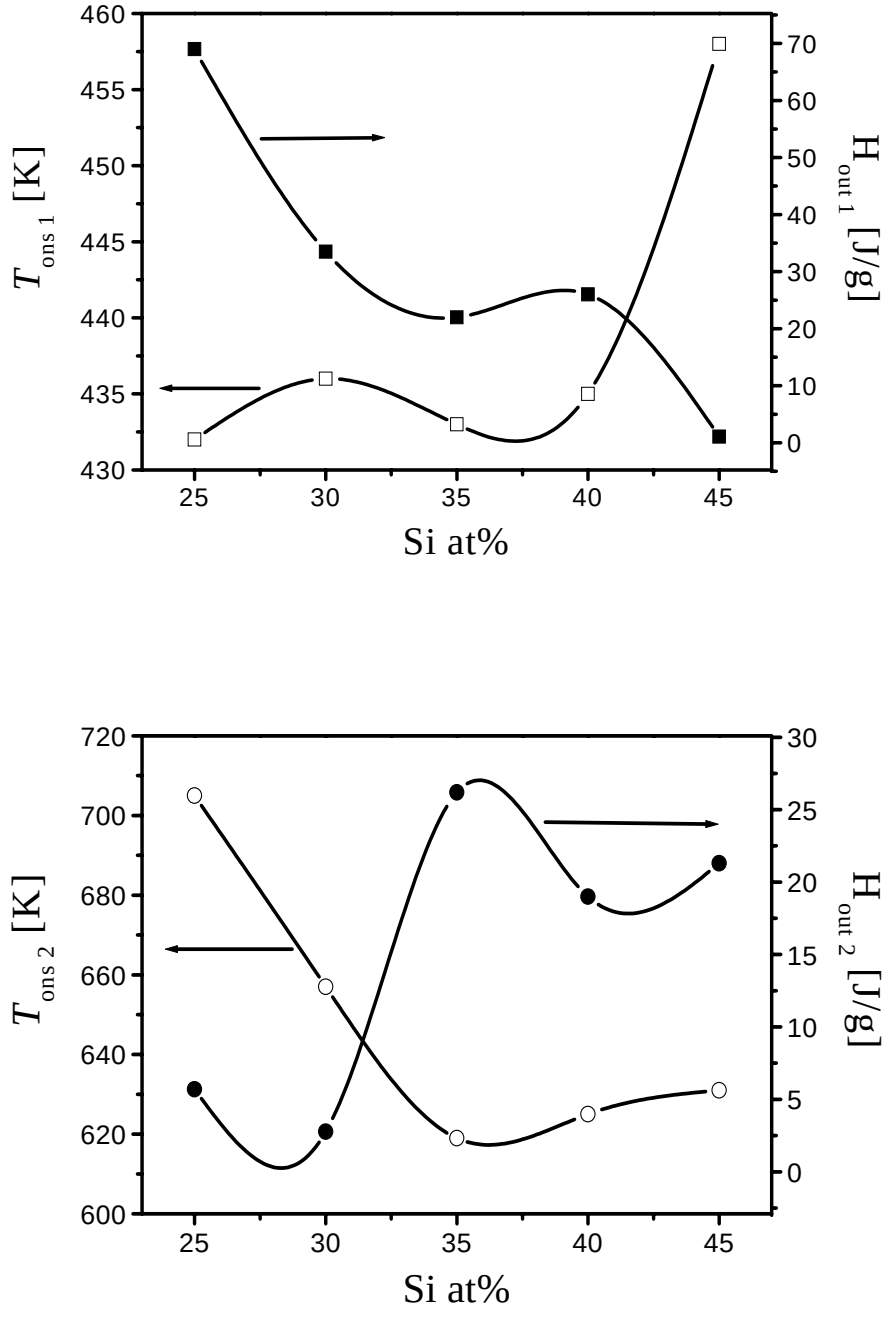

Figure 7. Dependence of T_{ons} and H_{out} on C_{Si}.

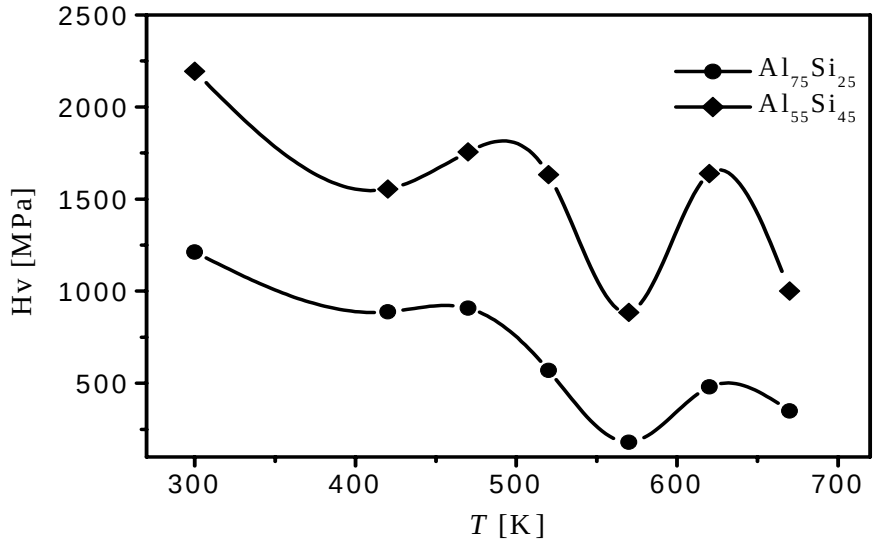

Figure 8 Vickers hardness (HV) curves of $Al_{75}Si_{25}$ and $Al_{55}Si_{45}$ alloys after the annealing at different temperatures.

In summary, five quenched Al-Si alloys with different compositions have been manufactured and whose mechanical properties and structures are determined. The results show that the alloys consist of supersaturated α-Al nanocrystals, amorphous matrix and primary Si crystals. When 30%<C_{Si}%<40%, there is more than 50% amorphous phase in the corresponding alloy. Crystallization of the amorphous phases and Si separation from the supersaturated α-Al nanocrystals occur as temperature increases.

3. THERMAL STABILITY OF TERNARY AMORPHOUS AL BASED ALLOYS

Alloys with Al content of 80 to 90% have a combination of good ductility and high strength [19-22,43-45] due to their full amorphous structure. For these kinds of Al-based alloy, crystallization is the essential factor affecting the properties of the amorphous alloys, and the extent of crystallization is consequently crucial to the alloy′s application. It has been reported that partial crystallization may enhance the alloy's strength [46] although the full crystallization leads to embattlement of the alloys [47]. The necessary conditions to avoid the full crystallization are that the alloy has a higher activation energy of crystallization E_a and a higher crystallization temperature T_x, which is obtained through alloying [48]. Moreover, it has been found that ternary alloys having 80 to 90% Al crystallizes in several stages [49-53]. X-ray results show that the precipitation in the first stage is the primary precipitation of α-Al while in the second stage intermetallic compounds of Al_3La, La_3Al_{11}, Ni_5La and Al_3Ni are present [53-54]. The multiple stages of crystallization benefit the formation of a composite structure where the amorphous phase is partly crystallized to increase strength of alloys.

However, if T_x, which is the precipitation temperature of supersaturated α-Al, is too low, the growth of Al grains and precipitation from the supersaturated α-Al must lead to a strong drop of strength. T_x is composition dependent and can be adjusted by alloying since alloying improves the glass forming ability of the Al based alloy and stabilizes the amorphous phase with larger values of E_a and T_x where E_a is the activation energy for crystallization. On the other side, in industry, the alloying amount should be as small as possible. The necessary smallest amount of alloying on the thermal stability of AlLaNi alloys can be determined by changing La and Ni amount in Al.

Fig. 9 shows the crystallization curves of $Al_{82}La_9Ni_9$ amorphous alloy at different q's with q being heating or cooling rate. The corresponding T_x values are given in table 1. Two peaks on the curves indicate clearly two stages of crystallization the same as other AlLaNi alloys [53-54] where crystallization enthalpies for the first and the second crystallization ΔH are 29.96 and 57.47 J/g, respectively with q = 40 K/min. The first crystallization curve represents the precipitation of α-Al while the second denotes that of La_3Al_{11}, Al_3Ni, Ni_5La and Al_3La intermetallic compounds. At higher q, a small decalescence peak can be observed, which is caused by glass transformation before the first crystallization. The glass transition cannot be found in the thermal analysis curve at low q since crystallization occurs at the same temperature. It is shown that precipitation of α-Al is slow and the crystallization fraction of α-Al increases with temperature increasing.

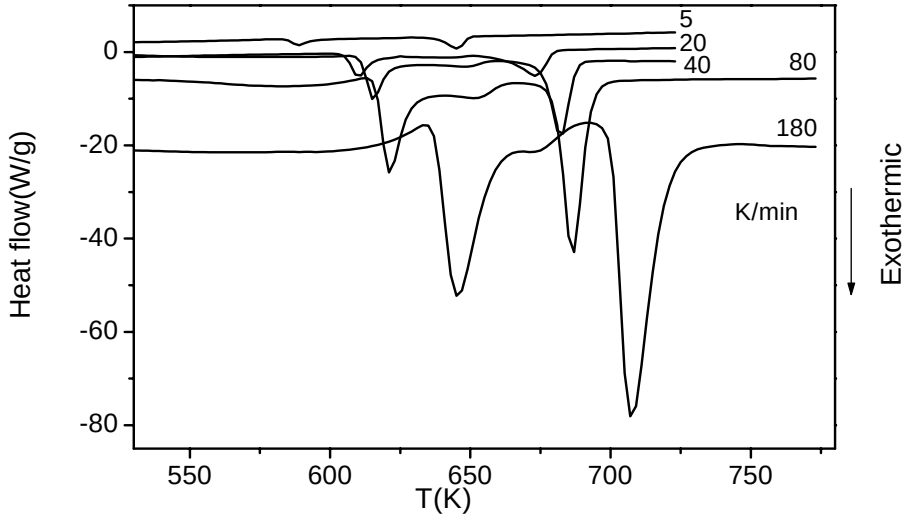

Figure 9. DSC curves of $Al_{82}La_9Ni_9$ alloy at different heat rates q.

Table 1. The crystallization temperature of an $Al_{82}La_9Ni_9$ amorphous alloy with different heating rates *q*

q, K/min		5	20	40	80	180
1st peak	T_x/K	585	606	611	637	637
2nd peak	T_x/K	639	661	675	677	698

By use of the Kissinger method [51], the corresponding E_a for the precipitation of α-Al determined from Fig. 9 is shown in table 2. The relevant AlLaNi and AlYNi alloys are also shown in table 2 and Fig. 10. It is found that E_a in measuring error range remains a constant as La(Y)+Ni content increases. This result implies that the supersaturated amount of La and Ni in α-Al is the same in the composition range of 9% < La(Y)+Ni < 18%. Since ΔH of $Al_{82}La_9Ni_9$ for the first peak is about 1/3 of the total ΔH, if the La and Ni are randomly distributed in the alloys, the saturated solution of La (Y) and Ni in Al is about 6 at.%. Thus, it is possible that any further increase of La (Y) and Ni does not change E_a as long as La(Y)+Ni > 6%.

Fig. 11 gives a comparison of T_x values of AlLaNi and AlYNi alloys for the first transition peak. It is clear that as RE+Ni increases where RE denotes rare earth elements, T_x values increase with a slope about 20 K/[(RE+Ni)at.%]. From the view of thermal stability for industrial application, T_x value of an alloy must be at least 500 K. Under this condition, if La(Y) and Ni in the alloy has the same content, the necessary alloying composition for AlLaNi alloy is $Al_{88}La_6Ni_6$ while that for AlYNi alloy is $Al_{85}La_7Ni_7$. Thus, the AlLaNi alloys have better thermal stability than AlYNi alloys with the same alloying amount. Moreover, for a ternary system, Al content of the alloys cannot be larger than 88% for any possible industrial application in the above alloying systems although full amorphous structures can be built even if Al = 91at.% [53].

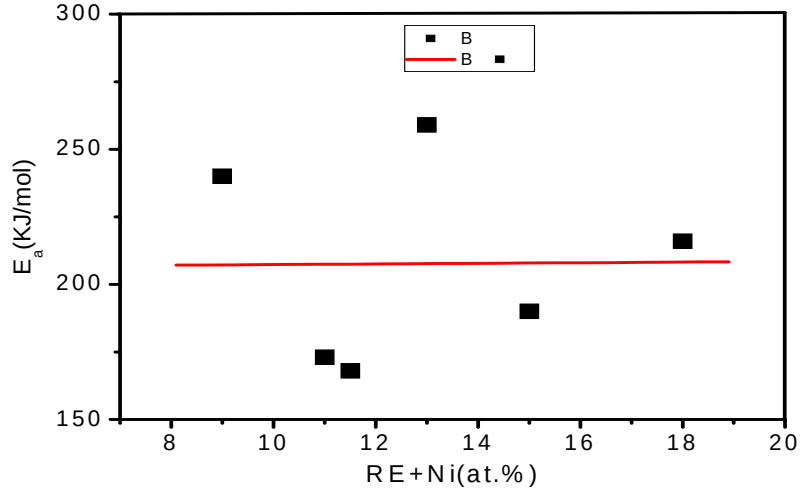

Figure 10. E_a of the precipitation of fcc Al as a function of concentration of RE+Ni where RE denotes the elements of La or Y.

Table 2. E_a of $Al_{82}La_9Ni_9$ alloy compared with that of relevant alloys

E_a, KJ/mol	1st	2nd	3rd	Ref.
$Al_{82}La_9Ni_9$	216	222		[57]
$Al_{89}La_6Ni_5$	173	207		[58]
$Al_{91}La_5Ni_4$	240±39	229±7		[54]
$Al_{85}Y_{10}Ni_5$	190			[56]
$Al_{88.5}Y_{6.5}Ni_5$	168	163	285	[59]
$Al_{87}Y_8Ni_5$	259	413	317	[60]

Table 3. T_x of $Al_{82}La_9Ni_9$ alloy compared with that of relevant alloys with q = 20 K/min

T_x, K	1st	2nd	3rd	Ref.
$Al_{82}La_9Ni_9$	606	661		[57]
$Al_{89}La_6Ni_5$	500	612		[58]
$Al_{91}La_5Ni_4$	413			[54]
$Al_{85}Y_{10}Ni_5$	531			[56]
$Al_{88.5}Y_{6.5}Ni_5$	453	469	600	[59]
$Al_{87}Y_8Ni_5$	488	582	622	[60]

4. HIGH STRENGTH AL-BASED ALLOYS PREPARED BY POWDER METALLURGY METHOD

Among Al alloys, Al-RE-TM (TM = V, Cr, Mn, Fe, Mo) amorphous Al alloys of melt-spun ribbons possess high strength [60-64]. The tensile strengths of the alloys σ_b are more than 1000 MPa while the highest σ_b value reaches 1250 MPa. If supersaturated α-Al or supersaturated icosahedral Al quasi-crystals embedded in amorphous matrix with coherent interfaces are in nanometer size, the strengths of the alloys can be further improved [65-68]. Although these ribbons exhibit σ_b values exceeding the performance of conventionally produced Al-alloys by a factor of two to three, they cannot be directly utilized as structural materials due to their small size. Thus, the P/M (powder metallurgy) technique was recently utilized to fabricate bulk alloys [69-72]. The mechanical properties, such as strength, plasticity and wear resistance, of AlCeMn and AlLaNi alloys prepared by P/M are reported. It is found that when different P/M treatments are utilized due to emphasis to a special mechanical property, different materials characterizations can arise, which is meaningful for multiformity of materials applications.

The alloys were prepared from Al, Ni, La, Ce, and Mn elements with purities of 99.9% by melting them together in a vacuum induction furnace under argon atmosphere. The powders of the alloy were obtained by ultrasonic atomization method with a cooling rate about 10^3 K/s, the sizes of the powders were among 5 and 40 μm. The compositions of the alloy powders were $Al_{85}La_{10}Ni_5$ and $Al_{90}Mn_8Ce_2$ (at%). The bulk alloys were obtained by hydraulic pressing at different temperatures between 453 and 853 K under a pressure of 1.2 GPa. The porosity of the alloy δ was determined as follows:

$$\delta=(\rho_t-\rho_m)/\rho_t, \quad (3)$$

where ρ_m and ρ_t are the measured density of the alloy and the theoretical density determined by the density of the constituent elements.

Fig. 12 shows how the porosity of the alloys changes as a function of the pressing temperature *T*. In Fig. 12, as *T* increases, δ decreases. δ < 2% at *T* > 753 K. Note that the theoretically calculated δ values differ a little from the measured δ value due to differences of δ values between elements and compounds. Therefore, δ values are only approximate results.

The corresponding microstructures of the above alloys are present in Fig. 13. The microstructures in Fig. 13 support the above observation on δ values: When *T* = 473 K, the original spherical powders in diameter of 5-30 μm remain. As $T \rightarrow 753$ K, crystallization or re-crystallization arises and evident porosity is microscopically absent where δ < 2%. At *T* > 753 K, the structure remains.

The X-ray result of the alloys in Fig. 14 shows the presences of α-Al, intermetallic compounds and alumina at *T* = 753 K. The appearance of the compounds and alumina should contribute to the strength of the alloys.

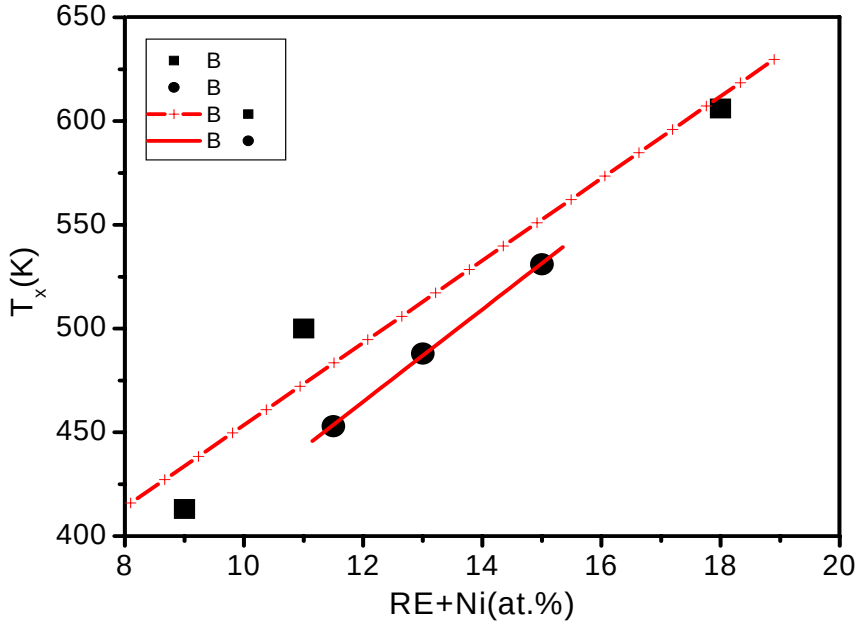

Figure 11. T_x of the precipitation of fcc Al as a function of concentration of RE+Ni where RE denotes the elements of La or Y.

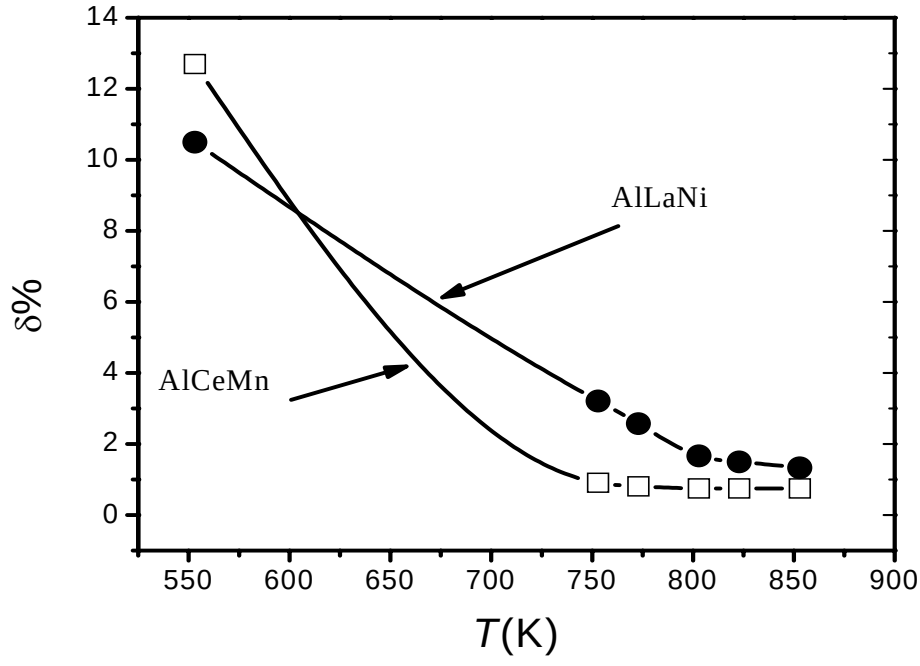

Figure 12. Porosity of the alloy as a function of pressing temperature.

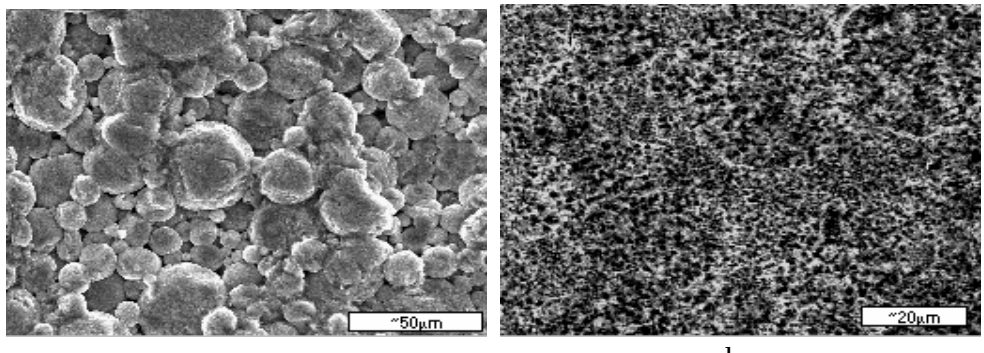

a b

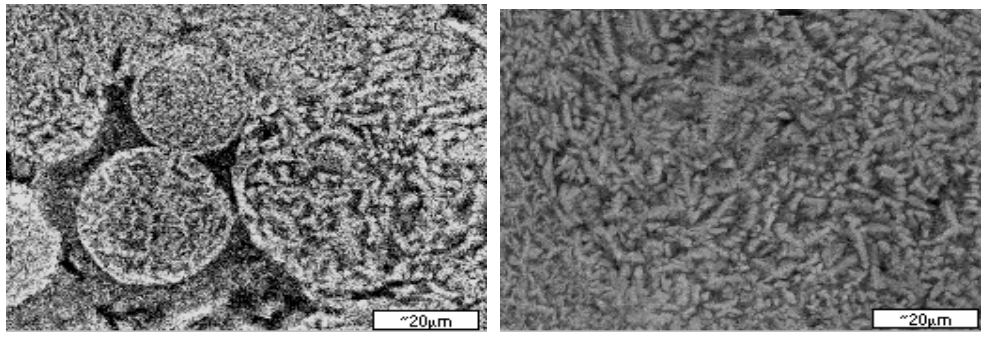

c d

Figure 13. SEM micrographs of the alloy pressing at different *T*. (a) AlCeMn alloy at 473 K, (b) AlCeMn alloy at 753 K, (c) AlLaNi alloy at 473 K, (d) AlLaNi alloy at 753 K.

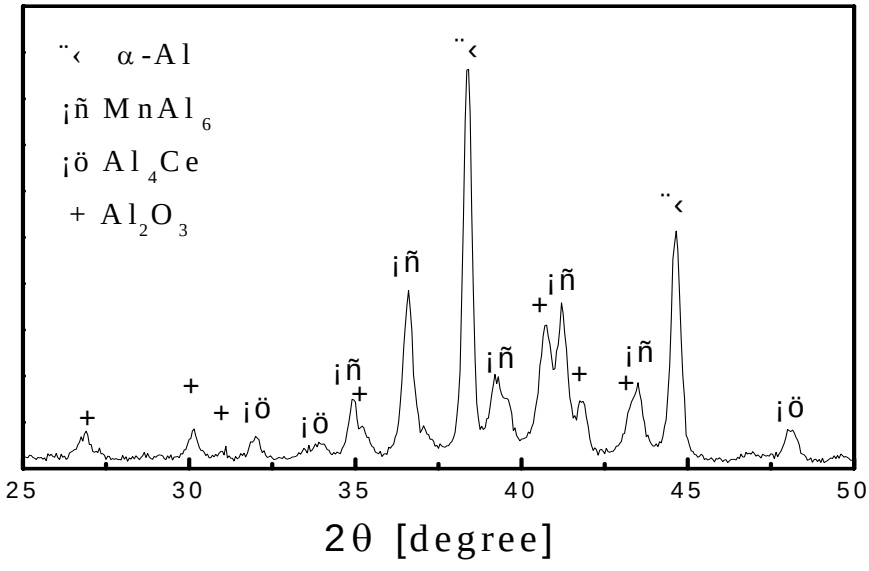

a

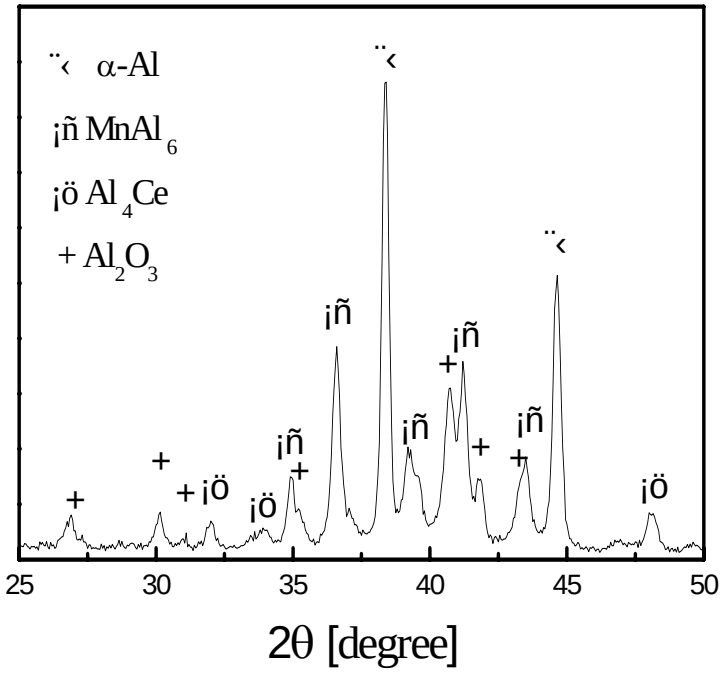

b

Figure 14. X-ray structure analysis of the sample pressing at 753 K. (a) AlCeMn alloy, (b) AlLaNi alloy.

To obtain compact P/M products, surface melting even melting must occur. The former takes place when $T > 0.8T_m$ (T_m denotes the melting temperature) [55-56, 73-74]. When the surface melting is present, full density P/M alloys are possible to obtain under larger pressure. The DSC results show that T_m = 922 K for AlCeMn alloy and T_m = 894 K for AlLaNi alloy [66-67]. Therefore, when $T > 0.8T_m$ = 740 K, δ may take its minimum. On the other side, a too high pressing temperature leads to grain growth or grain coarsening, which leads to drop of the strength. Thus, to achieve the highest strength, $T < 800$ K should be selected. Note that existed alumina on powder surfaces produced during both the manufacture and storage of the powders is the essential reason to decrease packing density of the alloys. Only when surface melting of the alloys occurs, which leads to mechanical instability of alloy surface or that of interface between alloy surface and alumina surface layer. Under this condition, the alumina surface layers on the powder surface can be easily destroyed and the fresh surfaces of the powders are in contact directly. As a result, a compacted bulk alloy can be obtained. Note also that the destroying of the alumina surface layers also brings out dispersion distribution of alumina powders, which evidently improves the plasticity and ductility of the alloys.

Fig. 15 shows stress-strain curves of the alloys pressing at different *T*. According to the figure, as *T* increases, the compression strength increases due to the precipitation of the compounds. The alloy presents hardly plasticity at $T < 653$ K or $T > 803$ K. The former is produced by existence of large amounts of porosity while the latter is due to appearance of large amount of compounds accompanied with the grain growth. The highest compression strength of AlMnCe and AlLaNi alloys are 850MPa and 950 MPa at 803 K respectively. At 753 K, the compression strength is 725 MPa with a plastic strain of 5.5% for AlCeMn alloy, and 700 MPa with a plastic strain of 5% for AlLaNi alloy. Further increase of *T* leads to an increase of strength but a drop of plastic strain.

The above results for temperature dependence of strength and plasticity of the alloys are supported by the microstructure observations shown in Fig. 16. Fig. 16a and Fig. 16c give the microstructure of the fracture of the sample at T = 753 K, which denote a ductile dimpled fracture while the cleavage fracture of the sample in Fig. 16b and Fig. 16d are fully brittle at T = 803 K.

The excellent strength of the alloy may be accompanied with high wear resistance. The P/M Al alloy presents improved wear resistance over the A355 aluminum alloy as shown in Fig. 17. The AlCeMn alloy pressed at 753 K and AlLaNi alloy pressed at 773 K exhibit the best wear resistance among the alloys, which are three times as high as the A355 Al alloy.

Fig. 18 presents the SEM micrographs of wear surface of the alloys, which consists of ploughs and areas where obvious plastic flow occurs. Thus, the good wear resistance of the alloy pressed at 753 K should be related with not only good strength, but also good plasticity of the alloy.

In summary, the bulk of AlCeMn and AlLaNi alloys manufactured by P/M method have high strengths due to their complicated structures. The best mechanical properties of the alloy made by P/M technique are obtained under the following processing conditions: The pressing temperature is 753 K and pressure is 1.2 GPa where the δ reaches the minimum, the plasticity reaches the maximum with a moderate strength.

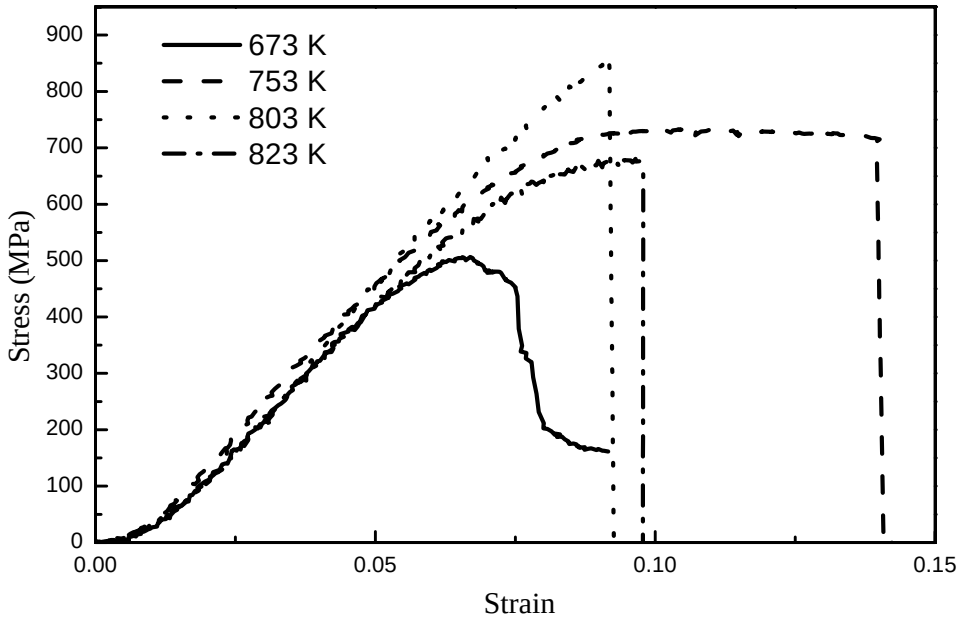

a

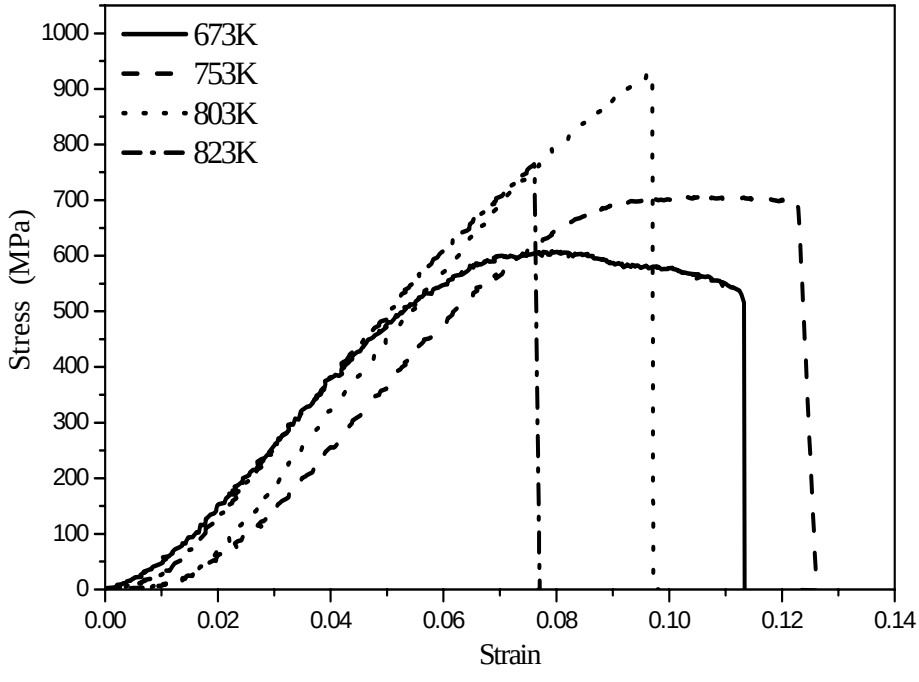

b

Figure 15. Stress-strain curve of the alloy as a function of *T*. (a) AlMnCe alloy, (b) AlLaNi alloy.

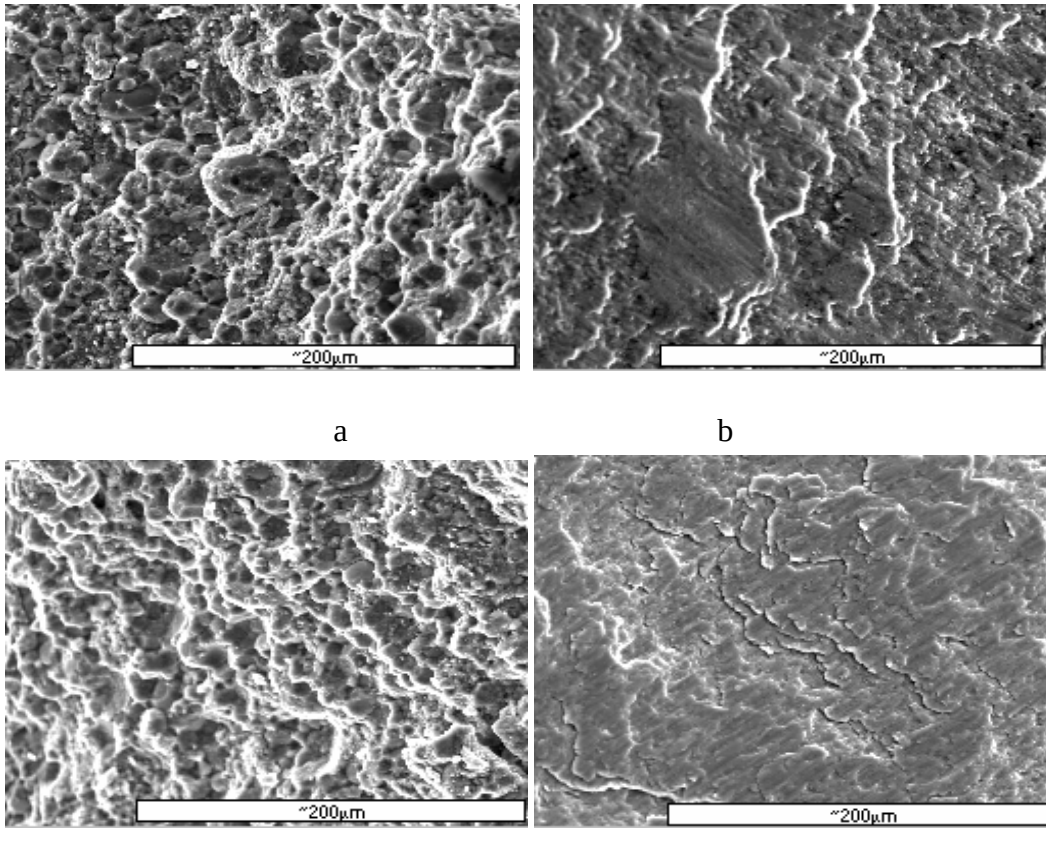

Figure 16. Fracture structure of the alloy at different *T*. (a) AlCeMn alloy at 753 K, (b) AlCeMn alloy at 803K, (c) AlLaNi alloy at 753 K, AlLaNi alloy at 803 K.

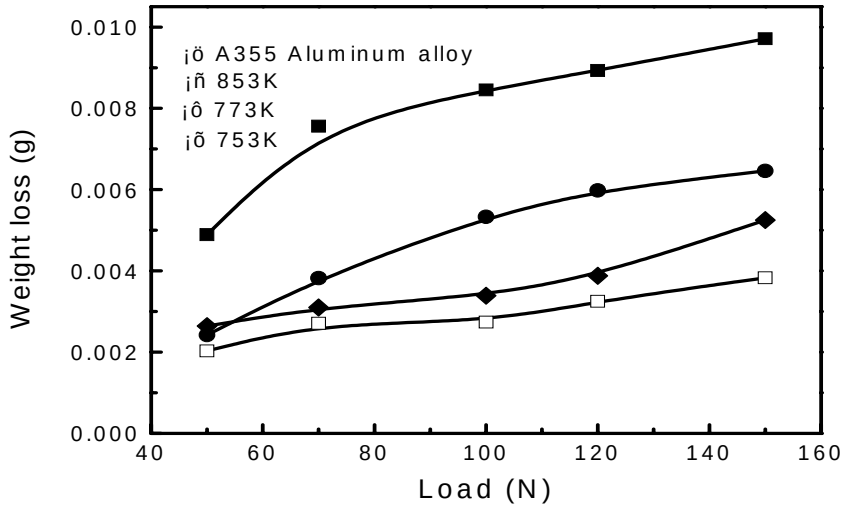

a

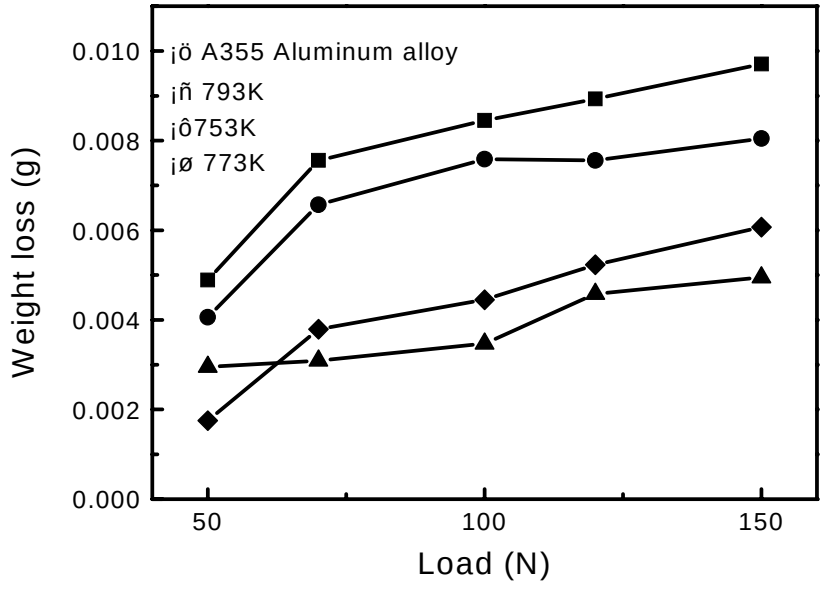

b

Figure 17. Wear curve of the alloy pressed at 753 K with different sliding times under 150 N. (a) AlCeMn alloy, (b) AlLaNi alloy.

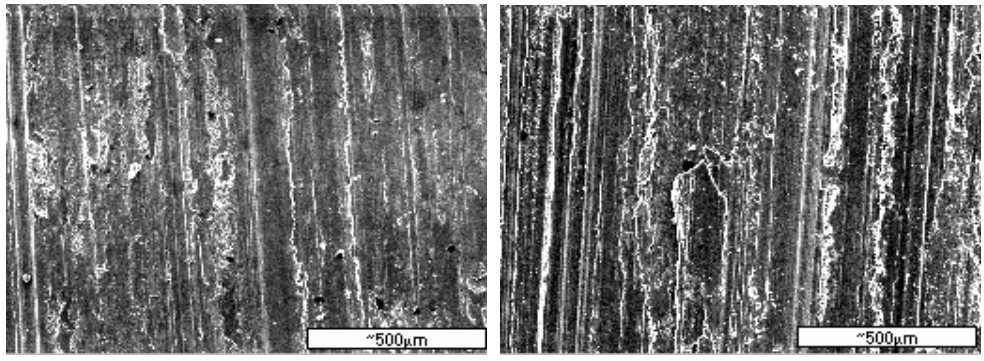

a b

Figure 18. SEM micrograph of wear surface of the alloy pressed at 753 K. (a) AlMnCe alloy, (b) AlLaNi alloy.

5. THE CONSIDERATION ON FURTHER DEVELOPMENT

5.1. Nanostructured High-Entropy Alloys with Multiple Principal Elements

The large numbers of intermetallic compounds of amorous Al alloys is expected to result in brittleness, difficulty in processing, and challenging in analysis. Thus, although alloying is a good technique to increase strength of an alloy, usual alloying elements are less than 50% except that the alloying element has full solubility in matrix element. However, a recent progress for high alloying is achieved by considering high entropy in an alloy based on thermodynamics, which focused on a new approach to alloy design with multiple principal elements in equimolar or near-equimolar ratios [75].

Based on a general understanding of physical metallurgy and facts concerning binary and ternary phase diagrams, the formation of many intermetallic compounds using multiple principal elements may be anticipated [76], which has discouraged alloy design with multiple principal elements. Nonetheless, solid solutions of many elements will tend to be more stable because of their large mixing entropies. Following Boltzmann′s hypothesis on the relationship between entropy and system complexity [76], the configurational entropy change per mole, ΔS_{conf}, during the formation of a solid solution from n elements with equimolar fractions may be calculated from the following equation,

$$\Delta S_{conf} = -k \ln w = -R\left(\frac{1}{n}\ln\frac{1}{n} + \frac{1}{n}\ln\frac{1}{n} + \ldots\frac{1}{n}\ln\frac{1}{n}\right) = -R\ln\frac{1}{n} = R\ln n \qquad (4)$$

where k is Boltzmann′s constant, w is the number of ways of mixing, and R is the gas constant. By Richards′ rule [76], the entropy changes in fusion of the most metals are only empirically equal to R at their melting points, In comparison, equimolar alloys with three elements already have a ΔS_{conf} value of 1.10R, larger than that of metal fusion, let alone those

with five or more constitute elements. In fact, considering other positive contributions from factors such as vibrational, electronic, and magnetic moment randomness, ΔS_{conf} of an equimolar alloy is even higher than that calculated [76]. Furthermore, if the formation enthalpies of two strong intermetallic compounds, such as NiAl and TiAl were divided by their respective melting points, the resulting ΔS_{conf}, 1.38*R* and 2.06*R*, are in the same range as the entropy changes of mixing in a system with more than five elements. This indicates that the tendency of ordering and segregation would be lowered by the high ΔS_{conf} [77]. Consequently, alloys with a higher number of principal elements will more easily yield the formation of random solid solution during solidification, rather than intermetallic compounds, except for those with very large heats of formation. In practice, to fully utilize the merit of high mixing entropy in the liquid- or solid-solution state, which is defined by such high-entropy alloys (HE alloys) as those composed of five or more principal elements in equimolar ratios. Extensive trials have led to many alloy systems with simple crystalline structures of fcc, bcc and fcc+bcc and extraordinary properties [75,78-79]. These simple structures with high alloying lead to that the alloys could hold high strength and good plastics at the same time.

Although many trials in alloying systems have been carried out, the light alloy systems can never be considered. Thus, the above alloying method can be applied to light alloys, especially Al base alloys. The possible alloy element selections for Al base alloys are Li, Mg, Si, RE, B etc. The adding of these elements will remain the characteristic of low specific weight of the Al alloy. However, the corresponding strength will increase evidently. The corresponding works are in progress.

5.2. Spark Plasma Sintering Technique for P/M Processing

The powders of Al base alloys are usually covered with alumina film due to the rapid oxidation ability of the alloys. Thus, the alloys with a high packing density cannot be sintered by normal and hot press sintering under usual temperature since alumina films with high melting temperature on the surface of the powders remain perfect and cannot be broken and/or removed. Even if the powders are forged into a dense body under high temperature sintering conditions, the plasticity of the high strength Al alloy prepared by M/P method is lower.

To avoid the above problem, a best way during the use of M/P technique is that heating the powders in an inhomogeneous mode, namely, the temperature at the powder surface is much higher than that within the particles. This mode leads to, in the one side, the melting of the alunima on the powder surface and re-solidify in particle shapes with small size; and in the other side, the tendencies of the precipitation of compounds and grain growth in the particles are inhibited. Both guarantee the alloys having a good plasticity and a high strength. In addition, since the sintering temperature can be much lower, the cost of the P/M processing technique is lowered in many aspects. This kind of consideration can be realized by the Spark Plasma Sintering (SPS) technique [80-83].

SPS is a new sintering technology developed in recent years [80-85]. It enjoys certain inherent advantages, which are the following:

1. A high thermo-efficiency, which is determined by the way of heating as in a SPS furnace, the electricity is put directly into the samples and the electricity conducting dies bearing the samples and is transformed into thermal energy.
2. A quick heating-up, which is mainly due to the high pulse power source.
3. A better self-purification of the surface of the particle and sintering activity. A strong enough electrical field is produced in the small gaps of the particles to make the electrons, cations and anions to strike the surface of the opposite particle and purify its surface.
4. Enabling fast sintering under low temperatures. On one hand, the movement of the above-mentioned particles fulfils the material transportation and a local high temperature is created in the contacting areas of the particles resulting in the quick formation of the neck while the temperature is still comparatively low. On the other hand, the temperature at the neck is much higher than that of the inside of the particles. The neck grows quickly and fast sintering is done.

The present authors have used the above technique to manufacture new series of Al base alloys with high strength and high plasticity under a low sintering temperature. Evident advances have been achieved. The ultimate goal of the research is to find a new Al-base alloy with a σ_b value of more than 1000 MPa and a plasticity of more than 6-8%.

ACKNOWLEDGEMENTS

The financial supports from Foundation of National Key Basic Research and Development Program under Grant No. 2004CB619301 and Project 985-Automotive Engineering of Jilin University are acknowledged.

REFERENCES

[1] Klement W., Willens R. H., Duwez P. (1960). Non-crystalline structure in solidified gold-silicon alloys. *Nature*, 187, 869-870.
[2] Luborsky L. E. (1983). *Amorphous Metallic Alloys*, London, Butterworths.
[3] Masumoto T. (1982). *Materials Science of Amorphous Metals*, Tokyo, Ohmu.
[4] Inoue A. (2000). Stabilization of metallic supercooled liquid and bulk Amorphous alloys. *Acta Mater*., *48*, 279-306.
[5] Chen H. S. (1980). *Glassy metals*. *Rep. Prog. Phys*., *43*, 353-432.
[6] Kui H. W., Greer A. L., Turnbull D. (1984). Formation of bulk metallic glass by fluxing. *Appl. Phys. Lett*., *45*, 615-616.
[7] Ramachandrarao P., Scott M. G., Chadwick G. A. (1972). Constitution and microstructure of rapidly solidified aluminium-germanium alloys. *Philosophical Magazine*, 25, 961-982.
[8] Ramachandrarao P., Laridjani M., Cahn R. W. (1972). Diamond as a splat-cooling substrate. *Z. Metallkd*., *63*, 43-49.

[9] Davies H. A., Hull J. B. (1973). Noncrystalline phase in splat-quenched germanium. *Scrip. Metall., 7*, 634-641.

[10] Chattopadyay K., Ramachandrarao R., Lele S., Anantharaman T. R. In: Grant NJ, B. C. Giessen, editors. (1977). Proceedings of 2nd international conference on rapidly quenched metals, Cambridge, MA: MIT Press, p. 157.

[11] Furrer P., Warlimont H. (1977). Crystalline and amorphous structures of rapidly solidified Al-Cr alloys. *Mater. Sci. Eng., 28*, 127-137.

[12] Davies H. A. (1981). Diffuse scattering and chemical short range order in binary metallic glasses. *Trans Indian Inst. Met., 31*, 292-297.

[13] Inoue A., Kimura H. M., Masumoto T., Tsai A. P., Bizen Y. (1987). Al-Ge-(Cr or Mn) and Al-Si-(Cr or Mn) quasicrystals with high metalloid concentration prepared by rapid quenching. *J. Mater. Sci. Lett., 6*, 771-774.

[14] Suzuki R. O., Komatsu Y., Kobayashi K. E., Shingu P. H. (1983). Formation and crystallization of Al-Fe-Si amorphous alloys. *J. Mater. Sci., 18*, 1195-1201.

[15] Inoue A., Matsumoto N., Masumoto T. (1990). Al-Ni-Y-Co amorphous alloys with high mechanical strengths, wide supercooled liquid region and large glass-forming capacity. *Mater. Trans. JIM, 31*, 493-500.

[16] Kim Y. H., Inoue A., Masumoto T. (1990). Ultrahigh tensile strengths of $Al_{88}Y_2Ni_9M_1$ (M=Mn or Fe) amorphous alloys containing finely dispersed fcc-Al particles. *Mater. Trans. JIM, 31*, 747-749.

[17] Inoue A., Ohtera K., Tsai A. P., Masumoto T. (1988). Aluminum-based amorphous alloys with tensile strength above 980 MPa. *Jpn. Appl. Phys., 27*, 479-482.

[18] Inoue A., Kimura H. (2000). High-strength aluminum alloys containing nanoquasicrystalline particles. *Mater. Sci. Eng. A, 286*, 1-10.

[19] Rizzi P., Doglione R., Battezzati L. (2004). Mechanical properties of Al-based amorphous/nanocrystalline alloys. *Mater. Sci. Eng. A, 375-377*, 969-974.

[20] Hu L., Bian X., Wang W., Zhang J., Jia Y. (2004). Liquid fragility and characteristic of the structure corresponding to the prepeak of AlNiCe amorphous alloys. *Acta Mater., 52*, 4773-4781.

[21] Boucharat N., Rösner H., Perepezko J. H., Wilde G. (2004). Devitrification of Al-based glass forming alloys. *Mat. Sci. Eng. A, 375-377*, 713-717.

[22] Zhu A. Joseph Poon S., Shiflet G. J. (2004). On glass formability of Al– Gd– Ni (Fe). *Scripta Mater., 50*, 1451– 1455.

[23] Shingu P. H., Ishihara K. N. (1993). *Rapidly solidified alloys*. New York, Marcel Dekker.

[24] Schwarz R. B. (1993). *Rapidly solidified alloys*. New York, Marcel Dekker.

[25] Catalog Y. K. K. (1994). *High-strength aluminium alloys.* Tokyo, GIGAS.

[26] Ohtera K., Inoue A., Terabayashi T., Nagahama H., Masumoto T. (1992). Mechanical properties of an $Al_{88.5}Ni_8Mm_{3.5}$ (Mm=misch metal) alloy produced by extrusion of atomized amorous plus fcc-Al phase powders. *Mater. Trans. JIM, 33*, 775-787.

[27] YKK Catalog. (1995).

[28] Inoue A., Kimura H. M. (1997). High-strength Al-based alloys consisting mainly of nanoscale quasicrystalline or amorphous particles. *Mater. Sci. Forum, 235-238*, 873-880.

[29] Suzuki R. O., Komatsu Y., Kobayashi K. E., Shingu P. H. (1983). Formation and crystallization of Al-Fe-Si amorphous Alloys. *J. Mater. Sci*., *18*, 1195-1201.

[30] Inoue A., Bizen Y., Kimura H. M., Yamamoto M., Tsai A. P., Masumoto T. (1987). Development of compositional short-range ordering in an AlGeMn amorphous alloy upon annealing. *J. Mater. Sci. Lett*., *6*, 811-814.

[31] Zhao Z. K., Li J. C., Jiang Q. (2004). Hypereutectic Al-Si binary alloys prepared by melt spinning method. *Adv. Eng. Mater*., *6*, 303-306.

[32] Johnson W. L. (1986). Thermodynamic and kinetic aspects of the crystal to glass transformation in metallic materials. *Prog. Mater. Sci*., *30*, 81-134.

[33] Jiang Q. (2000). A contribution to the kauzmann temperature. *Z. Metallkd*., *99*, 97-100.

[34] Egami T., Waseda Y. (1984). Atomic size effect on the formability of metallic glasses. *J. Non-cryst. Solids*, *64*, 113-134.

[35] Egami T. (1997). Universal criterion for metallic glass formation. *Mater. Sci. Eng. A*, *226-228*, 261-267.

[36] Massalski T. B. (1986). *Binary alloys Phase Diagrams. Vol. 1*, Metals Park, Ohio, American Society for Metals, p.158.

[37] King H. K. (1970). *Physical Metallurgy.* Amsterdam, North-Holland Pub. Co. p.59.

[38] Bendijk A., Delhez R., Katgerman L., Keijser Th. H. De., Mittemeijer E. J., Van Der Pers N. M. (1980). Characterization of Al-Si alloys rapidly quenched from the melt. *J. Mater. Sci*., *15*, 2803-2810.

[39] Antonione C., Battezzati L., Marino F. (1986). Structure and stability of rapidly solidified Al-Si based alloys. *J. Mat. Sci. Lett*., *5*, 586-588.

[40] Inoue A., Horio Y., Kim Y. H., Masumoto T. (1993). New amorphous Al-Ni-Fe and Al-Ni-Co alloys. *Mater. Trans. JIM, 34*, 85-88.

[41] Apaydin N., Smith R. W., (1988). Microstructural characterization of rapidly solidified Al-Si alloys. *Mater. Sci. Eng. A, 98*, 149-152.

[42] Eckert J., Reger-Leonhard A., Weiß B., Heilmaier M. (2001). Nanostructured materials in multicomponent alloy systems. *Mater. Sci. Eng. A, 301*, 1-11.

[43] Inoue A., Yamamoto M., Kimura H. M., Masumoto T. (1987). Ductile aluminium-base amorphous alloys with two separate phases. *J. Mater. Sci. Lett., 6*, 194-196.

[44] Inoue A., Ohetera K., Tsai A., Masumoto T. (1988). Aluminum-based amorphous alloys with tensile strength above 980 MPa (100 kg/mm^2). *Jpn J Appl Phys, 27*, L479-L482.

[45] Kim Y. H., Inoue A., Masumoto T. (1990). Ultrahish tensile strengths of $Al_{88}Y_2Ni_9M_1$ (M=Mn or Fe) amorous alloys containing dispersed fcc-Al particles. *Mater. Trans. JIM*, *31*, 747-749.

[46] Inoue A. (1998). Amorphous, nanoquasicrystalline and nanocrystalline alloys in Al-based systems. *Prog Mater Sci*, *43*, 365-520.

[47] Manov V., Rubshtein A., Popcl P., Vereshagin, A. (1994). Effect of melt temperature on the electrical resistivity and crystallization temperature of $Al_{91}La_5Ni_4$ and Al_{91} Ce_5Ni_4 amorphous alloys. *Mater. Sci. Eng*. A, *179-180*, 91-96.

[48] Lück R., Jiang Q., Predel B. (1990). Specific heat investigation of the glass transition and crystallization of amorphous $NiZr_2$ using low heating rates. *J Non-Cryst Solids, 117-118*, 911-914.

[49] Lu K. (1996). Nanocrystalline metals crystallized from amorphous solids: nanocrystallization, structure, and properties. *Mater Sci Eng R, 16*, 161-221.

[50] Ye F., Lu K. (1999). Crystallization kinetics of amorphous solids under pressure. *Phys Rev B, 60*, 7018-7024.

[51] Allen D. R., Foley J. C., Perepezko J. H. (1998). Nanocrystal development during primary crystallization of amorphous alloys. *Acta Mater 46*, 431-440.

[52] Pradell T., Crespo D., Clavaguera N. (1997). Kinetics of microstructural development in nanocrystalline materials. *Nanostruc. Mater., 8*, 345-357.

[53] Tokar A., Levin L. (1998). The amorous metallic $Al_{91}La_5Ni_4$ alloy: Kineties of crystallization. *Z. Metallkd 89*, 16-22.

[54] Ye F. (1999). Pressure effect on crystallization kinetics of an Al-La-Ni amorphous alloy. Ph. D thesis, Shenyang, Institute of metal research, Chinese Academy of Science.

[55] Kissinger H. E. (1957). Reaction kinetics in differential thermal analysis. *Anal. Chem. 29*, 1702-1706.

[56] Li J. C., Zhou X. H., Jiang Q. (2001). Crystallization kinetics of $Al_{82}La_9Ni_9$ amorphous alloy. *J. Mater. Sci. Lett., 20*, 1679-1680

[57] Kwong V., Koo Y. C., Thorpe S. J., Aust K. T. (1991). Crystallization behaviour of $Al_{85}Y_{10}Ni_5$ by isochronal and isothermal annealing. *Acta Metall. Mater., 39*, 1563-1570.

[58] Cao B., Li S., Yi D. (1991). Study on the crystallization of $Al_{88.5}Y_{6.5}Ni_5$ (at.%) amorphous alloy. *J. Less-Comm. Metals, 171*, 1-8.

[59] Yewondwossen M., Dunlap R. A., Lloyd D. J. (1992). Thermal and electronic properties of amorphous $Al_{87}Y_8Ni_{5-x}TM_x$ (TM=Mn, Fe, Co, Cu). *J. Phys. Condens. Matter, 4*, 461-472.

[60] Inoue A. (2000). Stabilization of metallic supercooled liquid and bulk amorphous alloys. *Acta Mater., 48*, 279-306.

[61] Kawamura Y., Mano H. and Inoue A. (2001). Nanocrystalline aluminum bulk alloys with a high strength of 1420 MPa produced by the consolidation of amorphous powders. *Scrip. Mater., 44*, 1599-1604.

[62] Watanabe M. and Inoue A. (1993). High mechanical strength of rapidly solidified $Al_{92}Mn_6Ln_2$ (Ln = lanthanide metal) alloys with finely mixed icosahedral and Al phases. *Mater. Trans. JIM, 34*, 162-168.

[63] Takagi M., Ohta H., Imura T. and Inoue A. (2001). Wear properties of nanocrystalline aluminum alloys and their composites. *Scripta Mater., 44*, 2145-2148.

[64] Schurack F., Eckert J., Schultz L. (2000). Quasicrystalline Al-alloys with high strength and good ductility. *Mater. Sci. Eng. A, 294-296*, 164-167.

[65] Manaila R., Macovei D., Popescu R., Devenyi A., Jianu A., Vasile E., Barna P. B. and Labar J. L. (2000). Nano-icosahedral Al-Mn-Ce phases: structure and local configurations. *Mater. Sci. Eng., A, 294-296*, 82-85.

[66] Adachi H., Osamura K., Ochiai S., Kusui J. and Yokoe K. (2001). Mechanical property of nanoscale precipitate hardening aluminum alloys. *Scrip. Mater., 44*, 1489-1492.

[67] T. Mukai, K. Higashi, (2001). Ductility enhancement of ultra fine-grained aluminum under dynamic loading. *Scrip. Mater., 44*, 1493-1496.

[68] Schurack F., Eckert J. and Schultz L. (2001). Synthesis and mechanical properties of cast quasicrystal-reinforced Al-alloys. *Acta Mater., 49*, 1351-1361.

[69] Li J. C., Zhao Z. K. and Jiang Q. (2002). Bulk high strength $Al_{85}La_{10}Ni_5$ alloy prepared by hot pressing. *Mater. Res. Bull., 37*, 297-304.

[70] Li J. C., Zhao Z. K. and Jiang Q. (2003). Properties of high strength $Al_{85}La_{10}Ni_5$ alloy. *Mater. Sci. Eng. A, 339*, 205-208.

[71] Li J. C., Zhao M. and Jiang Q. (2002). Bulk high hardness $Al_{90}Ce_2Mn_8$ alloy prepared by a powder metallurgy method. *Powder Metallurgy, 45*, 80-82.

[72] Li J. C., Zhao Z. K. and Jiang Q. (2003). Mechanical properties of high strength $Al_{90}Mn_8Ce_2$ alloy. *Adv. Eng. Mater.*, 5, 119-122.

[73] Dash J. G. (1999). History of the search for continuous melting. *Rev. Mod. Phys., 71*, 1737-1743.

[74] Wen Z., Zhao M., Jiang Q. (2003). Surface melting of polycrystals Pb and In within 1 K below melting temperature. *Mater. Lett., 57*, 2515-2518.

[75] Yeh J. W., Chen S. K., Lin S. J., Gan J. Y., Chin T. S., Shun T. T., Tsau C. H., Chang S. Y. (2004). Nanostructured high-entropy alloys with multiple principal elements: novel alloy design concepts and outcomes. *Adv. Eng. Mater., 6*, 299-303.

[76] Greer L. A. (1993). Confusion by design. *Nature, 366*, 303.

[77] Swalin R. A. (1992). *Thermodynamics of solid*. NY, Wiley.

[78] Boer F. R. de, Boom R., Mattens W. C. M. (1998). *Cohesion in metals: Transition metal alloys.* NY, Elseveir.

[79] Huang P. K., Yeh J. W., Shun T. T., Chen S. K. (2004). Multi-principal-element alloys with improved oxidation and wear resistance for thermal spray coating. *Adv. Eng. Mater., 6*, 74-78.

[80] Hsu C. Y., Chen S. K., Yeh J. W., Shun T. T. (2004). Wear resistance and high-temperature compression strength of fcc CuCoNiCrAl0.5Fe alloy with boron addition. *Meatll. Mater. Trans. A, 35*, 1465-1469.

[81] Risbud S.H., Shan C.H. (1995). Fast consolidation of ceramic powders. *Mater. Sci. Eng. A, 204*, 146-151.

[82] Hong J., Gao L., Torre S. D. D. L., Miyamoto K., Miyamoto H. (2000). Spark plasma sintering and mechanical properties of $ZrO_2(Y_2O_3)$-Al_2O_3 composites. *Mater. Lett., 43*, 27- 31.

[83] Gao L., Wang H. Z., Hong J. S., Miyamoto H., Miyamoto K., Nishikawa Y., Torre S. D. de la. (1999). SiC-ZrO_2(3Y)-Al_2O_3 nanocomposites superfast densified by spark plasma sintering. *Nanostruct. Mater., 11*, 43-49.

[84] Wang Y. C., Fu Z. Y. (2002). Study of temperature field in spark plasma sintering. *Mater. Sci. Eng. B, 90*, 34-37.

[85] Xü C.Y., Jia S. S., Cao Z. Y. (2005). Synthesis of Al–Mn–Ce alloy by the spark plasma sintering. *Mater. Charact., 54*, 394-398.

In: Nanomaterials: New Research
Editor: B.M. Caruta, pp. 197-218
ISBN: 1-59454-369-0

Chapter 6

QUANTITATIVE ANALYSES OF NANOCLAY DISPERSION IN MOLDED EPOXY DISKS: EFFECTS OF MIXING TEMPERATURE

Levent Aktas, Sudha Dharmavaram, Youssef K. Hamidi and M. Cengiz Altan*
School of Aerospace and Mechanical Engineering
University of Oklahoma, Norman, OK 73019

ABSTRACT

Effects of mixing temperature on the quality of dispersion of nanoclay in an epoxy resin are investigated. Cloisite® 25A nanoclay is mixed at 5wt.% loading with EPON 815C epoxy resin at 30, 50 and 75°C by the aid of a sonicator. The resin/nanoclay compound is then mixed with Epi-cure 3282 curing agent and molded into center-gated disk shaped parts with a diameter of 152.4mm. From each molded disk, a sample along the radius is cut and dispersion of nanoclay on its through-the-thickness surface is analyzed. It is observed that nanoclay exists in the form of clusters with sizes ranging from nano-meter scale up to ~50 m. Nanoclay clusters larger than 1.5 m are characterized by performing digital image analyses on the scanning electron micrographs taken along the disk radius, whereas clusters smaller than 1.5 m are quantified by wavelength dispersive spectrometry. It is found that increasing mixing temperature leads to larger nanoclay clusters. For instance, contribution of large clusters (Area>50 m^2) to the overall nanoclay content increased from 8.9 to 10.4% when the mixing temperature increased from 30 to 75°C. Similarly, in the same temperature range, contribution of small clusters (Area<3 m^2) decreased from 43.3 to 40.8%. The size and shape evolution of nanoclay clusters in the flow direction are also analyzed. Considerable nanoclay breakdown is observed in the radial direction. Contribution of small clusters to the nanoclay content at the outer edges of the disk is observed to be as much as 30% higher compared to the

* Correspondent author. E-mail: altan@ou.edu

inlet. Cluster breakdown also caused the nanoclay clusters to assume more irregular shapes at the outer edges of the disk.

1. INTRODUCTION

Particulates of nano-meter scale, such as carbon nanotubes and nanoclay, are receiving considerable research interest since they are likely to improve the properties of polymers, even when they are introduced at minor amounts [1]. Among these nano-particulates, nanoclay has gained acceptance as a viable commercial material and is being used in products such as food packaging materials and automobile semi-structural components. A series of pioneering work conducted by Toyota Research Labs [2-4] introduced the application of nanoclay to reinforce conventional polymeric resins. The problem of nanoclay particle agglomeration in polymers is overcome by surface modification of the originally organo-phobic surface of the nanoclay platelets through cation exchange reaction [2]. Later, the organo-philically modified nanoclay in Ref. 2 is mixed with ε-caprolactam, the monomer for nylon 6 [3]. Upon polymerization, the resulting nanocomposite is examined by x-ray diffractometry (XRD) and transmission electron microscopy (TEM) for the changes in gallery spacing of the nanoclay. The results revealed over 600% increase in basal spacing of the nanoclay due to combined effects of insertion of ε-caprolactam into the gallery spacing and its swelling during polymerization [3]. Kojima et al. tested various mechanical properties of the nanocomposite fabricated in Ref. 3. Despite slight decrease in impact resistance, tensile and flexural properties improved by as much as 122% over pristine nylon 6 with the addition of 4.7wt.% nanoclay.

Following the work done by Toyota research group, several researchers implemented both modified and unmodified nanoclay in various polymeric resins. Most commonly, these studies focus on possible improvements in thermo-mechanical properties of polymers [4-16]. For instance, Lan and Pinnavaia [5] prepared nanoclay from Na^+-montmorillonite by an ion exchange reaction with alkylammonium chloride or bromide salts. The resulting nanoclay was then introduced to EPON 828 epoxy resin at loadings ranging from 2 to 23.2wt.%. Both x-ray diffractometry (XRD) and transmission electron microscopy (TEM) results indicated complete exfoliation of nanoclay platelets in epoxy matrix. Consequently, tensile testing confirmed up to 12- and 18-fold increase in tensile stiffness and strength, respectively. However, with the choice of poly(ether amine) as the curing agent, the fabricated nanocomposites had sub-ambient glass transition temperatures. Lan and Pinnavaia [9] also report that the improvements in mechanical properties for systems at glassy state were rather marginal. Similarly, Wang et al. [6] mixed three commercially available nanoclay types: Cloisite® 20A, Cloisite® 30A and Nanomer® I30, with various thermoplastic polymers. Although XRD analyses indicated increased basal spacing for nanoclay platelets upon polymerization, the improvements in mechanical properties were rather limited. 2.7-fold increase in elastic modulus is followed by 39% and 87% decreases in tensile and impact strengths, respectively for polystyrene/nanoclay systems [6]. Abot et al. [7] observed a similar behavior for epoxy polymer reinforced with organically modified nanoclay. The authors reported up to 31% increase in elastic modulus as the tensile strength deteriorated by as much as 28% over the nanoclay loading range of 0 to 20wt.%. In addition to deterioration in tensile

strength, Abot et al. [7] reported up to 28% reduction in glass transition temperature as determined by dynamic mechanical analysis (DMA). On the other hand, Shen et al. [8] were able to simultaneously improve strength and stiffness. Authors in this study used an organo-clay modified from montmorillonite specially for applications of nylon 6 and nylon 6,6. Akin to Kojima et al. [4], nanocomposite is prepared by melt compounding using a twin-screw extruder. With the aid of a nanoindentation technique, the authors measured the strength and stiffness of nylon 6,6 reinforced with 5wt.% nanoclay. Compared with pristine polymer, the results indicate 15.2% and 27.9% increase in strength and stiffness, respectively.

The large variations in the mechanical property improvement with the addition of nanoclay may be due to inadequate dispersion and exfoliation of nanoclay particles. In particulate reinforced composites, the effective particle dimension is of particular importance as it dictates the mechanical properties for a given loading [17-22]. Singh et al. [17], for instance, investigated the effect of aluminum particle size on the mechanical properties of polyester/aluminum composites. Aluminum particles of three different dimensions (i.e., 100nm, 3.5μm and 20μm) were added to liquid polyester resin by mechanical blending at loadings ranging from 1 to 10wt.%. Overall stiffness of the composite at a given loading is observed to be independent of the particle size, whereas strength is found to decrease monotonically with increasing particle size. Correspondingly, Cai and Salovey [18] used polystyrene particles of sizes ranging from 0.315μm to 1.250 μm to reinforce polysulfide matrix. In the range of particle sizes studied, 10.2% improvement was observed in stiffness versus a decrease of more than 47% in strength. Degradation of strength with an increase in stiffness was also observed by Wang et al. [6] and Abot et al. [7] for nanoclay reinforced epoxies. Consequently, one can conclude that the reduction of strength with the addition of nanoclay may be due to agglomeration of nanoclay particles and their lack of dispersion into individual platelets. Nonetheless, compared to post-dispersion changes in thermo-mechanical properties, dispersion characterization did not receive adequate attention. In order to have predictive capability over the mechanical properties of nanoclay reinforced composites, it is essential to be able to characterize nanoclay dispersion at multiple length scales.

Among the small number of studies devoted to nanoclay dispersion [23-24], Park and Jana [23] studied epoxy aided dispersion of nanoclay in PMMA matrix. Transmission electron microscopy (TEM) and wide angle x-ray diffractometry (WAXD) were implemented to compare the state of dispersion of nanoclay in PMMA with that of a ternary system epoxy/nanoclay/PMMA. The results indicated that a priori mixing of nanoclay in epoxy is more likely to produce exfoliated clay structures. Park and Jana [24] also approached the problem from a rheological point of view. The authors attribute the increase of basal spacing between nanoclay platelets to the elastic forces exerted by the polymer matrix as the cross-linking takes place. Furthermore, it was concluded that the expansion in gallery spacing takes place as long as the ratio of storage modulus to complex viscosity is over $2\text{-}4s^{-1}$.

Traditionally, the characterization of dispersion as well as intercalation and exfoliation of nanoclay is performed by using two methods: x-ray diffractometry (XRD) and transmission electron microscopy (TEM). X-ray diffractometry is preferred by the majority of researchers to describe the intercalation and exfoliation in a quantitative manner. In this method, a well characterized x-ray (most of the time Cu-Kα) is sent onto the surface of interest. Based on the angle of diffraction of the x-ray from the surface, the basal spacing between the nanoclay platelets is calculated through Bragg's Law [26]. Although X-ray diffractometry enables precise nanoclay basal spacing measurements at Ångström scale, it is prone to certain

shortcomings. According to Kornmann et al. [27], broad distribution of nanoclay basal spacing may lead to indistinguishable intensity peaks and thus may lead to inaccurate conclusions on the state of dispersion. On the other hand, transmission electron microscopy, due to its capability of high magnification imaging, is suitable for qualitative analysis of dispersion. However, its high magnification limits the size of imaging area and thus the obtained results may not be representative of the whole sample. Especially, if the spatial variation of dispersion state is large, such as presence of local tactoids, TEM would be a poor choice of characterization [28].

As an alternative to the above-mentioned traditional methods, researchers gradually used rheological techniques in the characterization of dispersion [28-30]. For instance, Wagener and Reisinger [28] studied rheological characterization of dispersion in poly(butylenes terephthalate)/clay nanocomposites. Based on scanning electron micrographs and tensile properties of the nanocomposites, the authors concluded that the shear thinning coefficient may be used as a semi quantitative method in describing the state of dispersion. However, the setback of rheological methods is that the measured quantity is a bulk property of the sample under consideration. Therefore, the state of dispersion obtained through rheological methods does not yield information on spatial variation.

The current study investigates the effects of mixing temperature on the state of dispersion of nanoclay particles in epoxy matrix. For this reason, 5wt.% nanoclay is mixed into epoxy resin at three different temperatures, (i.e., 30°C, 50°C and 75°C) by sonication. The resulting epoxy/nanoclay compound is then used to fabricate center-gated disks to be used in analysis of nanoclay dispersion. To characterize the dispersion of nanoclay as a function of cluster size and spatial position, a novel method combining scanning electron microscopy (SEM) and wavelength dispersive spectrometry (WDS) is implemented [31]. Scanning electron micrographs taken at various magnifications indicated the presence of nanoclay clusters of various sizes. Thus, a sample is cut in the radial direction of the disk and its through-the-thickness plane is analyzed for nanoclay clusters. Nanoclay clusters larger than 1.5μm are analyzed by performing digital image analysis on the scanning electron micrographs taken at 50x magnification, whereas, clusters of smaller dimensions are analyzed by wavelength dispersive spectrometry. Temperature dependence of the radial distribution of nanoclay sizes and shapes are also presented.

2. EXPERIMENTAL STUDIES

2.1. Materials

Cloisite® 25A of Southern Clay Products (Gonzales, TX) is mixed with EPON 815C epoxy resin (Shell Chemicals) at a loading of 5wt.%. This particular type of nanoclay is modified by the manufacturer to increase the organo-philicity of its gallery region, thus resulting in better dispersion in various types of resins. EPON 815C is a low viscosity resin with a room temperature viscosity of 0.74Pas (740cp) that is primarily preferred in molding applications. It is also well known that addition of nanoclay into polymeric resins result in sharp increases in viscosity and adversely affects the processibility. The epoxy resin used in this study is especially suitable for mixing nanoclay particles due to its low viscosity. The

epoxy/nanoclay compound is cured with Epi-cure 3282 curing agent from Shell Chemicals at a weight ratio of 5:1 of resin to curing agent. At this particular mixing ratio, the gel time is approximately 20 minutes. In this study, the mold cavity is filled under 10s, well before the cross-linking starts.

2.2. Mixing of Nanoclay in Epoxy Resin

Nanoclay is mixed into the epoxy resin with the aid of a 42kHz, constant amplitude sonicator. Initially, the resin is placed into a beaker which is immersed into the sonicator filled with water. Then proper amount of nanoclay is gradually added into the resin. To help dispersion of large aggregates, 5 minutes of hand mixing is applied before the sonication starts. Total sonication time is chosen as 60 minutes, beyond which a visual change in the resin/nanoclay compound is not observed. The amount of nanoclay added into the resin is determined by accounting for the curing agent needed during molding stage, such that the final nanoclay weight fraction of 5% is achieved.

In order to investigate the effects of the mixing temperature on the state of nanoclay dispersion, nanoclay is mixed with epoxy resin at three different temperatures of 30°C, 50°C and 75°C. A cupper tubing connected to a constant temperature water bath is placed into the sonicator to keep the water surrounding the beaker containing the resin/nanoclay compound at the desired temperature.

At the end of sonication, a thin layer of small air pockets are formed on the surface of the resin/nanoclay compound. As these air pockets would weaken the final properties of the nanocomposite and might affect the dispersion state, the compound is kept aside for degassing for an additional hour before molding.

2.3. Molding and Sample Preparation

Samples used in investigating the effects of mixing temperature on the dispersion of nanoclay are fabricated by a custom made molding setup. The schematic representation of the setup is given in Figure 1 and described in detail elsewhere [32,33].

The two hollow cylinders on the molding setup serve as the reservoirs for epoxy/nanoclay compound and Epi-cure 3282 curing agent. The inner diameters of the cylinders are machined to 55.47 and 25.43mm which yield 4.7:1 volumetric ratio for the resin and curing agent, respectively. A 80-kip hydraulic press is utilized to force the epoxy/nanoclay compound and curing agent out of the cylinders via two plungers. Outflows from both cylinders are then combined by a tee-connector and passed through a static inline mixer with 32 alternating helical elements placed in a polypropylene tube to provide thorough mixing. Well mixed nanoclay/epoxy compound and curing agent are injected into a mold that is positioned inline with the system. The constant speed of the ram results in a volume flow rate of 5.32cm^3/s during mold filling.

The mold is composed of three main parts, two mold walls and a spacer plate. The 228.6mm x 228.6mm spacer plate is a 3.175mm (1/8in) thick square with a 152.4 mm (6in) diameter circle cut out from the center. The disk shaped cavity is formed by placing the spacer plate between 6.35mm (1/4in) thick aluminum mold walls. The resin/nanoclay/curing

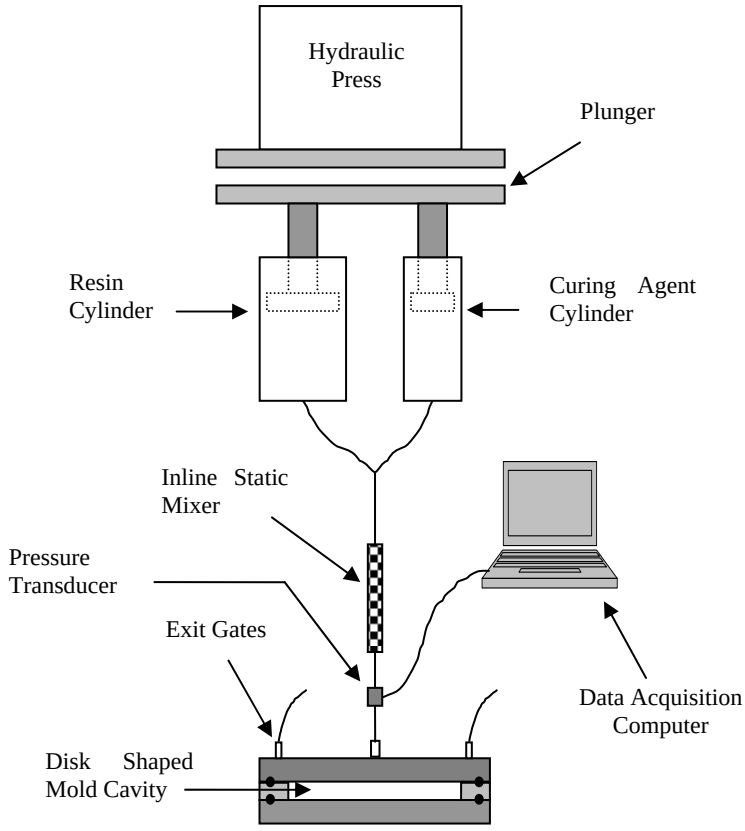

Figure 1. Experimental molding setup used to fabricate center-gated disks.

agent mixture enters the mold cavity through a fitting, mounted at the center of the top mold wall. Other than the inlet, four exit vents are placed symmetrically at the outer edges of the top mold wall. The injection is continued until the mixture comes out of the exit gates, after which the press is stopped. The molding is then completed by sequentially clamping the exit gates and the inlet gate. Since some amount of post-fill pressure improves the part quality [34], the press is operated for an additional second before clamping the inlet gate to apply a modest packing pressure.

A total of three disks reinforced with Cloisite® 25A nanoclay are fabricated. The resin/nanoclay compound used in each disk is prepared at different temperatures, i.e., 30°C, 50°C and 75°C. A sample is cut along the radius of each disk (i.e., 76.2mm long) as depicted in Figure 2 and radial variation of dispersion state is analyzed on through-the-thickness surfaces of these samples.

2.4. Quantification of Dispersion

Preliminary microstructural analysis of the nanocomposites is carried out on a JEOL-880 high resolution scanning electron microscope. The images obtained from scanning electron microscope indicate that the nanoclay exists primarily in the form of clusters of various sizes.

Further analysis at magnifications ranging from 100X to 25000X revealed that there is a continuum of cluster sizes from nanometer scale up to 50μm. A sample microstructural image taken at 2500X showing various nanoclusters is depicted in Figure 3.

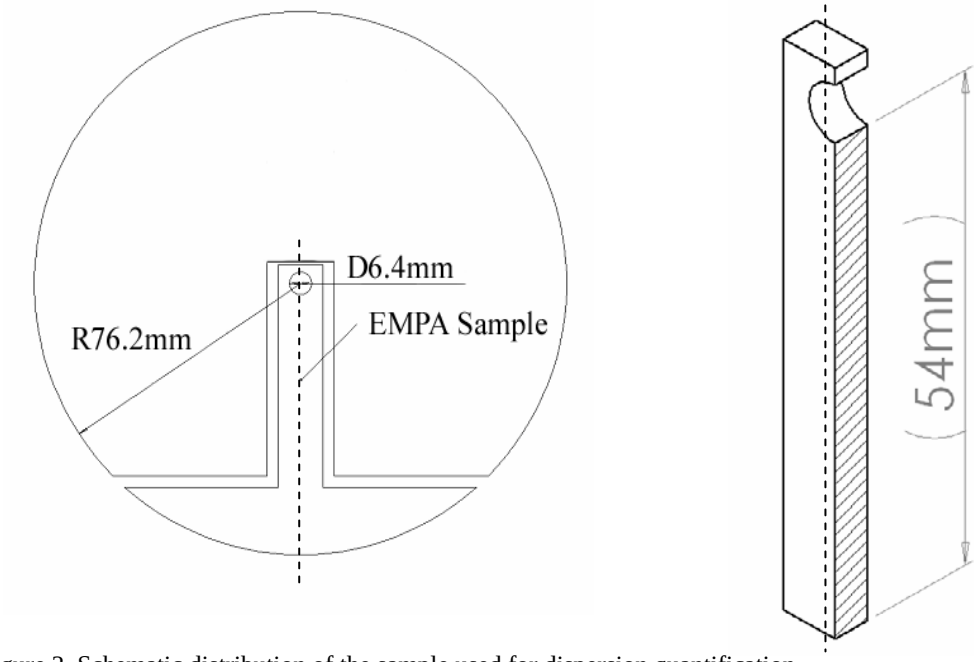

Figure 2. Schematic distribution of the sample used for dispersion quantification.

To characterize the state of dispersion accurately, one needs to consider nanoclay clusters at all relevant scales. The traditional methods of dispersion characterization are lacking spatial coverage and are usually inadequate to characterize large nanoclay clusters. In nanoclay composites, nanoclay most likely exists in the form of clusters. In such cases, spatial coverage of the method used to characterize dispersion is especially important, as it is well known that thermo-mechanical properties of the material strongly depend on the cluster size and their spatial distribution. To assess the required spatial and dimensional coverage, we utilized an electron microprobe analyzer (EMPA) and characterized the dispersion at various radial locations of the molded composite disks.

The dispersion state of the nanoclay composites is characterized using Cameca SX-50 electron microprobe analyzer (EMPA). This particular EMPA, in addition to its imaging capability through scanning electron microscopy, is capable of performing detailed compositional analysis via wavelength dispersive spectrometry (WDS) and energy dispersive x-ray analysis (EDXA). In particular, five wavelength dispersive spectrometers positioned around the column are capable of detecting elements with atomic numbers 5 and above with properly chosen diffraction crystals. Both imaging and compositional analysis of the EMPA are provided by a PC-Based SAMx data acquisition system.

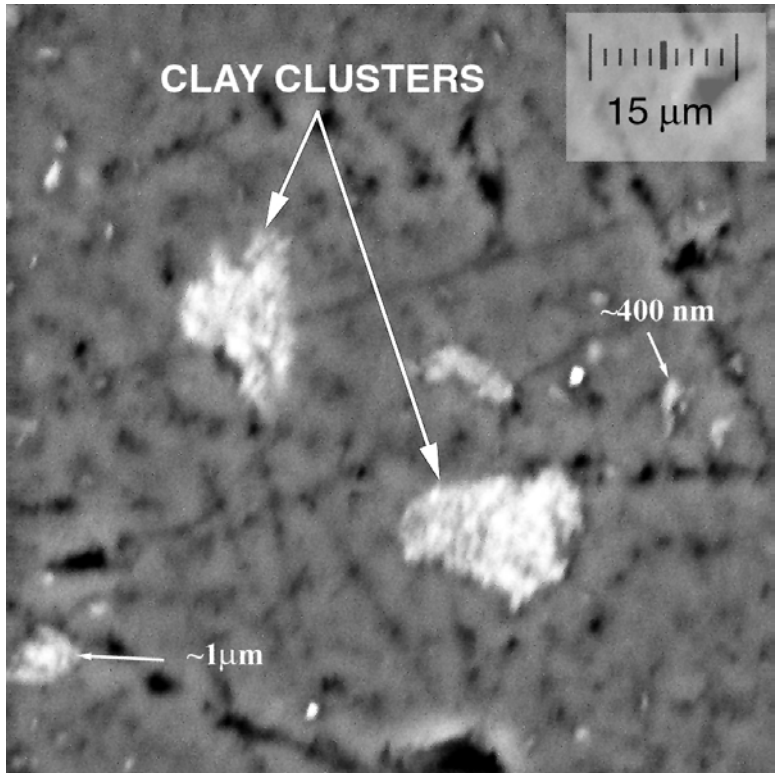

Figure 3. Scanning electron micrograph of the nanocomposite micro-structure taken at 2500X. Clusters of various sizes are indicated.

One sample from each disk is cut radially from the inlet gate at the center to the outer edge of this disk. These samples are then embedded into EMPA sample holder sidewise such that the through-the-thickness surface is exposed for analysis. To cover a wider range of nanoclay cluster sizes, the dispersion analysis is carried out in two categories. Nanoclay clusters that are visible at 50X magnification scanning electron micrographs are quantified by performing digital image analysis. At the utilized imaging resolution, one pixel at 50X magnification is equivalent to 1.5μm. Hence, nanoclay clusters quantified by digital image analysis are larger than 1.5 μm. This category of nanoclay clusters will be referred to as *micro-scale clusters* throughout the article. The nanoclay clusters that were not visible at 50X magnification are analyzed by wavelength dispersive spectrometry (WDS) and will be referred to as *nano-scale clusters*.

Digital image analysis is utilized to quantify the *micro-scale clusters*. For each of the three approximately 56mm-long samples, scanning electron micrographs are gathered along the center line of the surface of interest at 4mm intervals. A total of 72 images are captured in the back scattered electron mode at an accelerating voltage of 20kV and a beam current of 5nA. Images are then stored into 1024X1024 pixel arrays and subjected to digital image analysis using UTHSCSA Image Tool® software. The first step of digital image analysis involved a thresholding process, thereby converting the originally 8-bit grey scale images to binary images. The thresholding process is repeated 7 times in order to quantify and reduce the uncertainties involved in the image analysis. Figure 4 depicts a thresholded image that is further used in quantification of *micro-scale cluster* dispersion. All these binary images are

later analyzed to obtain nanoclay cluster content, number of nanoclay clusters and nanoclay cluster roundness.

Wavelength dispersive spectrometry (WDS) is preferred for quantification of *nano-scale clusters*. Prior to WDS analysis, compacted Cloisite® 25A nanoclay is analyzed by energy dispersive x-ray analysis in order to determine its constituent elements to be targeted in WDS analysis. The major elements are determined as silicon, calcium, magnesium and iron. These elements are targeted by wavelength dispersive spectrometers of the electron microbeam analyzer along the cross-section of the sample at 500μm intervals. Along the length of the samples, a total of 320 locations are analyzed by WDS. A pristine epoxy polymer is also analyzed by WDS and used as background corrections for the quantification of *nano-scale clusters.* Prior to data collection, a trial sample is analyzed at various beam conditions in order to determine the optimum beam condition for maximum precision and minimum beam damage on the analytical volume. As a result, all analyses are conducted at a beam current of 5nA and a spot diameter of 20μm.

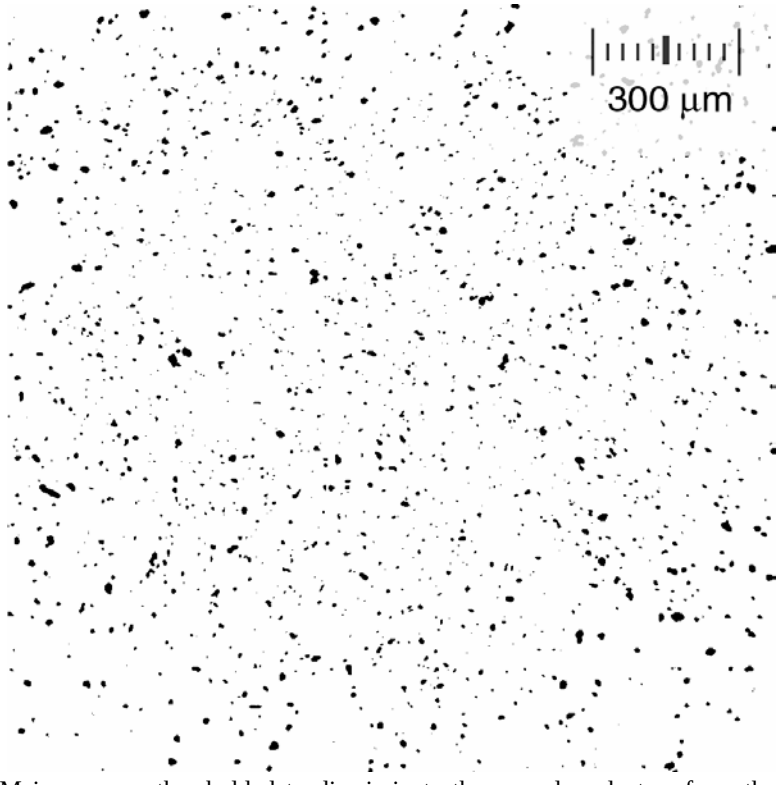

Figure 4. SEM images are thresholded to discriminate the nanoclay clusters from the matrix. The image depicted is taken at 50X magnification.

3. RESULTS AND DISCUSSION

3.1. Dispersion of Micro-Scale Clusters

Dispersion and exfoliation of micro-scale nanoclay clusters down to sub-micron size are particularly essential since existence of nanoclay aggregates is often encountered and is known to extensively affect the final mechanical performance of the nanocomposites. In that respect, we investigated the phase fraction and morphology of nanoclay present in the form of aggregates in epoxy matrix as a function of temperature.

Researchers often attempted solving the problem of agglomeration by changing parameters such as temperature, during mixing of nanoclay into the polymer matrix [35,36]. However, the effects of mixing parameters are quantified either by the dispersion characterization methods mentioned earlier, which are lacking spatial coverage, or by elaborating on the final thermo-mechanical properties of the nanocomposites. Investigation of micro-scale nanoclay cluster dispersion by the method implemented here provides information that was previously unavailable as it contains complete spatial coverage of the sample.

Radial distribution of *micro-scale cluster* content is depicted in Figure 5 together with 95% confidence intervals for each of the three different mixing temperatures studied. Each data point in Figure 5 is formed by determining the phase fraction of nanoclay from the images captured by scanning electron microscopy starting from r=3.2mm (r is radial distance). Figure 5 indicates that volume fraction of *micro-scale clusters* do not display a significant change in the radial direction, regardless of the temperature. The average micro-scale cluster content is calculated as 2.8, 3.4 and 4.0vol.% for mixing temperatures of 30, 50 and 75°C, respectively. The increase in micro-scale cluster (clusters larger than 1.5μm) content with the increase in mixing temperature indicates the presence of lesser amounts of nano-scale clusters at higher mixing temperatures. Based on these results, a more effective dispersion of nanoclay seems to take place at lower mixing temperatures. It should be noted that the nanoclay content calculated by digital image analysis is expressed as volume fraction rather than weight fraction since the density of nanoclay is unknown at its current degree of compaction.

This trend may be attributed to the higher viscosity of the epoxy resin at lower temperatures. It is believed that shear forces developed during mixing are responsible for cluster breakdown and improved dispersion of the nanoclay. Since the mixing is performed with a constant amplitude and frequency sonicator (i.e., constant strain rate), lower viscosities of the resin/nanoclay compound would result in lower shear stresses acting on the nanoclay clusters. Thus, as observed in binary SEM images, average micro-scale cluster content is higher for the higher mixing temperatures. This trend is observed by Park and Jana as well [24]. The authors argue that the lower resin temperatures result in higher viscous forces and therefore yields higher levels of exfoliation. In a recent study, Lertwimolnun and Vergnes [36] investigated the effects of several mixing parameters on the degree of exfoliation of polypropylene/organoclay nanocomposites. Cloisite® 20A is mixed with polypropylene in an extruder at two different temperatures: 180°C and 200°C. Although the XRD peak positions are not affected by the mixing temperature, rheological observations revealed that the degree of exfoliation is considerably higher at 180°C compared to 200°C.

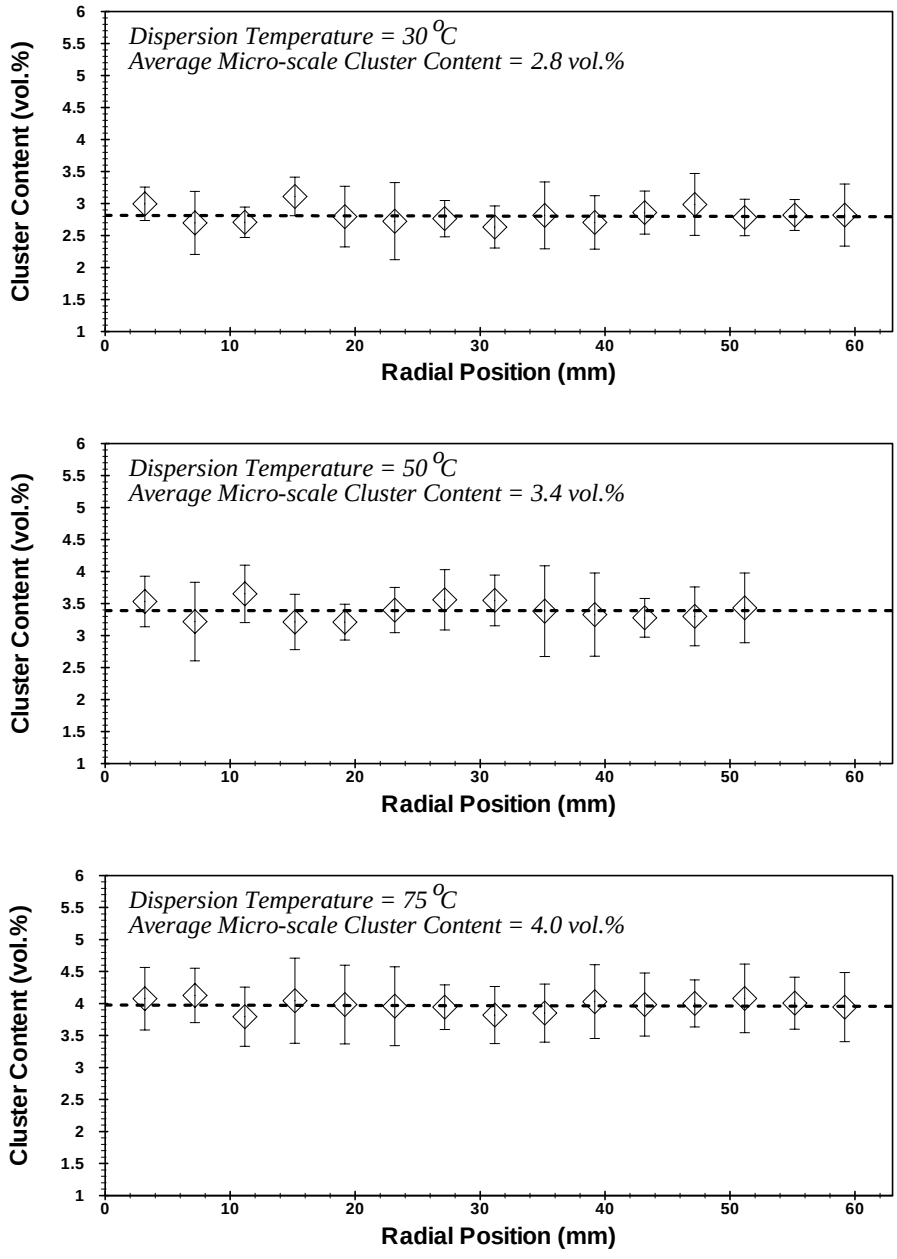

Figure 5. Micro-scale cluster distribution along the radius for the mixing temperatures of 30, 50 and 75°C.

As Figure 5 indicates, *micro-scale cluster* content remains constant along the radius of the molded disks, yet nanoclay clusters may exhibit a preferential size distribution. During filling of the disk-shaped mold cavity, nanoclay particles are subjected to shear forces due to narrow gapwidth and compressive forces due to decelerating flow [37]. These forces may result in cluster breakdown and consequently, preferential variation of nanoclay cluster sizes. If there is such a variation regardless of constant nanoclay content, the nanoclay cluster density, i.e., number of nanoclay clusters per unit area, should vary in the radial direction.

Figure 6 shows a distinct variation of cluster density in the radial direction for all three disks. At the outer edges of the disks, *micro-scale cluster* density is observed to be as much as 50, 70% and 44% higher than that of the inlet for 30, 50 and 75°C, respectively. Knowing that the *micro-scale cluster* content remains constant along the radius, increase in the *micro-scale cluster* density indicates that nanoclay clusters are becoming finer close to the edges of the disks.

The breakdown of nanoclay clusters into smaller particles may be further demonstrated by the change in percentage contribution of *small clusters* (i.e., $A<3\mu m^2$) to the overall nanoclay cluster content at various points along the disk radius. Figure 7 depicts the percentage contribution of *small clusters* as a function of the radial position and mixing temperature. At all mixing temperatures studied, the percentage contribution of small clusters increases by as at least 8% towards the outer edges of the disks.

These results indicate that nanoclay clusters are preferentially transported and/or broken down along the flow direction due to the viscous stresses. A more thorough analysis can be performed by identifying this preferential distribution for a broader range of nanoclay clusters. For this reason, nanoclay clusters are categorized into four groups based on their area, A. These four nanoclay cluster groups are: *i*) $A<3\mu m^2$, *ii*) $3\mu m^2 \leq A<20\mu m^2$, *iii*) $20\mu m^2 \leq A<50\mu m^2$ and *iv*) $A\geq 50\mu m^2$. Percentage change of contribution of different cluster sizes are calculated with respect to the first data point, i.e., r=3.2mm. To illustrate the reduction of nanoclay cluster size, percentage contribution of each nanoclay cluster group at a particular radial location is divided by the percentage contribution of the same nanoclay cluster group near the inlet (i.e., r=3.2mm).

For example, at the mixing temperature of 30°C, clusters with $A<3\mu m^2$ make up 35% of the total clusters at the inlet, whereas same size clusters make up 41.3%, 43.3%, 49.7% and 45.5% of the total clusters at r=19.2, 31.2, 43.2 and 55.2mm, respectively. Thus, as shown in Figure 8, the percentage contribution ratios of small clusters is, 18.1, 23.7, 41.1 and 30.2% , respectively. The percentage contribution ratios are calculated for all four nanoclay cluster size categories and three mixing temperatures. It should be noted that the analyses for nanocomposite disk with a mixing temperature of 50°C is performed on three radial locations due to smaller length of this particular sample compared to others. The percentage contribution ratios are represented in Figure 8. One can deduce that percentage contribution ratio of all cluster sizes are reduced compared to the inlet except for the small clusters with $A<3\mu m^2$. Therefore, at the outer edges of the disk small clusters are a greater portion of the nanoclay clusters compared to the inlet. On the contrary, larger nanoclay clusters are decreasing radially along all disks. The results presented in Figures 6-8 clearly depict a preferential variation in nanoclay cluster size in the flow direction. This spatially non-uniform cluster size variation may have been caused by two factors. First, smaller clusters are more mobile and may move faster with the flow during mold filling and accumulate at the outer edges of the disk. However, small cluster sizes and viscous nature of the resin result in creeping flow with negligible inertial effects. Thus, the local flow is dominated by viscous effects and all clusters move with the flow. Second and more likely explanation is the breakdown of nanoclay clusters due to the viscous stresses formed by the flow kinematics. It is well known that the small gap thickness causes high shear stresses that are dominant over the planar stresses. In addition to high shear rates acting on nanoclay, the circular disk geometry causes decelerating flow and forms compressive stresses on the nanoclay particles

suspended in the flow. The combination of shear and compressive stresses are likely to affect the breakdown and transport of nanoclay clusters.

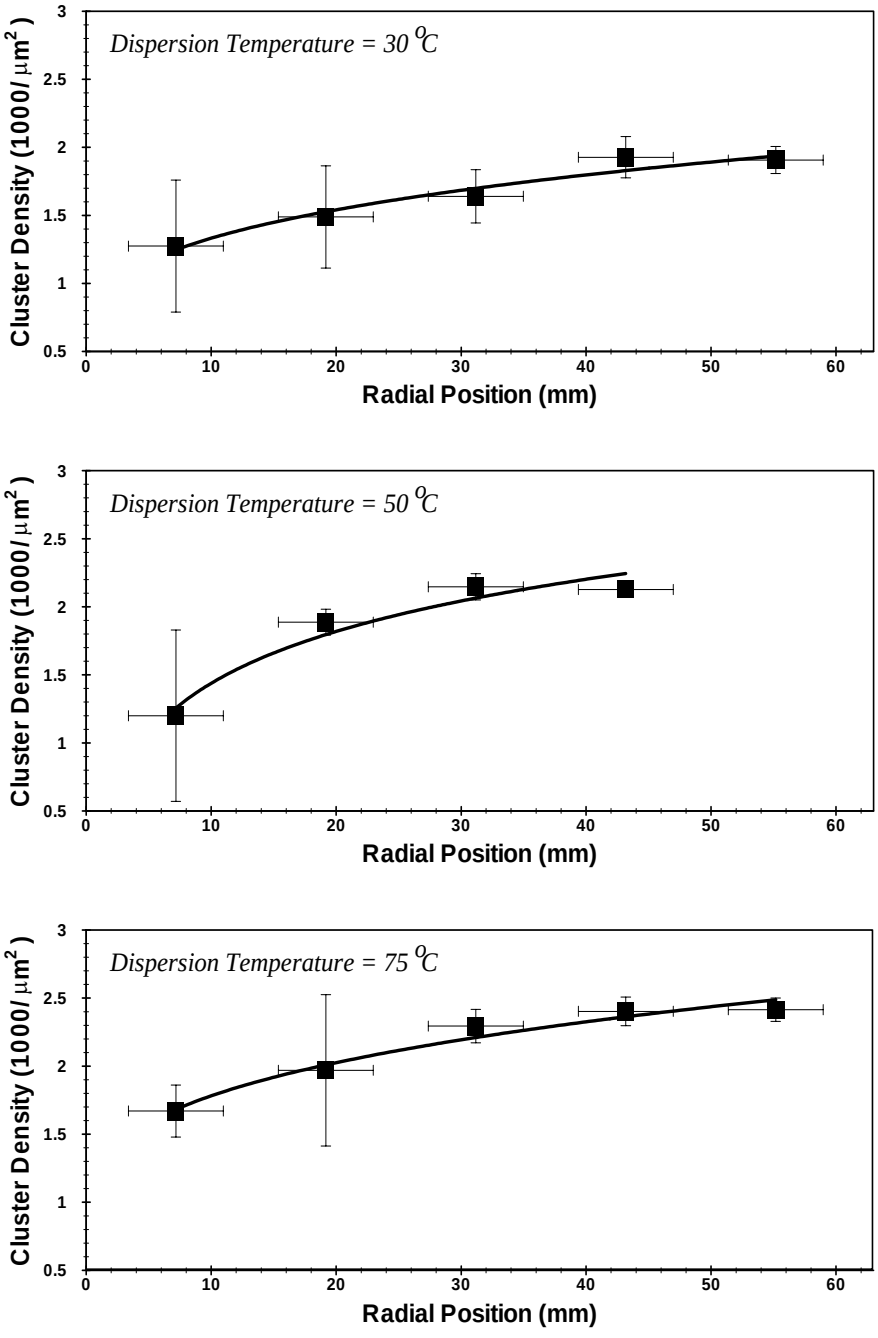

Figure 6. Change in micro-scale nanoclay cluster density in the radial direction. Increasing trends are indications of nanoclay cluster breakdown.

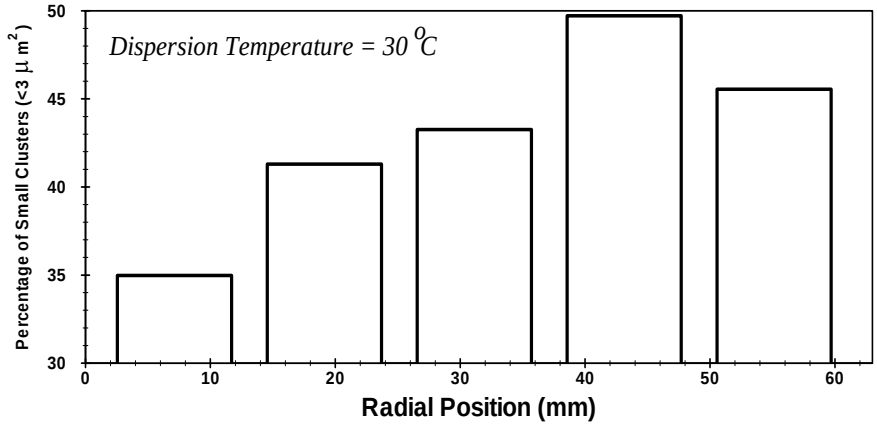

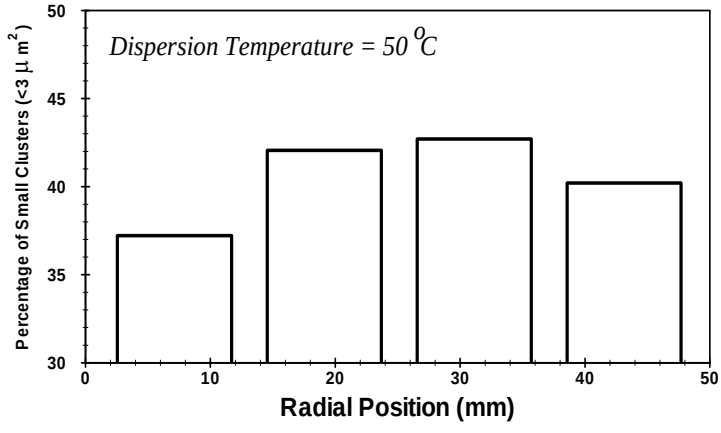

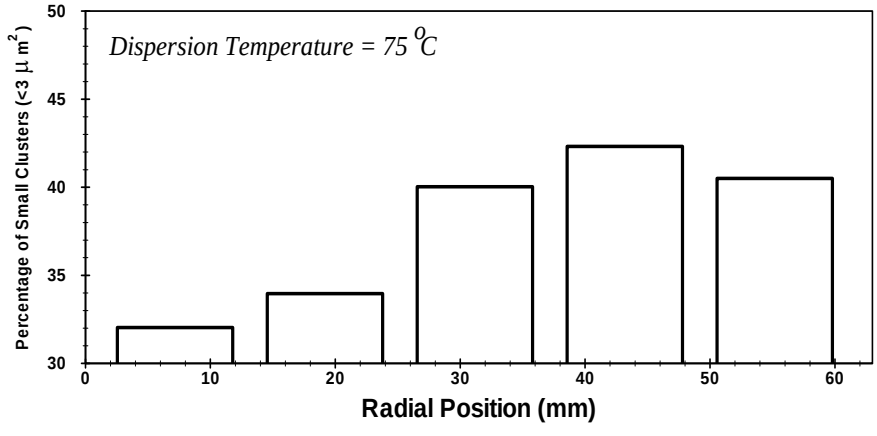

Figure 7. Percentage of small nanoclay clusters (*Area*<3μm^2) in the flow direction.

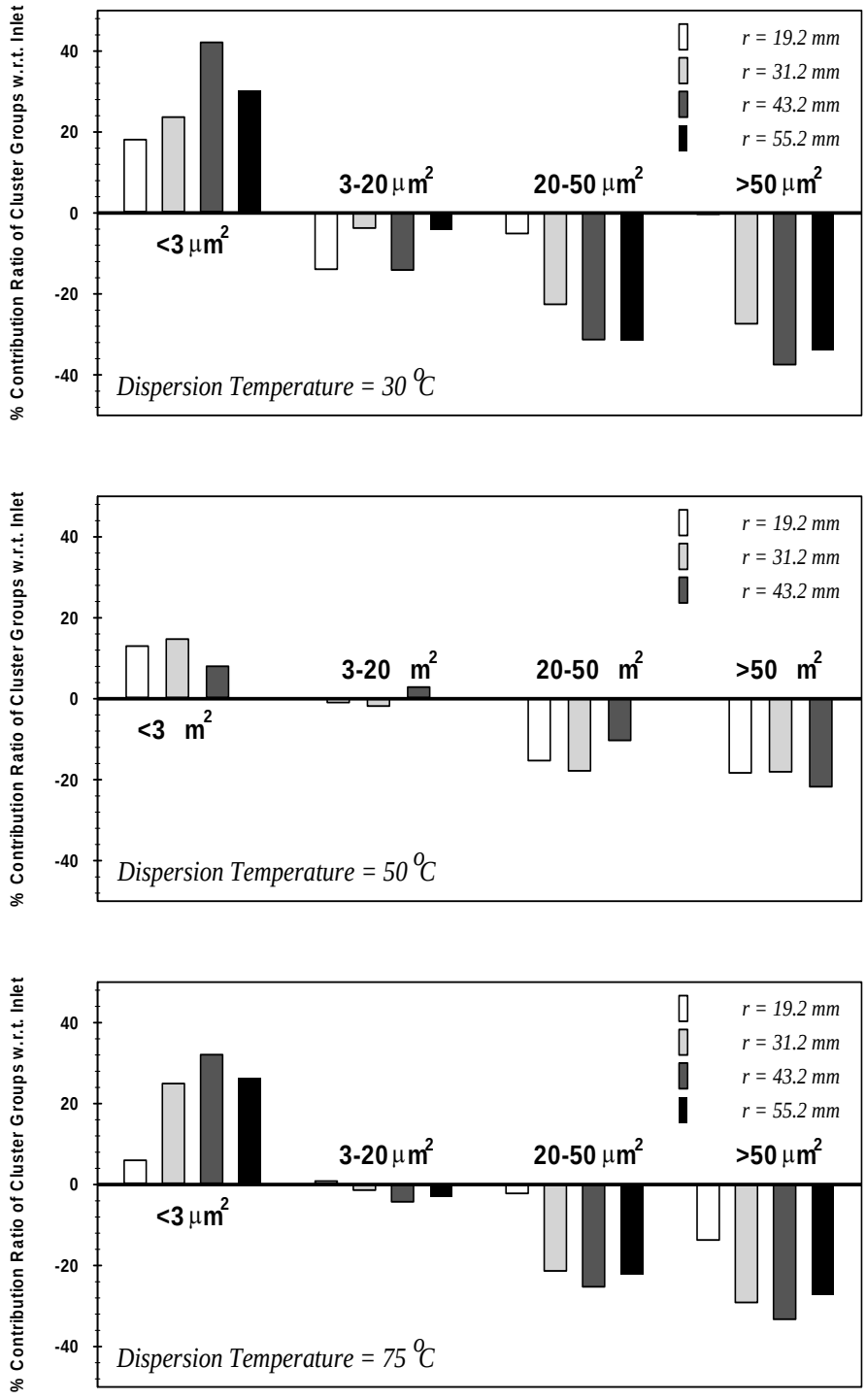

Figure 8. Percentage contribution ratio of nanoclay clusters of different sizes along the flow direction calculated with respect to the cluster size distribution near the inlet.

As the nanoclay clusters are broken down, it is expected that their shape characteristics would change as well. To investigate the shape change of nanoclay clusters along the flow

direction, the average roundness at near the inlet and at the outer edge of the disk are calculated. In this study, roundness of a nanoclay cluster is defined as,

$$\frac{4\pi \times Area}{(Perimeter)^2} .$$

When defined according to the above equation, the roundness varies between 0 and unity. A roundness value of unity indicates a perfect circular shape, whereas irregular, elongated shapes assume a roundness value that is closer to 0.

Figure 9 depicts the roundness distribution of the nanoclay clusters in the first and last image taken along the disk radius. The locations of data bars of both inlet and outlet data are slightly shifted for the clarity of the plot. The solid and dashed lines, on the other hand, are quadratic fits to these data points which identify the distribution peaks clearly. At all mixing temperatures, the peak is observed to shift toward smaller roundness values, indicating that the nanoclay clusters are becoming less circular as they move and break into smaller clusters in the flow direction. It should as well be noted that the nanoclay clusters analyzed for roundness are the ones that are larger than 60pixel^2 (i.e., A>140μm^2) which make up of at least 18.5% of the nanoclay content. Using roundness values for smaller clusters would not be representative of the cluster breakdown as the number of pixels used would be insufficient to quantify the changes in cluster shape.

Figure 10 depicts the effects of mixing temperature on the state of dispersion of nanoclay. Percent contribution of small (A<3μm^2) and large (A>50μm^2) nanoclay clusters to the overall nanoclay content are depicted for mixing temperatures of 30, 50 and 75°C. As the mixing temperature is increased from 30 to 75°C, percent contribution of small nanoclay clusters decrease from 43.3% to 40.8%, whereas that of large clusters increase from 8.9 to 10.4%. Due to the lower viscosity of the resin at high temperatures, the shear stresses that are breaking down the nanoclay aggregates decrease and result in less favorable nanoclay cluster size distribution.

3.2. Dispersion of Nano-Scale Clusters

Dispersion of nanoclay clusters smaller than 1.5μm is analyzed using wavelength dispersive spectrometry (WDS). Prior to compositional analyses, a compacted nanoclay sample is analyzed using energy dispersive x-ray analyses (EDXA) to determine the major constituent elements of the nanoclay. The EDXA spectrum of Cloisite® 25A is depicted in Figure 11. Interpreting the intensity peaks and their energy levels, the major constituents are determined as magnesium, aluminum, silicon and iron. Presence of these elements is targeted by WDS. At least 102 locations that are 500μm apart are analyzed along the radius of each sample. After background corrections using the data obtained from a pristine polymer sample, the weight percentages of nanoclay clusters that are smaller than 1.5μm are depicted in Figure 12.

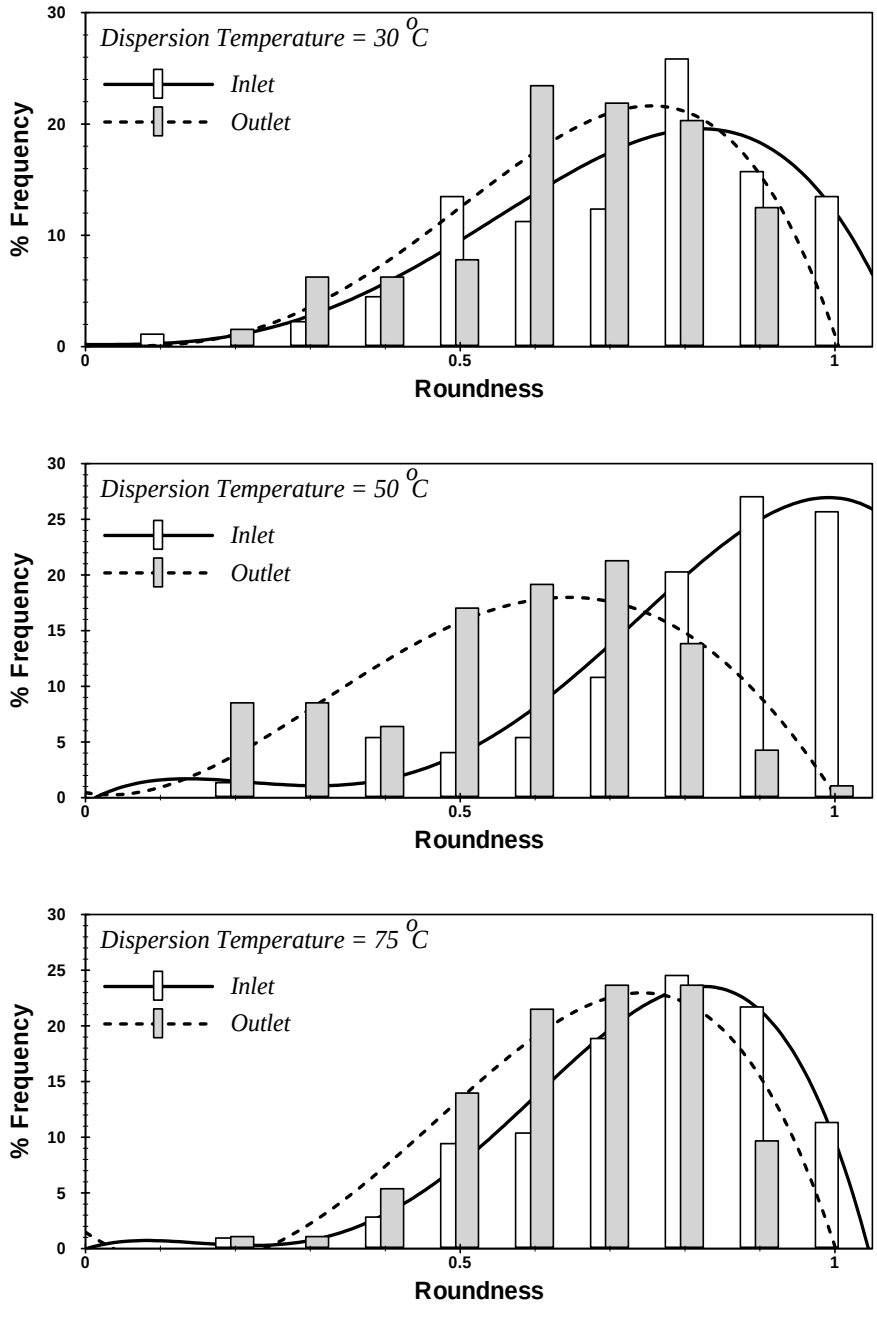

Figure 9. Roundness distribution of nanoclay clusters at the inlet and outer edge of the nanocomposite disks.

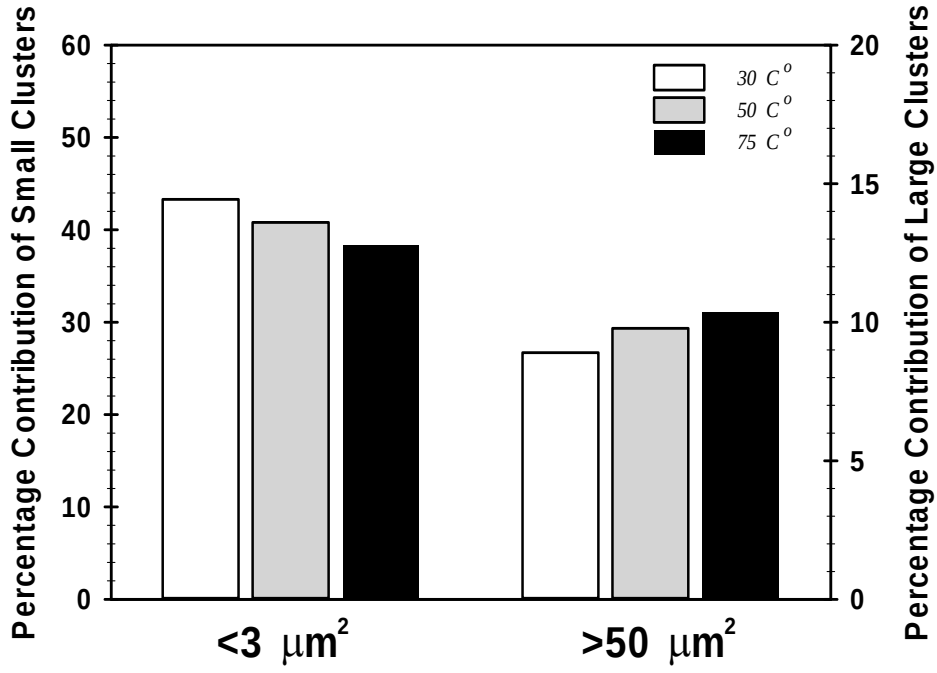

Figure 10. Overall percentage of small (*Area*<3μm^2) and large (*Area*>50μm^2) nanoclay clusters as a function of temperature.

Akin to dispersion of micro-scale clusters, nano-scale cluster content did not indicate dependence on the radial position. An average nanoclay content of 2.5, 2.2 and 2.1wt.% are obtained for mixing temperatures of 30, 50 and 75°C respectively. Since the total nanoclay contents are equal for the three mixing temperatures investigated here, the increase in micro-scale cluster content with increasing temperature is corroborated with the opposite trend in nano-scale cluster content. The points that are targeted with microbeam for WDS analyses are carefully chosen not to include micro-scale clusters that are visible on the surface. However, the finite analytical volume of WDS is formed by the penetration of microbeam 5μm below the sample surface. Therefore, invisible micro-scale clusters below the surface may have contributed to the variations in nanoclay content shown in Figure 12. In fact, the spikes in Figure 12 that reach up to 6wt.% may possibly be the points with invisible nanoclay clusters that are beneath the sample surface.

For the given beam current and analyses time, 3σ minimum detection limits (MDL) are determined for the targeted elements. For magnesium, aluminum, silicon and iron, the MDL's are determined as 0.02, 0.02, 0.03 and 0.04wt.% respectively. Since the nano-scale cluster contents reported here are much larger than the MDL's, it can be concluded that the peak to background intensity and counting times were adequate throughout the study.

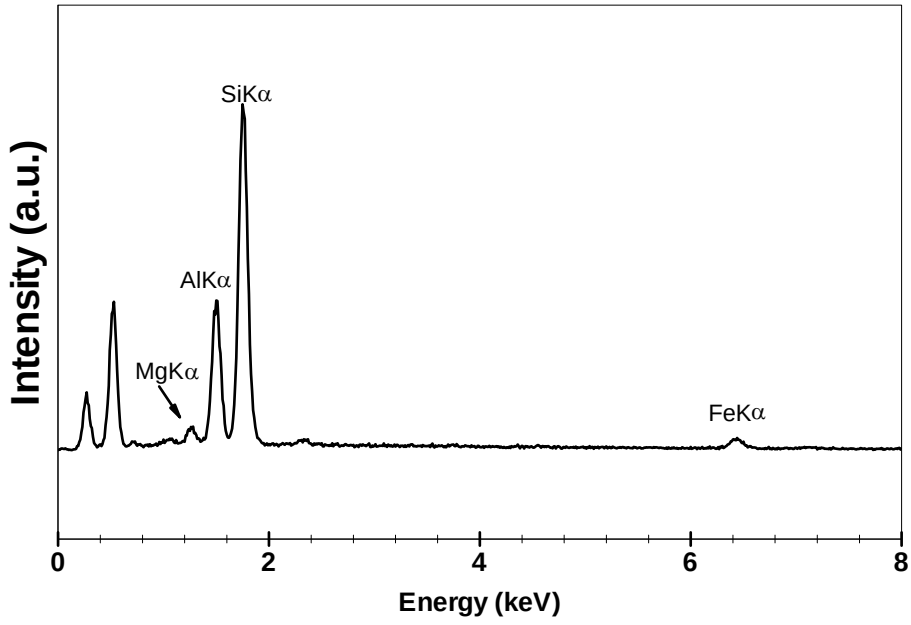

Figure 11. Energy dispersive x-ray analysis (EDXA) spectra of Cloisite® 25A used to identify the constituent elements.

4. CONCLUSION

Effects of mixing temperature on the quality of dispersion of Cloisite® 25A in an epoxy resin are investigated by combining scanning electron microscopy (SEM) and wavelength dispersive spectrometry (WDS). For each mixing temperature, a disk-shaped nanocomposite containing 5wt.% Cloisite® 25A is fabricated. One sample along the radius of each disk is cut and its through-the-thickness cross-section is analyzed to quantify the dispersion state. Nanoclay clusters larger than 1.5μm are analyzed by performing digital image analyses on the scanning electron micrographs taken along the radius, whereas smaller clusters are analyzed by WDS.

It is found that increasing mixing temperature results in larger nanoclay clusters. The contribution of nanoclay clusters smaller than $3\mu m^2$ to the overall nanoclay content is observed to decrease from 43.3 to 40.8% when the mixing temperature is increased from 30 to 75°C. In the same mixing temperature range, contribution of large nanoclay clusters (i.e., $A>50\mu m^2$) is increased from 8.9 to 10.4%. This observation is attributed to the lower viscosity of resin at higher temperatures, which in turn causes reduction of shear forces responsible from the breakdown of agglomerates during mixing.

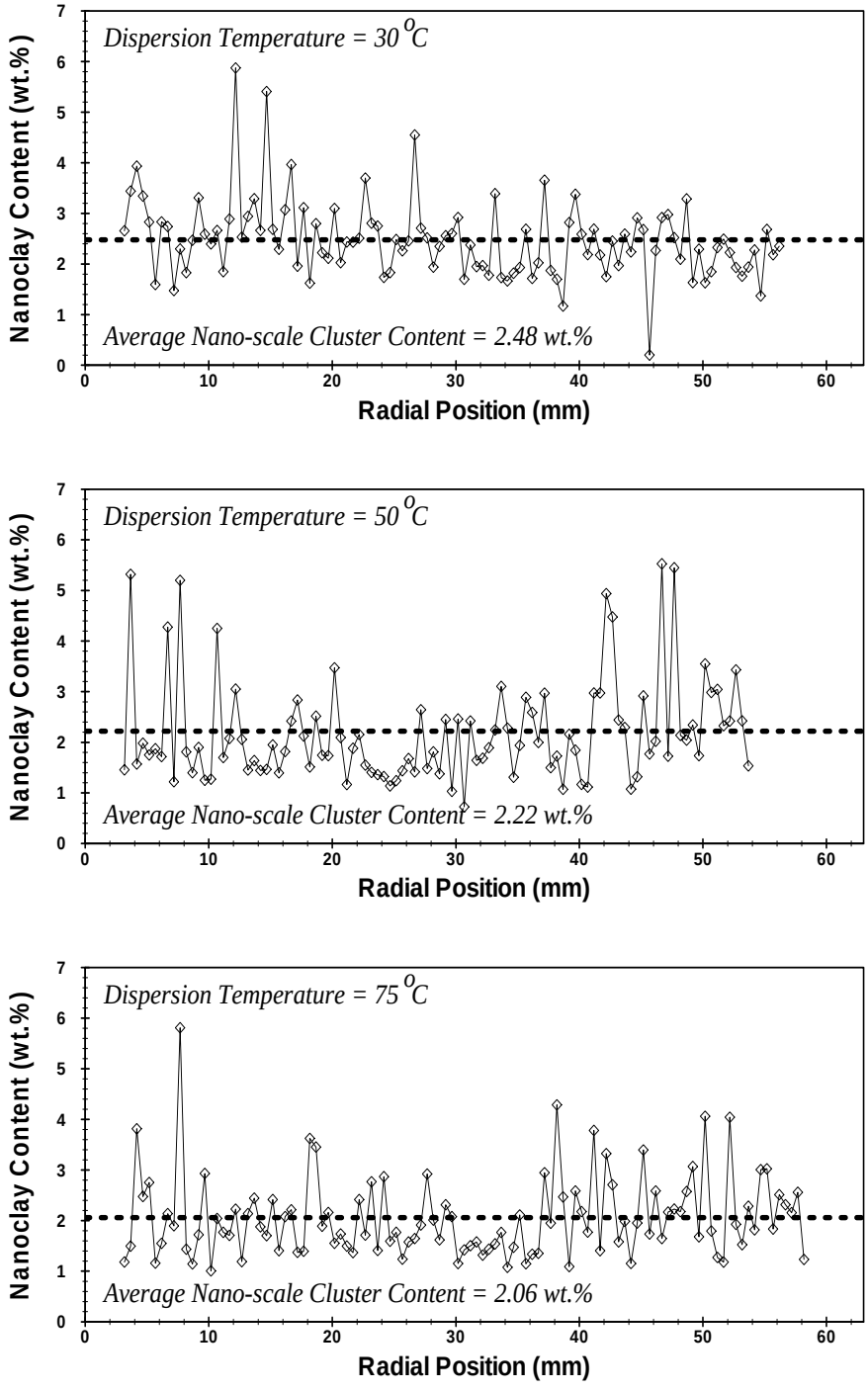

Figure 12. Radial variation of nanoclay dispersed in nano-scale. The data is obtained by wavelength dispersive spectrometry (WDS).

Size and shape distribution of nanoclay clusters along the radius of each disk are also analyzed using the binary SEM images. It is found that nanoclay clusters are broken into

smaller clusters along the flow direction and form smaller nanoclay particles at the outer edges of the disk. For instance, percentage contribution of small clusters (i.e., $A<3\mu m^2$) increased by as much as 30% in the flow direction due to cluster breakdown. It is believed that the cluster breakdown is induced by the viscous stresses due to the small cavity gapwidth and by the compressive forces due to the flow deceleration during the filling of the disk-shaped cavity.

5. REFERENCES

[1] Ahmadi, S. J.; Huang, Y. D.; Li, W. *J. Mater. Sci.* 2004, *39*, 1919-1925.

[2] Usuki, A.; Kawasumi, M.; Kojima, Y.; Okada, A.; Kurauchi, T.; Kamigaito, O. *J. Mater. Res.* 1993, *8*, 1174-1178.

[3] Usuki, A.; Kojima, Y.; Kawasumi, M.; Okada, A.; Fukushima, Y.; Kurauchi, T.; Kamigaito, O. *J. Mater. Res.* 1993, *8*, 1179-1184.

[4] Kojima, Y.; Usuki, A.; Kawasumi, M.; Okada, A.; Fukushima, Y.; Kurauchi, T.; Kamigaito, O. *J. Mater. Res.* 1993, *8*, 1185-1189.

[5] Lan, T.; Pinnavaia, T. J. *Chem. Mater.* 1994, *6*, 2216-2219..

[6] Wang, H.; Zeng, C.; Elkovitch, M.; Lee, L. J.; Koelling, K. W. *Polym. Eng. Sci.* 2001, *41*, 2036-2046.

[7] Abot, J. L.; Yasmin, A.; and Daniel, I. M.; *Mater. Res. Soc. Symp. Proc.* 2003, *740*, 162-177.

[8] Shen, L.; Phang, I. Y.; Chen, L.; Liu, T.; Zeng, K. *Polymer* 2004, *45*, 3341-3349.

[9] Pinnavaia, T. J.; Lan, T.; Kaviratna, P. D.; Wang, Z.; Shi H. *Polym. Mater. Sci. Eng.* 1995, *73*, 117-118.

[10] Yasmin, A.; Abot, J. L.; Daniel, I. M. *Mater. Res. Soc. Symp. Proc.* 2003, *740*, 75-80.

[11] Becker, O.; Varley, R. J.; Simon, G. P. *J. Mater. Sci. Lett.* 2003, *22*, 1411-1414.

[12] Kinloch, A. J.; Taylor, A. C. *J. Mater. Sci. Lett.* 2003, *22*, 1439-1441.

[13] Isik, I.; Yilmazer, U.; Bayram, G. *Polymer* 2003, *44*, 6371-6377.

[14] Xu, Y.; Brittain, W. J.; Xue, C.; Eby, R. K. *Polymer* 2004, *45*,3735-3746.

[15] Dazhu, C.; Pingsheng, H. *J. Comp. Mater.* 2003, *37*, 1275-1287.

[16] Kashiwagi, T.; Harris, R. H.; Zhang, X.; Briber, R. M.; Cipriano, B. H.; Raghavan, S. R.; Awad, W. H.; Shields, J. R. *Polymer* 2004, *45*, 881-891.

[17] Singh, R. P.; Zhang, M.; Chan, D. *J. Mater. Sci.* 2002, *37*, 781-788.

[18] Cai, J. J.; Salovey, R. *J. Mater. Sci.* 1999, *34*, 4719-4726.

[19] Siviour, C. R.; Gifford, M. J.; Malley, S. M.; Proud, W. G.; Field, J. E. *J. Mater. Sci.* 2004, *39*, 1255-1258.

[20] Mani, G.; Fan, Q.; Ugbolue, S. C.; Eiff, I. M. *AATCC Review* 2003, *3*, 22-26.

[21] Liang, Y. M.; Zhoa, J. H. *J. Mater. Sci.* 1999, *34*, 2175-2181.

[22] Cardoso, R. J.; Shukla, A.; Bose, A. *J. Mater. Sci.* 2002, *37*, 603-613.

[23] Park, J. H.; Jana, S. C. *Polymer* 2003, *44*, 2091-2100.

[24] Park, J. H.; Jana, S. C. *Macromolecules* 2003, *36*, 2758-2768.

[25] Pattanayak, A.; Jana, S. C. *61st Annual Technical Conference-Society of Plastics Engineers* 2003, *2*, 1424-1428.

[26] Bragg, W. H.; Bragg, W. L. *Proceedings of Royal Society of London (A)* 1913, *88*, 428-438.
[27] Kornmann, X.; Lindberg, H.; Berglund, L. A. *Polymer* 2001, *42*, 1303-1310.
[28] Wagener, R.; Reisinger, T. J. G. *Polymer* 2003, *44*, 7513-7518.
[29] Wagner, N. J.; Bender, J. W. *Mater. Res. Soc. Bull.* 2004, *29*, 100-106.
[30] Akkapeddi, K.; Facinelli, J.; Worley, D. *61st Annual Technical Conference-Society of Plastics Engineers* 2003, *2*, 2240-2244.
[31] Aktas, L.; Hamidi, Y. K.; Altan, M. C. *Plastics, Rubbers and Composites* 2004, 33, 267-272.
[32] Aktas, L.; Hamidi, Y. K.; Altan, M. C. *J. Mater. Process. And Manuf. Sci.* 2002, *10*, 239-254.
[33] Barraza, H. J.; Aktas, L.; Hamidi, Y. K.; Long, J Jr.; O'Rear, E.A.; Altan, M. C. *J. Adhes. Sci. Technol.* 2003, *17*, 217-233.
[34] Olivero, K. A.; Barraza, H. J.; O'Rear, E. A.; and Altan, M. C. *J. Comp. Mater.* 2002, *36*, 2011-2028.
[35] Wang, D.; Zhu, J.; Yao, Q.; Wilkie, C. A. *Chem. Mater.* 2002, *14*, 3837-3843.
[36] Lertwimolnun, W.; Vergnes, B. *Proceedings of Polymer Processing Society 20th Annual Meeting* 2004, Paper No: 229.
[37] Altan, M. C.; Rao, B. N. *J. Rheol.* 1995, *39*, 581-599.

In: Nanomaterials: New Research
Editor: B.M. Caruta, pp. 219-235
ISBN: 1-59454-369-0

Chapter 7

SYNTHESIS OF THIOL-DERIVATIZED GOLD AND ALLOYED GOLD-SILVER CLUSTERS WITH CONTROLLED MORPHOLOGY

G. Carotenuto*[*], *B. Martorana*[1], *P. Perlo*[1] *and L. Nicolais
Institute of Composite and Biomedical Materials. National Research Council.
Piazzale V. Tecchio, 80 - 80125 - Napoli. Italy.
[1] FIAT Research Center, Strada Torino 50 – 10043 Orbassano TO. Italy.

ABSTRACT

Thiol-derivatized gold clusters (thioaurites) are nanostructured materials potentially useful for a number of technological applications mainly in the fields of optics, non-linear optics, electronics, catalysis, etc. However, the technological exploitation of these nanoscopic objects requires perfect control over their morphology and structure. In this paper, a recently developed chemical route for the controlled synthesis of thiol-deriatized clusters of pure-gold and gold/silver alloyed clusters is described. This synthesis scheme is very simple and may allow preparation of high-purity gold cluster compounds having a tunable metal core size and different types of alkane-thiol shell.

1. INTRODUCTION

Thiol-derivatized gold clusters play an important role in many different research and technological areas. For example, they can serve as model systems to experimentally probe the effects of quantum confinement on electronic, catalytic, and other properties. They have

[*] Istituto per i Materiali Compositi e Biomedici (IMCB). Consiglio Nazionale delle Ricerche; Piazzale Tecchio, 80 – 80125 Napoli (Italy); E-mail: giancaro@unina.it

also been widely exploited for use in catalysis, biological labelling, photonics, optoelectronics, surface enhanced Raman scattering (SERS), etc. The unique properties of a nano-sized metallic phase are mainly determined by size, shape, composition, crystallinity, and structure (solid versus hollow). In principle, one could control each one of these parameters to fine tune the characteristics of nanostructures and working devices based on them. However, still limited are the synthesis schemes available for the preparation of thiol-derivatized metal crystals that may offer a complete morphological control (i.e., type of organic shell and metallic core size, shape, and composition).

Alcoholic reduction of metal ions in presence of poly(vinylpyrrolidone) (PVP) as a protective agent is one of the oldest and simplest chemical routes to produce colloidal noble metals (e.g., Ag, Au, Pt, etc.). In addition, co-reduction and step-reduction of metal ions allow to produce bimetallic clusters with controlled composition and core/shell structure, respectively. The cluster growth stage can be simply end by addition of a non-solvent liquid (e.g., acetone, tetrahydrofurane, etc.) to the reactive mixture, since polymer flocculates and clusters are isolated in a polymer-embedded form [1]. Consequently, a complete control over cluster size and core/shell structure is possible. Recently, the possibility to use this synthesis scheme to produce metallic nanoparticles of controlled shape has been also investigated [2]. In particular, it has been shown that the preferential absorption of PVP molecules to different crystal faces may direct nanoparticles growth into various shapes by influencing the growth rates along the different crystal axes. Nano-spheres, nano-rods, nano-wires, nano-cubes, and nano-prisms of silver, gold, and platinum have been obtained by alcoholic reduction of metal ions at room or slightly higher temperatures.

In this paper, the possibility to obtain thiol-derivatized metal clusters by extraction of gold and alloyed Au-Ag clusters from the protective PVP matrix simply by treatment with alcoholic solutions of thiols is described [3]. Alcoholic reduction of metal ions in presence of PVP followed by thiol treatment represents a very powerful synthetic scheme for the controlled preparation of these special cluster compounds. Details on the spectrophotometric (UV-Vis) approach to control the size of produced thiol-derivatized pure-Au clusters or the composition of thiol-derivatized Au-Ag alloyed clusters are given.

2. TRADITIONAL SYNTHESIS

Colorful aqueous solutions of gold colloids date back to Roman times and were known to the medieval alchemists as aurum potabile [4]. In most cases gold particles were charge-stabilized in an electrolyte solution, and hence their isolation as a pure product without significant irreversible particle coalescence was not possible. The notion that gold sols indeed contain small metallic particles was first expressed in 1857 by Faraday [5], who conducted a very elegant and simple study of the optical properties of thin films prepared from dried colloidal solutions. He observed reversible color changes of the films upon mechanical compression. Under pressure the films appeared green, like thin continuous gold films, while they became bluish-purple when the pressure was released, resembling more the gold particle solutions.

Important aspects in nanoparticle research are: (i) control of particle morphology during synthesis in order to fine-tune properties, (ii) manipulation and study of individual particles,

and (iii) assembly of two- and three-dimensional materials and structures in which nanoparticles are closely packed. The chemical stability of nano-sized particles is a crucial point to avoid degradation processes such as partial oxidation or undesired sintering. In the past, the lacking of sufficient chemical stability of metal nanoparticles has impeded the development of real world applications of these nanostructured materials., and it represents the reason why gold, as a relatively inert metal, has played an important role in pioneering experiments. The stability of naked gold clusters has been improved by development of clusters compounds like thiol-stabilised gold clusters, from which new opportunities for fundamental and applied studies have arisen. Probably in the future a large variety of metal clusters will be handled and used in such passivated form.

The first paper concerning thiol-stabilised gold nanoparticles appeared ten years after the discover of self-assembled monolayers (SAMs) of organosulphur compounds on gold surfaces, in the 1983 [6]. In this study, gold hydro-sols were capped with alkane-thiols to make them soluble in a non-polar solvents [7]. Then, the particles were deposited electrophoretically onto a carbon specimen holder for inspection by transmission electron microscopy (TEM). Two-dimensional hexagonal super-lattices in a fully reversible deposition process were found. In addition, the interparticle spacing was found to be adjustable with molecular precision by the choice of alkanethiol ligands of different lengths. A simple preparative method for bulk quantities of thiol-stabilised gold particles was developed one year later [8] and it become very popular as a starting point for a broad range of nanoparticle studies. This chemical route involved the phase transfer of an anionic Au(III) complex from aqueous to organic solution in a two-phase liquid/liquid system, followed by reduction with sodium borohydride in presence of the thiol-stabilizing ligand. Dark brown solutions of moderately polydisperse particles in the size range of 1-3.5 nm, containing from 100 to 3,500 gold atoms can be obtained by this chemical approach. The typical ruby-red color of colloidal gold emerges with particle sizes above ca. 3.5 nm. This is due to the plasmon absorption of free electron gas which is absent in smaller particles. Detailed studies of particle shape revealed that the truncated cuboctahedron is the predominant structural motif, but other geometries such as decahedra, dodecahedra, and icosahedra are also present in the obtained product. The particles can be purified and kept in the solid state under ambient conditions for months without showing significant aging effects. However, not all types of thiol ligands lead to the same extraordinarily high degree of stability that can be achieved by the use of alkane thiols with a hydrocarbon chain length of C_5 to C_{18}. Hydroxo-functionalized particles stabilized by 4-mercapto-phenol, for example, are somewhat less stable and degrade slowly over several weeks under ambient conditions. The same trend is observed if shorter (C_2 to C_4) thiol molecules are employed as stabilizers.

The principal disadvantage of this preparative method is that in some cases (e.g., ω-substituted thiols) an excessive product purification is required since a layer of the ammonium surfactant covers the thioaurite compound. A solution to this problem has been the one-phase synthesis developed by the same research group and carried out in methanol as solvent and sodium borohydride as reducing agent [9]. Gold nano-particles covered with 4-mercaptophenol have been successfully prepared and this compound has been modified by successive reactions on the shell surface, broadening the application of thiol-derivatized gold nano-particles from a stable but chemically inert compound toward a truly functional reagent. However, owing to solubility issues, methanol is not the ideal solvent for the broad variety of alkane- or arene-thiol compounds. Such a fundamental restriction prevents a full exploitation

of this synthesis scheme. Chemical functionalities can be introduced in the alkyl shell by a post-synthesis place-exchange reactions, but this strategy is employed only to obtain multifunctional ligand shells since the synthesis of homogeneous thiol shells and inert n-alkyl derivatives requires direct introduction of thiol molecules. A further disadvantage of these synthetic schemes is that a growth stage is practically absent in the cluster formation, and therefore the core size in the resulting material can be only lightly modified by adjusting the amount of gold salt. The thioaurite compounds properties (e.g., color, electrical conductivity, etc.) are strictly size-dependent and the possibility to fine tune the metal core size is of a fundamental importance from a technological point of view.

3. SIZE-CONTROLLED SYNTHESIS

An alternative technique for the synthesis of thiol-derivatized gold particles is based on a well-known approach for colloidal gold solutions preparation, i.e., the alcoholic reduction of ionic gold in presence of a polymeric stabilizer (e.g., poly(N-vinylpyrrolidone)) [10]. The primary polymer function is to avoid cluster sintering, but it also allows particle size control by co-precipitation. In fact, polymer absorbs on particle surface, making possible their separation from the reactive mixture by addition of a non-solvent liquid. The obtained polymer-protected nanometric gold particles may dissolve in alcoholic solutions of thiol molecules that promptly remove polymer from particle surface, giving a hydrophobic thioaurite product. Such hydrophobic compound can be easily isolated, purified, and fractioned by size-selective precipitation or Gel Permeation Chromatography (GPC). The synthesis route is interesting principally for the possibility to prepare particles of controlled size. In fact, since the reactive medium is perfectly transparent and it slowly develops a ruby-red color during the metal phase separation, cluster nucleation-growth process can be *in situ* on-line monitored by optical spectroscopy and the growth process can be end at the required size value by co-precipitation with polymer.

For example, the preparative scheme for the synthesis of gold clusters protected by dodecanethiol involved the mixing under stirring of a poly(N-vinylpyrrolidone) (PVP, Aldrich, M_w*=10,000 a.m.u.*) solution in ethylene glycol (stabilized at a temperature ranging from 60°C to 110°C) with a little quantity of a concentrated tetrachloroauric acid ($HAuCl_4$, Aldrich) solution in ethylene glycol. In particular, the first solution was prepared by dissolving 4g of PVP into 20ml of ethylene glycol and the second one by dissolving 5mg of $HAuCl_4$ in 1ml of ethylene glycol. After gold nanoparticle formation the solution had a ruby-red color. In order to end the reaction, the reactive mixture was cast into a large amount of acetone (250ml) and the system was sonicated for a few minutes to allow for the ethylene glycol removal from the Au/PVP nanocomposite. The product was washed several times with pure acetone and then dried at room temperature under vacuum. The obtained solid Au/PVP system was dissolved into a dilute ethanol solution of normal dodecanethiol ($C_{12}H_{25}$-*SH*, Aldrich, 98%). Dodecanethiol is able to produce a continuous protective mono-layer on gold clusters. These molecules bonded the gold surface much stronger than PVP side-groups, and therefore the polymeric stabilizer was completely removed from cluster surface. Thiol molecules were chemisorbed on the gold surface according to a red-ox reaction. After a short time, the exchange reaction was completed and the hydrophobic thiol-coated nanoparticles

were easily separated from the PVP/ethanol solution by centrifugation. In order to remove all thiol excess, the product was accurately washed with ethanol. A waxy, purple solid product was obtained. This material can be handled like a simple chemical compound (for example, it can be dissolved and dried several times without decomposition) and it is stable for months in air at room temperature. Thiol-derivatized gold clusters have a hydrophobic nature and consequently result very soluble in aliphatic and aromatic hydrocarbons, chlorine solvents, and ethers; moderately soluble in styrene; and insoluble in esters, acetone, alcohol, and water.

A number of high-nuclearity thioaurite compounds have been equivalently obtained by treatment of PVP-embedded gold clusters with alkane-thiol solutions in alcohols. In particular, thioaurites based on octadecanethiol and hexadecanethiol were prepared too.

4. PRODUCT CHARACTERIZATION

4.1. Morphological and Structural Characterization

The microstructure of both gold clusters embedded into a PVP matrix and thiol-derivatized gold clusters has been accurately investigated by Transmission Electron Microscopy (TEM, Philips EM208S). As visible in Figure 1a, all particles had a pseudo-spherical shape, which in some cases corresponded exactly to a polyhedron, and aggregates were not present in the samples. When the reaction was performed at a temperature of 60°C for 20min, the particle size was moderately poly-dispersed and a monomodal distribution approximately described by a Gaussian function with μ=7nm and σ=5nm resulted (see Figure 1b). Reaction time and temperature affected the particle size distribution, however the average particle size was widely controlled by varying the tetrachloroauric acid amount.

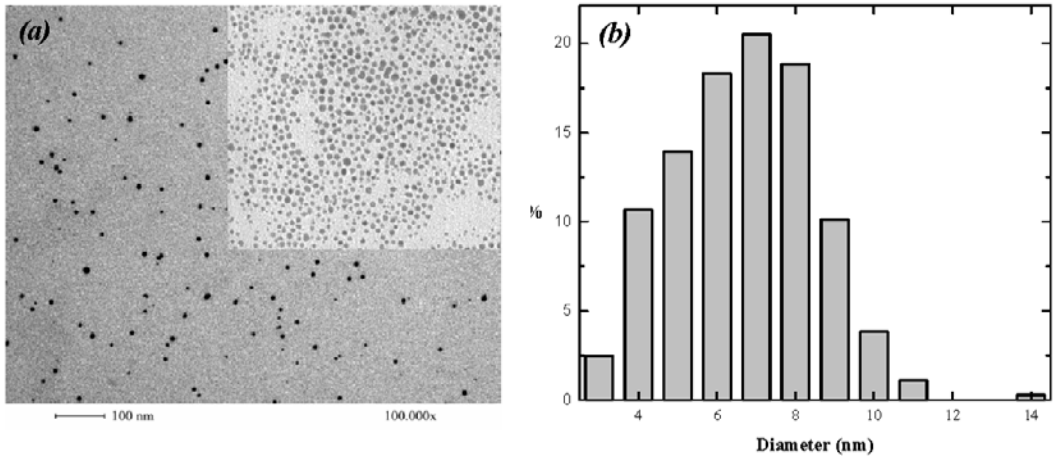

Figure 1. TEM micrographs of PVP-embedded gold clusters and thiol-derivatized gold clusters (insert) (a) and related histogram (b).

Heptane suspensions of gold particles passivated by normal dodecanethiol spontaneously produced self-organized submicron-sized domains of hexagonally close-packed nanoparticle arrays after solvent evaporation (see insert in Figure 1a). Clusters aggregates produced by

sintering of the metal cores were not contained in the final product, and thus the ligand-exchange process was complete and effective.

Thioaurite compounds were structurally characterized by X-ray diffraction (XRD, Rigaku DMAX-IIIC goniometer), using Cu-K_α radiation (λ=0.154056 nm) and a pyrolytic graphite monochromator. The XRD-pattern of Au/PVP nanocomposite is reported in Figure 2. The typical peaks of a face centered cubic (fcc) gold lattice are well-visible superposed to a background produced by amorphous PVP. The obtained lattice parameter of 4.077(2) Å coincides with pure bulk gold value, indicating that nanoparticles were not subjected to lattice distortion due to interstitial impurities. The average crystallite size derived from peak broadening analysis always resulted quite close to the nanoparticle diameter obtained by TEM measurements, suggesting that nanoparticles were single-crystals.

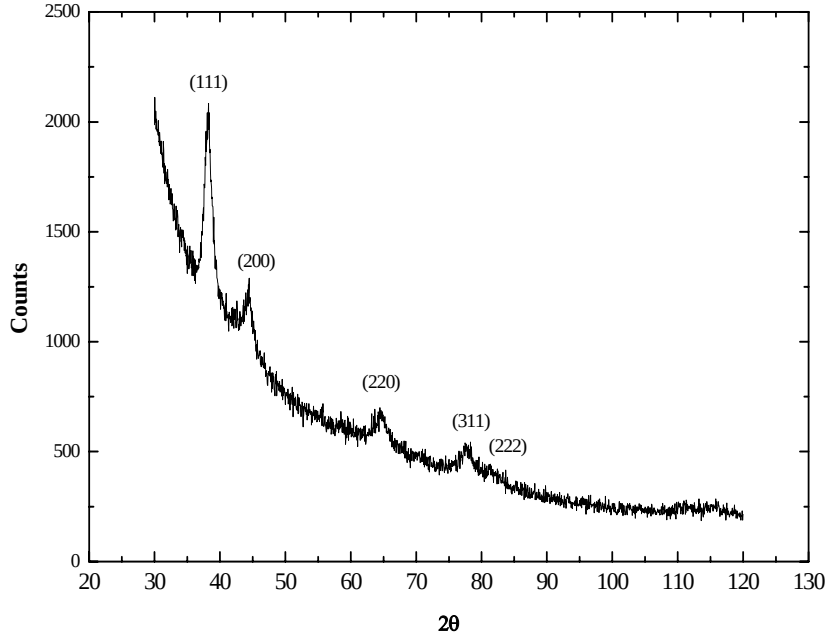

Figure 2. XRD spectrum of PVP-embedded gold nanoparticles (65s at 80°C). The Bragg peaks of fcc gold are labeled.

4.2. In Situ On-Line Spectrophotometric Sizing

The formation-growth process of gold clusters in the reactive liquid mixture was monitored by UV-Visible spectroscopy, looking at the very intensive surface plasmon absorption resonance that characterized the nano-sized metallic phase [11]. Absorption spectra were obtained under isothermal condition at stepped reaction times by using a diode-array UV-Visible spectrophotometer (HP-8453 UV-Vis spectrophotometer), equipped with a

Peltier apparatus to control the reaction temperature (from 0 to 100°C with accuracy of ±0.1°C). The system employed a magnetic stirrer and far-UV quartz cuvettes. Absorption spectra were monitored and recorded on a personal computer connected to the spectrophotometer. Since the reaction rate increased with temperature, shorter sampling times were required at higher temperatures. For example, at 25°C a sampling time of 120s was selected, whereas at 100°C it was of 0.5s. Typical UV-Visible spectra at two reaction times, namely 37s and 65s, are shown in Figures 3a,b respectively.

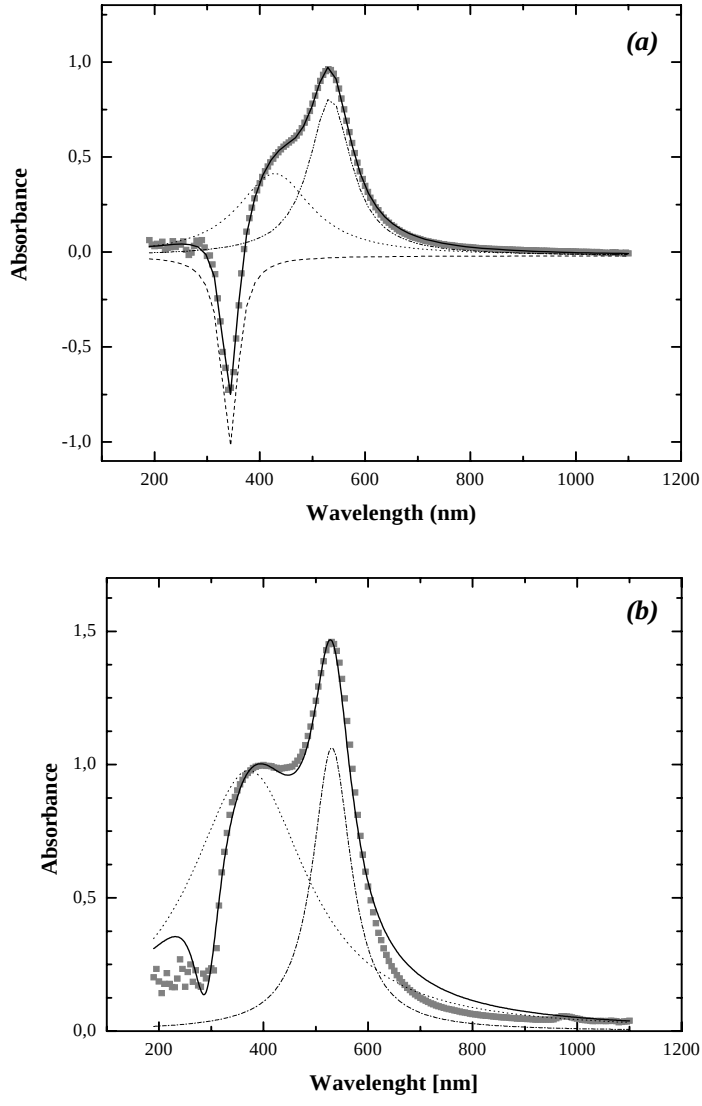

Figure 3. Optical spectrum of a gold mixture corresponding to a reaction time of (a) 37s, and (b) 65s. The curves obtained from data convolution are also plotted, dashed lines are the three contribution (i), (ii) and (iii), while the grey squares represent their sum.

The shape of recorded optical spectra is determined by combination of three main absorptions: (i) that produced by glycolic Au^{3+} complexes, (ii) the *5d→6sp* interband transition of gold clusters, and (iii) the surface plasmon resonance band of gold clusters. An example of spectra convolution by Lorentzian functions is reported in Figures 3a,b. Since Au^{3+} ions are reduced to the zero-valence state, the peak intensity (proportional to the Au^{3+} concentration) becomes more and more negative during the reaction. Spectra convolution allows accurate determination of plasmon peak parameters, *i.e.* maximum absorption wavelength, full width at half maximum (FWHM), integral absorption, etc. Gold clusters sizing can be obtained from these plasmon absorption parameters. In particular, there are theoretical models [12] that allows correlation between plasmon peak characteristics and morphological-topological information concerning the gold nano-particle systems. As visible in the TEM micrograph, gold particles are spherical in shape and aggregate-less, consequently the particle formation-growth mechanisms can be predict from the simple Mie's theory. Such theory predicts, that optical absorption, *A*, is dependent on the number, N, and the size, *R*, of clusters and such dependence is governed by a simple proportionality law, $A \propto NR^3$, where *N* and *R* change continuously during reaction. The nucleation process increases the N value and different particle growth mechanisms may affect in a different manner the temporal evolution of radial growth, R. Therefore, the behavior of the cubic root of measured absorbance *vs.* the reaction time is clearly indicative of which mechanism is dominating in particle growth [12]. A quantitative analysis of optical spectra in terms of cluster dimension can be performed under the hypothesis that the number of clusters in the solution do not change during the reaction. This condition is achieved when nucleation rate is high enough, and nucleation and growth processes are separated stages. In other words, if temperature is high enough, clusters are approximately of the same dimensions since all metal nuclei are generated at same time and grow simultaneously. In such experimental conditions, the temporal evolution of cubic route of absorbance can be directly related to the cluster size evolution. Two different kinetic mechanisms for particle growth maybe involved: (i) diffusion-controlled and (ii) deposition-controlled. The dominant mechanism being the slowest one. Under a diffusion-controlled kinetic mechanism, the radial development of clusters should scale according to a $t^{1/2}$ law, whereas it should result linear with time in the case of a deposition-controlled kinetic mechanism [13]. Data shown in Figure 4 clearly suggest that a deposition-controlled mechanism is the predominant one at reaction temperatures above 70°C. While, at temperatures below 70°C, absorbance cubic root *vs.* time curves do not follow a linear behavior, that can be explained on the basis of a continuous formation of new nuclei during the reaction.

TEM analysis demonstrated that the nanoparticles average size grew linearly with the reaction time at temperatures above 70°C (see Figure 5). This behavior confirms that a surface-deposition controlled kinetic mechanism should be involved in these experimental conditions. Similar behaviors have been also reported for gold cluster formation in formaldehyde-based systems [14]. Finally, *in situ* optical spectroscopy represents a very good approach for size-monitoring during nanoparticle synthesis, because it allows accurate control of final average dimension.

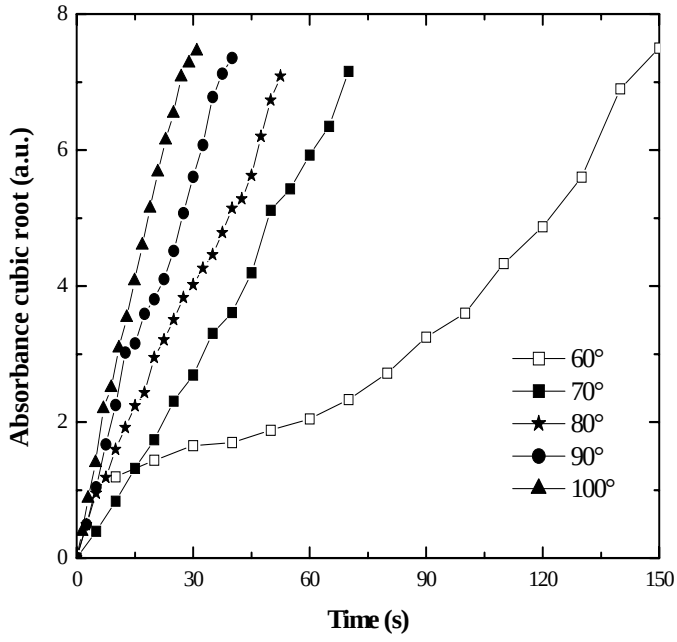

Figure 4. Time dependence of the cubic root of the absorbance at different reaction temperatures.

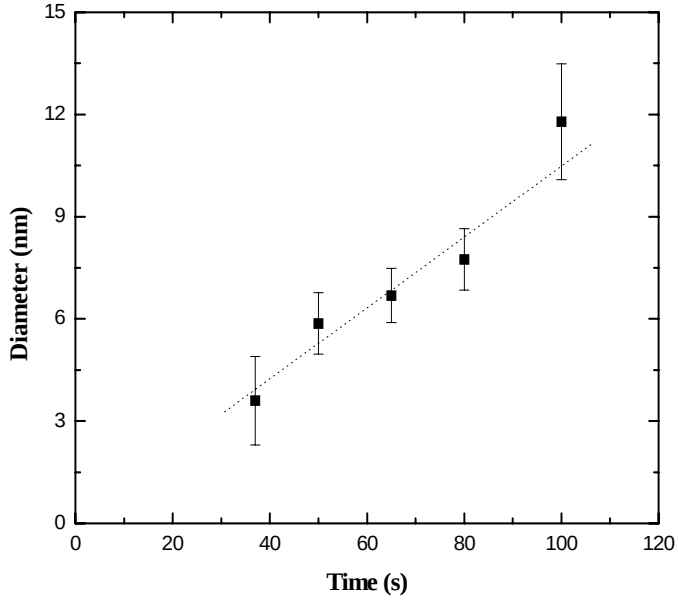

Figure 5. Nanoparticles diameter measured by TEM *vs.* reaction time for a sample obtained at 80°C.

4.3. Thermal Characterization

The thermal stability of dodecylthioaurites was investigated by Thermogravimetric Analysis (TGA, TA-Instrument Mod.Q500). The TGA-thermogram (performed at 10°C/min, under fluxing nitrogen) showed two signals: a first intensive weight loss occurring at a temperature of ca. 250°C and a second small signal was located at 400°C (see Figure 6a). Such weight-loss was probably caused by the evaporation of organic shell decomposition products. When unpurified products were investigated by TGA, a further weight loss was detected in the thermograms at ca. 200°C, probably due to the evaporation of free thiol molecules present in the samples.

Important structural information about thiol-derivatized compounds at solid state were obtained by Differential Scanning Calorimetry (DSC, TA-Instrument Mod.Q100). As visible in Figure 6b, the DSC-thermograms showed the presence of a thermal transition corresponding to melting of crystalline regions produced by interdigitation of thiol chains [15]. When the product was not accurately purified, a further endothermic peak appeared in the thermograms, owing to the presence of pure thiol crystals. Pure dodecanethiol melts at -7°C, while thioaurites showed a very intensive endothermic transition at ca. 30°C. DSC-thermograms obtained on cooling runs of samples previously heated up to 100°C, showed the presence of one exothermic peak produced by the formation of interdigitated n-alkyl chain crystals. The crystallization temperature resulted inferior to the melting point value and cooling rate dependent, owing to super-cooling effects.

5. THIOL-DERIVATIZED ALLOYED AU-AG CLUSTERS

Metal clusters characterized by surface plasmon absorption can be conveniently used as pigments in the fabrication of plastic optical limiters (e.g., colour filters, UV-absorbers, polarizers). However, the possibility to control the frequency of the plasmon absorption is of primary importance for such a kind of application. The absorption frequency of plasmon-based pigments can be finely tuned by alloying metals characterized by surface plasmon resonance located at different frequencies (e.g., Pd-Ag, Au-Ag, etc.) [16]. For a complete control of absorption frequency between the limit values of pure metals, the two metals should give solid solutions in the full composition range. Plasmon resonances in a wide spectral range (430-530nm) can be achieved by alloying gold with silver. Thiol-derivatized Au-Ag clusters of different compositions are very promising as pigments for colour filters, these hydrophobic compounds can be mixed with a number of optical plastics to fabricate advanced optical devices.

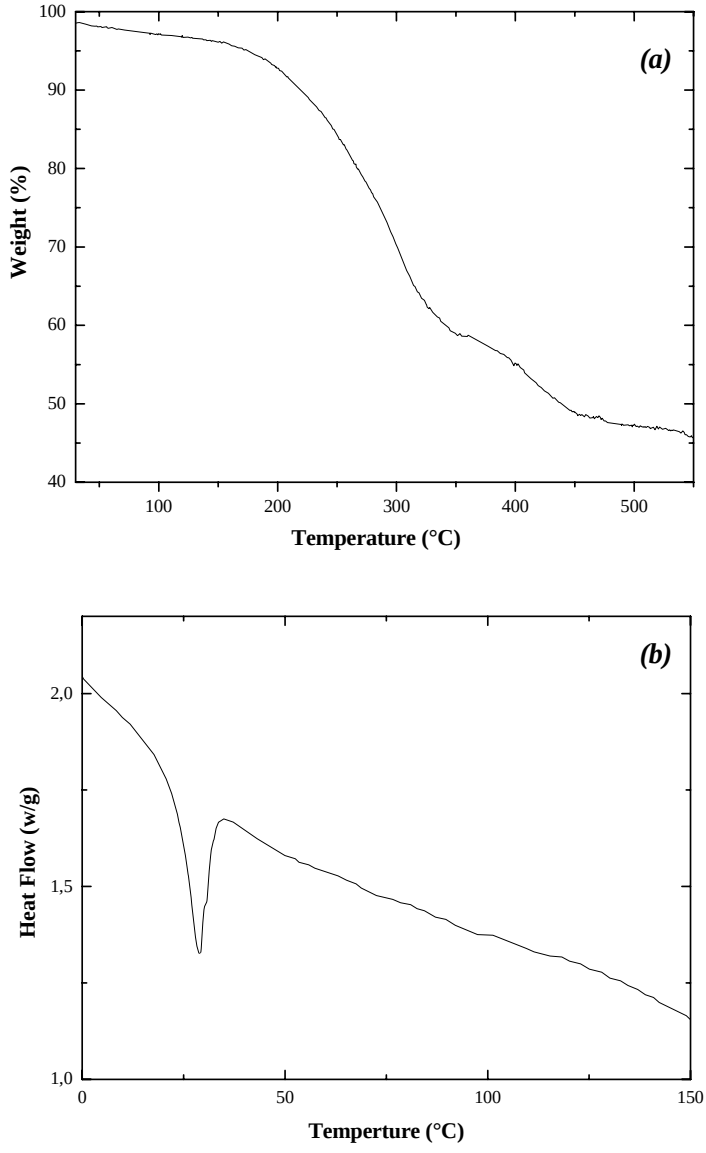

Figure 6. TGA-thermogram (a) and DSC-thermogram (b) of a gold dodecylthiolate sample.

Thiol-derivatized Au-Ag clusters can be obtained by the above described chemical route. In particular, gold and silver ions can be simultaneously reduced by ethylen glycol in presence of poly(vinyl pyrrolidone) as sterical stabilizer to produce alloyed bimetallic nanoparticles. Since Au^{3+} and Ag^{+} ions have similar atomic radius and crystal structure (cubic face centered), Au-Ag solid solutions can be obtained in the full composition range simply by modifying the quantities of two ionic precursors. The obtained Au-Ag clusters can be isolated

from the reactive mixture by co-precipitation with acetone and, analogously to PVP-embedded pure-Au clusters, they can be treated by alcoholic solutions of thiols to give thiol-derivatized clusters. Since the reduction of gold ions by ethylene glycol in presence of PVP has an induction time (due to the initial reduction of Au^{3+} to Au^{+}), typically the reaction was done by mixing a solution of $HAuCl_4$ and PVP in ethylene glycol with a freshly prepared silver solution in ethylene glycol. Since silver require the presence of PVP for reduction, the silver reduction-precipitation process starts just after mixing of two solutions. Cluster growth was end by addition of acetone to the reactive mixture, and the isolated PVP-embedded Au-Ag clusters were dissolved in the alcoholic solution of thiol (e.g., dodecanethiol/ethyl alcohol). Dodecane thiol-derivatized Au-Ag clusers is a stable hydrophobic product that can be easily isolated and purified from the reactive mixture and stored for months without degradation.

Since both silver and gold have optical absorptions in the visible spectral region, important structural information (temporal evolution of average composition) about the growing clusters system maybe obtained by *in situ* on-line spectroscopic monitoring of their formation-growth process. Such analysis is based on the measurement of the wavelength of maximum surface plasmon absorption band of alloyed Au-Ag clusters during their formation process. In particular, the optical absorption spectrum of gold-silver alloyed clusters does not correspond neither to monometallic silver nor to monometallic gold cluster spectra. Both shape and position of alloyed cluster absorption band is exactly an average of two characteristic bands. The exact position of absorption band is related to the cluster composition, and it can be used for such measurement. Since plasmon absorption depends exclusively on the cluster surface composition, the temporal evolution of cluster composition should correspond to radial one if a linear growth law is valid.

In particular, it is known that the frequency of the surface plasmon absorption of pure metal clusters, ω_{sp}, is proportional to the plasmon absorption frequency of the bulk metal, ω_p:

$$\omega_{sp} \propto \omega_p \tag{1}$$

and that:

$$\omega_p = (4\pi n e^2/m)^{1/2} \tag{2}$$

where n is the electron density (i.e., ratio between the conduction electron number and cluster volume), e is the electron charge, and m is the effective electron mass. Since the electron density of alloyed Au-Ag nanoclusters, n_a, depends on the metal composition, (gold volume fraction), according to the following expression:

$$n_a = \phi\, n_{Ag} + (1-\phi)\, n_{Au} \tag{3}$$

the maximum wavelength of the alloyed clusters, $\lambda_{a,max}=2\pi c/\omega_{sp}$, can be written as:

$$(1/\lambda_{a,max})^2 = x/(\lambda_{Ag,max})^2 + (1-x)/(\lambda_{Au,max})^2 \tag{4}$$

Where x is the molar fraction of gold in the alloy that coincides with gold volume fraction, ϕ, since gold and silver have similar values of the molar volume (10.2 cm^3/mol for gold and 10.27 cm^3/mol for silver). Equation (4) can be used to obtain x from experimental measurements of $\lambda_{a,max}$.

The temporal evolution of Au-Ag cluster composition for different reactive mixture composition calculated according to (4) is shown in Figure 7a. According to the experimental determination of surface plasmon absorption of pure Ag and Au clusters produced in a PVP/ethylene glycol medium, the value of $\lambda_{Ag,max}$ and $\lambda_{Au,max}$ have been taken equal to 430nm and 530nm, respectively. Such behaviour may correspond to the radial one if cluster radius develops according to a linear law. As visible, at beginning of reaction the gold content in the clusters is zero, then cluster composition changes, gold amount grows and stabilize on a constant value. Probably, since the two metallic phase have a different nucleation rate (silver nucleate faster than gold), the phase separation process starts with silver core formation and then the co-precipitation of two metals follows according to a heterogeneous nucleation process. During co-precipitation, the alloy composition may slightly vary because of the different consumption of two metals. Consequently, the radial composition of clusters is not uniform, but gold amount slowly decreases during the process. Figure 7b shows the correspondence between the reactive mixture composition (expressed as molar fraction of gold, Y) and the cluster composition (expressed as atomic fraction of gold, X). As visible, the percentage of gold in the cluster increases quickly with increasing of gold salt amount in the reactive mixture. Probably, the nucleation stage is faster for a pure silver phase but the rate of gold atoms deposition at cluster surface is higher than that of silver atoms.

6. APPLICATIONS

Thiol-stabilised gold and Au-Ag clusters prepared by the above described chemical techniques can be used for a number of technological applications. A short description for the prominent potential application of these materials follows.

Thin films of self-organized thiol-stabilized gold clusters have been shown to change their electrical conductivity rapidly and reproducibly in presence of organic vapors [17]. This effect is based on the reversible swelling of the material upon gas absorption, which leads to an increase in spacing between the metal cores. Since the typical electron hopping conductivity in these materials depends very sensitively on such distance, the absorption of organic vapor leads to a strong decrease in electrical conductivity. This phenomenon has been exploited for the development of novel gas sensors [17].

Films of gold nanoparticles exhibit strong optical anisotropy if nanoparticles are aligned into parallel rows. Transmitted light polarized parallel to the rows will be absorbed as if it were passing through a continuous thin metal film, while light polarized perpendicular to the rows will interact with individual particles. This effect can be exploited for polarizing filters for displays. Two different approaches have been developed to align the particles. In the first method, gold nanoparticles have been deposited onto friction-transferred lines of PTFE on glass substrates and optically anisotropic windows were obtained after subsequent drastic heat treatment close to the melting point of the plastic material [18]. In the second method, similar effects were achieved by mechanical stretching of polyethylene films previously loaded with nanoparticles [19]. The particles were found to align parallel to the stretch direction

producing ‘neck-lace’ like structures. For example, for silver-based systems, the perceived color of the transmitted light was yellow if polarized perpendicular to the rows, and red if polarized in parallel.

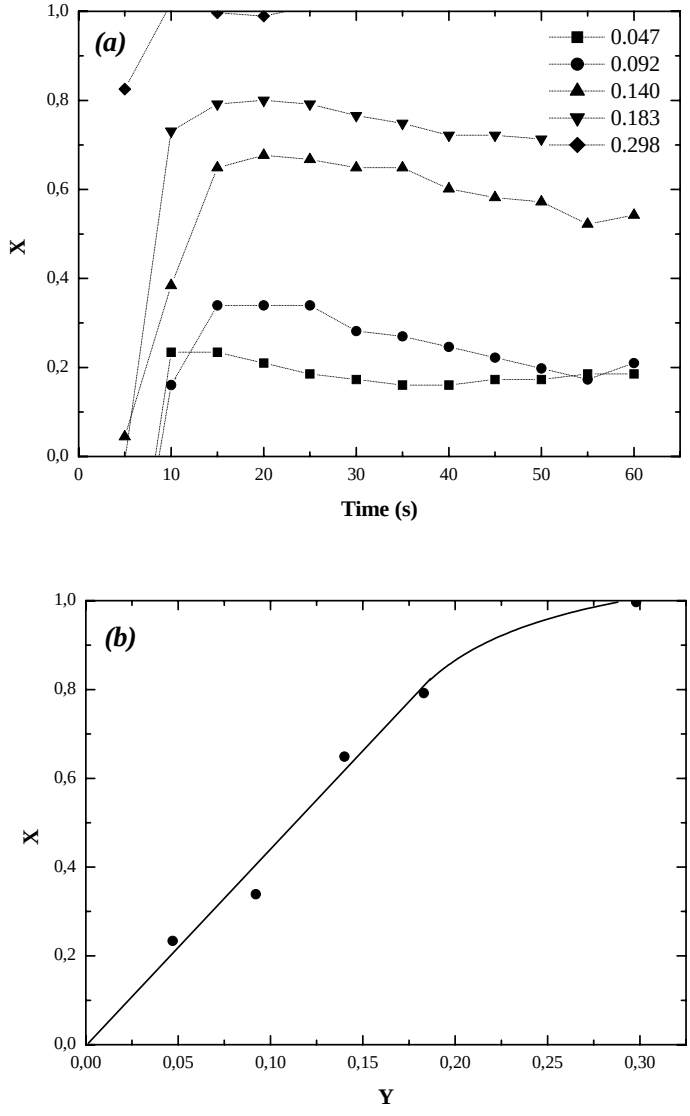

Figure 7. Temporal evolution of Au-Ag alloyed cluster composition for different reactive mixture compositions (a), and correspondence between cluster composition, X (molar gold fraction), and reactive mixture composition, Y (molar gold fraction) (b).

Aggregation of gold nanoparticles produces a color change from ruby-red to blue. This has been exploited to develop extremely sensitive colorimetric methods of DNA analysis, capable of detecting trace amounts of a particular oligonucleotide sequence. This approach also allows to distinguish between perfectly complementary DNA sequences and those that exhibit different degrees of base pair mismatches [20]. The relations between structure and optical properties in these systems have been studied quantitatively [21] by electrodynamics calculations involving aggregates of a large number of particles.

Applications of thiol-stabilized gold nanoparticles in catalysis include asymmetric dihydroxylation reactions [22], carboxylic ester cleavage [23], electro-catalytic reductions by anthraquinone-functionalized gold particles [24] and particle-bound ring opening metathesis polymerization [25]. These catalytic applications have in common the exploitation of carefully designed chemical functionality of the ligand shell, rather than the potential catalytic activity of a nanostructured clean metal surface.

One of the most important potential long-term applications for metal nanoparticles coated by a thin dielectric layer is the development of new, ultimately small, electronic devices. Several promising attempts to construct devices have already been reported, based on gold nanoparticles and Au_{55} clusters [26]. In particular, the single electron transistor action has been demonstrated for systems that contain ideally only one particle in the gap between two electrical contacts separated by only a few nanometres. This central metal particle represents a Coulomb blockade and exhibits single electron charging effects due to its extremely small capacitance. It can also act as a gate if it is independently addressable by a third terminal, for example, the substrate itself, or an appropriately positioned STM tip.

Recently, it has been demonstrated the possibility to fabricate an electrochemically addressable nano-switch based on a single gold particle attached to a gold surface via a small number of dithiol molecules containing a redox-active viologen moiety [27]. It was shown by *in situ* STM that electron transfer between gold substrate and gold nanoparticle depended strongly on the redox-state of the viologen, which could be switched electrochemically.

6. CONCLUSION

Thiol-derivatized pure-gold and gold-silver clusters are nanostructured materials useful for a number of technological applications. The few synthetic methods available in the literature do not offer enough control over thioaurite structure which is of fundamental importance for properties tuning. Consequently, the availability of new chemical routes for the controlled synthesis of these materials result of primary importance. Alcoholic reduction is a well-known technique for preparing colloidal noble metal solutions. This technique is also used in the synthesis of layered core/shell and alloyed clusters. Cluster growth can be monitored by optical spectroscopy and the presence of a polymeric stabilizers makes possible to isolate metal clusters by co-precipitation with polymer with a non-solvent liquid (e.g., acetone), thus allowing size control. Clusters stored in a stable polymer-embedded form can be used as precursor for thioaurite synthesis. The composite solid is alcohol soluble, consequently gold clusters maybe treated by thiols in an alcoholic medium. The thiol molecules chemically adsorb on the gold surface through a red-ox reaction (S-Au bond formation), removing polymer, and the hydrophobic thioaurite product spontaneously

separate. This novel synthesis scheme has been investigated for a number of alkanethiol molecules and it can be utilized also for the preparation of alloyed Au/Ag clusters. The main advantages of this chemical route lies in its simplicity, low toxicity of reactants used, high product purity, and complete control over the compound structure (both nature of the organic shell and size of the metal core).

REFERENCES

[1] G. Carotenuto, Appl. Organomet. *Chem*., 15(2001)344-351; G. Carotenuto, S. De Nicola, G.P. Pepe, L. Nicolais, *Eur. Phys. Journal B* 24(2001)437-441; G. Carotenuto, S. De Nicola, L. Nicolais, *Journal of Nanoparticle Research*, 3(2001)467-473

[2] Y. Sun, Y. Xia, *Science*, 2002, 298, 2176-2179

[3] G. Carotenuto, L. Nicolais, *J. Mater. Chem*., 2003, 13, 1038-1041; G.Carotenuto, L.Nicolais, *Composite: Part B* 35(2004)385-391

[4] W. Caseri, *Macromol. Rapid Commun*. 21(2000)705-722.

[5] M. Faraday, *Philos. Trans. R. Soc. London* 147(1857)145

[6] R.G. Nuzzo, D.L. Allara, *J. Am. Chem. Soc*. 105(1983)4481

[7] M. Giersig, P. Mulvaney, *Langmuir 9*(1993)3408

[8] M. Brust, J. Fink, D. Bethell, D.J. Schiffrin, C.J. Kiely, *J. Chem. Soc., Chem. Commun.* (1995)1655

[9] D. Bethell, M. Brust, D.J. Schiffrin, C.J.J. Kiely, *Electroanal. Chem*. 1996, 409, 137-143

[10] F. Fievet, in *Fine Particles Synthesis, characterization, and mechanism of growth*, ed. T. Sugimoto, New York, 2000, p. 460-496

[11] J. Turkevich, P.C. Stevenson, J. Hillier, *Discussion Faraday Soc*. 11(1951)55-75

[12] U. Kreibig, M. Vollmer, *Optical Properties of Metal Clusters*, Springer-Verlag (1995)

[13] V.K. LaMer, R.H. Dinegar, *J. Amer. Chem. Soc*. 72(1950)4847-4854

[14] R. Zsigmondy, E. Hückel, Z. Physik. *Chem.* 116(1925)291-305

[15] R.H. Terril, T.A. Postlethwaite, C.H. Chen, C.D. Poon, A. Terzis, A. Chen, J.E. Hutchinson, M.R. Clark, G. Wignall, J.D. Londono, R. Superfine, M. Falvo, C.S. Johnson, Jr., E.T. Samulski, R.W. Murray, *J. Am. Chem. Soc*. 117(1995)12537–12548; T. Prozorov, A. Gedanken, *Adv. Mater*. 10(7)(1998)532–535

[16] H. Remita, J. Khatouri, M. Treguer, J. Amblard, J. Belloni, Z. *Phys. D* 40(1991)127-130

[17] H. Wohltjen, A.W. Snow, *Anal. Chem*. 70(1998)2856; S.D. Evans, S.R. Johnson, Y.L. Cheng, T. Shen, *J. Mater. Chem*. 10(2000)183

[18] A.H. Lu, G.H. Lu, A.M. Kessinger, C.A. Foss Jr., *J. Phys. Chem*. B101(1997)9139

[19] Y. Dirix, C. Darribere, W. Heffels, C. Bastiansen, W. Caseri, P. Smith, *Appl. Opt*. 38(31)(1999)6581-6586.

[20] J.J. Storhoff, R. Elghanian, R.C. Mucic, C.A. Mirkin, R.L. Letsinger, *J. Am. Chem. Soc*. 120(1998)1959

[21] A.A. Lazarides, G.C. Schatz, *J. Phys. Chem. B* 104(2000)460

[22] H. Li, Y.-Y. Luk, M. Mrksich, *Langmuir* 15(1999)4957

[23] L. Pasquato, F. Rancan, P. Scrimin, F. Mancin, C. Frigeri, *Chem. Commun.* (2000)2253

[24] J.J. Pietron, R.W. Murray, *J. Phys. Chem. B* 103(1999)4440

[25] M. Bartz, Jo¨rg Ku¨ ther, Ram Seshadri, W. Tremel, Angew. Chem., *Int. Ed. Engl.* 37(1998)2466
[26] T. Sato, H. Ahmed, D. Brown, B.F.G. Johnson, *J. Appl. Phys*. 82(1997)1007; S.H.M. Persson, L. Olofsson, L. Hedberg, *Appl. Phys. Lett*. 74(1999)2546
[27] D.L. Gittins, D. Bethell, D.J. Schiffrin, R.J. Nichols, *Nature* 408(2000)67

INDEX

G

H

I

K

L

M

N

O

P

Q

R

S

T

U

W

X

Z